AN ABSTRACT OF THE THESIS OF

MICHAEL JAMES UNGS for the degree of DOCTOR OF PHILOSOPHY

in FOREST SCIENCE presented on August 28, 1980 .
date

Title: DISTRIBUTION OF LIGHT WITHIN THE CROWN OF AN OPEN-GROWN DOUGLAS-FIR.

Abstract approved: _____
John C. Gordon

A systematic investigation was made of the distribution of short wave radiation within the crown of an open-grown Douglas-fir tree. The study tree was 23 years old, 14 meters tall and had a maximum crown diameter of about ten meters.

Global radiation was measured every 15 cm along eight different horizontal transects through the crown. All radiation measurements taken within the crown were measured by four Kipp pyranometers mounted on a trolley-track system. Three different levels of the crown were examined : the lower 10%, 25%, and 40% vertical position of crown height. At each of these three levels, two horizontal transects were made at right angles to each other along compass directions (i.e., North-South, East-West). Two additional transects were made parallel to the East-West transect at the 25% level but horizontally displaced from the center of the tree.

Global radiation measurements were taken along these transects

approximately every two hours throughout the day during cloudless sky conditions. Measurements were taken during various months of the season over a period of two years. Global radiation was also taken on several overcast days throughout the season.

The penetration of global radiation into the crown on cloudless days was found to be highly variable and was a function of solar position and branch foliage distribution. The greatest penetration occurred when the zenith angle of the sun was equal to the branch angle. The penetration of diffuse radiation was deeper and less variable than that of direct radiation.

Since the study tree could not be destructively sampled, a control experiment using detached branches from other Douglas-fir trees was performed. From the control experiment, it was shown by a photographic technique that a modified form of Beer's Law of radiation penetration was valid for Douglas-fir branches.

A simple geometrical model using solid circular cones is presented. This model can be used to predict the distribution of radiation within the tree crown.

Distribution of Light Within the Crown of an Open-Grown Douglas-fir

by

Michael James Ungs

A THESIS

submitted to

Oregon State University

in partial fulfillment of
the requirements for the
degree of

Doctor of Philosophy

June 1981

APPROVED:

Head of Department of Forest Science
in charge of major

Dean of Graduate School

Date thesis is presented August 28, 1980

Typed by researcher for Michael James Ungs

COMMITTEE MEMBERS

John C. Gordon

H. Richard Holbo

F. Tom Lindstrom

David A. Perry

Larry Boersma

ACKNOWLEDGEMENTS

The author takes this opportunity to acknowledge the advice and assistance given by many throughout this study. Photographic assistance was provided by Alan Doerksen of the Oregon State University Forest Research Lab. Help with the fabrication and the repair of equipment was provided by the machine shop at the Forest Research Lab.

Appreciation goes to Dr. John C. Gordon who as director of my research program, extended the facilities and funds at his disposal to provide assistance with this project.

Special thanks goes to Dr. H. Richard Holbo who gave me more time than he should have, provided helpful counsel, a stimulating atmosphere for research and taught me a working knowledge of instrumentation.

I gratefully acknowledge the assistance and support of Dr. Warren Webb who initiated this project and provided me with the zeal and forethought to complete it.

In addition I give thanks to Dr. Larry Boersma for his vision of unifying mathematics and biology and to Dr. Robert W. Cleary of Princeton University for his vision in applying mathematics to real systems.

TABLE OF CONTENTS

LIST OF TABLES

LIST OF FIGURES

DISTRIBUTION OF LIGHT WITHIN THE CROWN OF AN OPEN-GROWN DOUGLAS-FIR

I. INTRODUCTION

Every organism, plant or animal, on the surface of the earth is immersed in an environment of solar radiation. The total radiation flux within a given site is highly variable, changing with time of day, season, weather and other factors. The above-ground parts of a plant exchange energy by radiative, convective, conductive, metabolic and evaporative processes. Radiation accounts for the greatest percentage (Gates, 1965;Monteith, 1973) of the total amount of energy transferred across the surface of a plant on a daily basis. Thus light, together with gravity, is one of the most important constituents of the environment in determining the course of development in plants. The growth and form of plants from the time of seed germination to maturity is directly affected by solar radiation, its spectral quality and its duration (Brown, 1971).

Plants depend upon radiant energy for the energy necessary to carry on photosynthesis and other physiological processes. The amount of photosynthate produced is dependent not only on the intensity of solar radiation but also on the distribution of this energy within the canopy. Although the importance of canopy structure has long been recognized among forest and crop ecologists, the quanti-

tative measurement of canopy structure and its relationship to light distribution has only recently received attention. Numerious theoretical models, usually based on Bouguer-Lambert's law (Beer's law), can be found in the literature. These models simulate the interrelations between the pattern of leaf arrangement in a canopy and the light interception by leaves. These studies are, however, implicitly restricted to plant communities which have a continuous canopy covering (e.g., cereal crops). In contrast, little is known of the light distribution in forest canopies and even less is known of the light distribution within individual plants or trees.

Study Objectives

The present study had three objectives. The first was to measure the diurnal and seasonal variation of light distribution within the crown of a single open-grown Douglas-fir. The second was to determine a mathematical relationship between light distribution and the variables of leaf area index, light intensity, crown position and solar position. Finally, the third objective was to predict the potential distribution of photosynthate produced within the crown as a function of the measured light distribution.

Literature Review Of Light Penetration:Early Authors

Most of the early papers on light penetration considered diffuse light only. Unfortunately, much of this work is in German and is not readily available. The following review of the German literature is in part taken from Geiger (1965) and Max (1975).

In 1907, Weisner summarized the results of studies of light radiation in plant stands made prior to that time. Weisner addressed two problems that are still of current interest :the significance of sunflecks (direct light) to the light distribution in plant stands and the effect of stand structure upon the penetratration of light into the stand.

Several studies have been conducted to relate the percentage of diffuse light penetrating the entire canopy to measures of the stand such as age, percent crown closure and number of stems per unit area. Wellner (1948) and Miller (1959) studied the relationship of diffuse light to stand age and crown closure in pine forests. Both found a non-linear relationship between the percentage of diffuse light penetrating the canopy and percent crown closure. Some of Miller's data, showing light penetration to the forest floor as a function of stand density, is also given in Geiger (1965). Roussel (1953) used stem density while Jackson and Harper (1955) used basal area to describe the penetration of diffuse light into a pine stand. Radiant flux densities typically decrease curvilinearly as stand density increases. Mitscherlich (1940) used

photographic exposure meters to measure light radiation at the floor of several fir stands and was able to relate light penetration to age of stand and yield class of fir. Some of Mitscherlich's data is also given in Geiger (1965).

Brocks (1939), Ellenberg (1939) and Nägeli (1940) investigated the horizontal spatial variation of light beneath forest canopies. Brocks observed the spatial variation of diffuse light that penetrated an oak and fir forest during leaf expansion. He observed that on clear days significantly more light penetrated the canopy from the direction toward the sun. In heavily shaded sites most of the light penetrated the canopy near the zenith. Nägeli (1940) measured diffuse light variation in mixed deciduous stands by taking measurements on overcast days. He concluded, in agreement with Brocks (1939), that most diffuse light penetrates the stand near the zenith.

Trapp (1938) found that the attenuation of light in a red beech forest followed a smooth, negative exponential, decay-type curve with increasing depth in the forest canopy. When data from clear and cloudy days were plotted seperately, Trapp found two distinct curves indicating that the vertical variation in direct light is different from that of diffuse. Baumgartner (1955) found similar results from his study of light penetration into both young pine and young beech stands.

A Review Of Beer's Law

Beer's law states that the extinction of a monochromatic beam of parallel rays of light in a homogeneous solution of particles of molecular dimensions can be described by a negative exponential relationship (Moneteith, 1973). At any depth x (normalized to make it unitless) in a medium the flux density of radiation can be written as

$$\Phi(x) = \Phi(0) \exp(-k\,x) \qquad (1.1)$$

where $\Phi(0)$ is the flux incident at x=0 and k is the extinction coefficient (unitless).

As stated in Eq. 1.1, Beer's law seems to have little in common with forest and crop canopies. Early workers, however, found that the exponential relationship given by Beer's law seemed to fit the attenuation of light in certain plant canopies.

Literature Review Of Light Penetration : Recent Authors

Monsi and Saeki (1953) concluded that the penetration of radiation into grain canopies is analogous to the attenuation of monochromatic radiation in perfectly turbid media as described by Beer's law (i.e., Eq. 1.1). In the case of vegetation where biomass is rarely distributed evenly with height, the parameter of depth in the exponent in Beer's law is replaced by the total leaf area index

in the vertical canopy layer above the level in question. Others such as Davidson and Philip (1958) and Brougham (1958) developed similar relationships. Monsi and Saeki (1953) considered the extinction coefficient to be a unique characterizing property of any plant association but Isobe (1962) showed that it is also a function of solar elevation and of the angle of leaf inclination. Monsi and Saeki attributed the attenuation of light entirely to the interception by leaves. Transmitted and reflected light were not considered directly. Later, Kasanaga and Monsi (1954) outlined the effects of multiple reflection and transmission by the spectrally selective foliage.

Verhagen et al. (1963) proposed a more general model than that of Beer's law. In Verhagen's model the light radiation at any level in the canopy was assumed to be proportional to the derivative of the function used to describe the vertical attenuation of light as a function of leaf area index and inversely proportional to the light absorption coefficient of the leaves.

Anderson (1966) showed that she and Monsi and Saeki (1953) were using essentially the same mathematical model as that of Wilson (1965). The model of Wilson assumes that light penetration is a function of the number of physical contacts made between a long, very thin needle and foliage when the needle is inclined at any angle. This technique is called the inclined point quadrat technique and has been used by many investigators of light distribution within crop canopies (e.g., Miller, 1969a;Cowan, 1968).

Duncan et al. (1967) modified the model of Monsi and Saeki (1953) to include a term to allow for leaf angle and solar position, the Poisson model. This new term is called the Wilson-Reeve ratio which is divided by the cosine of the zenith angle for the sky position under consideration. The Poisson model is of the form

$$P = \exp(-k\,LAI) \tag{1.2}$$

where P is the proportion of gaps in the foliage, LAI is the downward cumulative leaf area index and k is the extinction coefficient. The extinction coefficient is further defined by the foliage distribution as

$$k = \frac{G_{wr}}{\cos\theta} \tag{1.3}$$

where G_{wr} is the Wilson-Reeve ratio and θ is the zenith angle of the radiation. The Wilson-Reeve ratio described by Wilson (1960) and Reeve (1960) is the ratio of the mean projected area of leaf (i.e., projected onto a plane normal to the light originating from a given angle of θ) to the actual one-sided leaf area.

Nilson (1971) analyzed the gap frequency in plant stands as a function of foliage inclination and leaf area index. Nilson showed that a Poisson model (such as in Eq. 1.2) would describe the gap frequency distribution in stands with randomly dispersed foliage and a positive binomial model would describe the gap frequency distribution in regularly dispersed foliage. In addition, a negative binomial model would describe a clumped foliage

arrangement and for stands in which adjacent layers are not independent, he defined a Markov model.

If the foliage has no preferred orientation and no preferred inclination (spherical distribution of foliage normals), Nilson (1971) showed that the Wilson-Reeve ratio of the Poisson model equals 0.5. Thus the extinction coefficient of Eq. 1.3 reduces to

$$k = \frac{0.5}{\cos\theta} \tag{1.4}$$

Additional details of the above model can be found in Acock et al. (1970) and in Lemeur and Blad (1974).

Anderson (1971) considered the case of scattering and transmission of light radiation through a canopy. Vermilion (1975) developed a radiation model for the canopy of a Douglas-fir stand using Markov probability matrices. Several additional models have been developed to deal with the more complicated case of light interception by isolated plants. Both Charles-Edwards and Thornley (1973) and Mann et al. (1979) developed light penetration models for "ideal" isolated trees. Norman and Jarvis (1975) developed a "grouping" model for light penetration within a spruce canopy, Palmer's (1977) model is for hedgerow apple orchards, and the model of Stamper and Allen (1979) is developed for orange trees.

All of these models of light penetration use an extensively modified form of the Poisson model (Eq. 1.2) in order to improve the fit between theory and data but they also introduce numerous unknowns. Virtually any smoothly varying data set can be curve

fitted to a model if there are enough degrees of freedom (i.e., unknowns). Unless such unknowns can be determined independently of the data set or related to a physiological or morphological process, it makes little sense to use an overly complicated model. The Poisson, the binomial and the Markov models given by Nilson (1971) are basic to describing the process of light penetration into forest and plant canopies.

Literature Review Of The Sampling Problem

As early as 1911, Ramaan recognized that the size frequency of sunflecks from direct light radiation in plant stands was not normally distributed and concluded that the determination of mean levels of illumination was not satisfactory for many purposes. Mean values of radiation within plant stands are especially poor characterizations of radiation distributions for processes such as photosynthesis and transpiration which vary non-linearly with radiant flux density (Norman et al., 1971).

If a canopy were to consist entirely of uniformly dispersed elements of foliage, then only uniformly diffused solar radiation would reach the forest floor. The radiation distribution within such a canopy would be easy to evaluate since all temporal and spatial variations would be smoothed. Unfortunately, most canopies are not like this and the sampling problem becomes very complex because there are gaps that allow direct light radiation to penetrate unattenuated into the canopy. Thus, the radiation frequency dis-

tribution consists of two distinct components : one component consists of diffused solar radiation that is fairly uniformly distributed through the canopy by the scattering action of the canopy foliage, the other consists of direct light sunflecks (Gay et al., 1971).

Typically, frequency distributions of radiant flux densities in the upper portion of plant canopies are bimodal (Niilisk et al., 1970: Hutchison and Matt, 1977). With increasing depth into the canopy, this biomodal distribution decreases or disappears depending upon the character of the stand structure. Frequency distributions at the forest floor tend to be unimodal and highly skewed to higher flux densities (Ovington and Madgwick, 1955;Hutchison and Matt, 1977). Impens et al. (1970) found a bimodal and then a unimodal frequency distribution of net radiation with distance into the canopies of oats, beans, sunflower and corn.

Researchers have found that spatial variations within the canopy are significantly greater than temporal variations. Thus, increasing the number of spatial sampling points is more effective in characterizing the radiation regime than increasing the sampling frequency. Gay et al. (1971) found space averages more effective in reducing deviations about the mean than time averages when sampling in a loblolly pine plantation. Reifsnyder et al. (1971/1972) found that 18 replicate measurements of direct light at the forest floor were necessary in a hardwood forest to obtain instantaneous space means having standard errors of the means of 0.10 cal $cm^{-2}min^{-1}$ or

less. Only two replications of the diffuse measurement were necessary to attain this level of precision for that component. Under a red pine canopy, Reifsnyder found that 412 radiometers would be needed to estimate the instantaneous direct light radiation with the above precision. Only two radiometers would be needed to measure the instantaneous value of diffuse radiation. In a deciduous forest, Droppo and Hamilton (1973) concluded that variation in light radiation at a single location could not be significantly reduced by longer averaging periods in time. Droppo and Hamilton found that the variation at a single location was mostly spatial in nature.

Federer (1968) found that the range in net radiation for six sampling points located two to three meters above the canopy of a hardwood forest and 15 meters apart was about 0.02-0.07 cal $cm^{-2}min^{-1}$ and that arbitrary selection of a sampling point would have given a value within 0.02 cal $cm^{-2}min^{-1}$ of the mean.

Anderson (1964) and Reifsnyder and Lull (1965) surveyed a number of sampling schemes but found few that were very satisfactory. Anderson found that hemispherical photographs gave a reasonably accurate estimate of the mean percentage of diffuse and direct light. Others have successfully used moving sensors to get a spatial average (Allen and Lemon, 1972 ; Brown, 1973; Vermilion, 1975; and others). However, the output of such systems must be corrected in order to eliminate the distortion caused by a moving sensor that has a finite response time. Herrington et al. (1972) provides guidelines for the proper interpretation of information from moving radiometers.

Literature Review Of The Techniques To Measure Leaf Area

The determination of leaf area is an essential part of the light penetration models. Many techniques have been developed to measure leaf area and the particular choice of the method will depend on the objectives of the experiment. One may use either destructive or non-destructive methods and one may be interested either in the leaf area of a single branch, the leaf area of the entire tree, or the area of individual leaves. Leaf surfaces are rarely completely flat but most techniques for leaf area are planimetric. In order to determine the total leaf surface area (by taking into account its three-dimensional geometry) a plane-surface correction factor must be determined. Drew and Running (1975) use a glass-bead technique for correcting the planimetric area of conifer needles.

The historical development of the methods used to determine leaf area is a long one and early reviews of this subject can be found as far back as 1909. One of the most comprehensive and recent reviews is given by Kvet and Marshall (1971). A summary of the principal methods available for leaf area measurements is given in Table 1.1. For each of the techniques listed, a brief discription is given for the most suitable use of the technique (there are many combinations of area measurement techniques and Table 1.1 is not exhaustive). The final choice of any technique will depend on the logistics of the problem, sampling size, required accuracy and precision, cost and final use of the leaf area data. In addition, one technique may be used to calibrate another technique if the

latter is less time consuming, etc.

Most of the methods of estimating leaf area are applicable not only to fresh leaves but also to their images, whether drawn, recorded photographically on film or paper, or as blueprints. Such recording allows the leaf area measurements, which are time consuming, to be done at a more convenient time.

Table 1.1 Summary of techniques used to make leaf area measurements.

Technique	Most Suitable Use	References
counting squares	individual leaves	Kvet & Marshall(1971)
dot counting	broad and relatively short leaves or sets of them	Kvet & Marshall(1971)
leaf counting	sets of leaves, mixed plant communities	Kvet & Marshall(1971)
photographic quadrats	assessment of canopy cover, remote sensing	Williams(1979)
inclined point quadrats	stands, assessment of canopy structure	Wilson(1960)
hand planimetry	individual leaves or sets of leaves of simple shape	Kvet & Marshall(1971)
photoelectric planimetry	large individual leaves or sets of them	Kvet & Marshall(1971)
photographic-photoelectric planimetry	leaves of variable size and number	Marshall(1968)
photographic-electronic planimetry	large individual leaves of simple shape	Theis & Harvey(1979)
optical planimetry	individual leaves or sets of them	Drew & Running(1975)
radiation planimetry	large individual leaves or sets of them	Kvet & Marshall(1971)
airflow planimetry	sets of small leaves	Kvet & Marshall(1971)
photographic image analysis	silhouettes of whole branches	Natr(1968)
gravimetric method	leaves of simple shape	Kvet & Marshall(1971)

Table 1.1 (cont.)

linear measurements	sets of leaves	Kvet & Marshall(1971)
rating method	sets of leaves, foliage of stands, preferably samples of broad leaves	Kvet & Marshall(1971)
leaf weighing	sets of leaves, foliage of stands	Del Rio and Berg(1979) Kvet & Marshall(1971)
glass-bead method	small clusters of conifer needles	Drew & Running(1975)
hemispherical photography	stands, assessment of canopy structure	Evans & Coombe(1959) Anderson(1964)
visual estimation	plantation stands	Carbon et al.(1979)

II. METHODS AND EQUIPMENT USED IN THE STUDY TREE EXPERIMENT

Study Tree Description

The tree chosen for this study is a single 23 year old open-grown Douglas-fir. This tree is a F_1 progeny from a hybrid cross between a bigcone Douglas-fir (Pseudotsuga macrocarpa (Vasey) Mayr.) and a local Douglas-fir (Pseudotsuga menziesii (Mirb.) Franco). The female parent of the cross was selected locally and the pollen was obtained from a bigcone Douglas-fir in southern California (Ching,1959).

The study tree is 14 meters tall and has a 40 cm diameter bole at breast height. At its widest, the crown is about ten meters across. This tree is located next to the Forest Research Lab of Oregon State University in Corvallis, Oregon (latitude 44°33'N, longitude 123°17'W). A photograph of the tree is given in Figure 2.1 . The crown is complete and free from damage and disease. There are 20 live whorls, with branches extending all of the way down to the ground. Several hardwood trees exist to the North and South of this study tree, a building lies to the West and a blacktop road to the East but none are competive with the study tree and it has no physical contact with any of its neighbors. Nutrients and water are probably never limiting since the study tree is periodically fertilized and watered by a lawn sprinkler system.

To estimate the distribution of biomass in the study tree, an extensive series of physical measurements of the branches were taken. Each branch from the ground up to whorl ten (where whorl one is at the top of the tree) was tagged and numbered for identification. Measure-

Figure 2.1 South side of the study tree, a Douglas-fir, showing general relationship of towers and crown.

Figure 2.1

ments include the diameter of a branch at the bole, the horizontal distance to the branch tip, and branch orientation and inclination. All of this information and other branch data are given in Appendix A.

Solar radiation measurements are taken at three vertical levels in the tree, Level 1, Level 2, and Level 3. Level 1 is located between whorls 18-19, 140 cm from the ground, Level 2 is between whorls 15-16, at 320 cm and Level 3 is between whorls 12-13, 520 cm from the ground. At each level, radiation measurements are taken along two different orientations through the center of the tree crown, a North-South and a East-West (exactly along and perpendicular to magnetic North). Hence, a total of six transects are made. Along each transect, radiation measurements are recorded every 15 cm, starting from outside of the crown and progressing in 15 cm increments until exiting out the other side of the crown. All radiation data is taken with four pyranometers mounted atop a trolley. The trolley is moved along a 1000 cm aluminum track (see Figure 2.2).

Almost all of the radiation data was taken along these six transects but two additional transects were used on several occasions. These transects are called TS-1 and TS-2 and are located on Level 2 and oriented East-West with respect to the compass. Both TS-1 and TS-2 are parallel to the standard E-W track of Level 2 but are moved further South of the tree center. The spatial relationships of the track with respect to the tree center and the ground are given in Table 2.1 .

Radiation measurements are recorded throughout the day, throughout the year and under different sky conditions. In order to make all data comparable, the data runs are taken at the same time of the day,

Figure 2.2 South side of the study tree showing the location and relationship between Levels 1,2 and 3. Track rests on small wood blocks, mounted between horizontal 2x4 beams.

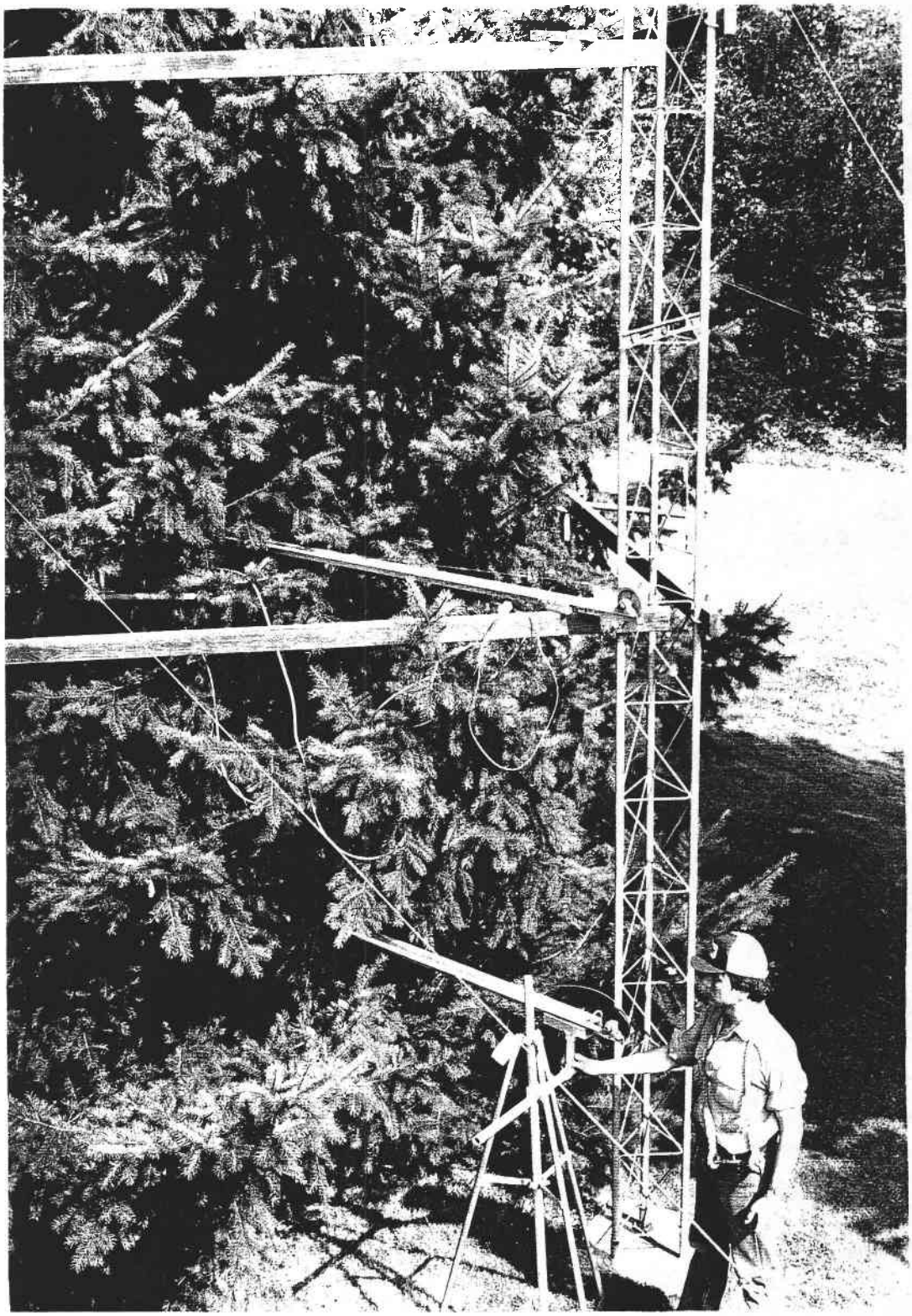

Figure 2.2

Table 2.1 Relationship of the track to the tree center and to the ground.

Track Orientation*	Track Level	Distance From Tree Center	Distance From Ground
N-S	1	44 cm	140 cm
E-W	1	56	140
N-S	2	47	320
E-W	2	30	320
E-W, TS-2	2	176	320
E-W, TS-1	2	261	320
N-S	3	54	520
E-W	3	27	520

* Along magnetic North-South and East-West

every two hours. Table 2.2 lists the dates on which global radiation was measured in the study tree. Table 2.3 lists the dates on which direct solar radiation measurements were taken in the study tree.

The track is carefully positioned along each transect so that all measurements are located within one centimeter of any previous measurement. To obtain a one centimeter precision in positioning the trolley to any given point along a transect, an external frame was constructed around the study tree. Seven TV antenna towers (Rohn Mfg. Co., Reno, Nevada) were erected inside and outside of the crown perimeter (see Table 2.4 and Figure 2.1). Three towers are positioned on the inside and four are positioned on the outside of the crown. Each tower is 550 cm tall and is triangular in cross-section. All towers are rigidly interconnected by sections of pipe and securely guyed with cable to nearby buildings and trees. A large plywood base plate keeps the towers from settling into the ground.

At each of the three levels (140,320 and 520 cm), 2x4 inch wooden

Table 2.2 Dates on which global radiation was measured in the study tree. Data was taken every 15 cm along the track.

Date	Track Orientation	Track Level	Time* (LST,hrs)	Sky** Conditions
7/14/78	N-S	2	12,14,16,18	
7/18/78	N-S	2	8	C
7/18/78	N-S	2	10	
7/19/78	N-S	2	8,9	
8/ 1/78	E-W	2	8,10,12,14,16,18	
8/ 8/78	E-W,TS-2	2	11	
8/ 8/78	E-W,TS-1	2	13	
8/ 9/78	E-W,TS-1	2	10,11,15,16	
8/ 9/78	E-W,TS-2	2	9,12,14,17	
10/ 3/78	N-S	2	12,14,16	
11/14/78	N-S	2	13	
11/14/78	N-S	1	15	
12/13/78	N-S	3	13	
12/29/78	E-W	3	11	
12/29/78	N-S	3	13	
12/29/78	N-S	1	15	
1/ 3/79	E-W	2	12	C
1/22/79	N-S	2	14	
1/22/79	E-W	2	15	
6/15/79	E-W	2	13	C
6/18/79	N-S	2	10	C
6/18/79	N-S	1	11	C
6/19/79	E-W	1	10	C
6/19/79	E-W	3	12	C
6/19/79	N-S	3	13	C
6/25/79	N-S	3	8,10,12,14,16	
6/27/79	E-W	3	8,10,12,14,16	
7/ 3/79	E-W	2	8,10,12	
9/11/79	E-W	2	12,14,16	
9/13/79	N-S	1	12,14,16	
9/14/79	E-W	1	12,14,16	
9/17/79	E-W	2	12,14,16	
9/24/79	N-S	2	12,14,16	
10/ 2/79	N-S	3	12,14,16	
10/ 3/79	E-W	3	12,14,16	

* Local standard time at which data run is started

** C: completely overcast; blank: very sunny, no visible clouds

Table 2.3 Dates on which direct solar radiation measurements were taken in the study tree.*

Date	Track Orientation	Track Level	Time (LST,hrs)	Sky Conditions
9/17/79	E-W	2	13	
9/24/79	N-S	2	15	
10/ 2/79	N-S	3	13	
10/ 3/79	E-W	3	13	
10/ 4/79	N-S	1	13	
10/ 4/79	E-W	1	14	
11/ 7/79	E-W	2	14	

* Direct solar radiation is obtained by first measuring the global radiation and then subtracting out the diffuse radiation which is measured by shading the trolley pyranometers with a clipboard. Data is taken every 60 cm along the track and the global and diffuse measurements are taken within 60 seconds of each other.

Table 2.4 Location of TV towers with respect to the center of the tree trunk.

Tower	Radial Distance(cm)	Angle* (degrees)
1	255	30
2	245	140
3	200	-100
4	460	25
5	465	95
6	465	-150
7	448	-80

* Angle is measured positive, clockwise from true North.

beams interconnect neighboring towers (see Figure 2.1). The wooden beams keep the track supported, leveled and positioned (see mid portion of Figure 2.2). The wooden beams at Level 1 of the outer circle of towers are removed to discourage vandalism. One meter tripods support the outermost portions of the track when using Level 1 (see lower portion of Figure 2.2).

Extreme care was taken when the towers and crossbeams were assembled to prevent damage to the foliage and branches of the study tree. No live branches with a diameter greater than 1.5 cm at the bole were removed. However, most of the dead twigs were removed in the "dead zone" near the bole of the tree (see Figure 2.3) to assist climbing and placement of the trolley-track system. To minimize branch damage, the trolley is moved through the tree crown by means of a cable-pulley setup. The operator normally stands outside of the tree when taking light data (see Figure 2.4) and positions the trolley by pulling on the cable that is connected to the trolley. The cable is marked off every 30 cm to aid in the positioning.

Data Acquisition System

The requirement for measurement precision and for ease in data handling virtually dictated that a digital data logger be used with the radiation measurements. During the two years over which data was collected, over 50,000 radiation measurements were taken and recorded. The output signals from all of the pyranometers were fed into a digital

Figure 2.3 Center "dead zone" of study tree, looking to the Southeast. Each branch is tagged and numbered for identification purposes.

Figure 2.3

Figure 2.4 Typical setup used in taking radiation data in the tree crown. Note remote data switch in left hand. Trolley is manually moved by means of a cable-pulley system.

Figure 2.4

data acquisition system. These signals were scanned every thirty seconds, converted into digital form, and recorded on paper (see Figure 2.5). Edited data was then punched on computer cards for analysis and storage.

A Non-Linear Systems (NLS) data acquisition system (Non-Linear Systems, Inc., Del Mar, California) is used. The NLS has a 25 channel, three wire per channel input capability with a sampling speed of 1.2 seconds per channel. The NLS data system consists of a Model 2310 scanner, a Model X-1 digital voltmeter, a Model 2610 serializer and a Model 2200 digital clock. In the 99.999 millivolt (direct current) range, the NLS digital voltmeter has an accuracy of 0.001 mV, plus or minus 0.005 percent of the reading.

Output of the NLS is routed to a Teletype Corporation Model ASR33 teletype (see Figure 2.6). Seven different variables are recorded during any given data scan. These include the day of the year, hour, minute, channel number, voltage polarity, voltage scale and finally the voltage output of the six pyranometers. The day and time information are only printed once per data scan. When sampling data from six pyranometers, the NLS takes a total of 12 seconds to turn itself on and to print out all of the data.

The NLS acquisition system is located indoors, in a small, insulated room. Room temperature is maintained between 15-25 degrees Celsius. The NLS is connected to the light sensors in the tree crown by a 60 meter insulated data cable. The 100 mV range of the NLS, when connected to the data cable, was tested against a precision Leeds and Northrup millivolt potentiometer, Model 8686. Testing from one to ten

Figure 2.5 Data acquisition system showing, in the background, the digital voltmeter, scanner, serializer and digital clock.

Figure 2.6 Teletype system showing the typical format of the data output. Note location of intercom in upper right corner of photo.

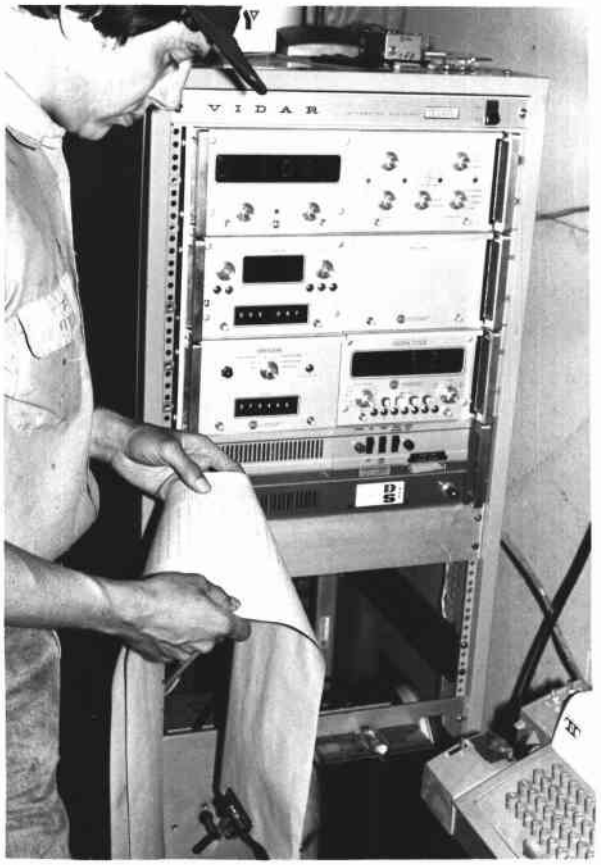

Figure 2.5

Figure 2.6

millivolts, the NLS and the standard agreed to within 0.005 mV. All six data channels were tested (one for each pyranometer). Finally, a zero-shift calibration test was performed by placing the trolley mounted pyranometers into a styrofoam box and kept in the dark for 24 hours. The NLS was connected to the sensors through the data cable. After the first few minutes, the NLS recorded an average value of 0.004 mV during the 24 hour period. The voltage output from a pyranometer is typically between 0.1 and 10. mV. Over this range, the above mentioned errors in the data acquisition system are considered negligible in comparison to the precision and accuracy of the pyranometers.

The NLS was programmed to automatically scan every 1,5,10 minutes, etc., by means of a synchronizing clock. This feature was not desired since the light sensors in the tree crown were moved manually and leveled before each reading. The NLS was rewired and a remote trigger switch was connected to the NLS. By pushing a button (see Figure 2.4) the NLS is activated to sample. A wrist watch showing minutes and seconds is used when sampling in the tree (see Figure 2.4) to make sure that data samples are made at least 30 seconds apart. A 30 second time interval is about three times longer than the time constant response of these pyranometers. This 30 second delay allows the pyranometers to reach an approximate equilibrium state before data is taken. Greater detail is given in a later section on how the time constant of the pyranometer is determined.

Since the teletype would occasionally jam, an open intercom is connected from the teletype to an outdoor speaker (see Figure 2.6). The click-clack noise of the teletype would stop when it jammed.

Trolley System

Measurements of transmitted global radiation within the crown of the study tree are made using a moveable trolley system. An overhead view of the trolley system is given in Figure 2.7 and bottom view is given in Figure 2.8. The trolley system consists of a sensor platform and a carriage platform. Four pyranometers (Kipp and Zönen) are bolted to a 0.64 cm thick, 16 cm by 27 cm slab of Plexiglas (acrylic plastic). The platform is bolted to the carriage platform. The carriage platform consists of a 0.64 cm thick, 20 cm by 24 cm slab of aluminum alloy. The carriage rides atop a track on four Teflon wheels. Grooved, spring loaded wheels on the side hold the carriage to the track and prevent the trolley from overturning. The carriage was salvaged from a previous experiment of Brown (1973).

Six pairs of 22 gauge, individually shielded wire are carried by a Belden 8778 cable from the trolley to the data acquisition system. The data cable is 60 meters long and is attached to the rear end of the trolley by means of a 19 pin connector (MS 3100A series). The data cable drags behind the trolley and is not used to pull or to maneuver the trolley. This arrangement allows for quick and easy attachment to the data system.

The pyranometers are mounted on the trolley platform in the form of a cross (see Figure 2.7). The two middle sensors are centered and mounted nine centimeters apart. The front and rear sensors are mounted 13 cm apart. A spirit level on each sensor allows each one to be leveled independently when the sensor platform is bolted to the trolley.

Figure 2.7 Overhead view of trolley with Kipp pyranometers mounted to it. Small vials connected to the sensors contain silica gel desiccant.

Figure 2.8 Bottom view of trolley showing spring-loaded side wheels which hold the trolley onto the track.

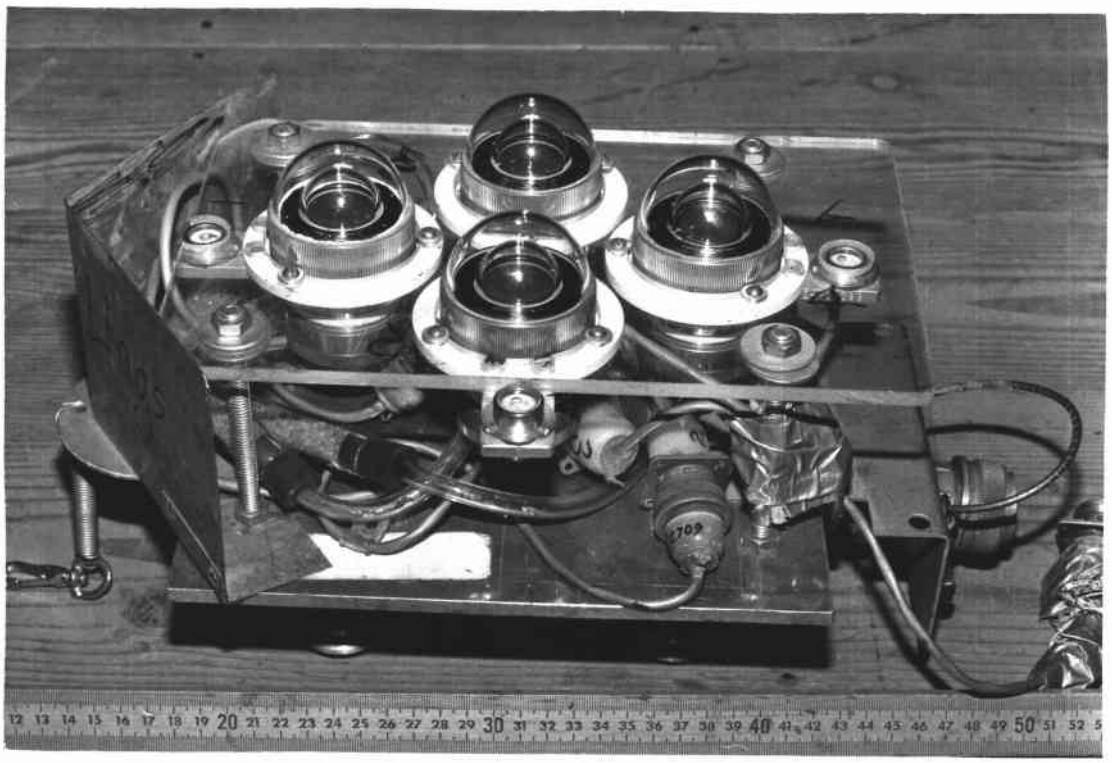

Figure 2.7

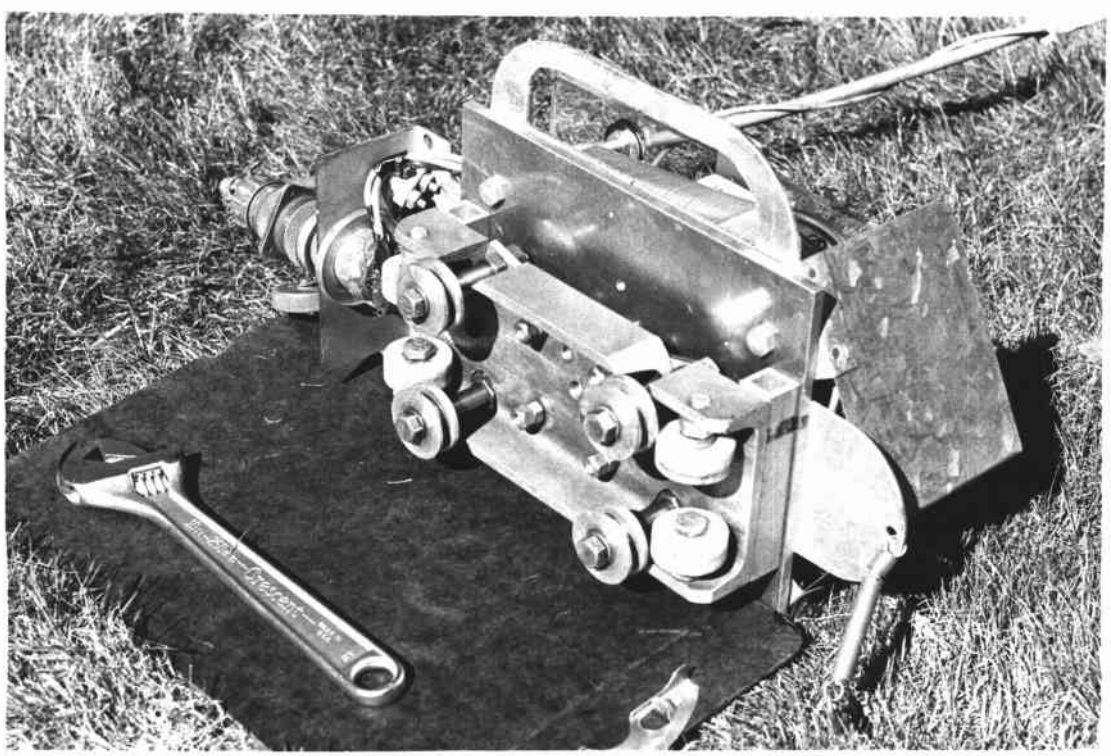

Figure 2.8

Track And Cable System

The trolley is pulled along a track by means of a cable-pulley system. The track is ten meters long and is made up of two bolted sections. Each track section is five meters long, weighs about 5.5 kg, 8.9 cm wide across the flanges, and is made from an extruded aluminum alloy, shape number 54603 (Pacific Metal Company, Seattle, Washington). The track is supported either by a series of 2x4 inch wooden beams strung between the TV towers (see Figure 2.2) or by a short section of track mounted atop a floor flange that is secured to a one meter tripod (see Figure 2.9).

A 20 m length of 0.32 cm diameter aircraft control cable is attached to the two ends of the trolley and around a 13 cm diameter pulley on both ends of the track. The trolley is moved by pulling on this cable. Tension in the cable is maintained by a spring inserted between the cable ends and the trolley. The location of the trolley with respect to the track is determined with the aid of small plastic numerals that are glued every 30 cm along the cable. The cable itself is impervious to both glue and ink since its exterior is protected by an armor plating with a core of oiled wire strands. Small sections of heat-shrinkable plastic tubing, however, will bond to the cable and marker tags are then glued to the outside of this plastic tubing (look closely at the cable line in Figures 2.9 and 2.10).

Data were taken from eight different transects in the tree crown. After removing the trolley, the track was pulled out of the tree and reinserted into a new position by one person. Repositioning and level-

Figure 2.9 Tripod system used to support the ends of the track on Level 1. Note method of attaching the track to the tripod.

Figure 2.10 Shading the trolley mounted sensors with a broom on the North-South Level 1 transect. Normally a clipboard is attached to the end of the broom. Note the small markers attached every 30 cm along the cable, next to the track.

Figure 2.9

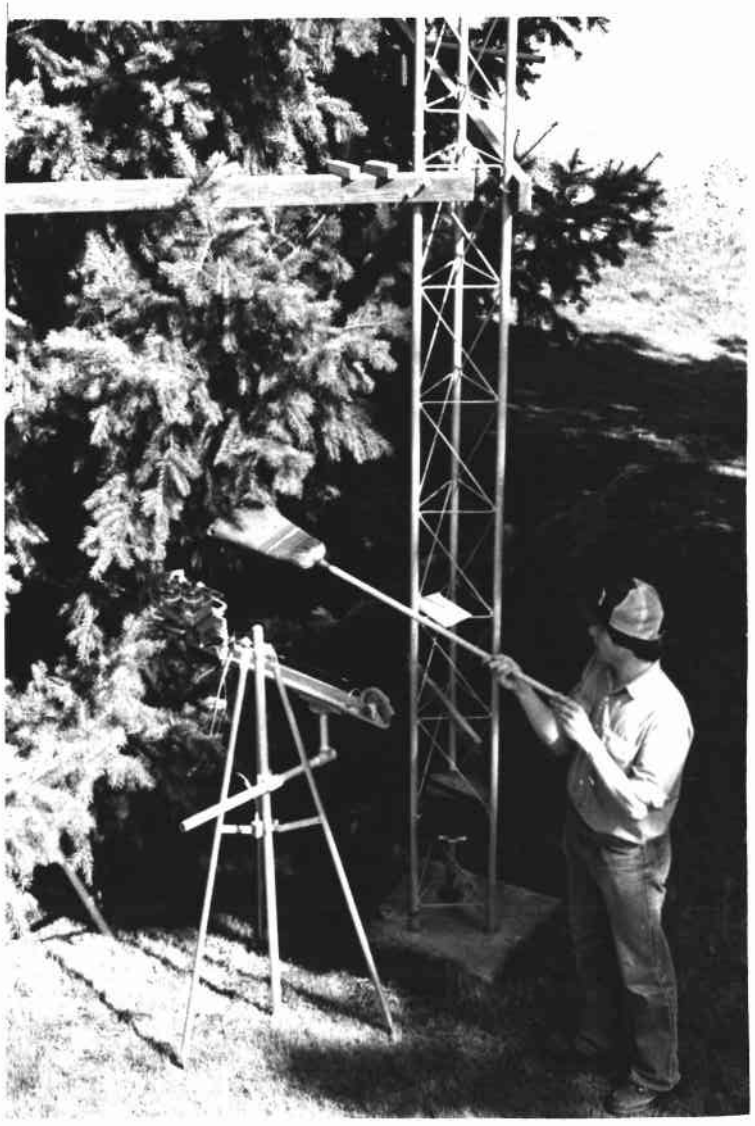

Figure 2.10

ing of the trolley-track system took about 30 to 45 minutes.

Kipp Pyranometer

A pyranometer is an instrument designed to measure solar radiation. The global radiation incident on a horizontal plane, G, is defined as the sum of the direct and diffuse components

$$G = I\cos\theta_z + D \quad (\text{cal cm}^{-2}\text{min}^{-1}) \tag{2.1}$$

where θ_z is the zenith angle of the sun (i.e. measured in degrees from the vertical), D is the intensity of the diffuse or scattered radiation (cal $cm^{-2}min^{-1}$) measured on a horizontal plane and I is the magnitude of direct solar radiation (cal $cm^{-2}min^{-1}$).

Pyranometers have a hemispherical field of view (i.e. a solid angle of 180 degrees) and measure the short wave segment of solar radiation. In this thesis, all global and diffuse radiation measurements are made with six pyranometers manufactured by Kipp and Zönen of Delft, The Netherlands. The trade name of the pyranometer is Solarimeter, Type CM-2 and is hence forth referred to as a Kipp pyranometer.

A list of all of the Kipp pyranometers is given in Table 2.5. A reference pyranometer (#2731) is mounted atop the roof of a building next to the study tree and provides a measure of global radiation in the opening. Another reference pyranometer (#2243) is also mounted atop the roof but is shaded by means of a circular disc and is used to measure diffuse radiation in the opening. A photograph of these reference pyranometers is given in Figure 2.12. Sensors #2271,2379,2709 and 3299 are mounted on a trolley platform and are used to measure

global radiation inside of the tree crown. A photograph of these sensors is given in Figure 2.7.

Table 2.5 Identification of the Kipp pyranometers.

Application	Factory* Serial Number	FRL Id.**
roof sensor (full sun)	CM2-662731	2731
roof sensor (shaded)	CM2-652243	2243
trolley sensor #1	CM2-652271	2271
trolley sensor #2	CM2-662709	2709
trolley sensor #3	CM2-652379	2379
trolley sensor #4	CM2-683299	3299

* Serial number designated by Kipp and Zönen where the first two numerical digits to the right of CM2 indicate the year of manufacture (e.g. 1966).

** Identification number used by the Forest Research Lab at Oregon State University.

The receiver of a Kipp pyranometer is a Moll-Gorczynski thermopile consisting of 14 strips of constantan-manganin in series. Strips of silver foil, arranged in a horizontal plane, are coated with a very fine carbon black and their ends are alternately connected to the constantan and manganin elements of the thermopile. These connections form the hot ends of the thermocouples, the cold ends being placed in a block of brass under the receiver (Kubin, 1971).

The receiver of a Kipp pyranometer is enclosed within two concentric, hemispherical glass domes. The glass is about 0.2 cm thick,

Figure 2.11 Calibration of the Kipp pyranometers (lower center) against a standard Kipp pyrheliometer (lower right). Instruments are shown for illustrative purposes only and are normally mounted atop the platform shown in the center. Study tree is in the background.

Figure 2.12 Roof mounted Kipp pyranometers used to measure global radiation in the open (right side) and diffuse radiation in the open (left side).

Figure 2.11

Figure 2.12

the inner and outer ones having, respectively, a diameter of 2.6 and 4.6 cm. A small bottle of silica gel desiccant is connected through a tube to the inside of the domes to prevent condensation. The glass domes have a uniformly high transmission characteristic for radiation in the 320 to 2500 nanometer (nm) spectral range. The transmission falls off rapidly beyound 2500 nm. The double glass domes cut out less than 3.2% of the total incident solar energy (Coulson, 1975).

A 30 cm white laquered tin screen prevents the base of the instrument from being heated by direct solar radiation. The sun screens are only used with the roof mounted reference pyranometers (see Figure 2.12) since they are always in direct sunlight. Sun screens are not mounted to the trolley pyranometers (see Figure 2.7) since they are too large to fit through the tree branches.

The total size of the thermopile receiver is 1.1 by 1.2 cm. The thermopile has a sensitivity of about nine millivolts per calorie per square centimeter per minute (mV/[cal $cm^{-2}min^{-1}$]) and has a resistance of about eight ohms. An experimental determination of the calibration constants and time constant for the instruments used in this thesis are given in later sections. A more detailed description of pyranometers is given by Coulson (1975), Kubin(1971) and Robinson (1966). A fairly thorough examination of the heat transfer in the Kipp pyranometer can be found in Anderson (1967).

Kipp Pyrheliometer

Direct solar radiation, I (cal $cm^{-2}min^{-1}$), is measured by a

Linke-Feussner pyrheliometer. The pyrheliometer is manufactured by Kipp and Zönen of Delft, The Netherlands, and is called an Actinometer, Type CM-1 (serial #CM1-640087, manufactured in 1964). This pyrheliometer is hence forth referred to as a Kipp pyrheliometer.

The Kipp pyrheliometer uses a specially designed Moll thermopile consisting of 40 manganin-constantan thermocouples arranges in two equal sectional arrays, which are connected in opposition. One section is exposed to the radiation being measured and the other is shaded (Coulson, 1975). The thermopile resistance is about 70 ohms and the sensitivity is about 13.3 mV/(cal $cm^{-2}min^{-1}$) at 20°C.

No mechanism is provided to compensate for the change of signal from the thermopile with the instrument temperature. The temperature calibration factor is given by the expression

$$I = \frac{E}{S_{20}[1-0.002(T-20)]} \quad (\text{cal } cm^{-2}min^{-1}) \qquad (2.2)$$

where E is the measured voltage (mV) from the Kipp pyrheliometer, S_{20} is the sensitivity coefficient at 20°C (i.e. 13.3 mV/[cal $cm^{-2}min^{-1}$]) and T is the temperature (°C) of the instrument. Instrument temperature is taken from a thermometer embedded in the mass of copper rings surrounding the Kipp pyrheliometer.

The Kipp pyrheliometer is attached to an azimuth and elevation mount by which the sensor may be oriented in any direction of the hemisphere. When measuring direct solar radiation, the instrument is first leveled and then pointed directly at the sun by means of a sighting mechanism. In addition, solar zenith may be measured by this instrument to within 0.1 degrees by means of a vernier scale. The Kipp pyrheliometer may be seen in the lower right corner of Figure 2.11

where it resembles a small cannon. Additional details are given by Kipp and Zönen (1961), Coulson (1975) and Robinson (1966).

Calibration Constant Of Kipp Pyranometers

The calibration constant defines the output response (measured in millivolts) of the Kipp pyranometer to a unit change of incident radiant flux density (cal $cm^{-2}min^{-1}$). Individual Kipp pyranometers of identical dimensions may have calibration constants varying from 7.7 to 8.7 mv/(cal $cm^{-2}min^{-1}$). These differences are probably due mostly to variations in the electrical efficiency of the thermocouples (Anderson, 1967).

Each Kipp pyranometer is calibrated at the factory when initially purchased. With time, however, this calibration factor will change due to a gradual degradation in the absorptivity of the optical black paint covering the thermopile elements. The black paint tends to flake off and/or becomes contaminated with moisture and dust under field conditions and frequent handling. Since most of the Kipp pyranometers were purchased in 1966, it was decided that they needed to be recalibrated. The calibration constant is determined by calibrating the Kipp pyranometer against a Kipp pyrheliometer using direct solar radiation measurements in the field. Using the Kipp pyrheliometer as a standard reference is somewhat arbitrary since it is also dependent on a calibration constant, S_{20}, computed by the factory. Of the two, however, the Kipp pyrheliometer has been the least exposed to rough handling and outdoor weather conditions.

The calibration procedure is as follows :

i) The pyrheliometer is leveled, aimed at the sun, its voltage E(mV) and instrument temperature T(°C) recorded and the solar zenith angle, θ_z(degrees), measured.

ii) Using the temperature compensation formula of Eq. 2.2 and the results of step i), compute the direct radiant flux density, I (cal $cm^{-2}min^{-1}$) as measured by the Kipp pyrheliometer.

iii) Level and record the voltage, G_v(mV), of the Kipp pyranometer in full sunlight, measuring the global radiation.

iv) Shade the Kipp pyranometer and record its voltage, D_v(mV), to obtain the diffuse radiation measurement.

v) The calibration constant of the Kipp pyranometer is computed from the formula

$$k_{pyra} = \frac{G_v - D_v}{I \cos\theta_z} \qquad (mv/[cal\ cm^{-2}min^{-1}]) \qquad (2.3)$$

Best results are obtained with this method by taking a series of determinations during a clear day when the sun is high above the horizon. One of the most critical aspects of this method is to make sure that the entire glass dome of the Kipp pyranometer is shaded and that the shading device subtends approximately the same solid angle at the Kipp pyranometer as that which is encompassed by the field of view of the Kipp pyrheliometer (Coulson, 1975). Only in that case is the Kipp pyranometer shielded from the same amount of radiation as that received by the Kipp pyrheliometer.

The Kipp pyrheliometer acceptance aperture is a cone of 10.2°

(total angle) and the diameter of the opening of the entrance diaphragm is 1.26 cm (Coulson, 1975; Kipp and Zönen, 1961). A 9.5 cm diameter circular shading disc located 50 cm from the Kipp pyranometer will subtend a solid angle of 10.9°.

Using the above procedures, it was found that the calibration constants of the Kipp pyranometers have decreased, on the average, three percent from their values given on the calibration certificates. This decrease in sensitivity amounts to only 0.2 percent per year. These results are consistent with those of Szeicz (1968) who reported a decline of 0.1% per year in the calibration constant for his Kipp pyranometers.

Temperature Coefficient Of The Kipp Pyranometers

The calibration constant of the Kipp pyranometer is a function of temperature (Robinson, 1966). Temperature affects the calibration constant k_{pyra}, by changing the conductivity of the air under the glass domes. Coulson (1975) and Robinson (1966) report that temperature decreases the calibration constant from 0.15 to 0.20 % per degree Celsius as the temperature increases. The calibration constant is adjusted for temperature by the expression

$$k_{prya}(T) = k_{pyra}(20°C)(1-0.002[T-20]) \quad (mV/[cal\ cm^{-2}min^{-1}]) \quad (2.4)$$

where the value of 0.20% per °C is used for the temperature sensitivity coefficient and where T is the temperature of the pyranometer (°C).

If the Kipp pyranometers were originally calibrated at 20°C and if the temperature varies from zero to 40°C, then the calibration constant

will vary at most four percent above and below its standard value at 20°C.

Using the calibration procedure given in the previous section, the calibration constants of the Kipp pyranometers were computed, adjusted for temperature using Eq. 2.4 and listed in Table 2.6. Six observations were made for each sensor over a period of two hours. Sensors #2271,2379,2709 and 3299 were mounted to the trolley when tested.

Table 2.6 Calibration constants of the Kipp pyranometers.

Application	Identification	$k_{pyra}(20°C)$ mV/(cal $cm^{-2}min^{-1}$)
roof sensor (full sun)	2731	8.45 ± 0.07
roof sensor (shaded)	2243	8.99 ± 0.09
trolley sensor #1	2271	9.09 ± 0.10
trolley sensor #2	2709	8.60 ± 0.13
trolley sensor #3	2379	8.70 ± 0.10
trolley sensor #4	3299	8.00 ± 0.10

± 95% confidence interval

The affect of temperature may be eliminated by using hydrogen instead of air between the glass domes of the Kipp pyranometer (Robinson, 1966). In addition, a temperature compensating circuit may be added to the output of the Kipp pyranometer (Weaving, 1975). In this thesis, however, the calibration constant is adjusted for temperature by using the value of air temperature in Eq. 2.4 and the computed values of $k_{pyra}(20°C)$ in Table 2.6. Thus given the voltage

output D_v and G_v of a Kipp pyranometer, the diffuse and global radiation are determined from the expressions

$$D = \frac{D_v}{k_{pyra}(T)} \qquad (cal\ cm^{-2} min^{-1}) \qquad (2.5)$$

$$G = \frac{G_v}{k_{pyra}(T)} \qquad (cal\ cm^{-2} min^{-1}) \qquad (2.6)$$

where D_v and G_v are measured in millivolts and T in degrees Celsius. The magnitude of direct solar radiation is computed from

$$I = \frac{G - D}{\cos\theta_z} \qquad (cal\ cm^{-2} min^{-1}) \qquad (2.7)$$

where θ_z is the solar zenith angle, measured in degrees.

Cosine Response Of Kipp Pyranometers

One of the most common errors in using a pyranometer and perhaps the most difficult to eliminate, is the so called "cosine effect" produced by the instrument response being a function of the angle of incidence of the radiation. Unevenness in the surface of the thermopile and the dependence of reflectance and absorptance of surfaces to the angle of the radiation produces a departure from an exact cosine response (Coulson, 1975). Defects in the hemispherical glass domes, incorrect leveling, warped thermopile surfaces and internal reflections inside the instrument may also contribute to errors in radiation measurements.

If the Kipp pyranometer possessed a perfect cosine response and

if it were leveled on a horizontal surface, it would only measure the vertical component of direct radiation

$$I_{pyra} = I\cos\theta_z \qquad (\text{cal cm}^{-2}\text{min}^{-1}) \tag{2.8}$$

By comparing the direct radiation measurement of a Kipp pyranometer against the direct radiation measurement of a Kipp pyrheliometer, one may detect deviations from the ideal cosine response. Let $f(\theta_z)$ be the ratio of the vertical component of direct radiation measured by a Kipp pyranometer divided by that measured by a Kipp pyrheliometer

$$f(\theta_z) = \frac{I_{pyra}}{I(pyrh)*\cos\theta_z} \tag{2.9}$$

where I(pyrh) is the magnitude (normal incidence) of direct radiation measured by the Kipp pyrheliometer and I_{pyra} is the vertical component of the direct radiation measured by the Kipp pyranometer. Upon substitution for I_{pyra}, $f(\theta_z)$ reduces to

$$f(\theta_z) = \frac{G_v - D_v}{k_{pyra}(T)*I(pyrh)*\cos\theta_z} \tag{2.10}$$

Direct solar radiation measurements were taken on August 7, 1978, with Kipp pyranometer #2731 for solar zenith angles between 30 and 75 degrees. The results of this test are given in Table 2.7. The error in the cosine response varied from a high of +1.5% to a low of -1.2%, depending on the solar angle. A 95% confidence interval for this deviation from the cosine law is approximately ±1.2% for incidence angles of less than 75 degrees. For solar zenith angles greater than 80 degrees (e.g. during sunrise and sunset) the cosine error may become considerable. Fortunately for this thesis, solar measurements are

never taken for zenith angles greater than 80 degrees because of shadow interferences from nearby trees and buildings.

Table 2.7 Cosine response of Kipp pyranometer #2731.

Air Temperature T(°C)	Solar Zenith θ_z(degrees)	I(pyrh)* (cal $cm^{-2}min^{-1}$)	Cosine Deviation $f(\theta_z)$
42	29.3	1.288	1.015 ± 0.008
45	35.5	1.271	1.271 ± 0.008
46	45.3	1.227	1.011 ± 0.008
46	54.3	1.165	1.003 ± 0.008
46	64.8	1.050	0.992 ± 0.008
43	74.4	0.846	0.998 ± 0.008

± Approximate 95% confidence interval.

* Direct solar radiation measured by the Kipp pyrheliometer, 8/ 7/78.

The cosine error of ±1.2% for Kipp #2731 is comparable to those of the other Kipp pyranometers and of those tested by Coulson (1975) and Robinson (1966). Unlike the temperature correction factor of the previous section, there is no simple way of introducing a cosine correction factor. Not only is the cosine error a function of solar zenith, it is also a function of solar azimuth. The azimuthal dependence is produced by the nonsymmetric orientation of the thermojunctions of the Moll thermopile (Coulson, 1975).

For simplicity, the cosine correction factor for the Kipp pyranometer is only accounted for in the uncertainty term of the calibration constant as follows

$$k_{pyra}(T,\theta_z) = k_{pyra}(T)(1 \pm 0.012) \quad (mV/[cal\ cm^{-2}min^{-1}] \qquad (2.11)$$

The general rule for the variance of a product (see Appendix C) is used to carry out the multiplication of Eq. 2.11 to obtain a new extimate of the 95% confidence interval.

Time Constant Of Kipp Pyranometers

A special test was performed to determine the rate of response of the Kipp pyranometer to sudden changes in radiation flux densities. In this test, a Kipp pyranometer is exposed to full sunlight for several minutes and is then suddenly shaded with a clipboard, allowing only diffuse radiation to strike the sensor. The voltage from the Kipp pyranometer is recorded every 20 seconds. Once the shaded sensor reaches an equilibrium condition, the clipboard is suddenly removed and the sensor is exposed again to full sunlight. Data is taken until a new equilibrium condition is reached. All of the voltages are then normalized with respect to their minimum and maximum values and plotted.

When plotted on semi-logarithmic paper the data falls along a straight line, the slope of which equals the reciprocal of the time constant. The time constant is defined as the time it takes for the sensor to reach 36.8% of its initial value after a step change. However, the response is not strictly exponential after 40 seconds, and hence a unique time constant can not be defined. For most purposes, however, it is possible to define the time constant for the first 40 seconds.

A list of the time constants for the Kipp pyranometers is given in Table 2.8. Note that the time constant is different depending on

whether radiation is decreasing (i.e. being shaded) or increasing (i.e. shade removed). The average value for the six Kipp pyranometers is about 8.7 seconds for a step change of radiation from 1.18 cal $cm^{-2}min^{-1}$ to 0.14 cal $cm^{-2}min^{-1}$. The time constant is about ten percent slower when going from diffuse radiation to that of full sunlight. Weaving and Filshie (1977) determined the time constant for their Kipp pyranometer to be six seconds. Anderson (1967) computed a 4.5 second time constant for her Kipp pyranometer. The time constant is a function of the conductive heat transfer, the thermal capacity and the thermal diffusivity of the sensor and instrument body. The time constant will increase with decreasing light intensity (Anderson, 1967).

Table 2.8 Time constant of the Kipp pyranometers.

Application	Identification	Time Constant* (sec)	
		Radiation Decreasing	Radiation Increasing
roof sensor(full sun)	2731	8.2 ± 0.4	7.4 ± 0.5
roof sensor (shaded)	2243	8.0 ± 0.3	8.0 ± 0.4
trolley sensor #1	2271	9.1 ± 0.3	8.4 ± 0.3
trolley sensor #2	2709	10.2 ± 0.7	9.4 ± 0.6
trolley sensor #3	2379	8.3 ± 0.2	7.7 ± 0.4
trolley sensor #4	3299	8.2 ± 0.5	7.8 ± 0.5

± Approximate 95% confidence interval.

* Data collected July 24 , 1978, using seven observations for each sensor. The flux density of global radiation equalled 1.18 cal $cm^{-2}min^{-1}$ and for diffuse radiation it equalled 0.14 cal $cm^{-2}min^{-1}$.

Based on the above analysis, it was decided that a minimum of 30 seconds or about three times the time constant was needed for the Kipp pyranometer to reach a reasonable equilibrium condition following any major change in the light conditions. The Kipp pyranometers will reach at least 95% of their equilibrium condition after 30 seconds, following a step change in the radiation flux density. In all subsequent data collection procedures, a 30 second delay is maintained between sequential readings of the Kipp pyranometers.

Sun Shades

Throughout this thesis, various devices are used to block out direct solar radiation and to obtain a measure of diffuse radiation. Global radiation consists of both direct and diffuse components. The Kipp pyranometer measures global radiation whereas the Kipp pyrheliometer measures only direct solar radiation. However, because of its bulky size, weight, and fragileness, it is impractical to use the Kipp pyrheliometer in a tree crown or for general field use. The Kipp pyranometer is very suitable for field use. It can measure diffuse radiation if the direct radiation component is blocked out by means of a sun shade.

In general, two types of shading devices are available, namely, disc and ring. The disc type consists of a small, flat disc which is mounted in such a way that it casts a shadow on the Kipp receiver. The sun-disc-receiver orientation must be constantly aligned so that the disc always casts its shadow on the receiver as the sun moves. The

ring type consists of a ring or frame which constantly shades the receiver. The shadow ring need not be repositioned during the day. The plane of the shadow ring is set parallel to the equatorial plane.

The advantage of the disc lies in its well defined shadow (see Figure 2.12) which is only slightly affected by non-uniform sky conditions. In addition only a small proportion of the sky is blocked out. The disadvantage of the disc shading device is the constant need of repositioning it. However, because it provides a better measure of diffuse radiation, only the disc type sun shade is used in this thesis. Additional information on shadow rings is given by Coulson (1975) and Robinson (1966).

Figure 2.12 shows a circular disc shading Kipp pyranometer #2243. The cardboard disc is 9.5 cm in diameter, painted a flat black and maintained at a distance of 50 cm from the Kipp sensor. Note in Figure 2.12 that the shadow completely covers the outer glass dome rather than just the receiver area. This is done to avoid any internal light reflection within the domes.

The disc is repositioned every 15 minutes to keep the shadow centered over the Kipp pyranometer as the sun moves across the sky. Kipp pyranometers #2243 and #2731 and the shadow disc are mounted on the roof of a nearby building, next to the study tree. A plywood platform under the Kipp sensors prevents light from reflecting from the roof into the sensors.

The arrangement shown in Figure 2.12 worked well for the Kipp pyranometers used to measure diffuse radiation in the open. However, a different approach is used when taking diffuse radiation measure-

ments in the tree crown with the trolley mounted sensors. Because of the large size of the tree and because of the intermingling nature of the branch limbs, it is very difficult to insert any type of instrument into the tree crown without considerable interference. A portable, hand held shadow disc must be used. This shadow disc is rectangular in shape in order to simultaneously shade the four Kipp pyranometers on the trolley.

A 22 cm wide by 32 cm long clipboard was painted a flat black and mounted onto the wide end of a broom. When used in the tree crown, this shade device is held perpendicular to the sun rays and is kept a minimum of 75 cm from the Kipp pyranometers mounted atop the trolley. Figure 2.10 shows how the shadow disc is positioned to shade the trolley but note that the clipboard is removed in this photo. In the mid-left side in Figures 3.1 and 3.2, the shadow disc is shown to be mounted vertically onto a tripod when used in the branch-control experiment. In the branch-control experiment, the shadow disc is kept at a fixed distance of 270 cm from the trolley mounted sensors when measuring for diffuse radiation.

View Factor Of Sun Shades

A shadow disc is used to obtain diffuse radiation measurements from the Kipp pyranometers. However, the shadow disc itself intercepts a portion of the sky radiation and the Kipp pyranometer will underestimate the total amount of diffuse radiation. The percent of the hemisphere that is not blocked is called the view factor, F_{sky}.

The view factor may be obtained experimentally under cloudy-sky conditions by comparing the measurements of the pyranometer with and without the shadow disc in place. Under cloudy-sky conditions there is only diffuse radiation present. The view factor is assumed to be the same for clear-sky conditions as it is for cloudy-sky conditions. To obtain the total diffuse radiation, divide the measured diffuse radiation by the view factor,

$$D(\text{total}) = \frac{D(\text{measured})}{F_{sky}} \quad (\text{cal cm}^{-2}\text{min}^{-1}) \qquad (2.12)$$

The view factor for the various sun shading devices is given in Table 2.9. Four observations were made for each device under cloudy-sky conditions. The 9.5 cm circular disc was tested atop the roof, next to the study tree. The clipboard device was tested in two different locations, next to the tree crown (see Figure 2.10) and in front of the branch simulator (see Figure 3.1).

One may estimate the view factor by taking the ratio of the solid angle subtended by the device and dividing by 180 degrees(hemispherical view) and then subtracting this ratio from one. The theoretical estimate of F_{sky} for the circular disc and for the clipboard located at 270 cm is almost exactly that obtained experimently. The theoretical estimate of F_{sky} for the clipboard next to the tree crown is too large. The tree crown is apparently blocking 50% of the diffuse radiation from the sky, in addition to the clipboard blocking it. Hence, the true view of the Kipp pyranometer is a solid angle of only 90 degrees and not 180. Substituting in the various angles, one gets that

$$F_{sky}(\text{theoretical}) = (1\text{-}24/90) = 0.73 \qquad (2.13)$$

which is exactly that obtained experimentally (see Table 2.9).

As stated, the clipboard blocks 27% of the diffuse radiation when used in and next to the tree crown. This seems rather high but the clipboard would have to be moved over 400 cm away from the trolley if only 5% of the diffuse radiation is to be blocked. The other sun shading devices are used in relatively open areas with few obstructions but the 75 cm displaced clipboard is used next to the tree crown which effectively blocks out half of the horizon. As is, the clipboard is just large enough to simultaneously block out all four Kipp pyranometers on the trolley. Using a smaller sun shade would reduce the blocking factor but it would considerably increase the time to take data.

Table 2.9 View factor for the sun shading devices.

Device	Minimum Distance To Sensor	Solid Angle Subtended By Device	View Factor F_{sky}
circular disc	50 cm	11 degrees	0.94 ±0.02
clipboard *	75	24	0.73 ±0.06
clipboard **	270	7	0.96 ±0.01

± 95% confidence interval.

* Used in tree crown, 22 cm wide by 32 cm long.

** Used in branch-control experiment, 22 cm wide by 32 cm long.

III. METHODS AND EQUIPMENT USED IN THE BRANCH-CONTROL EXPERIMENT

Introduction

All data collected from the study tree had to be by non-destructive methods. This particular tree is involved in an ongoing genetics program and is being studied by other researchers. Up to this point, the only data collected was that of light intensity measurements and the measurements of the branch physical characteristics. One of the major goals of this research program is to estimate the potential rate of photosynthate production within a tree crown as a function of time and space. Photosynthate production is determined by many variables but two of the more important ones are those of light intensity and that of exposed leaf area. Light intensity may be measured directly within the tree crown. Leaf area, however, can not be measured very accurately by non-destructive techniques.

The following experiment is performed to develop a method to estimate the leaf area in the study tree. To do this, a light interception model will be developed. This model is calibrated using data taken from detached branches from another tree. A combination of photographic and destructive leaf sampling techniques are used. Since branch orientation, branch layering and the size of the branches are all under experimental control, this procedure is called the "branch-control experiment".

Branches Used In The Control Experiment

Branches chosen for this part of the study are taken from ten Douglas-fir (Pseudotsuga menziesii (Mirb.) Franco) trees. These trees are located at the 900 m elevation level of Marys Peak, the summit of the Coast Range in Oregon. Marys Peak is about 25 km to the South-West of Corvallis, Oregon (72 m elevation). A total of ten branches are used, one branch per tree. Each branch is labeled as C1,C2,...,C10 for identification. The branches were typically growing at the four meter level of a tree, facing due North and were growing without competition into a large clearing. Chosen branches are visibly free of disease and damage and uniform in length. The trees are in a second-generation, naturally regenerated forest stand. Physical characteristics of the branches are listed in Table 3.1. Photographs of each branch are given in Appendix B.

The branches were cut with a pruning saw mounted on the end of a long pole. As soon as the branches were brought back to Corvallis, they were set upright in a tub of water and stored in a cool, shaded and windless location outdoors. During the next 60 days of this experiment, little or no needle drop was noted.

Control Stand

In the branch-control experiment, detached branches are mounted in a stand. The stand, referred to as the "control stand", allows branches to be mounted at vertually any height and orientation. The control stand may be seen in Figure 3.1 with a single Douglas-fir branch mounted in it. Three branches are shown mounted in Figure 3.2.

Table 3.1 Physical characteristics of the branches used in the branch-control experiment.

Branch	Branch* Diameter cm	Length Of Branch cm	Max. Width Of Branch cm	Age** yrs
C1	2.7	260	150	8
C2	3.0	260	170	8
C3	3.0	270	150	17
C4	3.1	235	150.	9
C5	2.3	265	105	14
C6	3.4	290	105	16
C7	3.7	295	110	17
C8	3.1	240	190	18
C9	3.4	300	180	19
C10	3.4	280	175	16

* Diameter of branch stem at the "dead-live" transition point of the foliage.

** Number of rings counted in the stem wood at the "dead-live" zone.

The control stand is located on top of a large wooden platform on the roof of a building at the Forest Research Lab at Oregon State University. The building is about 200 m South-West of the study tree. Except for the guard rails and the control stand equipment, there is virtually an unobstructed view of the sky from atop this platform.

The control stand consists of a huge wooden "saw horse" and a metal stand (see Figure 3.1). Metal rods are suspended horizontally between the legs of the saw horse by a rack of nails. The rods may be positioned at height increments and several rods may be used simultaneously. The metal stand is a two meter tall electrical equipment rack that was converted into a stand by drilling holes into its vertical supports. Metal rods are inserted horizontally through these holes.

Metal sleeves are used to hold the proximal end of a branch(see Figure 3.3). The sleeves are v-shaped and have holes in them, through which rods of the metal stand are inserted. The sleeves are used to hold up the proximal end of the branch and prevent the branch from rotating. The distal end of the branch rests on the horizontal rods of the saw horse.

To prevent the detached branches from wilting and to reduce needle drop, the butt ends of the branches are always kept in contact with water. When a branch is not being used in the control stand, the butt end of the branch is kept in a tub of water. When a branch is mounted in the control stand, a rubber bladder is used. Rubber bladders are constructed from sections of motorcycle inner tubes.

Figure 3.1 Branch-control experiment, showing setup used with a single, detached Douglas-fir branch. Note location of clipboard, which is used as a sun shade. Trolley and light sensors are located under mid portion of branch.

Figure 3.2 Branch-control experiment showing multiple branch setup. Branch stems are located 15 cm apart along their central portion.

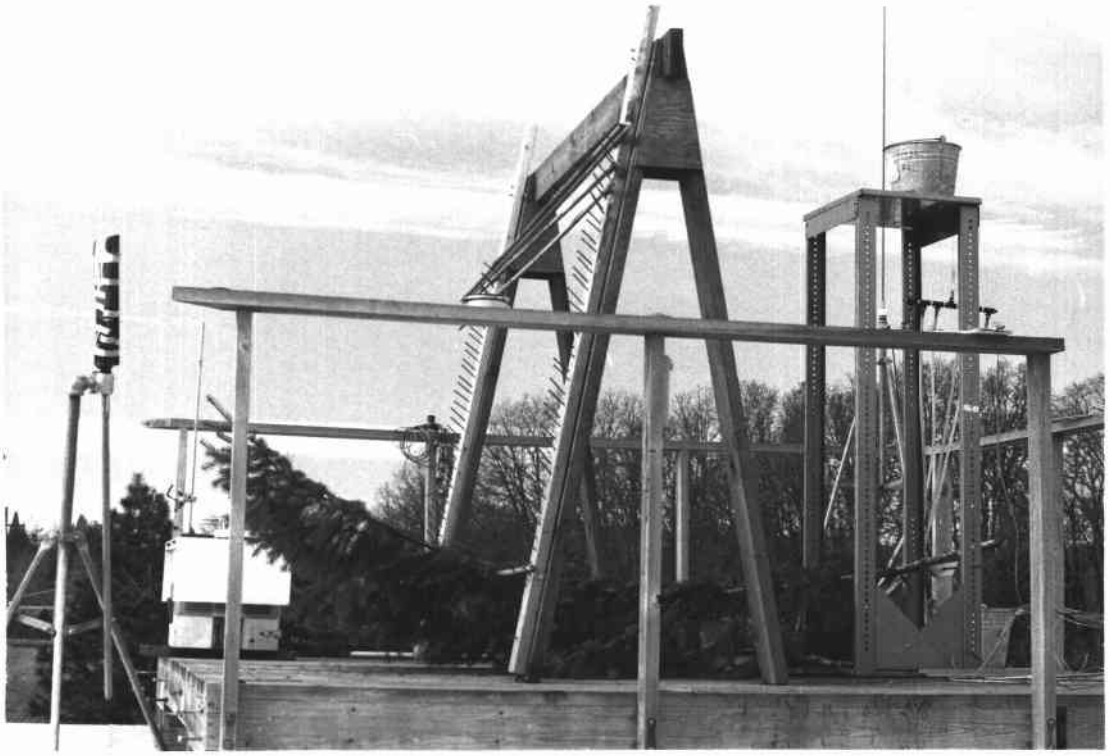

Figure 3.1

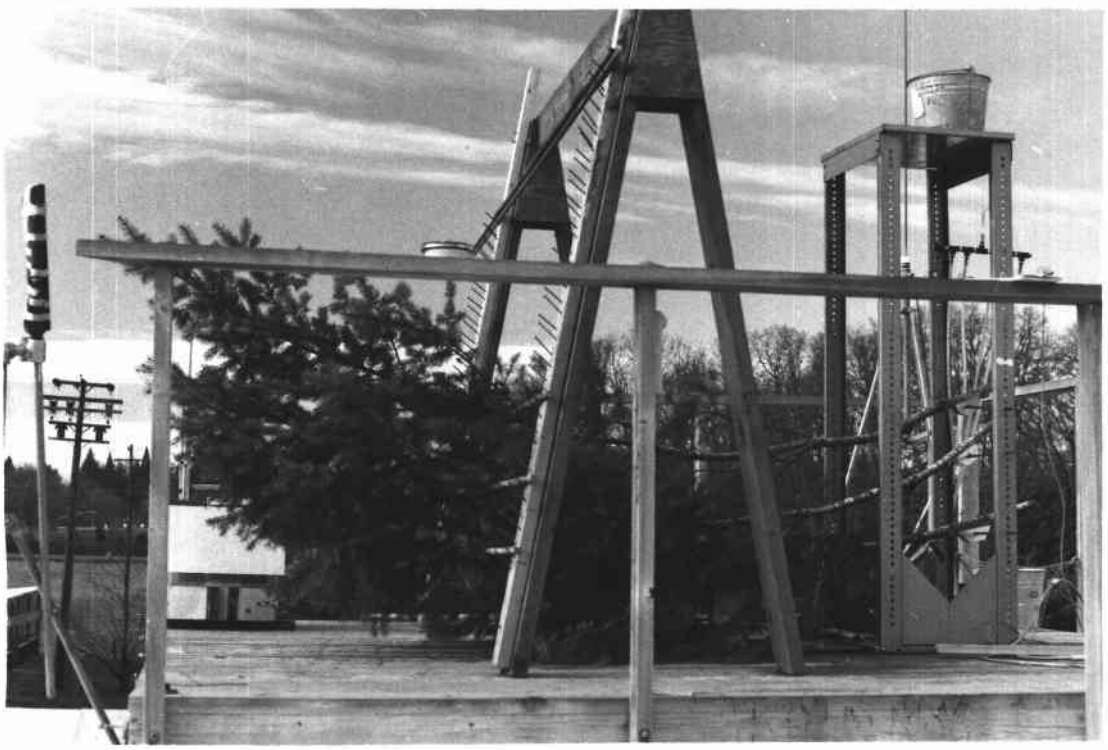

Figure 3.2

Figure 3.3 Metal stand used to support the proximal end of branch sections. Note tubing and rubber bladders attached to butt end of branches. Metal sleeves are used to attach branch stems to horizontal metal bars.

Figure 3.4 Relative location of sun shade (right), trolley (center) and "roof mounted" pyranometers (left) used in branch-control experiment.

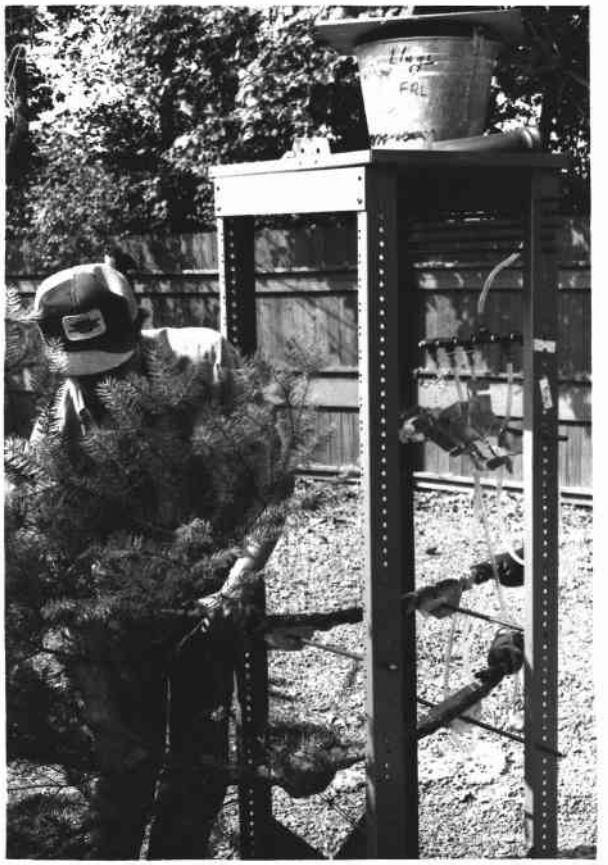

Figure 3.3

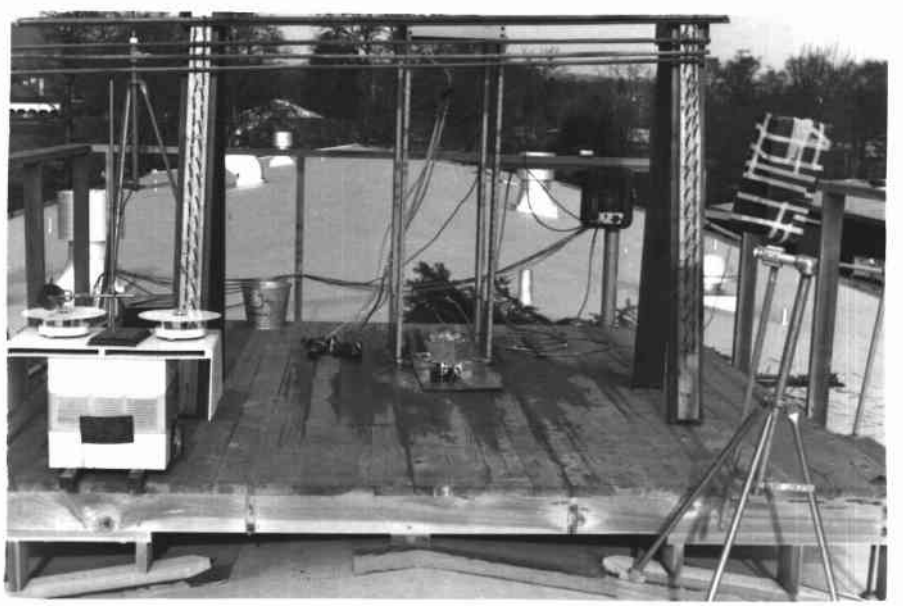

Figure 3.4

One end of the tube is fitted over the proximal end of the branch stem and the other end is fitted with a wooden plug and plastic nozzel (see Figure 3.3). A bucket of water continuously resupplies the bladder. On a hot, windy day, a branch would transpire as much as 100 ml of water while mounted in the control stand.

The relative location of the pyranometers in the branch-control experiment is shown in Figure 3.4. As in the study tree experiment a clipboard was used as a sun shade for the trolley mounted pyranometers to obtain measures of diffuse radiation. A clipboard was taped to the wide end of a broom, painted black and mounted vertically to a TV tripod (see right side of Figure 3.4). The trolley system and its Kipp pyranometers are the same as that used in the study tree experiment.

The main stem of the lowest detached branch is located 15 cm above the top of the trolley. In addition, the trolley is always positioned below section S1 of a branch. Section S1 corresponds to the proximal end of a branch with the oldest, but still living, foliage. This position is the most shaded when the branch is mounted horizontally and the distal end is oriented due South.

Two Kipp pyranometers are mounted atop a small platform to measure open light conditions (see lower left portion of Figure 3.4). These sensors are the same as the "roof mounted" sensors of the study tree experiment. One of these, #2731, measures global radiation and the other, #2243, is shaded and measures diffuse radiation. All six Kipp pyranometers are connected to the NLS data acquisition system by means of a 60 m data cable. Data collection procedures for light

are similar to that of the study tree experiment except the trolley bearing the Kipp pyranometers is always kept in the same position.

Preparation For Leaf Area Measurements

After all of the radiation measurements in the branch-control experiment were taken, the leaf area of these ten branches was measured. Leaf area is measured two different ways. One method measures the total one-sided planimetric leaf area without mutual shading and the other measures with mutual shading (i.e., shadow area). The first method uses a leaf weighing technique and the other uses a photographic technique.

All branches are cut along the main stem into 40 cm by 40 cm sections (see Figure 3.5). Foliage outside of these sections is removed and analyzed separately. Each section is numbered S1,S2,..., S7 where S1 indicates the most proximal section and S7 the most distal end.

Within 24 hours of being cut, the silhouette of each branch section was photographed. The silhouette consists of both leaf and stem area. The shadow area is determined from these photographs with a Quantimet image analyzer. Additional detail is given in Chapter V and in Appendix B.

After the photo work, a subsample of 100 needles were removed, five groups of 20 needles, from each branch section. The fresh leaf area and oven dry weight of the subsamples were determined. Fresh leaf area is then measured with an optical planimeter (LI-COR, Model

Figure 3.5 Photo positive (4x5 inch format) showing silhouette of branch C7, section S4. The number 298 refers to the identification code number of the 35 mm negative slide, imprinted by the Canon Data Back A device. Before the photo area is measured, all the black edges around the photo are trimmed off.

Figure 3.6 Photo positive of branch C7, section S4 after being oven dried and stripped of its needles.

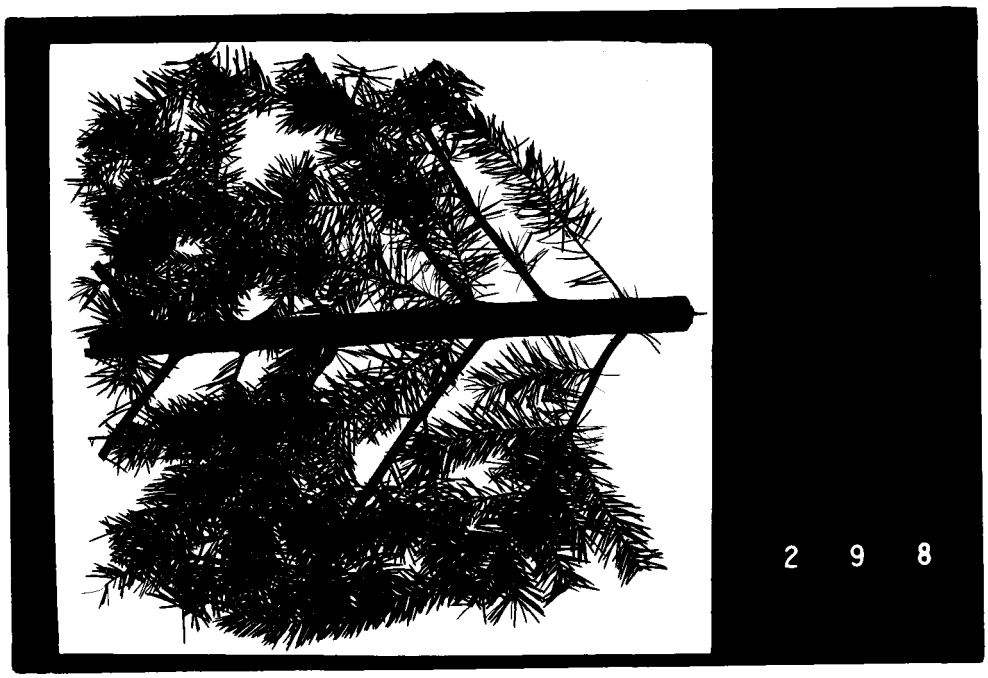

Figure 3.5

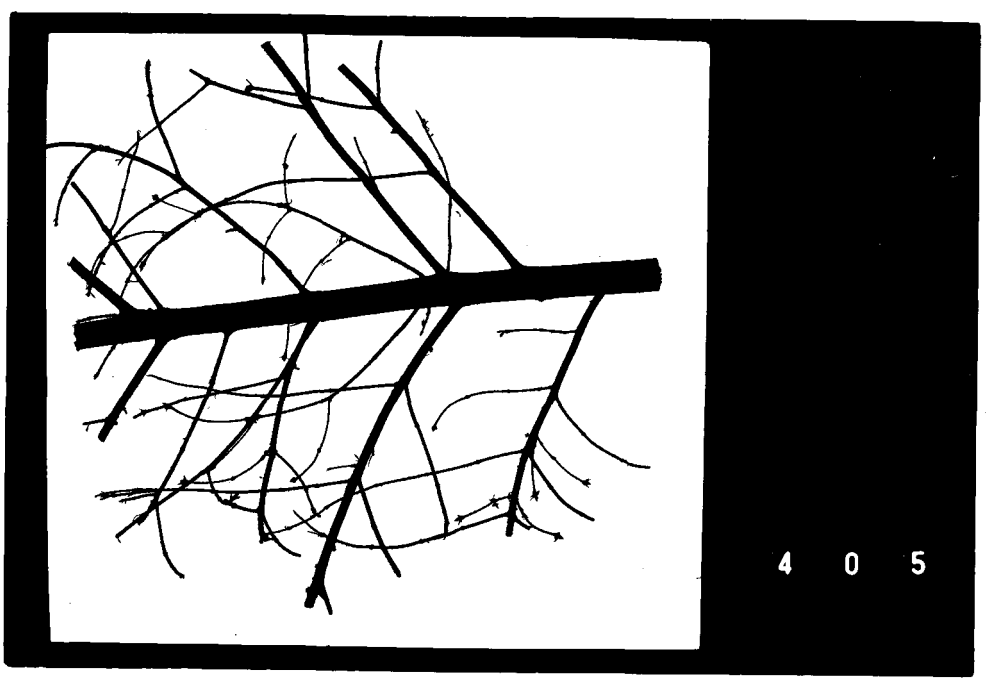

Figure 3.6

LI-3000). The branch sections are then oven dried at 70°C for 24 hours. All of the dried needles are carefully removed from the branches and then weighed. The total projected leaf area with no mutual shading was determined by taking the leaf area to dry weight ratio (i.e., $cm^2 g^{-1}$) from the subsamples and multiplying this ratio by the total dry weight of needles in each branch section. Results of the leaf area measurements are given in Appendix B and discussed in Chapter V.

Finally, the stripped branch stems of each section were photographed to determine the projected stem area. Results are given in Appendix B and discussed in Chapter V.

Measuring Fresh Leaf Area With A LI-COR Optical Planimeter

The fresh, one-sided projected leaf area of detached needles (groups of 20) are measured between two plates of glass by means of a flying spot optical planimeter. The instrument used was a LI-COR model LI-3000 portable area meter (Lambda Instruments Corporation, Lincoln, Nebraska). The instrument consists of a scanning head and a readout-control unit. Area data is accumulated on the readout-control unit display as the scanning head is passed over and under the glass plates holding the needles.

Objects are scanned by means of flying spot which appears on a row of 128 narrow-band red light emitting diodes (LED) located on 0.1 cm centers along a straight line of the upper scanning head section. The scanning head base contains a lens-photodiode system

which responds only to the collimated, pulsed light coming from the LED's. The total time for a scanning event is 896 microseconds (LI-COR, 1979). As the length encoding cord is drawn out the LED's are activated to produce the flying spot scan. This occurs once for every millimeter of cord travel. When a photodiode senses LED light, then that LED location does not contribute to the accumlating area. The leaf area is computed as the accumulated sum of all masked LED's (0.1 cm by 0.1 cm in size) as the scanning head is drawn over the needles.

Calibration Of The LI-3000

The LI-3000 area meter has a specified resolution down to 0.01 cm^2, with less than a two percent error for objects larger than 50 cm^2. However, LI-COR (1979, personal communication) recommends the instrument only for measuring objects larger than 0.1 cm^2. Unfortunately, Douglas-fir needles are about two centimeters long and 0.15 cm wide. Thus the model LI-3000 is marginally suited to measure needle area. LI-COR now manufactures a more accurate model LI-3100, but this model was not available for my use.

The LI-3000 area meter provides a "calibration" screw to either increase or decrease the sensitivity of the optical reader. The manufacture's intended use of the calibration screw is to eliminate spurious signals caused by the presence of dust particles and other impurities in the sample and to eliminate electronic noise. Unfortunately, the calibration adjustment also affects the accuracy of

the area measurement of small objects.

The measured area of several small objects is plotted in Figure 3.7 as a function of the setting of the calibration screw. The sensitivity of the LI-3000 increases when the screw is rotated in a clockwise manner. The zero o'clock position corresponds to the vertical, upright orientation, the three o'clock corresponds to the horizontal orientation, etc. Each point plotted in Figure 3.7 is the average of ten readings. The four objects measured are : 1) a series of 26 parallel lines, each being about 0.068 cm wide and about 6.1 cm long; 2) a group of 20 Douglas-fir needles, about 0.15 cm wide and two centimeters long ; 3) a group of 50 Douglas-fir needles; 4) a group of 32 small round dots, each with a diameter of about 0.67 cm.

When the fresh leaf area of the branch needles was measured, this author was unaware of the extreme sensitivity of the LI-3000 to the setting of this adjustment. The calibration screw was arbitrarily set to the zero o'clock position. As a result, all of the leaf area measurements have to be corrected since the zero o'clock setting gives an underestimate of the "true" leaf area.

The following procedure is used to recalibrate the data taken with the LI-3000 area meter.

i) A 10.0 cm^2 piece of paper is carefully cut from ruled graph paper. This piece of paper is called the reference.

ii) The reference is cut into ten smaller strips, each about one centimeter wide and one centimeter long. All ten of these strips are placed between two sheets of glass and then run through the LI-3000 at least five times. The

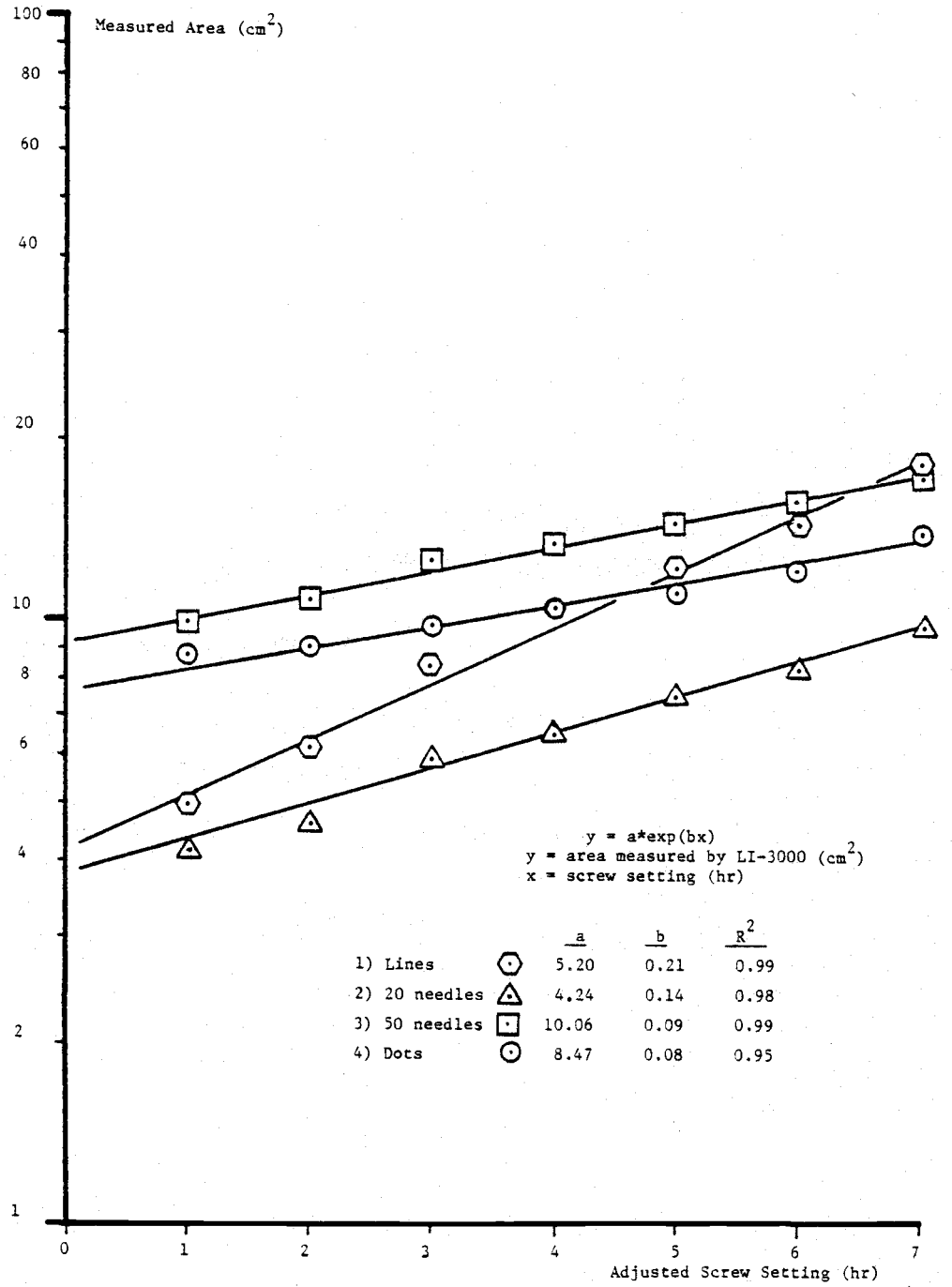

Figure 3.7 Measured LI-COR area as a function of the calibration screw setting.

average measured area is plotted on semi-logarithmic paper as a function of the calibration screw setting. The experiment is repeated with the screw at the zero o'clock position, the one o'clock, and so, on up to six o'clock. The procedure is then reversed and data is taken from the 6,5,...,1,0 o'clock settings.

iii) Using another piece of 10.0 cm^2 graph paper, it is cut into 25 strips, each about 0.2 cm wide and two centimeters long. Repeat step ii) using these strips.

iv) Repeat step ii) using 50 strips of 0.1 cm wide by two centimeter long paper.

Depending on the width of the paper strips, it was found that, on the average, the LI-3000 gave the correct result of 10.0 cm^2 if the calibration screw is set at the three o'clock position. However, the approximate 95% confidence interval for this setting is ± 1 hr.

The scale factors used to adjust the area readings previously taken with the LI-3000 are given in Table 3.2. Thus

$$\text{"true area"} = (\text{scale factor})(\text{LI-3000 area}) \ (cm^2) \quad (3.1)$$

The scale factor is a function of the calibration screw setting used when making the area measurement. The scale factor is computed from the data given in Figure 3.7 for a sample of 20 Douglas-fir needles. The measured area at three o'clock is divided by the area measured at the other calibration screw settings.

For the branch-control experiment, leaf area was underestimated with the LI-3000 by a factor of 1.49 ± 0.20.

Table 3.2 Scale factors to adjust area readings of the LI-3000 when measuring a sample of 20 Douglas-fir needles.

Clock Position Of* Calibration Screw	Scale Factor
0 hr	1.49 ± 0.20
1	1.39 ± 0.19
2	1.11 ± 0.15
3	1.00 ± 0.13
4	0.87 ± 0.11
5	0.81 ± 0.11
6	0.68 ± 0.09

± Approximate 95% confidence interval.

* Setting of calibration screw when making the area measurement.

Measuring Projected Leaf Area By A Photographic Technique

The total projected leaf area with mutual shading is determined from photographs. Photographs are taken of the branch silhouettes. The photographs are first taken with 35 mm, black and white, high contrast film. The negative images from the film are then projected onto 4x5 inch film. Thus the final image is a positive of the original. The silhouette area on the 4x5 inch film is then measured with a Quantimet image analyzer. A calibration procedure is developed to relate photo area to full scale area. The following sections will describe the photographic and calibration techniques in greater detail.

Camera System

Photographs of branch silhouettes used in the branch-control experiment are made with a Canon AE-1 camera fitted with a Canon FD 50 mm, f-1.8 lens. The Canon AE-1 is a 35 mm, single-lens-reflex camera. A 55 mm polarizing filter is fitted over the lens to keep off dust and to reduce the affect of reflected light. The standard film back cover is removed and replaced with the Canon Data Back A. The Data Back A is a data imprinting device that superimposes up to six digits of alpha-numeric information onto the lower right corner of the film. The imprinted code on the film is used to identify individual frames (see lower right corner of Figure 3.5).

The camera is mounted to the bottom of a tripod center column.

The tripod allows the camera to be positioned directly over a branch and then locked in place. The tripod is mounted atop a 120 by 120 cm platform of 0.95 cm plywood (see Figure 3.8). The bottom of each tripod leg is fitted into a small plastic coaster to prevent lateral movement of the camera system and to facilitate the positioning of the camera. The coasters are nailed to the plywood platform.

Background Lighting Used To Create Branch Silhouettes

The camera/tripod system is designed to photograph the silhouette of horizontal branch sections. The branch sections are inserted into the middle of a flat, rectangular shaped plywood box, enclosed on four sides (see lower portion of Figure 3.8). The box is 15 cm high, and 120 cm wide on a side and 120 cm long. The tripod is centered over the top of the box and the source of background light is located below the box. A 42 by 42 cm window is cut into the bottom and top sides of the box. The inside of the box is painted a flat black. Except for the background light source, all photographs are taken in a darkened room. Light passes through the lower window, through the branch, through the upper window and to the camera.

Background light is produced by two fluorescent light bulbs, spaced about 25 cm apart. A 0.32 cm thick, milky plastic cover is located about eight centimeters above the fluorescent bulbs to diffuse the light. The branch sections rest on top of this plastic cover.

Figure 3.8 Tripod system used to photograph branch silhouettes. Note the rectangular pattern of black dots in lower, central portion of photo. Dots are of known area and are used as a photographic reference.

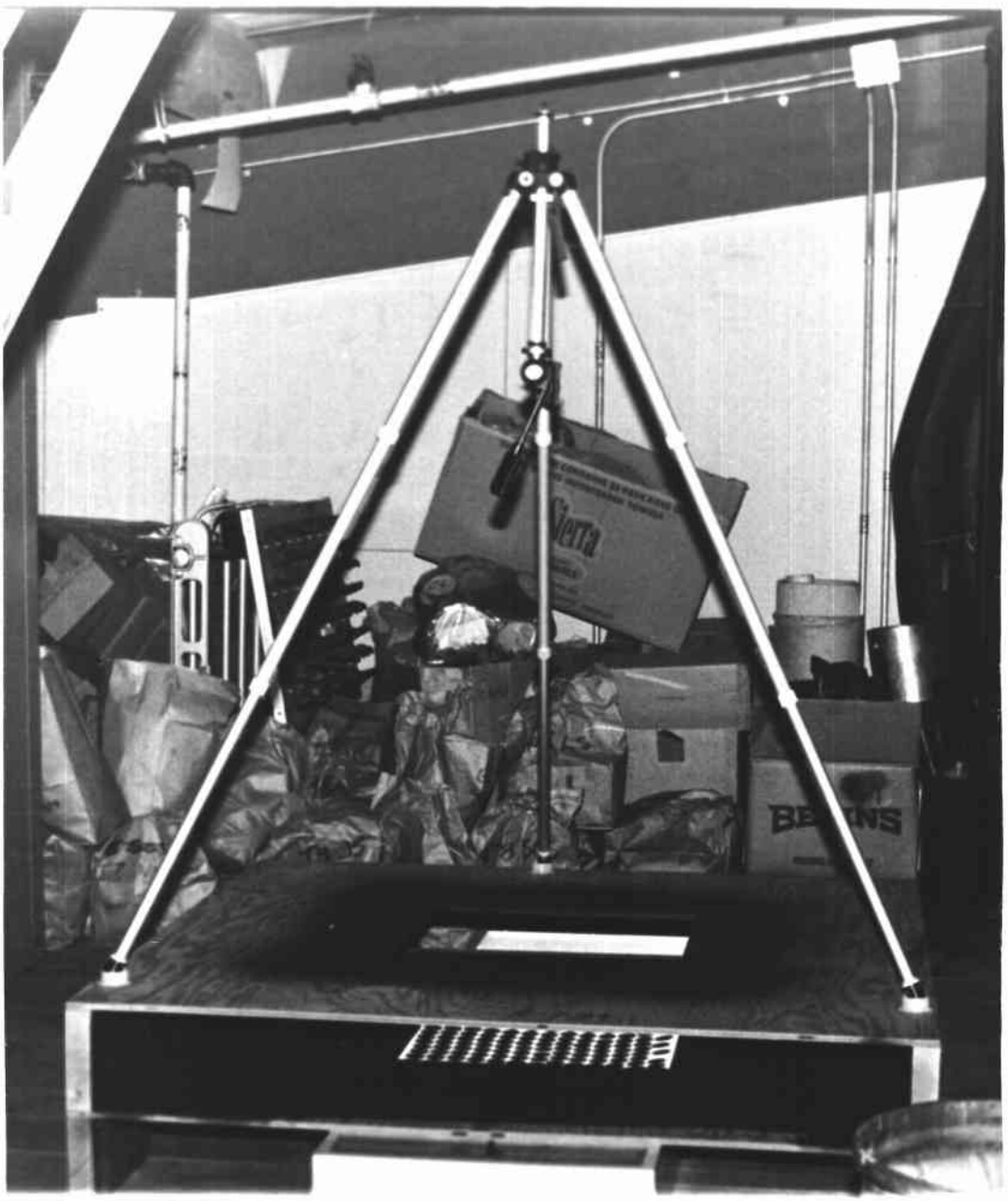

Figure 3.8

Photographic Negatives

Negative images of the branch silhouettes are made on Kodak's 35 mm, black and white, high contrast copy film, type 5069. This particular film is a panchromatic copy film with a micro fine grain. This gives it a very high contrast and resolving power (Kodak, 1979). The film comes in rolls of 36 frames.

It was found through trial and error that the greatest contrast was obtained by slightly underexposing the film and then overdeveloping it. Shutter speed of the camera is set to 1/8 second, aperture to f-11 and ASA is set to 25. This exposure setting is almost identical to that found by metering the background light source. The camera is focused to a distance of one meter. The resultant depth of field is about 15 cm.

The Kodak 5069 film is developed in Kodak Developer D-19 for nine minutes at 20°C, washed in water and then fixed with Kodak Fixer for four minutes. The above process will "push" an underexposed negative. Pushing is used to minimize the development of out-of-focus needles, branch bark and other unwanted surface detail. In addition, pushing reduces the variable contrast affect caused by non-uniform background lighting.

Photographic Positives

After developing the negatives, it became apparent that the photo area of a branch silhouette in a 35 mm negative was too small

to be measured accurately by an optical planimeter (i.e., LI-COR model LI-3000). The maximum picture area of a 35 mm frame is 24 mm by 36 mm. Photographing through a 42 by 42 cm reference window, the area of the image on the negative will be 306 times smaller than the full scale area. Linear dimensions are reduced by a factor of 17.5.

One method of increasing the image resolution is to use a larger film format, such as the 2.25x2.25 inch or the 4x5 inch format. However, the larger film formats require expensive camera systems. Larger format cameras are also bulky, heavy and are not very suitable for taking a large number of negatives. In addition, Kodak only makes high contrast black and white film in the 35 mm and the 4x5 inch format or larger.

A very practical way to increase the resolution is to enlarge the 35 mm negatives into 4x5 inch positives. In a positive image, the black corresponds to the black silhouette and white (i.e., clear) corresponds to the background light.

Kodak manufactures a high contrast orthochromatic sheet film called Kodalith Ortho film 2556, Type 3. This film is on a 0.004 inch Ester base and comes in a 4x5 inch format. The 35 mm negative is placed in a photo enlarger and the image is projected onto the unexposed 4x5 film. Trial and error methods are used to determine the proper exposure time and aperture setting of the enlarger. The 4x5 inch film is developed in Kodak Kodalith A-B developer for 2-4 minutes at 20°C, stopped in acetic acid and then fixed in Kodak Fixer. The entire enlarging and development process may be done

under illumination through a Kodak Safelight Filter No. 1A.

Using the same example as before, a full scale 42 by 42 cm image is reduced to a 9x9 cm positive, reduction in area by a factor of 22 and a linear reduction by a factor of 4.7. Hence, the 4x5 inch format increases the area resolution by a factor of 14 over that of the 35 mm film format.

With the above method, the 35 mm Canon AE-1 camera system is used to take all of the initial negatives and then selected photos are enlarged to a positive 4x5 inch format. Area measurements are made on the photo positives. An additional benefit of this two step process is the increase in black/white contrast. A special feature of the Kodalith A-B developer is its "infectious" nature which causes most of the weakly exposed area (the transitional areas between clear and dark) to become very dense. The developing dense areas "infect" the weak adjacent transitional areas and cause them to develop to high density. Thus the needle images appear more uniform.

Because of the infectious nature of the developer, however, greater care is needed in regulating the development time. If over-developed, the fine detail between needles will close over. One method for retaining fine detail is to use two parts of the "B" solution to one part of the "A" solution. This produces extremely sharp images but with a considerable loss of film speed. Through trial and error, excellent results were obtained using an exposure time of 30 seconds and developing the ortho film for three minutes in a solution of Kodalith A-2B developer at 20°C. The enlarger uses

a 55 mm lens and the aperture is set at f-11.

Since over 300 photos were to be processed, a "tank and hanger" system of development was used. The one quart development tank holds up to eight stainless steel holders of 4x5 inch film. Once mixed, the Kodalith A-2B solution has a very short storage life (about 30 minutes) and the solution becomes depleted after 16 or more photos are developed when using the one quart tank.

Measuring Photo Area With A Quantimet Image Analyzer

It was originally intended to use the LI-COR model LI-3000 area meter to measure the silhouette images on the 4x5 inch photos. However, the precision and accuracy of the LI-3000 in measuring objects less than 0.1 cm^2 had been found to be very poor. The image of a Douglas-fir needle is about 0.03 cm wide and 0.46 cm long in a 4x5 inch photo. After some research, it was discovered that the only suitable technique available to measure the area of small, irregularly shaped objects is that by a Quantimet image analyzer. The only Quantimet available on the West Coast, at this time, is located at the University of California, Davis, California.

All of the 4x5 inch photos were sent to Dr. Jack Pangborn to be analyzed. Dr. Pangborn is in charge of operating the Quantimet at Davis. Before sending the 4x5 inch photos (see Figures 3.5 and 3.6) the outer black margin was trimmed off, including the identification number. If the black trim is left on, the Quantimet will record this as being part of the branch silhouette area. Ideally,

I should have used a larger background light source and larger "photo window". Such a photo would be entirely white (i.e., clear) except for the central silhouette image. The trimmed photos were then individually placed into numbered, plastic sleeves. This indentification procedure is fairly fool-proof but it increases the time it takes for the Quantimet operators to analyze the photos.

The Quantimet, Model 720, is sometimes referred to as an Image Analyzing Computer (Natr, 1968) and is manufactured in the United States by Cambridge Instrument Company, Inc. (Mountain View, Calif.). With the Quantimet, the photographic image is recorded by a television camera and projected onto a monitor. The television image is decomposed into an array of 595 by 595 picture points (Pangborn, 1980). An electronic discriminator then decides whether areas (i.e., picture points) are darker or lighter than a chosen reference value. The television signals are transferred to a computer which evaluates them and the result is indicated as the number of picture points which are opaque. If the photo image is completely opaque, the Quantimet will give a reading of 354025 picture points. If the image is completely transparent or white, a reading of zero is given. Leaf area may be evaluated as either a percentage of the total number of picture points that are opaque or by using regression equations that correlate leaf area with picture points.

Either positive or negative photographic images of leaves may be used provided a certain minimum contrast exists between the leaf image and the background. Differences in contrast exceeding this minimum have practically no affect on the accuracy of the measure-

ments (Natr, 1968). Note that the Quantimet measures the opaque area of a photo. Hence, if one is using a photo negative, leaf area will be proportional to 354025 minus the number of picture points. When using photo positives, leaf area will be proportional to the number of picture points.

Calibrating The Quantimet

A calibration experiment is needed to relate photo area to full scale area. The calibration procedure is a follows. A series of paper dots are glued onto 42 by 42 cm sheets of thin, clear acetate. The dots are 3.18 cm in diameter, have a self-adhesive backing on them and are commerically available from stationery stores. Two dots are carefully placed on top of each other, where the outer one is sprayed with a flat black paint. The two dot technique produces a sharper contrast in the photo image. A series of dot patterns are produced, see Table 3.3, with the dots spread uniformly over the entire sheet.

For calibration, the silhouette of each dot pattern is photographed and the corresponding photo area of the 4x5 inch positive image is measured. The photo area is then regressed against the "true" or full scale area. Photo area is considered as the dependent variable . Given the photo area of any unknown object, the corresponding full scale area may be determined using a "regression in reverse" procedure (Brownlee, 1965).

A linear regression equation of the form

Table 3.3 An example of the dot patterns used to calibrate the Quantimet.

Number Of Dots	Photo Image #	Picture Points	Full Scale Area (cm^2)
0	418	0	0
1	420	1013	7.9
2	421	2031	15.8
4	422	4043	31.7
8	423	8106	63.3
16	424	16403	126.7
32	425	32593	253.4
64	426	65759	506.7
96	427	97372	760.1
128	428	131084	1013.4
160	429	163901	1266.8
15*	430	188646	1450.5
lines**	431	34187	262.3

* Using 7.62x12.7 cm rectangles, each having a measured area of 96.7 cm^2.

** Using 0.32 cm wide black matte tape, a total of 826 cm is used.

$$y = bx \qquad (3.2)$$

is used to calibrate the Quantimet, where y is the photo area (picture points) measured by the Quantimet and x is the full scale area (cm^2). For the data given in Table 3.3, the regression through the origin using Eq. 3.2 results in a r-square equal to 0.9999, a standard error of the variance estimate equal to 777 (12 degrees of freedom), a highly significant F-ratio ($P<0.001$) and a coefficient b equal to 130 ± 0.71 (picture points/cm^2 and 95% confidence interval).

The calibration equation, however, is very sensitive to changes in the position of the camera and the degree of enlargement used to make the 4x5 inch image. A new calibration is typically done for every two rolls of 35 mm film that are taken. Thus, out of every 72 frames, at least 13 of them are used for calibration (i.e., dot patterns). When shooting these 72 frames, the tripod/camera system is not moved, the film is developed in one batch and all of the enlargements are done in one sitting.

Checking The Precision And Accuracy Of The Quantimet

The Quantimet is supposed to be a very precise and accurate instrument. Since I do not have direct access to the Quantimet, only an estimate can be made of these properties. To check the precision of the Quantimet, I requested that multiple measurements were to be taken of certain photos.

A series of photos are made of detached Douglas-fir needles.

Groups of 50,100,150, etc., up to 1650 needles are photographed. The needles are arranged on a 42 by 42 cm sheet of 0.64 cm thick clear glass. Needles are allowed to touch but not overlap. After being arranged, another 0.64 cm thick sheet of glass is placed on top of the needles. The heavy glass is used to prevent the needles from curling. The glass sheets and needles are placed on the same light box used to photograph the branch sections. A photograph is taken of the needle silhouettes. At Davis, I instructed the Quantimet operator to take ten repeated measurements of these photos. Some of the results are listed in Table 3.4. Note that the standard error of the sample mean (i.e., expressed as the 95% confidence interval) is less than 0.3% of the expected or mean value.

The accuracy of the Quantimet is estimated by directly measuring the area of the silhouette image on several 4x5 inch photographs and comparing this to the photo area measured by the Quantimet. Photo area is manually measured using a magnifying lens and a ruler marked off to the 100-th of an inch.

Pangborn (1980) calibrated the Quantimet such that each side of a picture point is 0.0168 cm long. Since a picture point is square in shape, each picture point covers an area of 0.000282 cm^2. Thus the photo area measured by the Quantimet may be obtained by multiplying the number of picture points by 0.000282. The ratio of the ruler measured area divided by the Quantimet measured area gives an approximate estimate of the accuracy. Results are given in Table 3.5. The Quantimet is accurate to at least five percent of its measured value. Since the ruler is only marked off to the nearest 0.0254 of

a centimeter and the Quantimet measures to the nearest 0.0168 of a centimeter, the five percent error is probably due to the ruler and not the Quantimet.

Table 3.4 Estimating the precision of the Quantimet.

Number Of Needles	Photo Image #	Area (picture points)
0	465	0 ± 0
50	466	2603 ± 7
100	467	5424 ± 8
200	469	10779 ± 10
400	473	19390 ± 10
850	478	38917 ± 26
1650	484	74447 ± 71

± 95% confidence interval of the expected area, using ten observations per photo.

Table 3.5 Estimating the accuracy of the Quantimet.

Photo Image #	Description Of Photo	Area Ratio*
430	15 rectangles	0.97
466	50 needles	0.96
490	8 dots	1.05

* Ratio of ruler measured area divided by Quantimet measured area. All areas are measured on the 4x5 inch photos. Needle area is measured by assuming that they are shaped like a rectangle.

IV. MEASURED DISTRIBUTION OF RADIATION

Introduction

The amount of solar radiation passing per unit time through a unit area at right angles to the direction of the solar beam outside of the earth's atmosphere is called the solar constant. The standard value for the solar constant when the earth is at the mean distance from the sun is 1.94 cal $cm^{-2}min^{-1}$ (Coulson, 1975). This varies ±3.4% depending upon the distance of the earth from the sun. The sun, which subtends an angle of 30 minutes as seen from the earth, is generally considered a point source of radiation. Hence, rays of solar radiation reaching the outer atmosphere of the earth are nearly parallel.

Radiation penetrating the atmosphere is attenuated exponentially by atmospheric gases and by dust as a function of the radiation's wavelength. At sea level, the solar constant is reduced to about 1.40 cal $cm^{-2}min^{-1}$ (Robinson, 1966). As the radiation passes through the atmosphere, both its spectral as well as its directional properties are changed.

On cloudless days, most of the radiation reaching the earth's surface remains monodirectional and is called direct solar radiation. The transmittance of direct radiation is a function of the "air mass" (i.e., depth of atmosphere traversed by a solar ray), atmospheric pressure, amount of precipitable water vapor and the amount of dust in the atmosphere (Brooks, 1959).

The remaining radiation, called diffuse, that reaches the earth's surface is scattered by particles that are suspended in the atmosphere. Two general types of scattering particles are those called Rayleigh scatters (e.g., gaseous molecules of air) and Mie scatters (e.g., aerosol particles). These scattering particles affect both the spectral as well as the directional properties of diffuse radiation. The spectral distribution of skylight is relatively rich in blue light and poor in red. The angular distribution of diffuse radiation is a function of solar position but it cannot be described by any simple relation (Monteith, 1973). In general, diffuse radiation is stronger near the horizon than at the zenith on cloudless days.

Measuring Radiation In The Open : Cloudless Sky

Global and diffuse radiation were measured in the open, outside of the tree crown, on the roof of a building next to the study tree. A typical example of the diurnal variation in the solar radiation on clear, cloudless days is given in Figure 4.1 and Table 4.1. The global radiation, G, increases in the morning, peaks at solar noon (i.e., when the sun crosses the local meridian) and then decreases again in the afternoon. The morning and evening variation in global radiation are almost symmetrical about solar noon on cloudless days.

Diffuse radiation, D, increases in the morning, peaks and then decreases in the afternoon but it does not always reach its maximum value at solar noon. On August 1, 1978, the diffuse radiation reached a peak value of 0.14 cal $cm^{-2}min^{-1}$ at 14 o'clock (see Table 4.1).

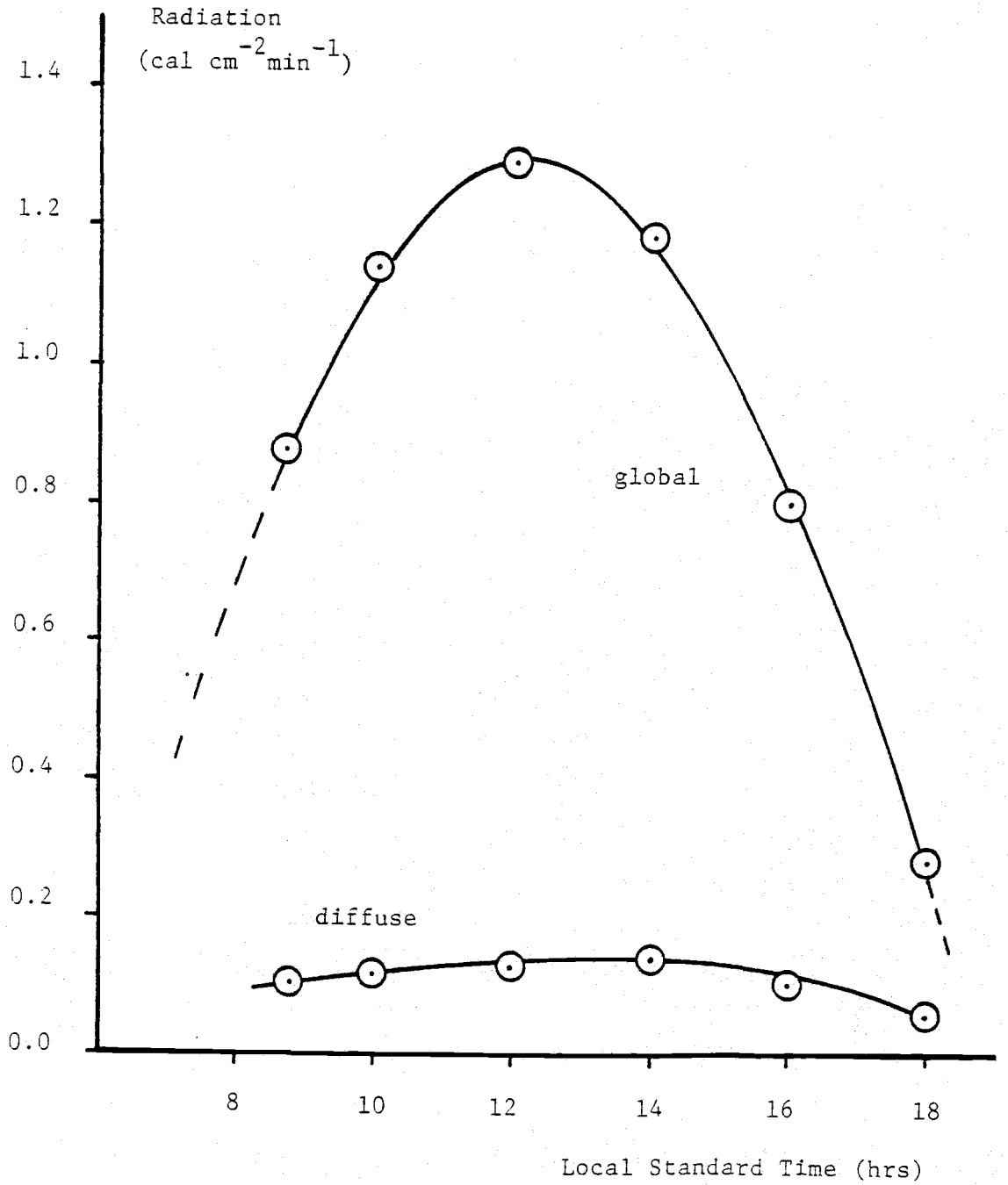

Figure 4.1 Global and diffuse radiation measured in the open on August 1, 1978.

Table 4.1 Solar radiation measured in the open on August 1, 1978.

LST (hrs)	θ_z^* (degrees)	Radiation (cal $cm^{-2} min^{-1}$) Global G	Diffuse D	Direct** $I\cos\theta_z$	Direct† I	Ratio D/G
8.7	52.6	0.88	0.10	0.77	1.27	0.11
10	39.2	1.14	0.12	1.03	1.33	0.11
12	27.0	1.29	0.12	1.17	1.31	0.09
14	34.2	1.18	0.14	1.04	1.26	0.12
16	53.0	0.80	0.10	0.70	1.16	0.13
18	74.0	0.28	0.06	0.22	0.80	0.21

* solar zenith angle

** vertical component of direct radiation : $I\cos\theta_z = G - D$

† magnitude of direct radiation : $I = (G-D)/\cos\theta_z$

The vertical component of direct radiation, $I\cos\theta_z$, is not measured directly by a Kipp pyranometer but is obtained by a difference technique (see Eq. 2.7). Even though the magnitude of direct radiation reaching earth's outer atmosphere is nearly a constant (i.e., solar constant), the amount reaching the ground at any instant varies as the "air mass" varies. Thus the vertical component of direct radiation is a function of both the air mass and the zenith angle, θ_z, of the sun. On cloudless days most of the diurnal variation in global radiation shown in Figure 4.1 is due to changes in the solar zenith.

The proportion of diffuse to global radiation is not a constant (see Table 4.1). On cloudless days, the D/G ratio depends mainly on the solar zenith and on the amount of aerosol suspended in the atmosphere (Liu and Jordan, 1960 ; Monteith, 1973). At sunset and sunrise, the D/G ratio equals one since all radiation is diffuse. As the solar zenith decreases, the D/G ratio decreases. Typically the minimum ratio is between 0.10 and 0.15 on cloudless days.

In addition to the diurnal variation in the vertical component of direct radiation there is also an annual variation. On a daily basis, the largest flux of direct radiation occurs at solar noon since the value of $\cos\theta_z$ is then a maximum. However, the solar zenith angle at solar noon varies on an annual basis. Figure 4.2 shows how the cosine of the solar zenith changes as a function of the Julian date (i.e., day of the year). Multiplying the cosine of θ_z by the solar constant at sea level (i.e., 1.4 cal $cm^{-2}min^{-1}$) will give an estimate of the vertical component of direct radiation at

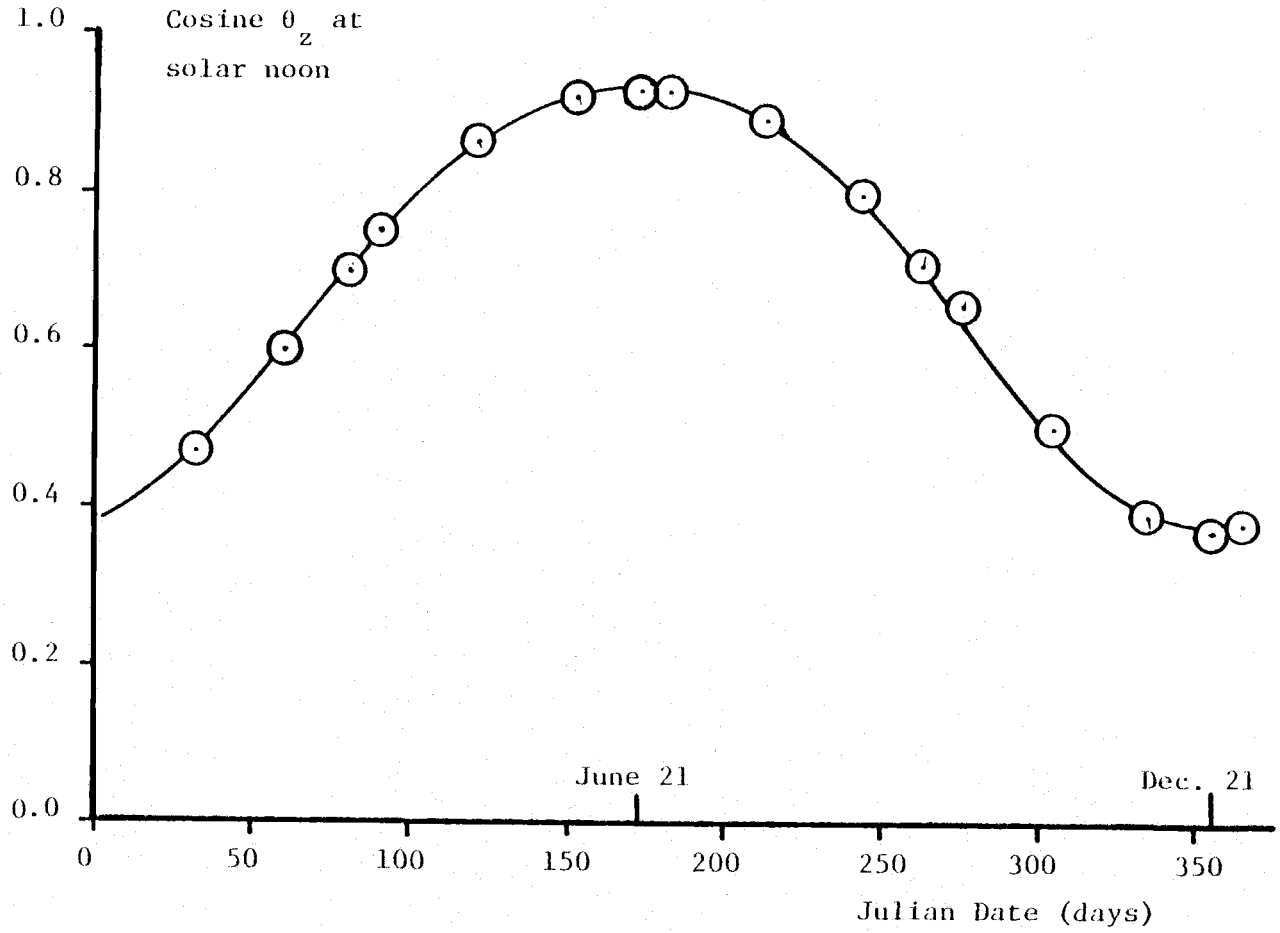

Figure 4.2 Cosine of solar zenith at solar noon as a function of Julian date. Results are computed for Corvallis, Oregon.

solar noon on cloudless days. Table 4.2 lists the values of the solar zenith angle at solar noon in Corvallis for a few selected dates in the year. In Corvallis, Oregon, the maximum solar zenith angle at solar noon occurs on December 21, reaching an angle of 68.1 degrees. This date is called the winter solstice. The minimum solar zenith angle at solar noon occurs on June 21 (θ_z = 21.1 degrees) and is called the summer solstice. The solar zenith angles may be computed from equations of celestial mechanics given by Smart (1965) and more simply by Frank and Lee (1966). A listing of a Fortran IV computer program used to compute the solar zenith and solar azimuth angles is given in Appendix D.

Measuring Radiation In The Open : Overcast Sky

When the sky is completely overcast, almost all of the radiation becomes diffuse. Figure 4.3 shows the global radiation incident upon a horizontal surface in the open on June 19, 1979. Note the rapid change in the radiation over a period of 30 minutes. The global radiation on an overcast day is substantially smaller than that of the global radiation on a clear day. An estimate of this reduction in flux can be computed as follows. From Appendix D the solar zenith at 13.45 o'clock on June 19, 1979 is computed to be 25.69 degrees. The estimated global radiation for an equivalent

Table 4.2 Solar position at certain times of the year.

Date	Julian Date (day)	Event	Solar Position	
			Declination (degree)	Zenith* (degree)
March 21	80	vernal equinox	0	44.6
June 21	172	summer solstice	23.5	21.1
Sept 21	264	autumnal equinox	0	44.6
Dec 21	355	winter solstice	-23.5	68.1

* zenith angle of sun at solar noon in Corvallis, Oregon.

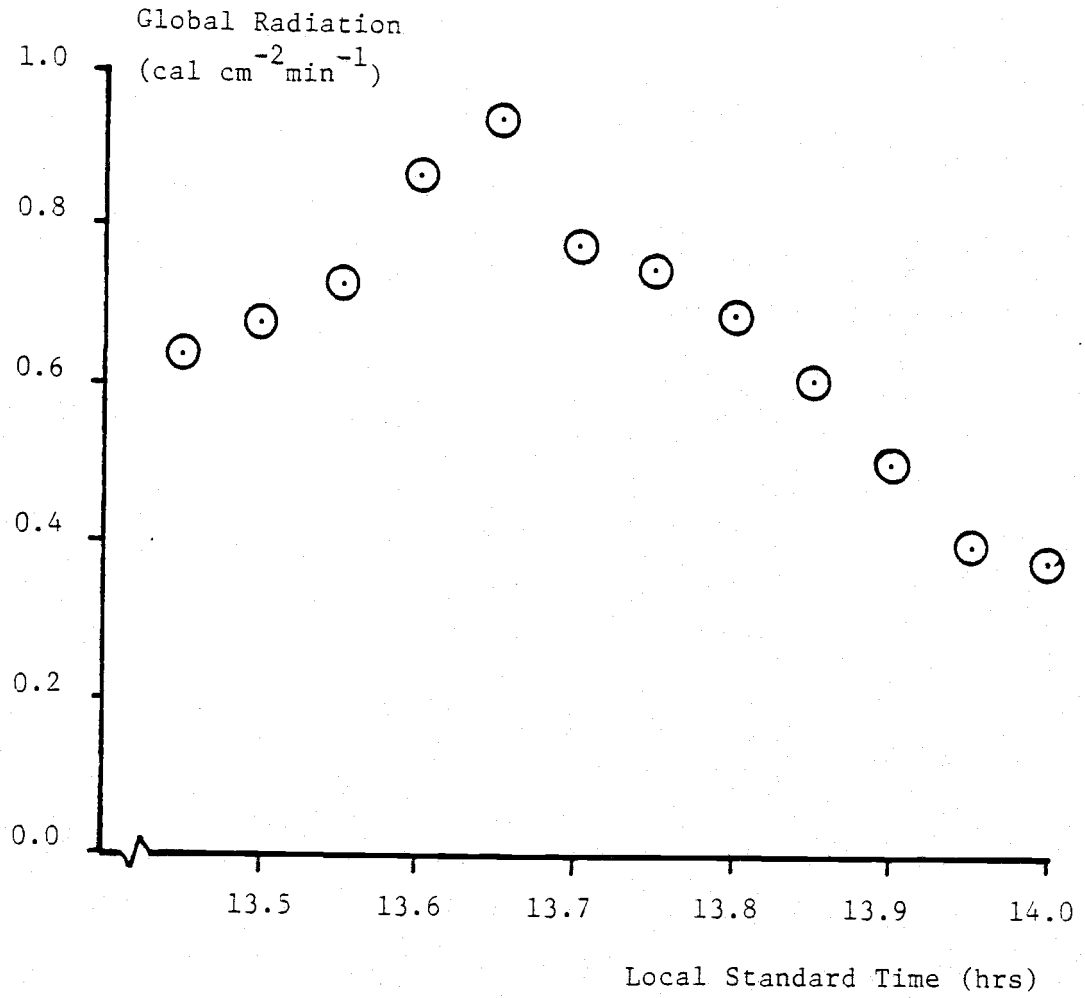

Figure 4.3 Global radiation measured in the open on an overcast day, June 19, 1979. Radiation is measured every three minutes over a period of 30 minutes.

cloudless day would be about

$$1.4\cos(25.69)(1+0.15) \qquad (4.1)$$

which equals 1.45 cal $cm^{-2}min^{-1}$ if we assume 15% diffuse radiation. Thus, the clouds are obscuring from 35 to 74 percent of the global radiation on this date. In addition to the reduction in the magnitude of the radiation during overcast days, there is a change in the directionality of the diffuse radiation. The average radiance of a heavily overcast sky is about three times greater at the zenith than at the horizon (Monteith, 1973).

During partly cloudy days, radiation intensities in the open may change even more rapidly and by larger amounts than that during overcast days. In addition, a few scattered cumulus clouds near the sun, but not obscuring the sun, may reflect more radiation to the ground than that of the solar constant outside of the earth's atmosphere (i.e., greater than 2.0 cal $cm^{-2}min^{-1}$). This effect is the result of strong forward scattering of radiation by water droplets near the edge of the cloud (Monteith, 1973).

Garnier and Ohmura (1968) have developed a theoretical model to compute the direct and diffuse radiation under clear skies. Thompson (1976) and Satterlund and Means (1978) developed theoretical models to estimate the daily total radiation under variable cloud conditions.

Spatial Distribution Of Global Radiation Within The Crown On Cloudless Days

The spatial variation in the distribution of short wave global radiation was systematically measured in the crown of the study tree. A schematic view of the spatial sampling scheme is given in Figure 4.4. Note that all transects through the crown are along compass directions (e.g., magnetic North), whereas the sun moves along cardinal points or celestial directions (e.g., true North). The angle (i.e., magnetic declination) between true North and magnetic North is about 20 degrees in Corvallis. Transects along compass directions were taken because it was easy to determine, but in retrospect it would have been more logical to have used cardinal directions.

Figures 4.5 a-f show typical measurements of global radiation within the crown at 12 o'clock(LST) on cloudless days in September and October of 1979. Percent penetration is plotted on semi-log paper as a function of the distance along the transects, where the center of the tree is defined as the zero distance. Percent penetration of global radiation is mathematically defined as the ratio of the global radiation measured within the crown, G(crown), divided by the global radiation measured in the open, G_o(open), (i.e., outside of the canopy). Thus the percent penetration is

$$\text{percent penetration of } G = \{G(\text{crown})/G_o(\text{open})\}100 \qquad (4.2)$$

Global radiation within the crown was measured with four Kipp pyranometers mounted on the trolley system described in Chapter II.

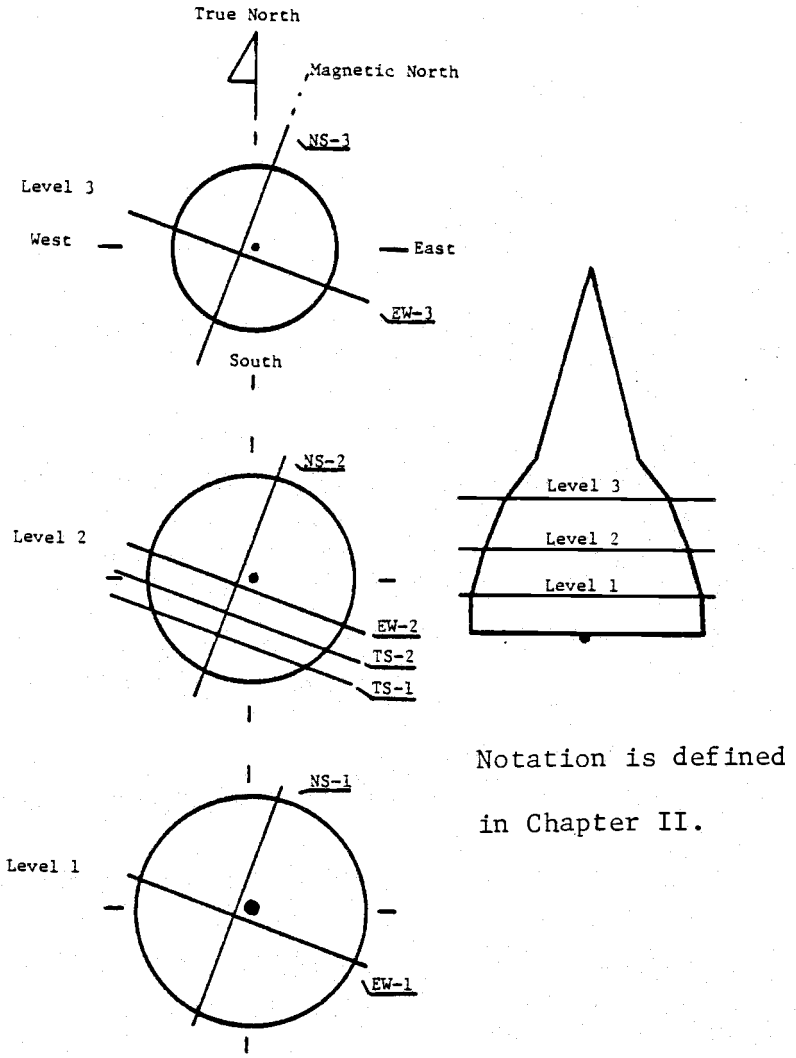

Figure 4.4 Schematic view of study tree showing the relative location and orientation of the eight transects along the three levels of the crown. Note that the transects are orientated along compass (i.e., magnetic) directions. Cross-sectional views of the crown do not show the actual branch distribution but all other dimensions and angles are to scale.

Figure 4.5 Spatial variation in the penetration of global radiation into the tree crown on cloudless days at 12 o'clock (LST) during the months of September and October, 1979. Total variability among the four Kipp pyranometers is shown by the length of the vertical bars. Figure 4.5a shows the variation along the East-West, Level 1 transect; 4.5b shows the results for the NS-1 transect; 4.5c shows for EW-2; 4.5d shows for NS-2; 4.5e shows for EW-3; and 4.5f shows for NS-3. See text for description of information given in "boxes". Note that the date is defined as :month/day /year.

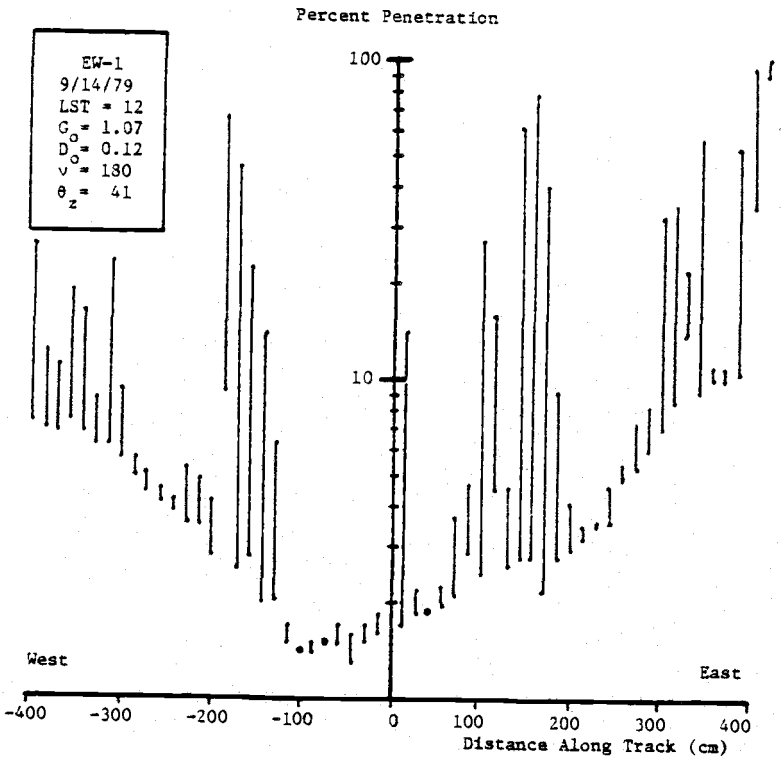

Figure 4.5a

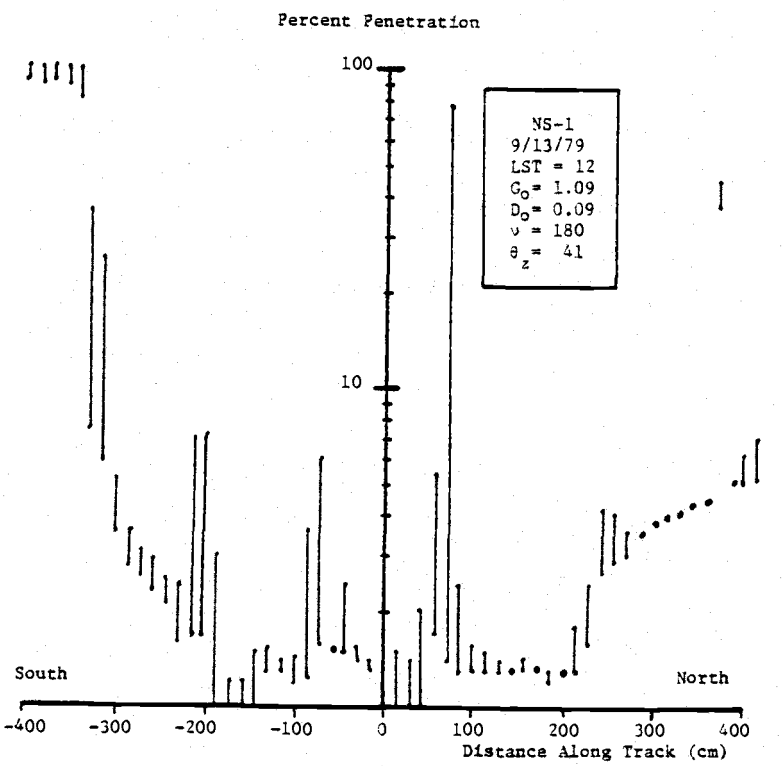

Figure 4.5b

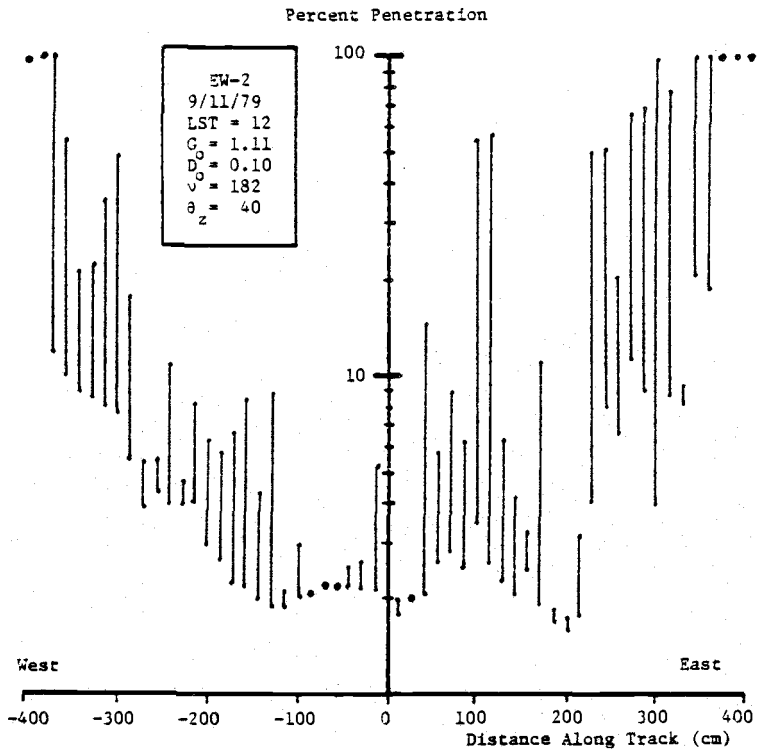

Figure 4.5c

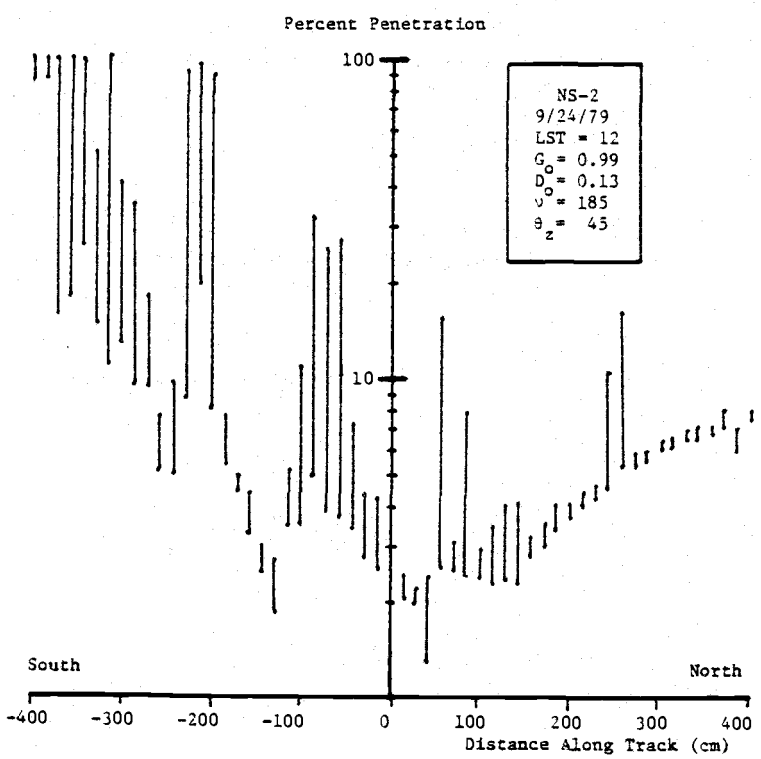

Figure 4.5d

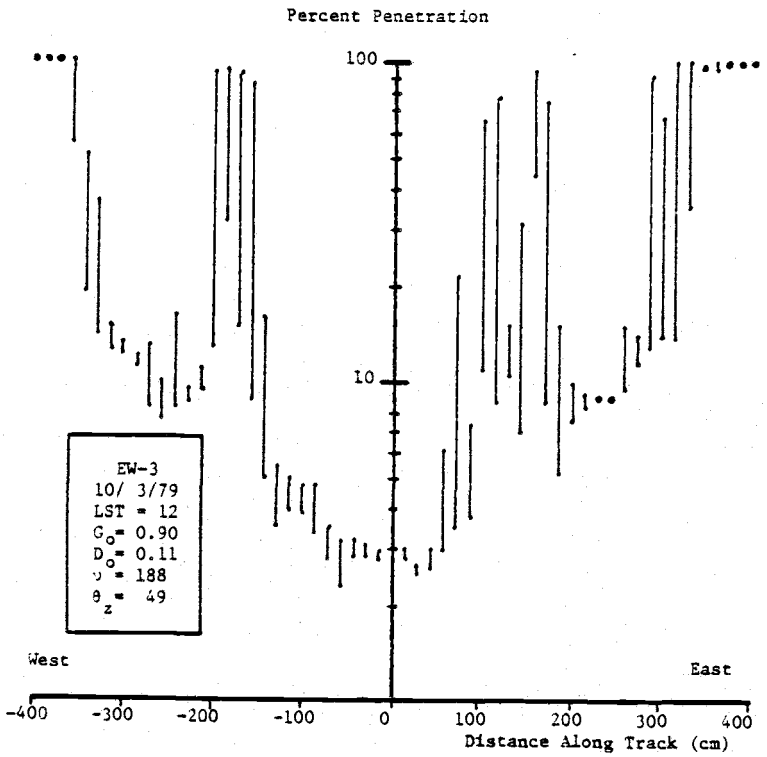

Figure 4.5e

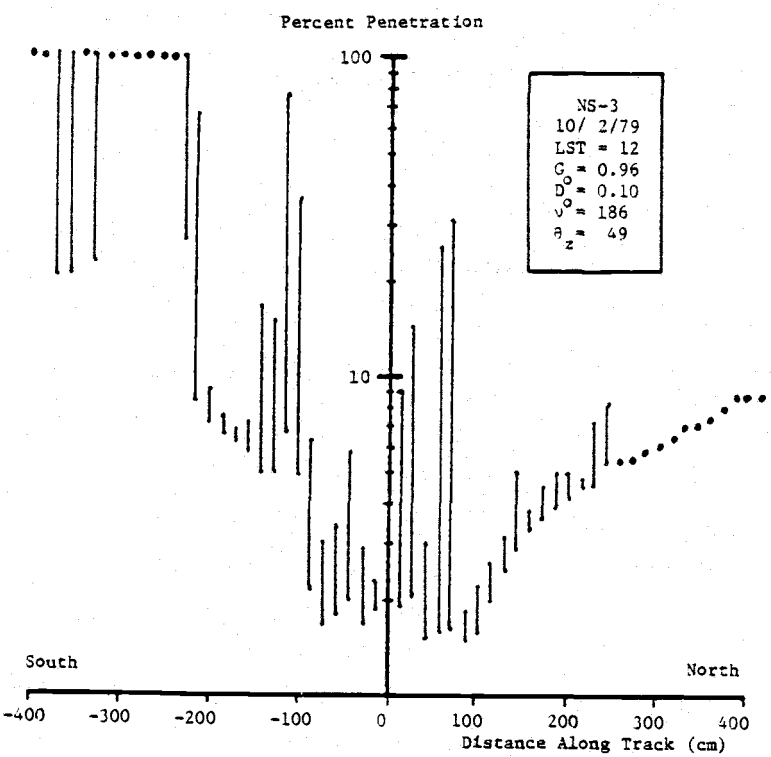

Figure 4.5f

Global radiation in the open was measured with a Kipp pyranometer mounted on the roof of a building next to the study tree. The range in radiation values (i.e., minimum and maximum) measured at a given instant in time from the four Kipp pyranometers is shown as a vertical bar and is plotted on the ordinate axis in Figures 4.5a-f. Only one set of radiation measurements were taken every 15 cm along the transect and each set was taken approximately 30 seconds apart. It took about 30 minutes to go from one side of the crown to the other.

In Figures 4.5a-f, all pertinent information related to the experiment is listed within the "box" shown in each figure. The first line of the box gives the transect of the run (e.g., East-West, Level 1 in Figure 4.5a), the date is given on the second line and the approximate time at which the run started (i.e., LST = local standard time in hours) is listed on the third line. On the fourth line, the average global radiation, G_o measured in the open is given (cal cm^{-2} min^{-1}). Multiplying the value of G_o(in the open) times the percent penetration in the crown will give the value of global radiation in the crown. The average azimuth, ν, and zenith, θ_z, angles (degrees) of the sun are respectively given on the sixth and seventh lines. Note that the azimuth angle is measured positive clockwise from true North (e.g., ν=180° is due South) and that the zenith angle is measured from the vertical.

A comparison of global radiation measurements along several parallel East-West transects of Level 2 are shown in Figure 4.6. The line marked EW-2 in Figure 4.6 is closest to the tree center

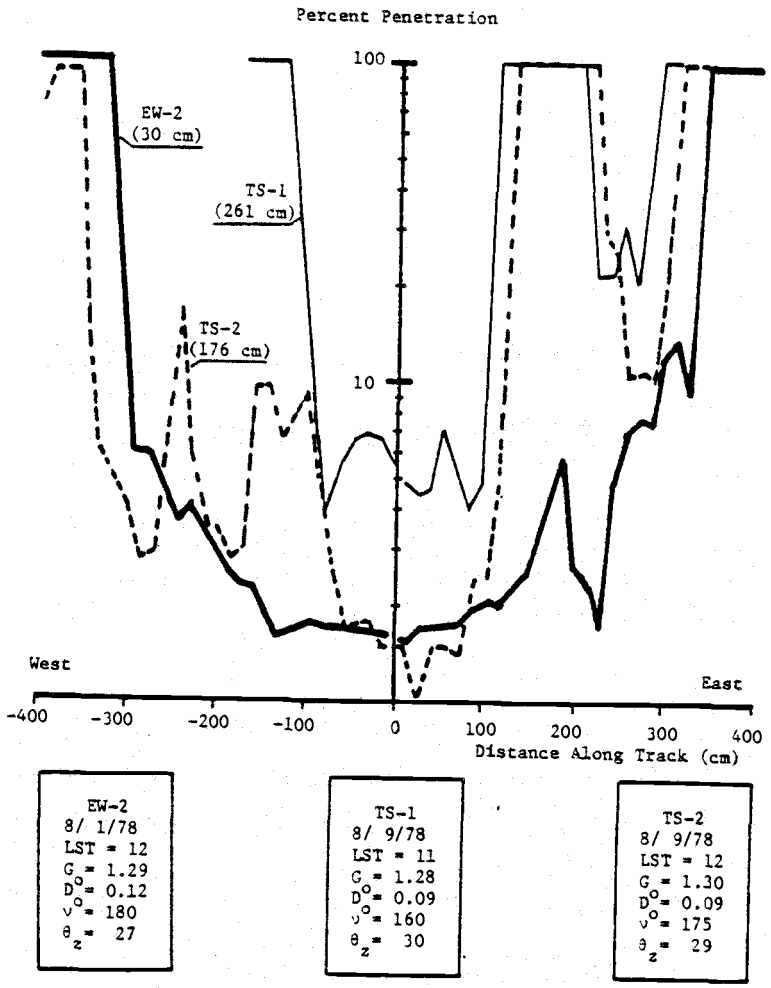

Figure 4.6 Comparing global radiation measurements along parallel East-West transects of Level 2. Only the smallest value of global radiation, as measured by the four Kipp pyranometers on the trolley, is plotted. This is because the smallest measurement of global radiation corresponds to that beam of radiation with the greatest interception.

(i.e., 30 cm from tree center) and the line marked TS-1 is the most distant (i.e., 261 cm from tree center). A schematic of these three track positions can be seen in Figure 4.4.

Upon examing Figures 4.5 and 4.6, several general observations can be made. Over 90% of the global radiation is intercepted within the first 50 cm of continuous foliage but large, bright sunflecks can penetrate into any portion of the crown, even into the very center of the tree crown. Along transects that are perpendicular to the sun's rays (e.g., East-West at noon), the penetration of global radiation is very symmetrical about the center of the tree. Thus at noon, the global radiation distribution in the East and West portions of the crown are essentially mirror images of each other. The spatial variance in the global radiation (as measured by the four Kipp pyranometers on the trolley) at any given point is largest near the outer edge of the crown and it decreases towards the center of the crown. In addition, the higher up into the crown (e.g., Level 3 versus Level 1), the greater the penetration and the greater the spatial variance. Less than three percent of the global radiation will reach the inner 250-300 cm radius of the crown at Level 1, less than three percent reaches the inner 200 cm radius of Level 2, and less than three percent will reach the inner 50-100 cm radius of crown on Level 3.

Along transects that are parallel to the sun's rays (e.g., N-S at noon), the penetration of global radiation is not symmetrical. On the sunny side penetration is similar to that of the above but on the shaded side, the global radiation remains below ten percent

of its full sun value. Hence, global radiation within the shadow or shaded side of the crown remains less than or equal to that of the diffuse radiation level in the open. Except for a few "spikes" of direct radiation, the spatial variance of the radiation is very low on the shaded side.

In general, the spatial distribution of global radiation is directly related to the distribution of foliage within the crown. The presence of deeply penetrating sun flecks indicate "gaps" in the canopy and areas of severe interception indicate "clumps" of foliage. Upon careful examination, the "outline" of individual branch tips can be seen in Figures 4.5 and 4.6 and identified with specific branches in the study tree.

Diurnal Variation Of Global Radiation Within The Crown On Cloudless Days

Measurements of global radiation along the East-West, Level 2 transect are given in Figures 4.7a-f for August 1, 1978. Starting at 8 o'clock (LST), the East side of the tree is in full sunlight and the West side is in complete shade (see Figure 4.7a). The global radiation penetrates the first hundred centimeters without interception since the outermost branches are widely seperated and parallel to direct radiation at these large zenith angles.

At 250 cm from the East side of the tree center, crown closure is more complete and global radiation is attenuated in the next 50 cm

Figure 4.7 Diurnal variation in the penetration of global radiation into the crown on a cloudless day along transect EW-2. Figures 4.7a to 4.7f show the distribution of radiation at 8,10,12,14,16 and 18 o'clock (LST), respectively. Note the change in solar azimuth, ν, and solar zenith, θ_z, angles at each of these sampling periods.

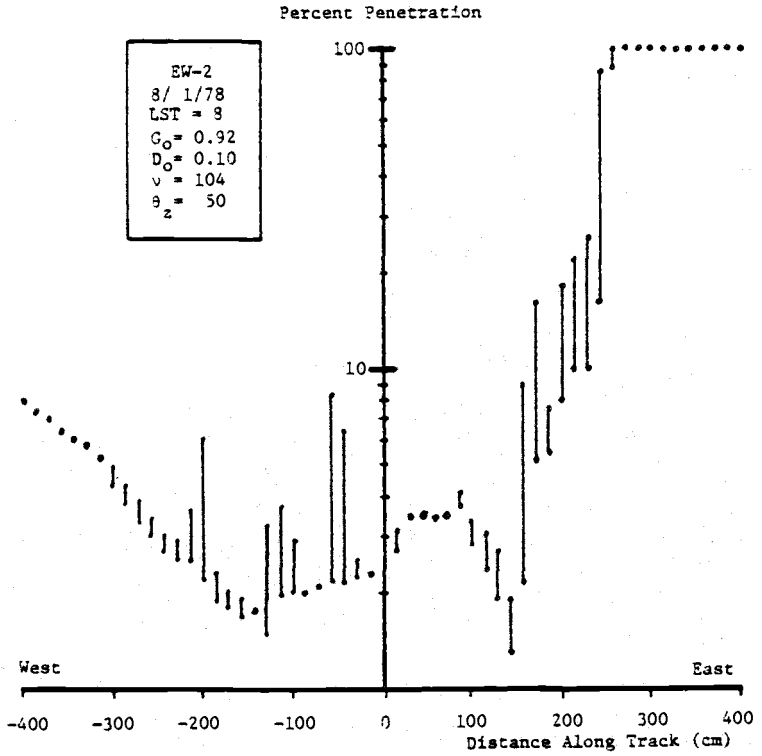

Figure 4.7a

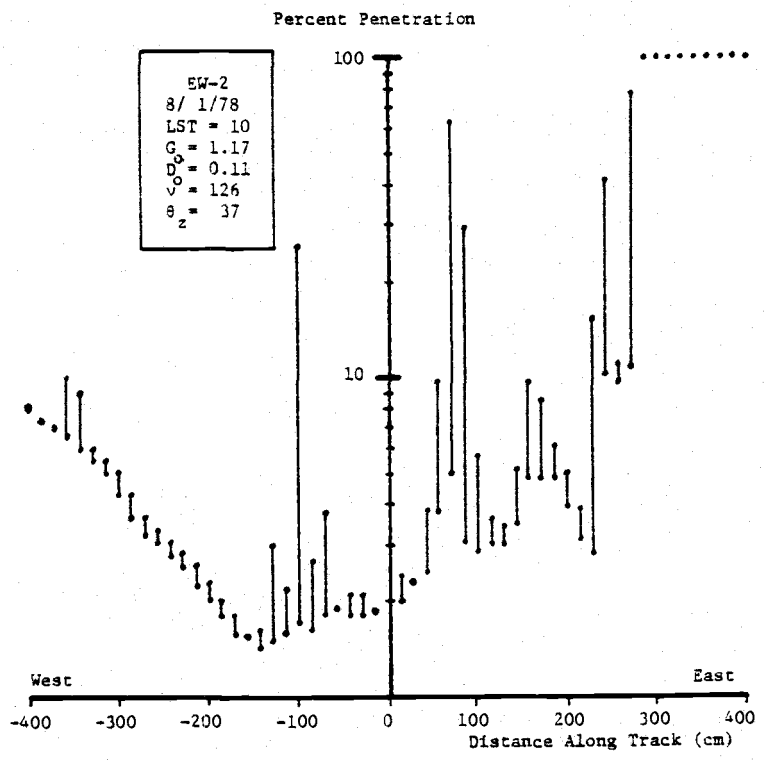

Figure 4.7b

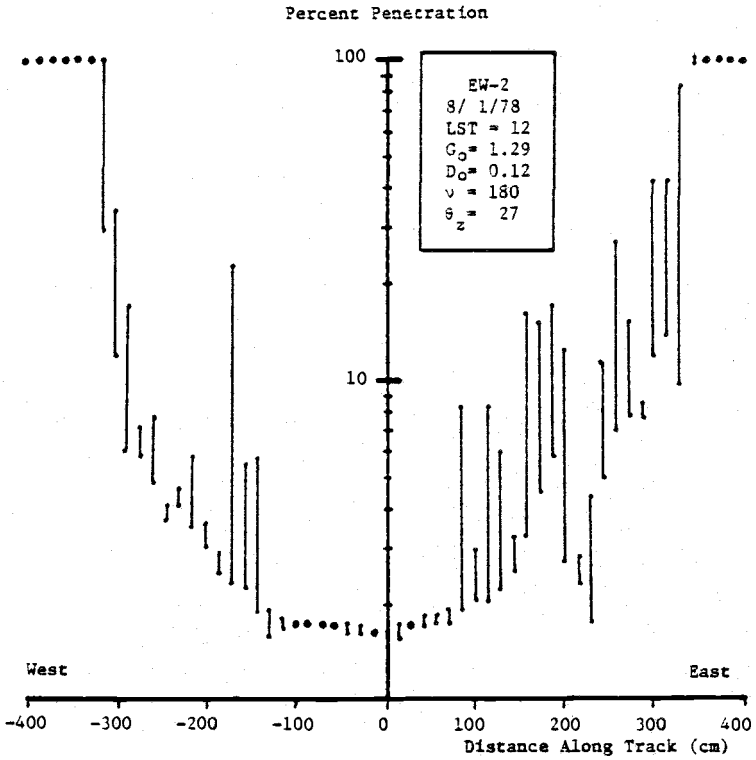

Figure 4.7c

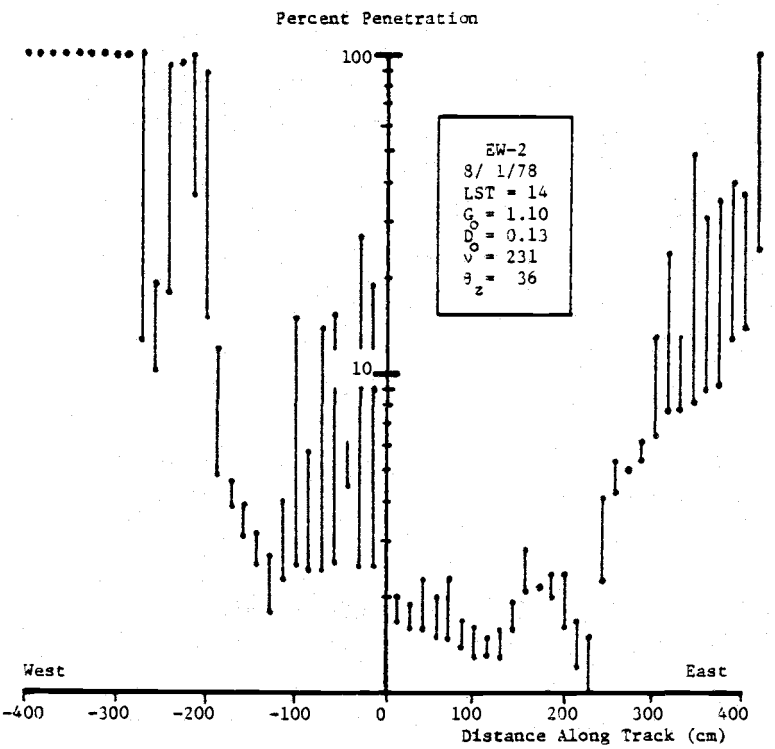

Figure 4.7d

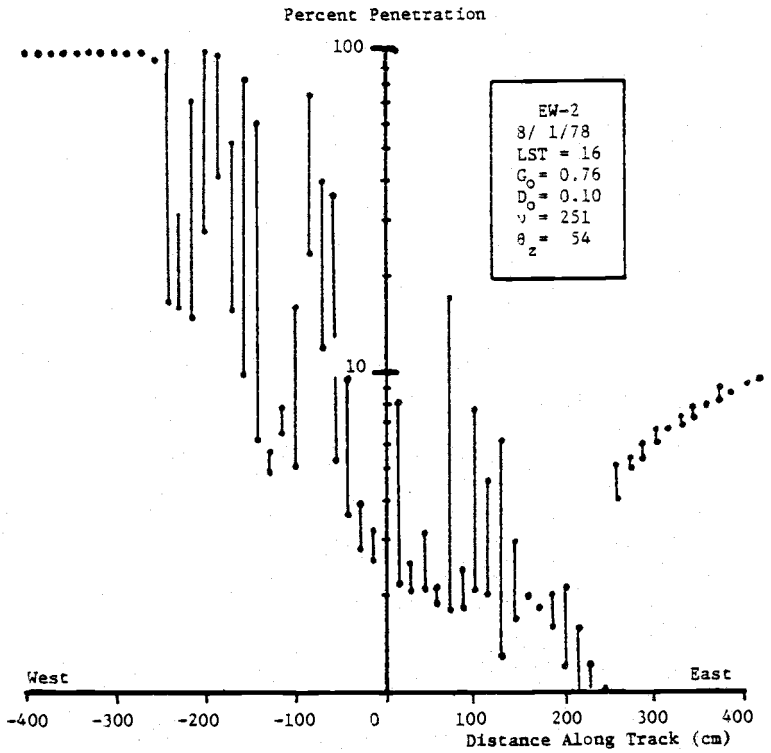

Figure 4.7e

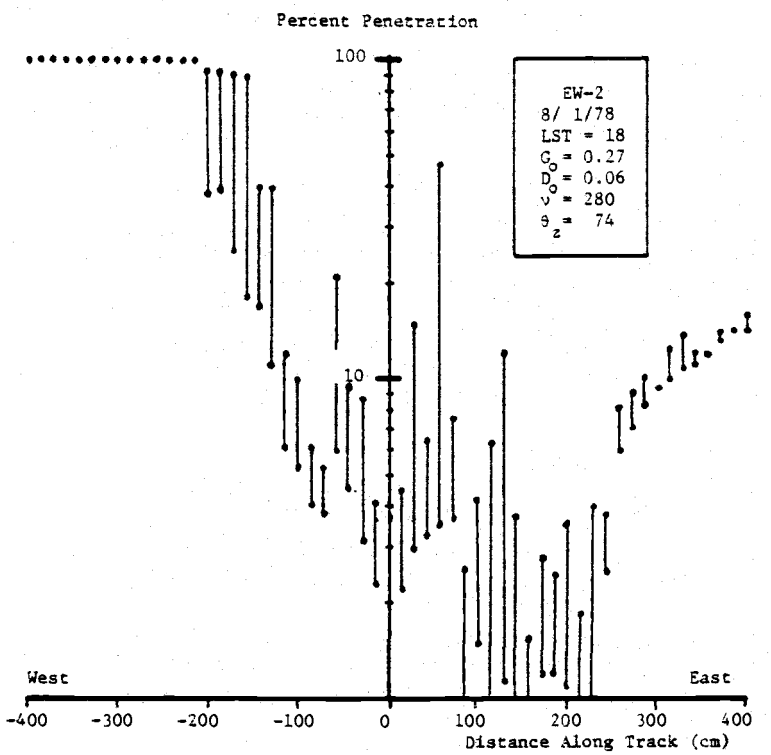

Figure 4.7f

of foliage. Less than three to four percent of the global radiation enters the remaining 200 cm of the tree crown center. Continuing along the transect into the western shaded side of the East-West transect, the global radiation continues to decline until about 150 cm from the tree's center. From 150 cm on out to the western edge of the crown, the global radiation increases but never gets above ten percent of the full sunlight value. The spatial variance in the radiation is greatest on the sunny side and smallest on the shaded side of the crown.

As the sun moves across the sky, the penetration of global radiation becomes more uniform along the EW-2 transect. At 12 o'clock (LST), the East and West portions of the crown are almost mirror images of each other (see Figure 4.7c). Both sides of the crown are now exposed to direct sunlight. At noon, however, global radiation is first intercepted at a distance of about 350 cm from the tree center whereas there was no interception up to a distance of about 250 cm at 8 o'clock. At noon the sun is apparently much higher in the sky than the branch angles. Even the outermost and widely seperated branch tips will cast a shadow towards the center of the tree at noon.

By late evening (see Figure 4.7f), the West side of the tree is in full sunlight and the asymmetric penetration of global radiation is similar to that of the morning, except now its distribution is reversed. Also note the deep penetration of global radiation into the edge of the crown on the West side as the sun and branch angles line up again.

Typical measurements of global radiation along the North-South, Level 2 transect are given in Figures 4.8a-f for several cloudless days in July, 1978. In the early morning and late evening, the North-South transect is nearly perpendicular to direct radiation. As a result, both the North and South sides of the tree crown are exposed to a uniform field of radiation and the resulting penetration is symmetrical. The apparent lack of symmetry in Figure 4.8a at 8 o'clock is due to the presence of a large "gap" in the branch distribution on the North side of Level 2. The description of the diurnal variation of the global radiation along the North-South transect is similar to that of the East-West transect. Figure 4.8e, however, highlights the previous discussion on the branch angle-sun angle interaction. At noon, less than one percent of the global radiation reaches the tree center but by 18 o'clock, more than five percent penetrates to the center.

Annual Variation Of Global Radiation Within The Crown On Cloudless Days

The annual variation in the distribution of global radiation within the crown of the study tree on cloudless days was studied. In Figure 4.9a, measurements of global radiation at noon (LST) along the East-West, Level 2 transect are plotted from two different days that are about a year apart, August 1,1978 and September 17, 1979. From Figure 4.9a, it is apparent that the distributions of global

Figure 4.8 Diurnal variation in the penetration of global radiation into the crown on cloudless days along transect NS-2. Figures 4.8a to 4.8f show the distribution of radiation at 8,10,12,14,16 and 18 o'clock (LST), respectively.

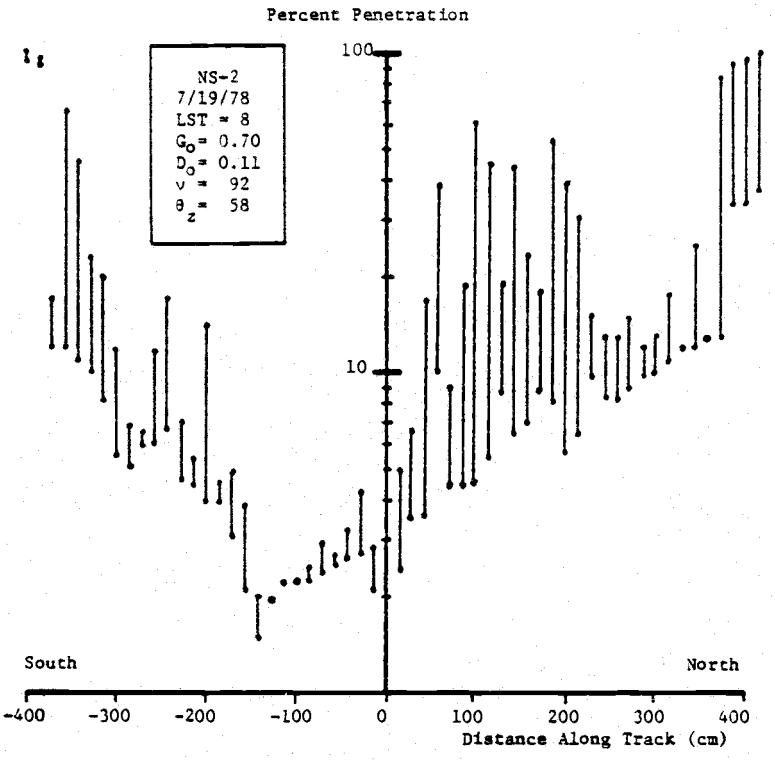

Figure 4.8a

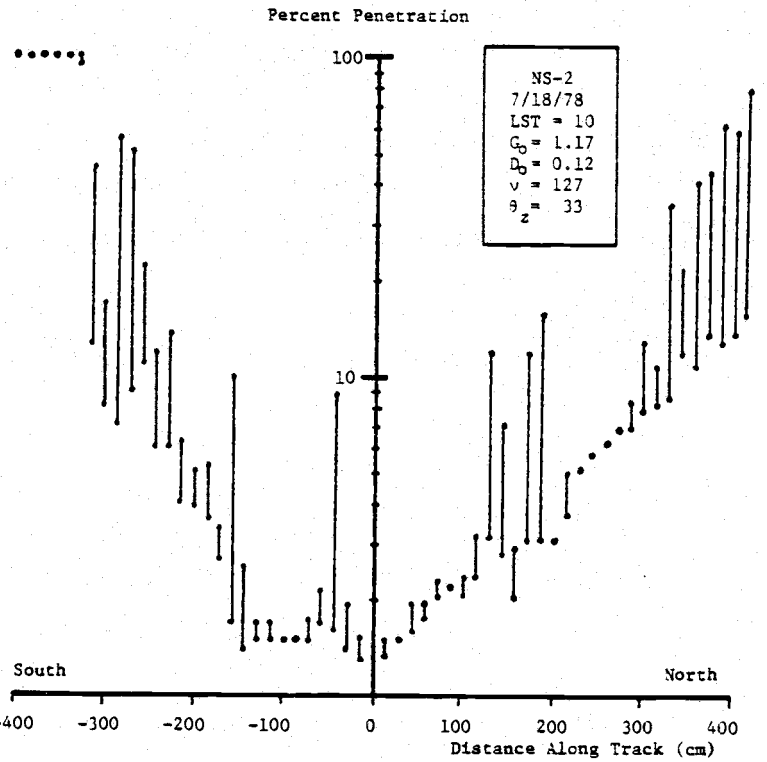

Figure 4.8b

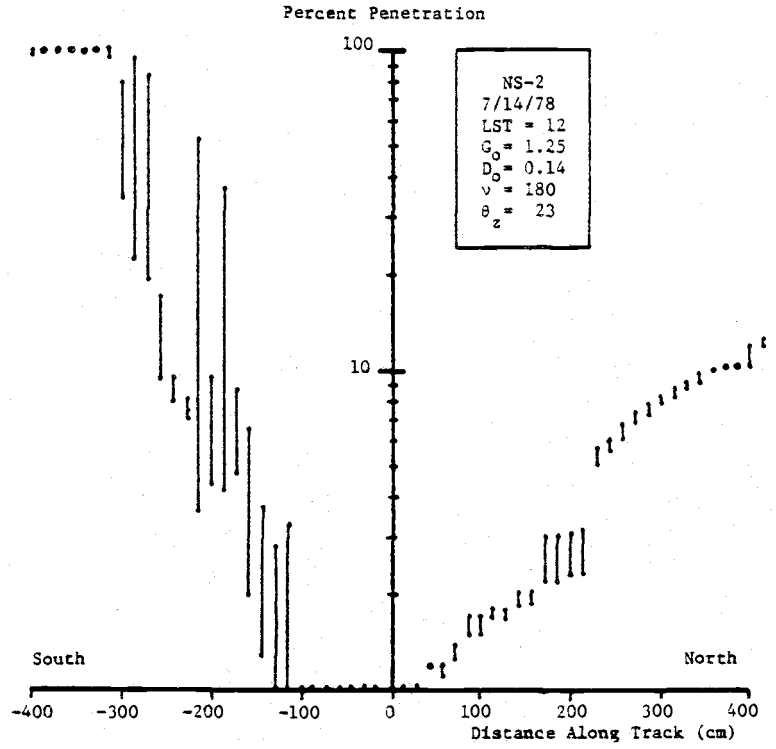

Figure 4.8c

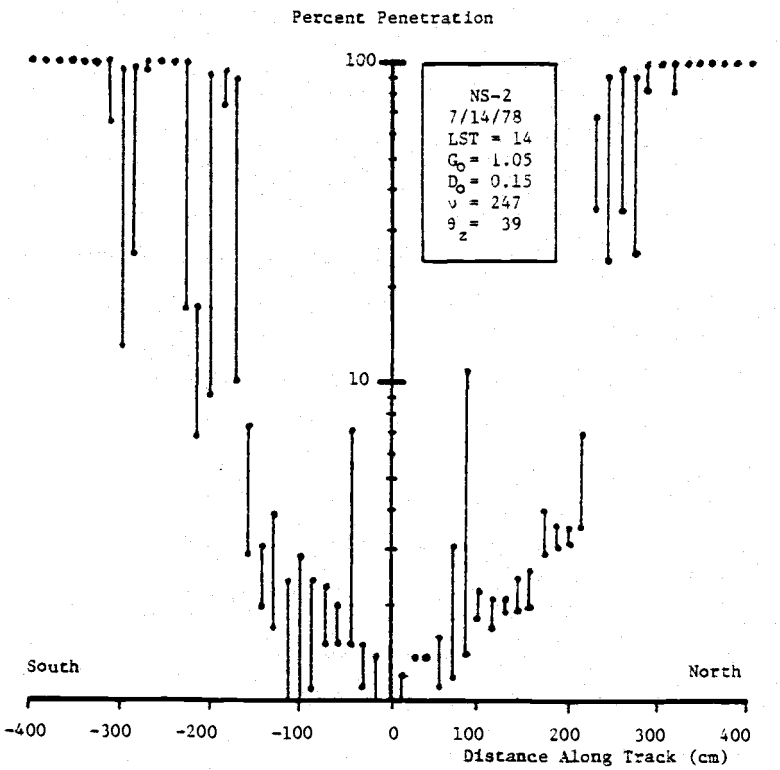

Figure 4.8d

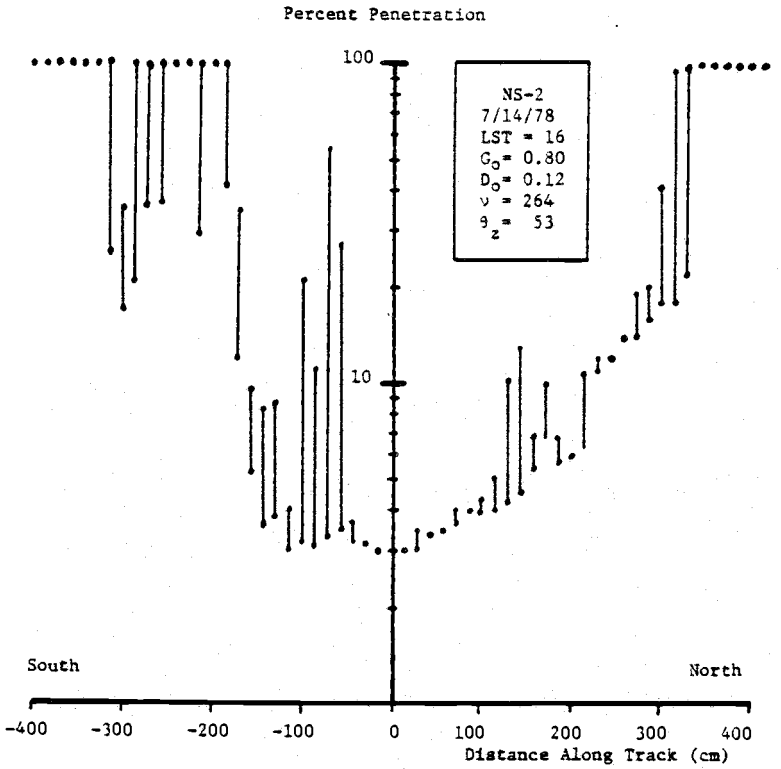

Figure 4.8e

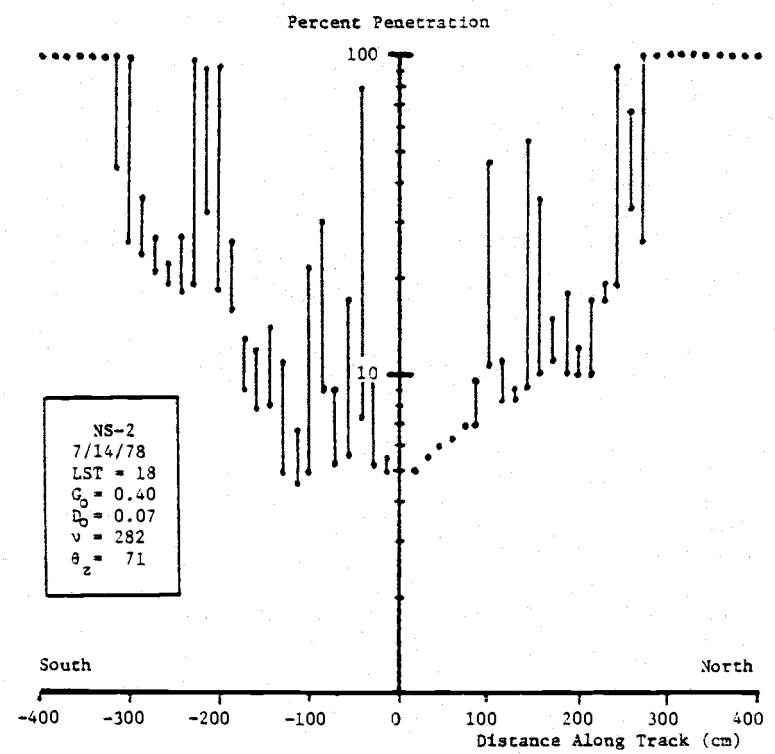

Figure 4.8f

Figure 4.9 Annual variation in the penetration of global radiation into the crown on cloudless days at 12 o'clock (LST). Only the smallest measurement (i.e., maximum interception) of global radiation is plotted. Figure 4.9a shows the distribution of radiation along the East-West, Level 2 transect on two different dates a year apart. Figure 4.9b shows the distribution of radiation along the North-South, Level 2 transect on three different dates over the uear.

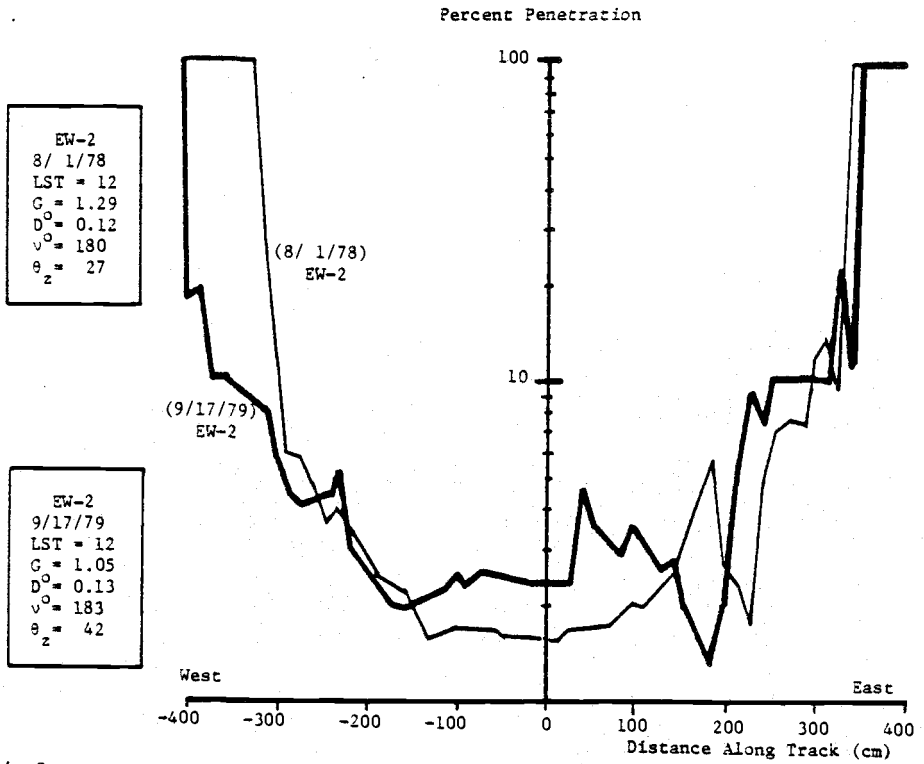

Figure 4.9a

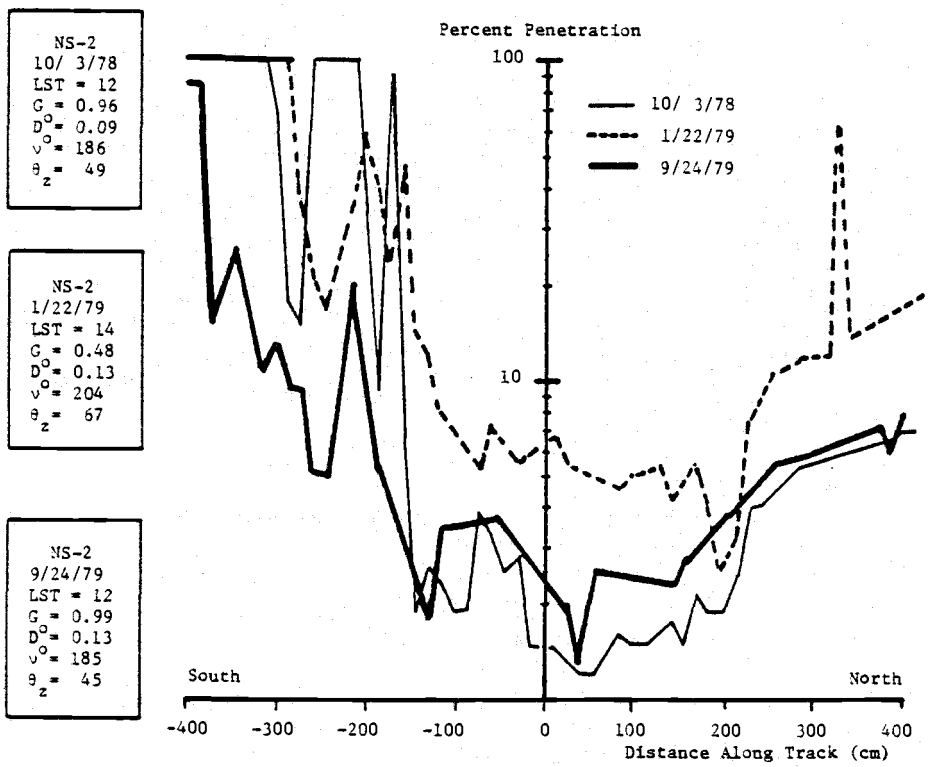

Figure 4.9b

radiation are very similar. However, the 1979 data indicates a greater penetration into the center of the tree but this is probably due to the larger solar zenith angle in September (i.e., $\theta_z = 27^o$ on 8/ 1/78 versus $\theta_z = 42^o$ on 9/17/79). My previous discussion on the diurnal variation of global radiation indicated that the global radiation would penetrate further into the crown as branch angle and sun angle lined up (see Appendix A for additional details on branch angles). However, there is an increased interception of radiation along the outer perimeter of the crown (see upper left corner of Figure 4.9a). This is just the opposite of what is expected at large solar zenith angles. One possible explanation for this increase in interception is that there is an increase in foliage along the outer edge of the crown from the 1979 growing season. In addition one might expect a slight increase in penetration in the inner portion of the crown as the older needles die and fall out (i.e., from the central "dead zone").

The annual variation in the global radiation along the North-South, Level 2 transect is given in Figure 4.9b. Data was obtained on October 3, 1978 at 12 o'clock (LST), January 23, 1979 at 14 o'clock (LST) and at 12 o'clock (LST) on September 24, 1979. The deepest penetration of global radiation occured on January 22, 1979. The deeper penetration is probably due to the large zenith angle of the sun (see Table 4.2) and from needle drop during the winter months of November and December. The decreased penetration of radiation into the outer edge of the crown during September 1979 (see upper

left corner of Figure 4.9b) is probably due to the new growth of foliage added on during the 1979 growth season.

Even though the global radiation will penetrate farther into the crown during the winter months and during the early morning and late evening of the day, the amount of global radiation may be less during these times. To obtain a plot of global radiation values versus position in the crown, simply multiply the percent penetration at any point in the crown by the amount of radiation measured in the open and divide by 100. Figures 4.5 to 4.9 contain both of these informations.

Spatial Distribution Of Global Radiation Within The Crown On Overcast Days

Figures 4.10a-f show typical measurements of global radiation within the crown on completely overcast days in June, 1979. As before, percent penetration of global radiation is plotted on semi-logarithmic graph paper as a function of position within the crown.

Several major differences are observed between the penetration of global radiation on cloudless days and on overcast days. On overcast days, global radiation penetrates far deeper into the canopy and is less attenuated than on cloudless days. On overcast days, global radiation can penetrate from 150 to 200 cm of crown foliage before 90% of it is attenuated as compared to only 50 cm on cloudless days. In addition, the distribution of global radiation

Figure 4.10 Spatial variation in the penetration of global radiation into the tree crown on overcast days in June, 1979. Figure 4.10a shows the variation along the East-West, Level 1 transect; 4.10b shows the results for NS-1; 4.10c is for EW-2; 4.10d is for NS-2; 4.10e is for EW-3; and 4.10f shows the results for the NS-3 transect.

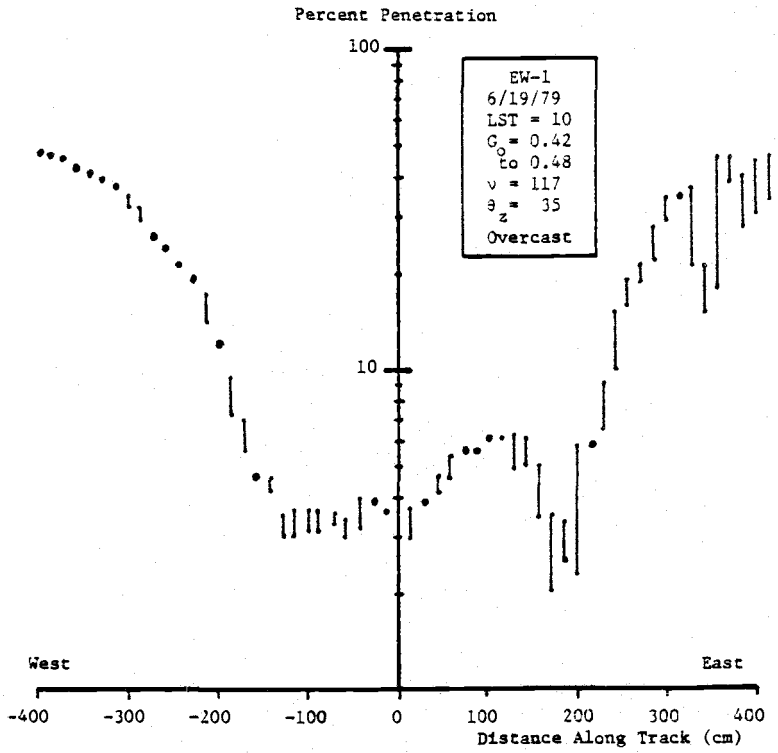

Figure 4.10a

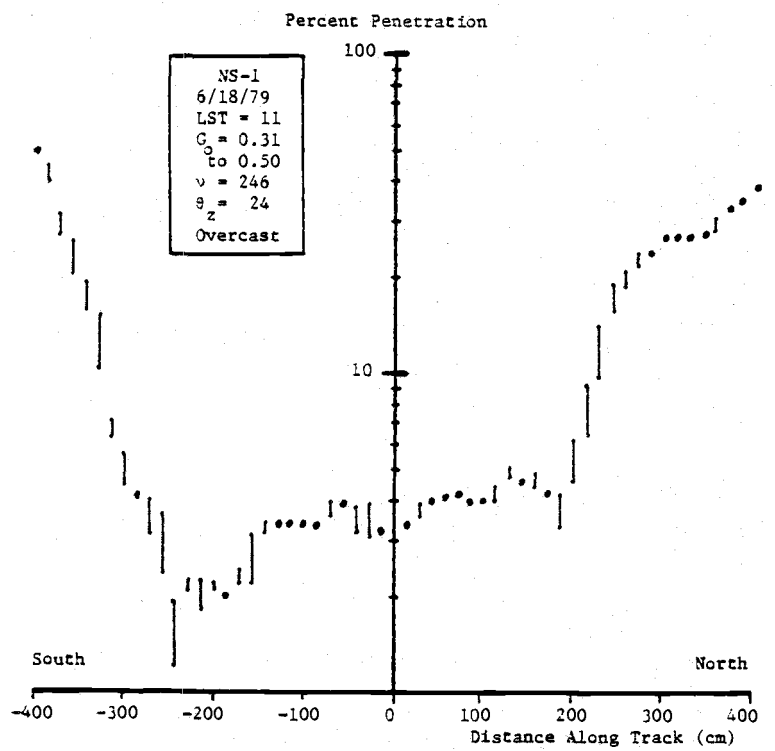

Figure 4.10b

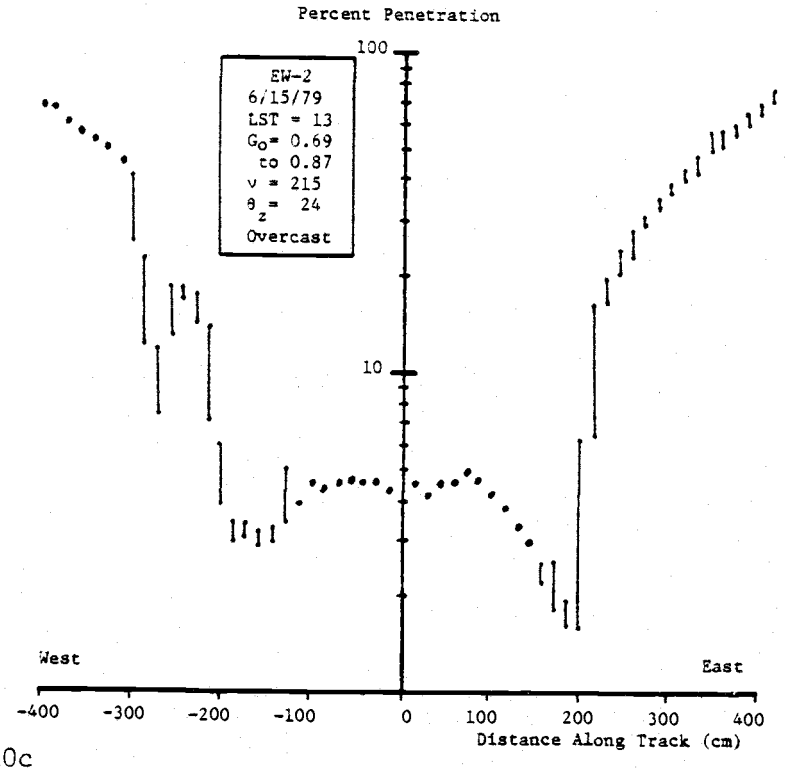

Figure 4.10c

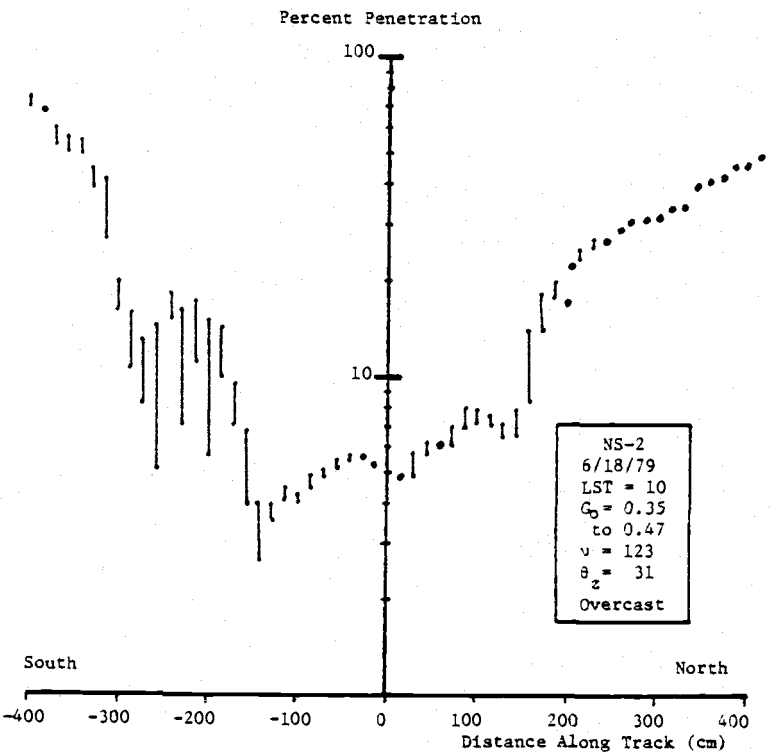

Figure 4.10d

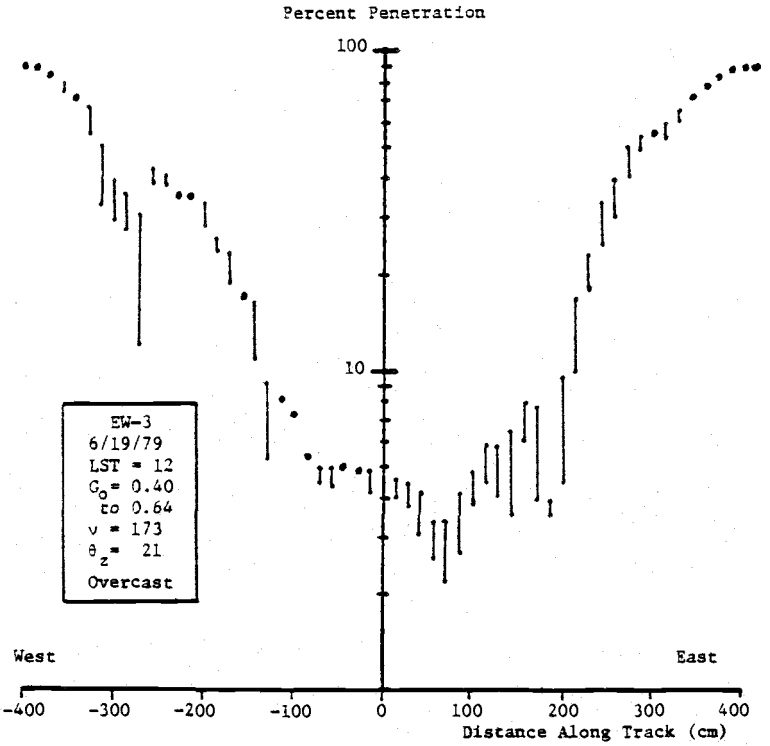

Figure 4.10e

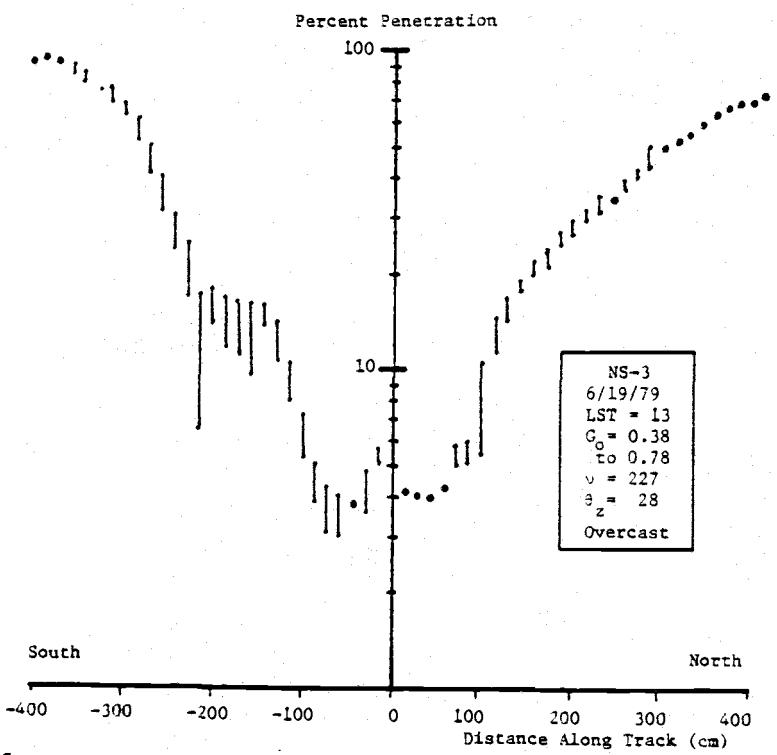

Figure 4.10f

on overcast days is symmetrical about the center of the tree along any given transect. The spatial variance in global radiation along a transect is less in comparison to that on cloudless days.

When comparing Level 1 (Figure 4.10b) against Level 3 (Figure 4.10f), the global radiation penetrates farther into the center of Level 3. There are no systematic differences between the East-West and North-South transects of a level. Any observed differences between E-W, N-S transects are due to small differences in branch and foliage distributions. The outline of individual branches can still be seen on overcast days in Figures 4.10a-f but only the larger, more isolated branch tips show through as hazy images.

However, there is a similarity between the distribution of radiation levels near the center of the crown on overcast and cloudless days. It is observed that on overcast days, less than three percent of the global radiation reaches the inner 200-300 cm radius of the crown at Level 1, less than three percent reaches the inner 150-200 cm radius of Level 2 and less than three percent reaches the inner 75-100 cm radius of Level 3.

Annual Variation Of Global Radiation Within The Crown On Overcast Days

The annual or seasonal variation in the distribution of global radiation within the crown on overcast days is shown in Figures 4.11a-b. A comparison between the winter and summer distributions

Figure 4.11 Annual variation in the penetration of global radiation into the crown on overcast days. Only the smallest measurement (i.e., maximum interception) of global radiation is plotted. Figure 4.11a shows the distribution of radiation along the East-West Level 2 transect on January 3, 1979 and June 15, 1979. Additional data for the June 15, 1979 run is given in Figure 4.10c. Figure 4.11b shows the distribution of radiation along the North-South, Level 2 transect on July 18, 1978 and on June 18, 1979. Additional data for the June 18, 1979 run is given in Figure 4.10d.

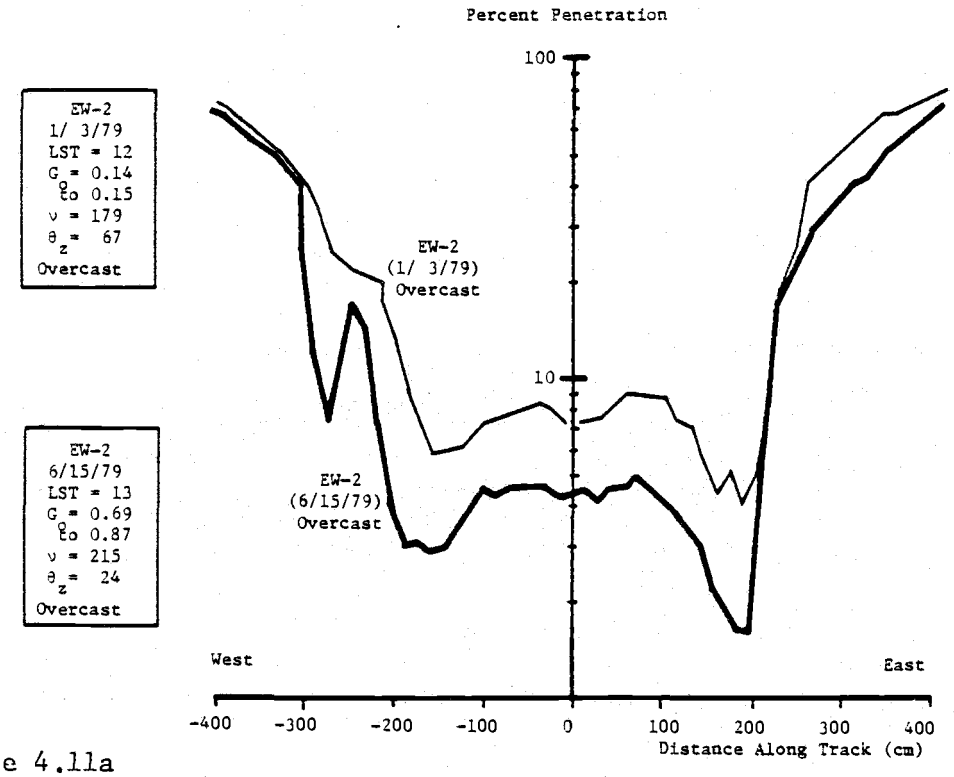

Figure 4.11a

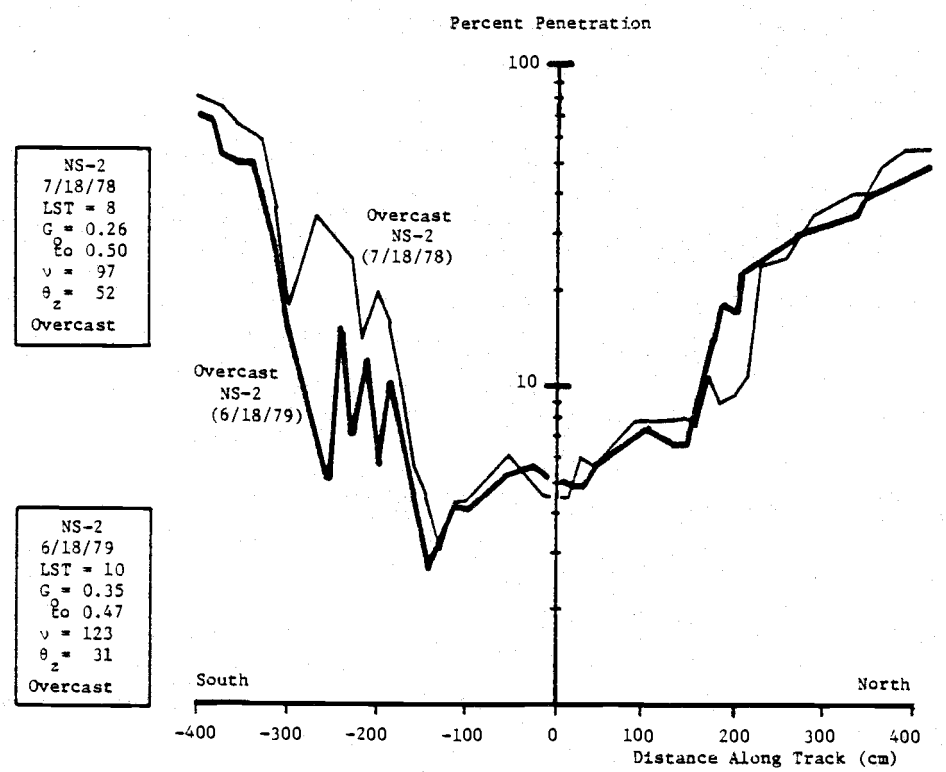

Figure 4.11b

for the East-West, Level 2 transect is given in Figure 4.11a. During the winter (January 3, 1979), the global radiation penetrates to the center of the tree more than during the summer (June 15, 1979). In addition, there is more interception along the outer edge of the crown during the summer.

A year to year variation in the global radiation distribution is given in Figure 4.11b for a North-South, Level 2 transect. Penetration of global radiation to the center of the tree is almost identical on both dates but there is a little less in 1979. There is a fairly significant increase in the interception (i.e., decrease in penetration) of global radiation on the South side of the crown during 1979.

Apparently needle drop during the winter allows a greater penetration of radiation into the tree's center and the growth of new foliage during the spring will decrease the penetration. The overall net affect is a yearly decrease in the penetration as the crown gets bigger.

Comparing Global And Diffuse Radiation Distributions Within The Crown On Cloudless And Overcast Days

Discussion up to this point has only dealt with the distribution of global radiation within the crown of the study tree. An additional experiment was performed to measure the diffuse radiation in the crown on cloudless days (see Table 2.3). Diffuse radiation was measured by shading the trolley mounted pyranometers with a clipboard

The percent penetration of global radiation is defined by Eq. 4.2. The percent penetration of diffuse radiation is defined as

$$\text{percent penetration of } D = \{D(\text{crown})/D_o(\text{open})\}100 \qquad (4.3)$$

where D(crown) is the diffuse radiation measured in the crown and D_o(open) is the diffuse radiation measured in the open. Typical results are given in Figure 4.12a for both the penetration of diffuse and global radiation along the EW-2 transect and Figure 4.12b gives results for the NS-2 transect.

From Figures 4.12a-b, it is apparent that the penetration of diffuse and global radiation are different. Diffuse radiation penetrates much farther into the crown. Ninety percent of the global radiation is intercepted in the first 50 cm of continuous crown but diffuse radiation can penetrate to the center of the tree with less than 90% interception. The penetration of diffuse and global radiation are similar in that both have the same general elliptical pattern, except near the edges of the crown.

On cloudless days, more diffuse radiation was measured at the edge of the crown than there was in the open. There is apparently an "enhancement" of diffuse radiation from the reflection of direct radiation from the outer layers of foliage. A summary of this diffuse radiation enhancement for various positions outside of the crown is given in Table 4.3. The greatest enhancement occurs on the side of the crown facing the sun. On the South side of the crown at Level 3, there was a 60% increase (i.e., an increase of 0.06 cal $cm^{-2}min^{-1}$) in diffuse radiation next to the crown over that measured in the open.

Figure 4.12 Comparing diffuse and global radiation distributions on cloudless days. Figure 4.12a shows results for the East-West, Level 1 transect on October 4, 1979. Figure 4.12b gives results for the North-South, Level 1 transect on October 4, 1979. Note that the diffuse radiation just outside of the crown (upper left corner of Figure 4.12b) is 20-30% greater than that in the open.

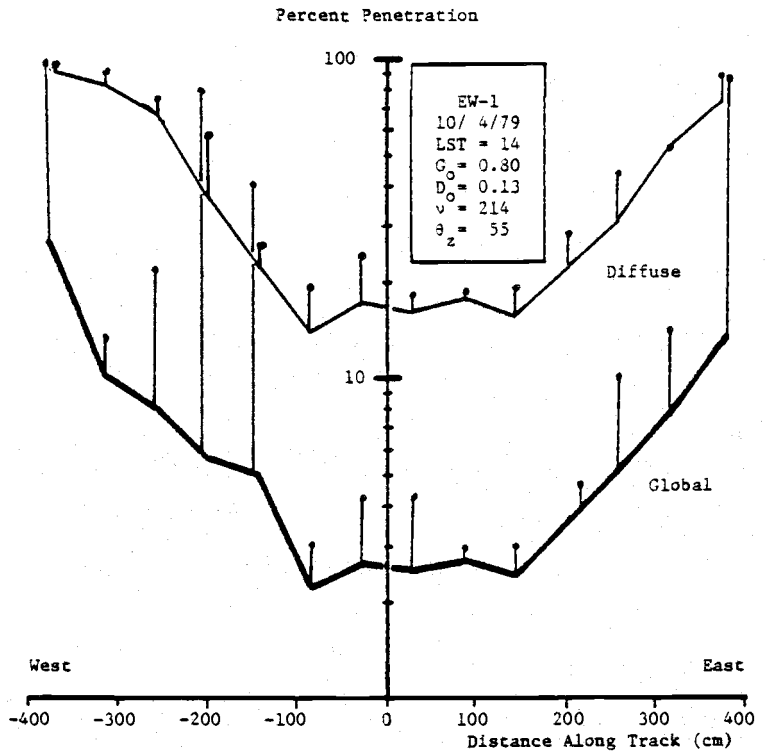

Figure 4.12a

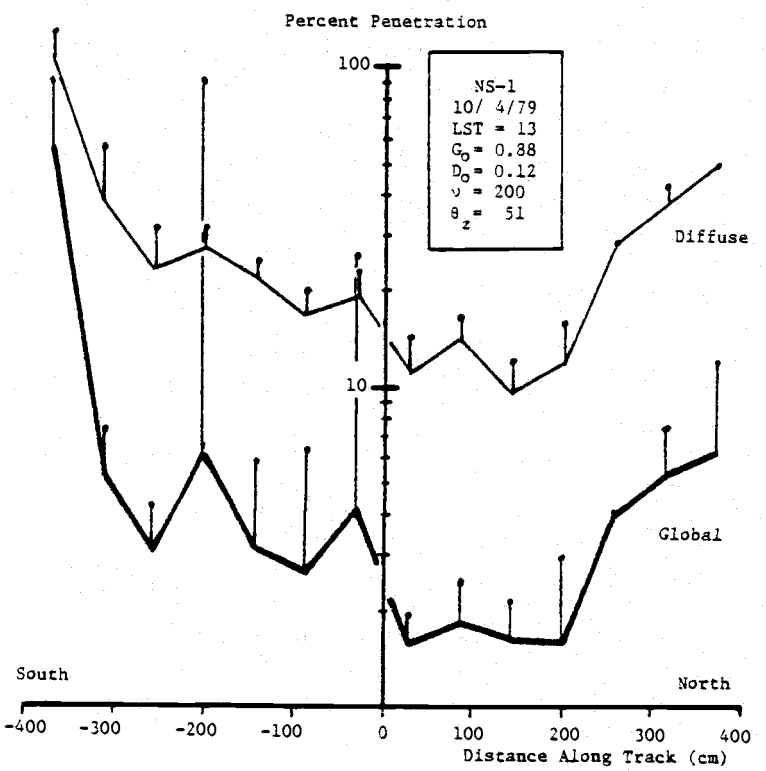

Figure 4.12b

Table 4.3 Enhancement of diffuse radiation outside the crown on cloudless days.

Transect	Crown† Aspect	Max $\frac{D(crown)}{D_o(open)}$	θ_z (degree)	ν (degree)	LST (hr)
EW-1	E,W	1.00	55	214	14
NS-1	S	1.30	51	200	13
EW-2	W	1.25	46	208	13
NS-2	S	1.50	58	231	15
EW-3	W	1.35	52	208	13
NS-3	S	1.60	52	209	13

† Side of the crown along the transect in which the maximum enhancement occured.

On the shaded side of the crown, diffuse radiation was always less than or equal to the open value.

These results on the enhancement of diffuse radiation are almost identical to those of Miller (1969b) who recorded an increase of 0.05 to 0.10 cal $cm^{-2}min^{-1}$ of diffuse radiation near the top of the canopy in a stand of aspen and a stand of oak on cloudless days. No increase occurred with overcast skies. Miller attributed this enhancement to an outward reflection of direct radiation from the canopy.

In Figure 4.13, a comparison is made between the penetration of diffuse and global radiation on overcast and cloudless days. It is apparent that the penetration of the diffuse radiation on overcast days is quite different from that on cloudless days. Overcast radiation is greatly intercepted near the crown edge. Of the three curves shown in Figure 4.13, the cloudless day penetration curves are more "elliptical" whereas the overcast penetration curve is more "Gaussian". The significance of the curve shapes will be discussed in greater detail in Chapter VII.

Before finishing this chapter on radiation measurements in the crown, a comparison is made between the relative proportion of diffuse and direct radiation. In Figures 4.14a-b, the ratio of diffuse (D) to global (G) radiation, D/G, is plotted for a EW-1 and NS-1 transect on cloudless days. The ratio of direct to global radiation is simply

$$1 - D/G \qquad (4.4)$$

The vertical bars in Figures 4.14a-b indicate the range of values

measured by the four Kipp pyranometers. The solid line joining the maximum values of the D/G ratio indicates those radiation measurements with the greatest interception. This is consistent with the method used in constructing Figures 4.6, 4.9 and 4.11, in that only the smallest value of global radiation is plotted.

From Figure 4.14, it is obvious that the proportion of diffuse and direct radiation is not a constant throughout the crown. In the open, diffuse radiation makes up only 10-15% of the global radiation on cloudless days but inside the crown, over 50% of the radiation consists of diffuse. Inside the shaded portion of the crown (see right side of Figure 4.14b) over 80% of the radiation is diffuse . Diffuse radiation penetrates farther into the crown than direct radiation.

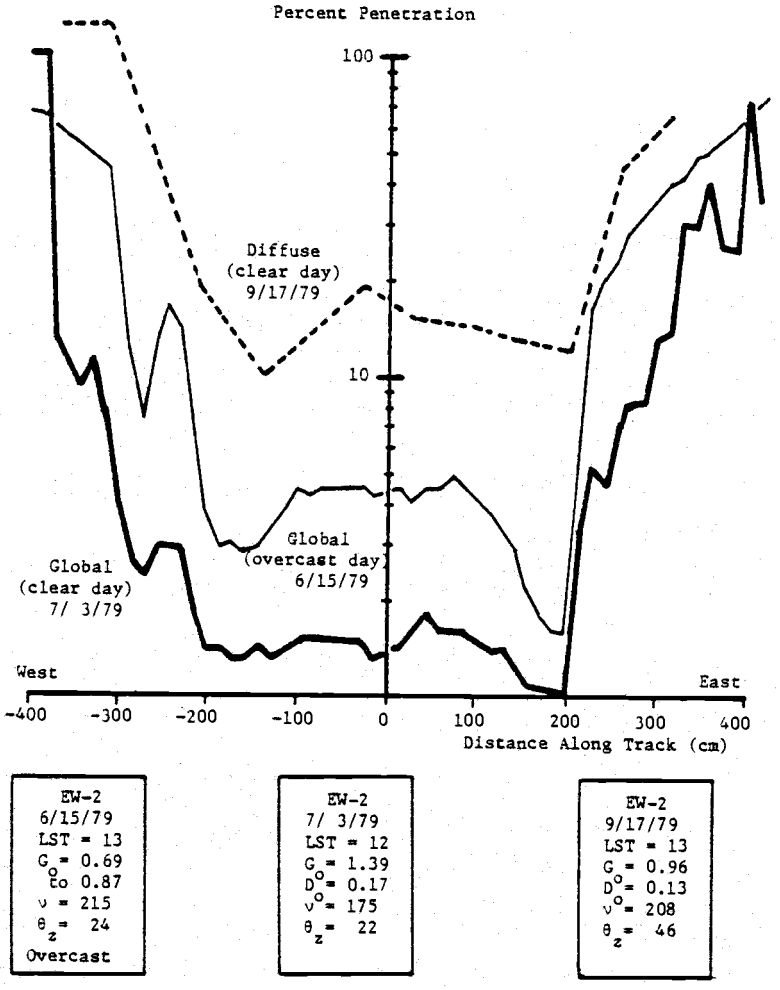

Figure 4.13 Comparing diffuse and global radiation on overcast and on cloudless days along the East-West, Level 2 transect.

Figure 4.14 The proportion of diffuse and direct radiation in the crown. The ratio of diffuse to global radiation along the EW-1 transect is given in Figure 4.14a and along the NS-1 transect is given in Figure 4.14b. Note the change in scale along the vertical (ordinate) axis.

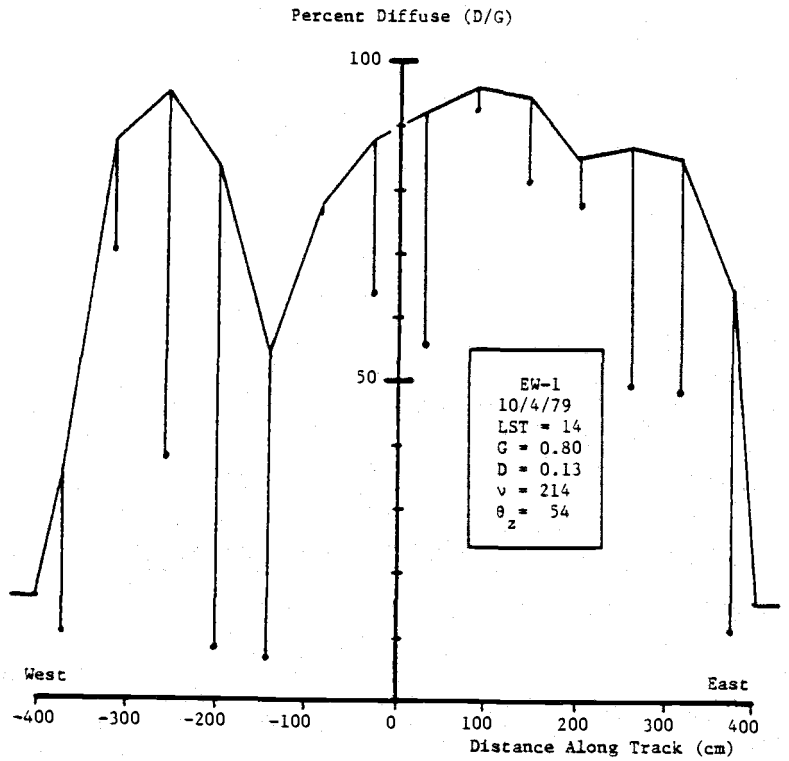

Figure 4.14a

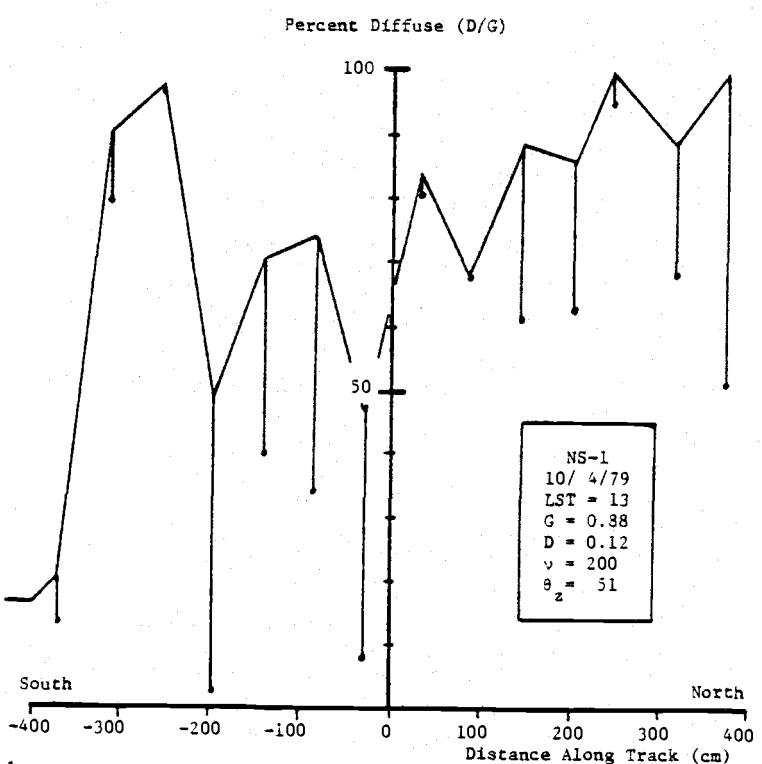

Figure 4.14b

V. CHARACTERIZING FOLIAGE DISTRIBUTION

Introduction

The photosynthetic production of a tree crown depends not only on the amount of foliage present but also on the configuration of leaves making up the canopy. Some of the most recent work dealing with the problems of modeling photosynthetic production and foliage configuration in plant stands may be found in Sestak et al. (1971). Much of the recent work has been developed from the earlier research of Japanese workers who pioneered the studies of the relationship between leaf configuration and the penetration of radiation into the canopy (Monsi and Saeki, 1953). Kvet and Marshall (1971) considered the following information to be essential to characterize a canopy and its net photosynthetic production :

a) total leaf area index (LAI) ;

b) the vertical profile of LAI;

c) the arrangement of the leaves, defined in terms of the distribution of their orientation (azimuth) and inclination (angle from a vertical or horizontal plane) within the whole canopy or finite layers of it;

d) the reflection and transmission of light by the leaves;

e) the photosynthetic characteristics of the leaves in different parts of the canopy.

In Table 5.1, a brief review is given of the studies that have addressed some of the above mentioned aspects of photosynthetic

Table 5.1 Review of studies concerning the factors that affect photosynthate production in mature Douglas-fir trees and forest stands.

Research Area	Author	Comment
Biomass distribution of foliage and wood	Webber (1977)	Young stands
	Burger et al. (1935) Newbold (1967) Reukema (1957) Reukema (1961)	Mature stands
	Denison et al. (1972)	Old-growth (> 450 yrs)
Distribution of foliage	Silver (1962)	Age distribution
	Dice (1968)	Distribution by whorl
	Mitchell (1974)	Life table analysis for young open-grown
Crown development	Campbell (1958)	Affect on stem volume
	Jensen (1976)	Crown structure and branch distribution
Penetration of radiation	Vermilion (1975)	Vertical profile of net radiation in stand. Also included reflection and transmission.
Photosynthate characteristics of crown	Helms (1963) Helms (1965)	Diurnal & seasonal variation in NA
	Woodman (1968) Woodman (1971)	NA activity in crown, by whorl position and crown aspect
	Leverenz (1974)	Relationship of NA to shoot hierarchy
	Salo (1974)	Influence of environmental factors on NA in crown

Table 5.1 (cont.)

Research Area	Author	Comment
Vertical profile of LAI in canopy	Kinerson and Fritschen (1971)	Simple canopy model
Simulation models of crown	Arney (1972) Mitchell (1975)	Simulated crown growth of individual trees

NA net assimilation

production in the canopy of mature Douglas-fir trees. However, no single research study has ever examined more than one or two aspects of this problem at a time.

From Table 5.1, it is apparent that few studies have examined leaf arrangement in Douglas-fir trees. Silver (1962) and Mitchell (1974) studied the age distribution of Douglas-fir needles but they did not examine how the needles were arranged (i.e., foliage inclination, orientation and distribution). Beer's Law has usually been assumed to be valid for the penetration of radiation into Douglas-fir canopies (e.g., Woodman ,1968; Pope, 1978). In order for Beer's Law to be correct, however, the foliage must be randomly distributed and homogeneous. Vermilion (1975) is the only one who has provided any light data to support this contention. Vermilion found that of the four models she considered (Poisson, which reduces to Beer's Law; positive binomial; negative binomial; and Markov), the Poisson model with a randomly dispersed, spherical distribution of foliage seemed to fit a stand of Douglas-fir most closely.

Considering the importance of radiation penetration to photosynthate production, the paucity in data to prove or disprove Beer's Law is alarming. The major obstacle to any such test, however, is the difficulty in accurately measuring leaf area index in the canopy. The following discussion examines a photographic method to measure leaf area of Douglas-fir branch sections and proposes a simple check of Beer's Law.

Measuring Leaf Area Index

Leaf area is generally calculated by first measuring leaf biomass distribution within the crown of a tree and then multiplying this by a constant specific leaf area (cm^2 leaf area g^{-1} dry weight leaf). Unfortunately, these constants are site specific and vary with needle age, crown position and crown aspect (Gholz et al., 1976; Del Rio and Berg, 1979). Morphological differences related to light intensity can cause the value of specific leaf area (one-sided) from the same age of foliage on the same species to increase from less than 50 cm^2g^{-1} to 150 cm^2g^{-1} from the top of the canopy to the bottom for Douglas-fir (Gholz et al., 1976).

Because of the anticipated variability in specific leaf area in the study tree and because the study tree could not be destructively sampled, a special control experiment was set up (see details in Chapter III). Ten Douglas-fir branches from a nearby forest were obtained, subdivided into 40 cm by 40 cm sections and then photographed. Obviously, the actual leaf area measurements of these branches are unique to only these branches but the general leaf arrangement and distribution is assumed to be a general characteristic of Douglas-fir foliage in mature trees.

In Figure 5.1, a schematic view is given of the various leaf area measurements. Let the one-sided, projected area of the i-th leaf equal A(i). The total one-sided leaf area, A, is defined as the sum of all leaf areas in a branch, $A = \Sigma A(i)$. This area, $A(cm^2)$, is the maximum area available for the interception of direct radi-

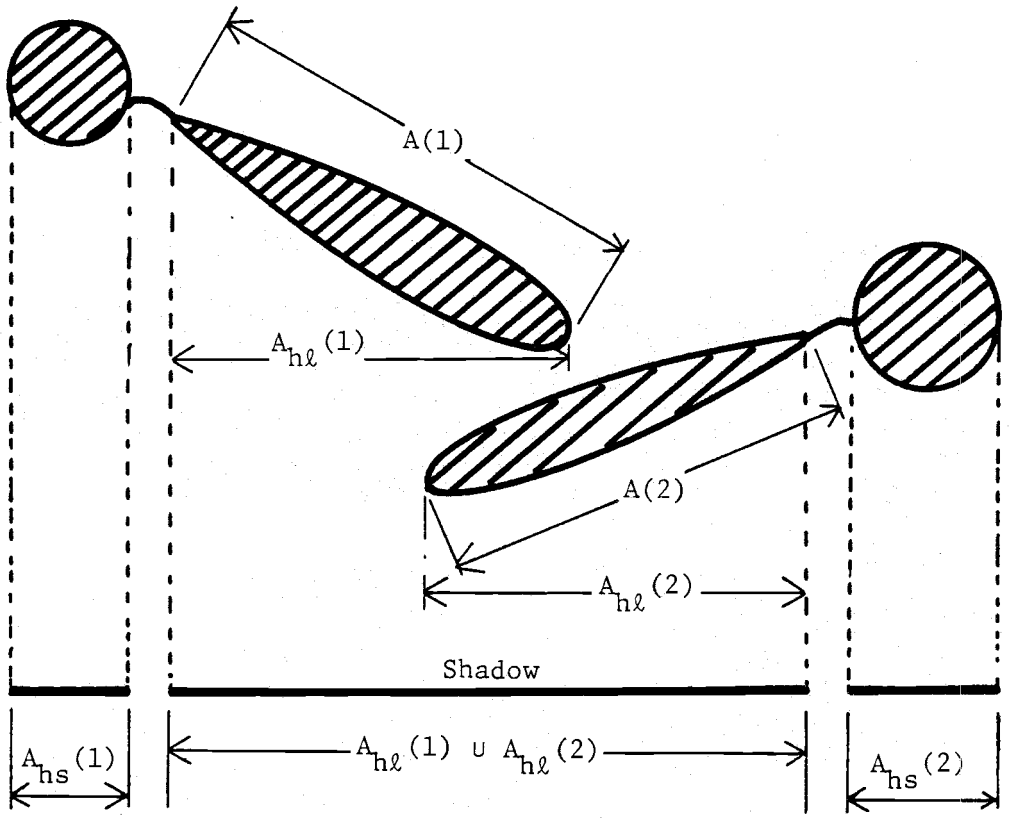

Figure 5.1 Schematic view of projected leaf area measurements. See text for definition of terms.

ation in a branch. The total one-sided leaf area depends upon the number of leaves and their individual sizes. The leaf area index, LAI, is computed by taking the value of A and then dividing it by a unit area of ground.

$$LAI = A/A_{grnd} \qquad (cm^2/cm^2) \qquad (5.1)$$

Clearly, for a branch with any appreciable leaf area there will be mutual shading between some of the leaves and the branch stems. A precise index of this shading is obtained by measuring the shadow cast by overlapping leaves and stems. Let $A_{h\ell}(i)$ be the horizontal projected area of the i-th leaf. The union of all such projected leaf areas onto a horizontal reference plane gives the horizontal leaf shadow area, $A_{h\ell}(cm^2)$, where $A_{h\ell} = \cup A_{h\ell}(i)$. The horizontal leaf shadow area is the area illuminated by direct radiation that is normal to the horizontal reference plane. This area, $A_{h\ell}$, depends upon the same factors as for A but in addition, it depends upon the angular orientation and spatial distribution of the leaves within the branch. Thus, $A_{h\ell}$ must always be less than or equal to A for any particular reference plane.

If we define $A_{hs}(j)$ as the horizontal projected area of the j-th stem, then the union of all such areas onto a horizontal reference plane gives the horizontal stem shadow area, $A_{hs}(cm^2)$, where $A_{hs} = \cup A_{hs}(j)$.

The total horizontal shadow area cast by a branch is equal to the union of all leaf and stem shadows. As an approximation to this, however, we shall assume that the total horizontal shadow area,

$A_{ht}(cm^2)$, is equal to the sum of the leaf and stem shadow areas (i.e., stem and leaf shadows are independent from each other but not amongst themselves).

$$A_{ht} = A_{h\ell} + A_{hs} \quad (cm^2) \tag{5.2}$$

From Figure 3.5, it is apparent that there are few needles attached to the larger stem sections. Thus, the approximate formulation given by Eq. 5.2 seems reasonable.

The total one-sided leaf area, A, of each branch section was determined by a leaf weighing method (see Chapter III). In this method, the oven dry weights of the branch needles are multiplied by the specific leaf area. Specific leaf area is determined from a sample of 100 needles per section and by measuring leaf area with a LI-COR , LI-3000, optical planimeter. The total horizontal shadow area, A_{ht}, was determined from photographs taken of branch silhouettes (see Figure 3.5). Horizontal stem shadow area, A_{hs}, was measured from photographs of branch sections from which the needles were completely stripped (see Figure 3.6). Horizontal leaf shadow area, $A_{h\ell}$, is computed from Eq. 5.2, using the measured values of A_{ht} and A_{hs}. Results of these measurements for the ten branches are given in Appendix B.

Specific leaf area for these branch sections varied between 54-88 $cm^2 g^{-1}$. Total one-sided leaf area varied from 105-3500 cm^2. The smallest leaf area was measured on the proximal end of a branch, the largest in the mid portion and with decreased area at the distal end. Horizontal leaf shadow area varied between 67-1055 cm^2 and

horizontal stem shadow area varied between 70-348 cm^2.

In Table 5.2, the average characteristics of the ten branches are given as a function of the distance along the branch. Note that needle distribution is almost symmetrical about the mid portion of the branch. This agrees with Jensen (1976) who found that the Douglas-fir foliage appeared to be nearly normally distributed along the length of older branches. The specific leaf area along the branch varied like that of total leaf area, maximum in the mid portion and minimum at both ends of the branch. This variation is probably due to the two competing factors affecting specific leaf area. Specific leaf area decreases substantially with age but increases when grown under low levels of radiation (Del Rio and Berg, 1979).

The ratio of $A_{h\ell}$ to that of A is called P_h, where

$$P_h = A_{h\ell}/A \tag{5.3}$$

This ratio is the proportion of horizontal leaf shadow area of the branch that receives direct radiation. This ratio may be interpreted as the efficiency in the arrangement of leaves for the capture of direct radiation (Max, 1975). The mean value of this ratio for the ten branches is plotted in Figure 5.2 as a function of position along the branch. Note that each branch segment is about 40 cm long. The greatest amount of mutual shading between needles occurs in the mid portion of the branches. On the proximal end of a branch, the needles are widely spaced as the innermost ones die out. On the distal end of the branch, needles are more widely spaced because the

Table 5.2 Average control-branch characteristics as a function of branch location. Each branch section is about 40 cm long and 40 cm wide.

	Section	Foliage* Weight (g)	Stem* Weight (g)	Specific Leaf** Area ($cm^2 g^{-1}$)	Specific Stem† Area ($cm^2 g^{-1}$)
(proximal)	S1	10	170	65 ±13	1.5
	S2	17	152	66 ±13	1.8
	S3	22	120	74 ±13	2.1
	S4	30	80	71 ±13	2.9
	S5	35	48	71 ±13	3.9
	S6	30	23	68 ±13	6.1
(distal)	S7	22	12	68 ±13	8.0

* oven dried at 70°C for 24 hours

** fresh, one-sided leaf area per oven dry weight

† approximate one-sided area of stem (oven dried) per oven dry weight

± approximate 95% confidence interval

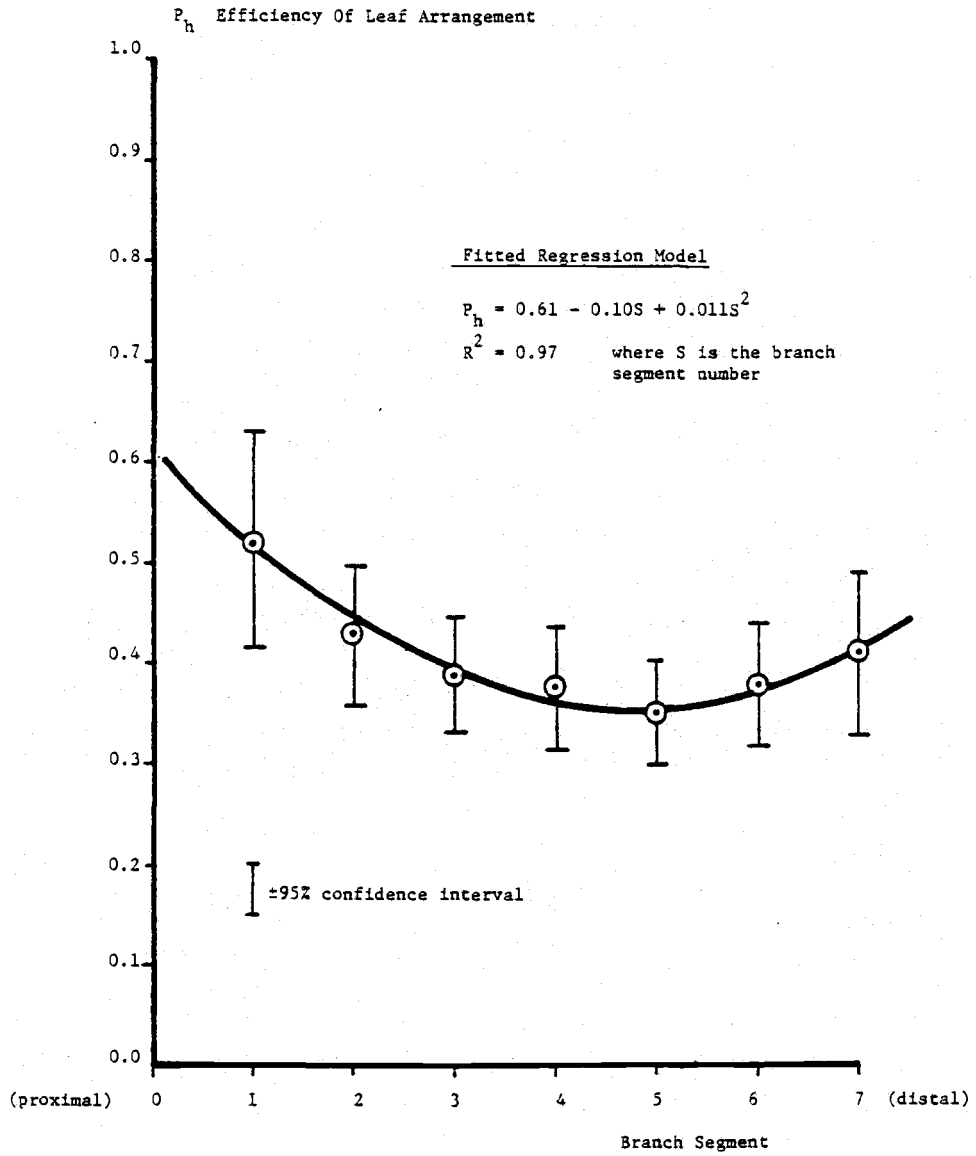

Figure 5.2 Efficiency of leaf arrangement as a function of distance along the branch. The mean value from ten Douglas-fir branches is plotted.

leading edge of the branch tips are growing into unoccupied space.

Leaf Arrangement

If the leaf arrangement in Douglas-fir branches follows that of the Poisson model (see Eq. 1.2), the proportion of direct radiation that is intercepted by the needles equals

$$\text{proportion of light intercepted} = 1 - \exp(-k\,LAI) \tag{5.4}$$

However, the cumulative leaf area index is defined in Eq. 5.1 where $A_{grnd}(cm^2)$ is the unit area of ground. A_{grnd} is measured directly from photographs of branch section silhouettes by tracing the outline of each branch section and then measuring the area within each outline. In Eq. 5.4, the proportion of direct radiation that is intercepted by leaves equals the proportion of ground area that is in leaf shadow. Thus, Eq. 5.4 may be written as

$$A_{h\ell}/A_{grnd} = 1 - \exp(-k\,LAI) \tag{5.5}$$

If leaf arrangement follows the Poisson model, then a semi-logarithmic plot of $(1-A_{h\ell}/A_{grnd})$ versus (LAI) will yield a straight line, the slope equalling the extinction coefficient, k. Data from the 65 branch sections of the branch-control experiment (see Appendix B) are plotted in Figure 5.3.

From the regression analysis of the data (see Figure 5.3 for more details), the slope of the regression line and its 95% confidence interval equalled -0.483 ± 0.0169. Thus the extinction

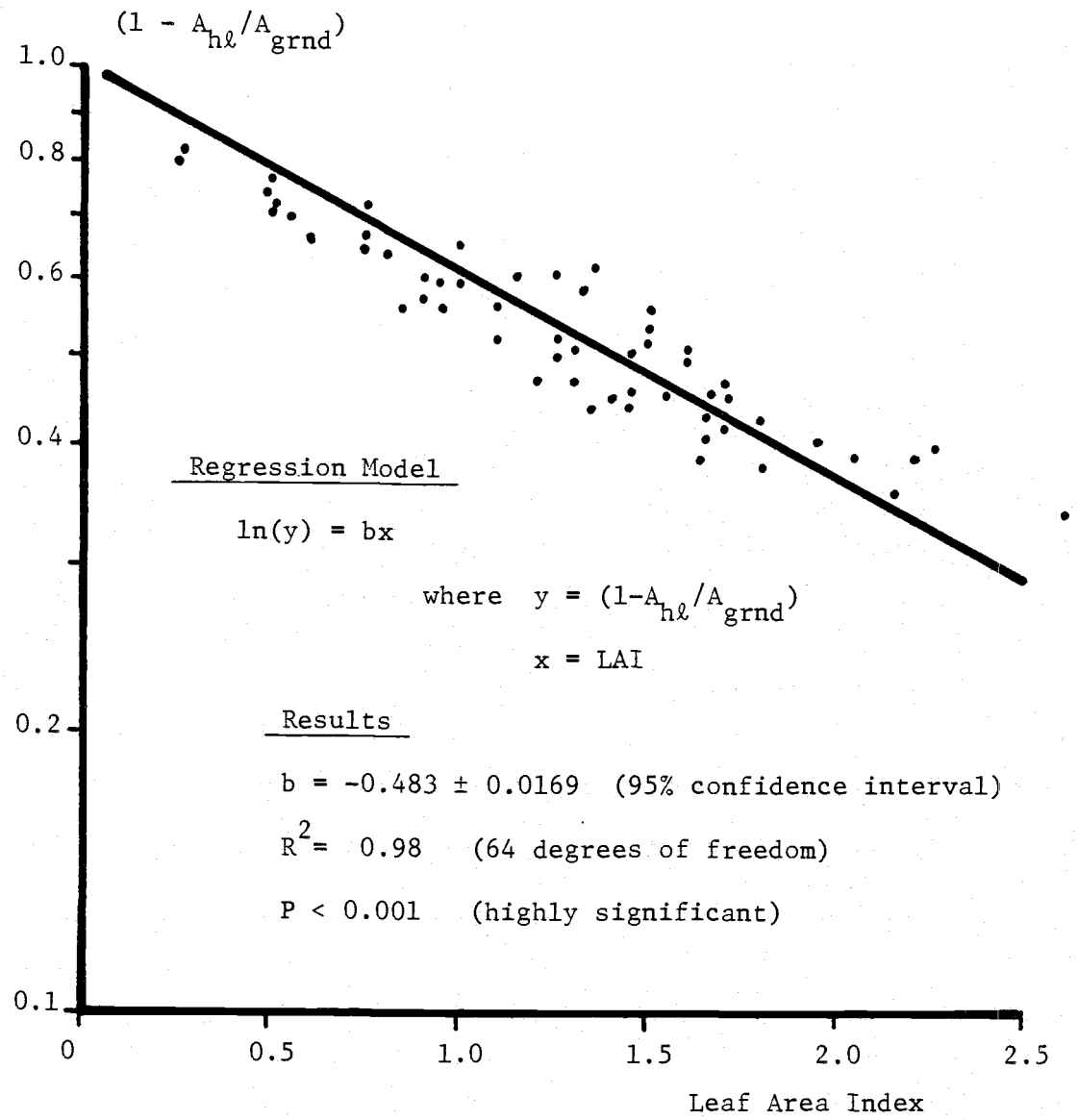

Figure 5.3 Semi-logarithmic plot of the proportion of ground area that is not in leaf shadow versus leaf area index of Douglas-fir branch sections. Data is obtained by a photographic technique in the branch-control experiment.

coefficient is approximately equal to 0.5. From Eq. 1.4, the Poisson model states that if the foliage has no preferred orientation or inclination and if the view angle is vertical (i.e., θ=90°), then the extinction coefficient of the Poisson model equals 0.5. This special case of the Poisson model is called Beer's Law and it describes the gap frequency distribution of the foliage. Thus, it appears that the needles of Douglas-fir branches have no preferred orientation and no preferred inclination. The fraction of foliage pointing in a given direction is the same for all directions (i.e., spherical leaf angle distribution).

The above analysis refers only to the light interception properties of the needles and excludes the presence of stem wood in the branch. Analogous to the leaf area index, one may also define the cumulative area of stem and leaf per unit area of ground as the shadow area index (SAI).

$$(SAI) = (A + A_{hs})/A_{grnd} \qquad (cm^2/cm^2) \quad (5.6)$$

Assuming the Poisson model is valid, the proportion of direct radiation that is intercepted by the needles and stem wood equals

$$A_{ht}/A_{grnd} = 1 - \exp(-k\,SAI) \qquad (5.7)$$

The variable $(1-A_{ht}/A_{grnd})$ is plotted on semi-logarithmic paper against SAI in Figure 5.4 using data from the 65 branch sections (see Appendix B). From the regression analysis of the data (see Figure 5.4 for more details), the slope of the regression line and its 95% confidence interval equalled -0.669 ± 0.0254. Thus the

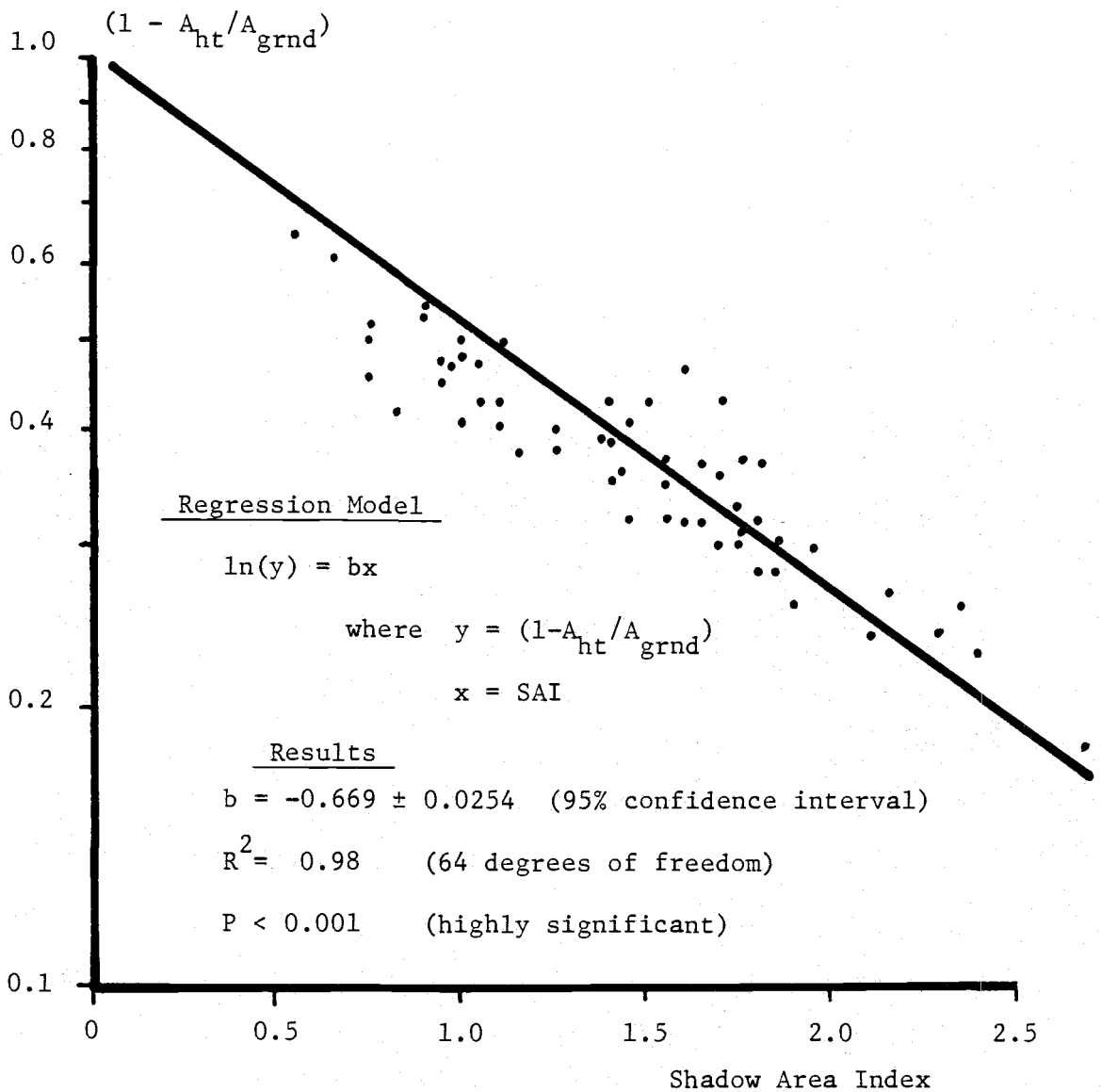

Figure 5.4 Semi-logarithmic plot of the proportion of ground area that is not in leaf+stem shadow versus shadow area index of Douglas-fir branch sections. Data is obtained by a photographic technique in the branch-control experiment.

extinction coefficient is approximately equal to 0.7. The attenuation of direct radiation by leaf+stem is substantially reduced in comparison to the attenuation by leaves only. The increase in the extinction coefficient is due to the non-random orientation and distribution of stem wood in the branch. If the stems had been randomly dispersed, the extinction coefficient of leaf+stem would have remained equal to 0.5. The penetration into leaf+stem is still described by the general process of a Poisson model (i.e., Eq. 5.7) but this model will now be called the modified Beer's Law to identify the non-random nature of stem wood in the branch.

Estimating Shadow Area Index In The Branch-Control Experiment

The shadow area index can be estimated from the penetration data of solar radiation. If we assume the Poisson model of Eq. 5.7 (i.e., modified Beer's Law) is correct, then the proportion of direct radiation that penetrates through an amount SAI of leaf+stem foliage equals

$$I/I_o = \exp(-0.7\,SAI/\cos\theta_z) \qquad (5.8)$$

where I_o is the flux density (cal $cm^{-2}min^{-1}$) of direct radiation measured in the open and perpendicular to the sun's rays; I is the flux density (cal $cm^{-2}min^{-1}$) of direct radiation within the canopy; SAI (cm^2/cm^2) is the shadow area index and θ_z is the solar zenith angle (degrees). Rearranging Eq. 5.8, one may solve for SAI if all of the other variables are known. Thus, SAI equals

$$SAI = - \ln(I/I_o)\frac{\cos\theta_z}{0.7} \qquad (cm^2/cm^2) \qquad (5.9)$$

In the branch-control experiment, both diffuse and global radiation measurements were taken under ten different Douglas-fir branches (see Capter III). Four Kipp pyranometers were mounted on a trolley and positioned beneath section S1 of the branches (see Figures 3.1 and 3.4). The branches were held in a horizontal position and their distal ends oriented due South.

Data from the branch-control experiment was taken on January 19, 1980 and the results plotted in Figure 5.5. The data from each branch is identified in Figure 5.5 as branch C1, C2, ..., C10. Direct radiation under the branch was estimated using the method given by Eq. 2.7 but the uncertainty in measuring global and diffuse radiation (i.e., $\pm$ 0.01 cal $cm^{-2}min^{-1}$) was similar in size to the value of direct radiation computed by Eq. 2.7. Thus, the penetration of global radiation is used in Eq. 5.9 and plotted along the vertical axis of Figure 5.5. The vertical bars in Figure 5.5 indicate the range of predicted values of SAI computed from data measured by the four Kipp pyranometers. The average measured values of SAI from branch sections S1 and S2 are computed from Eq. 5.6 and plotted along the horizontal axis of Figure 5.5. Even though the pyranometers were located below section S1 of the branch, solar radiation also passed through section S2 before reaching the pyranometers because of the large solar zenith angle.

If the measured and predicted values of SAI agree, they would

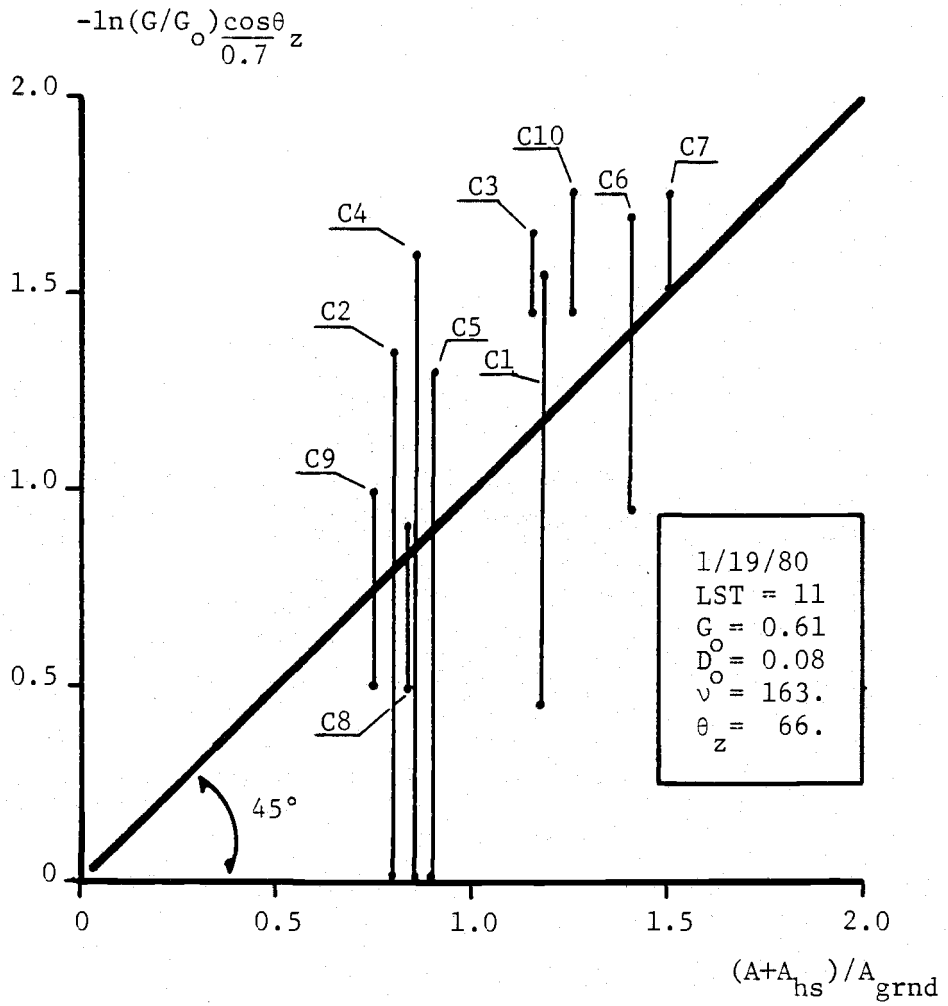

Figure 5.5 A comparison between predicted (vertical axis) and measured values (horizontal axis) of shadow area index in the branch-control experiment. The predicted value is computed from the penetration of global radiation and the measured value is computed from the photographic experiment. The range in data for each branch is indicated by a vertical bar.

fall along the diagonal line marked in Figure 5.5. In general, the agreement with average values is very good. The greater penetration through branches C2, C4 and C5 indicates the presence of large gaps in the foliage along sections S1 and S2. The unexpected decrease in penetration through branches C3 and C10 is due to the higher than average amount of stem wood area in sections S1 and S2 of these two branches (see branch data in Appendix B). The greater the area of stem, the less random the foliage becomes and hence greater the extinction coefficient.

Estimating Shadow Area Index In The Study Tree

In Chapter IV, the percent penetration was plotted on semi-logarithmic graph paper. Not only does this allow greater detail to be seen at low radiation levels, it also shows the apparent shadow area index as a function of crown position. This should be obvious by examining Eq. 5.9, since multiplying the ln(penetraation) of direct radiation by $(\cos\theta_z)/0.7$ gives SAI. Since most of the data given in Chapter IV is global radiation, the above interpretation of SAI is only approximate but still useful (see Figure 5.5). Consider the following

$$SAI \simeq - \ln(G/G_o)\frac{\cos\theta_z}{0.7} \qquad (cm^2/cm^2) \qquad (5.10)$$

Equation 5.10 is probably most accurate when using global radiation on cloudless days and on the sunny side of the crown (i.e., when the

D/G ratio is low). When the diffuse component of the global radiation becomes large, Eq. 5.10 will underestimate the value of SAI.

Equation 5.10 also points out one additional fact. When taking point, instantaneous measurements of radiation in the crown, one gets point, instantaneous measurements of the apparent SAI from Eq. 5.10. Since Eq. 5.10 is a non-linear transformation, it is important that one does not use "average" values of radiation to compute SAI. Radiation data must first be transformed and then it can be averaged. Better yet, don't average anything but express the results in terms of its range, as shown in Chapter IV and in Figure 5.5.

As an example, the global radiation data from Figures 4.5c-d were replotted in terms of the apparent SAI in Figures 5.6a-b using Eq. 5.10. Figures 4.5c and 5.6a are identical except for a multiplication factor (i.e., $(\cos\theta_z)/0.7$) and that the two figures are inverted from each other. Figures 4.5d and 5.6b are also directly related.

A schematic view of the crown is given in Figure 5.7 to emphasize how the shadow area index is measured. Since the term SAI refers to the cumulative shadow area per unit area of ground, measured along a vertical reference, dividing SAI by $\cos\theta_z$ gives the apparent shadow area index along the sun-pyranometer line-of-sight.

Figure 5.6 Spatial variation in the apparent SAI as "viewed" by the Kipp pyranometers. Vertical bars indicate the range in values. Figure 5.6a shows variation along the EW-2 transect and Figure 5.6b shows variation along NS-2.

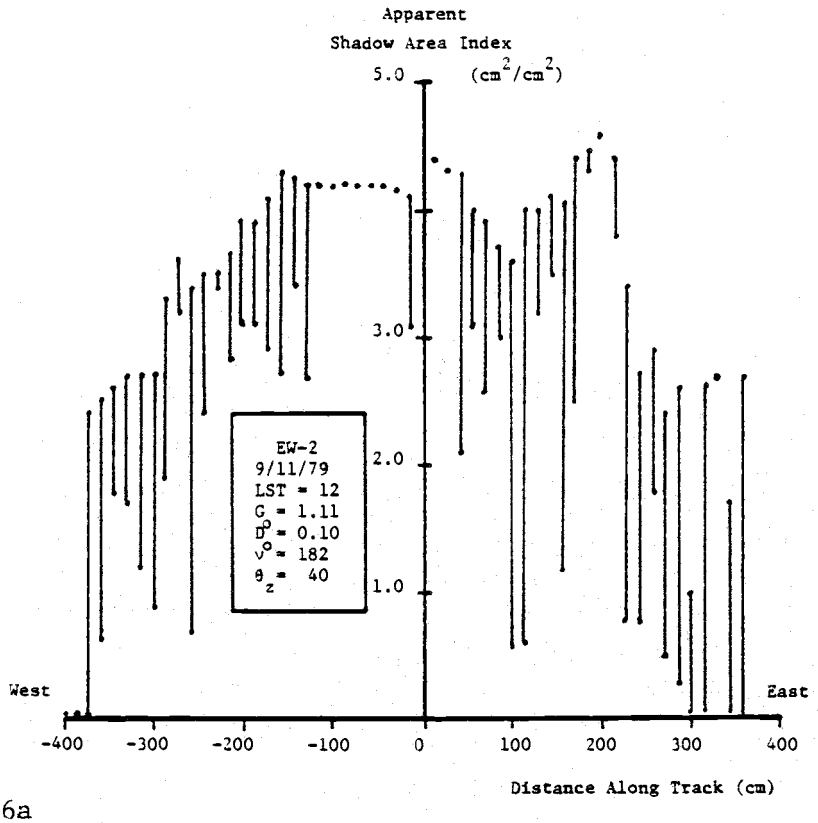

Figure 5.6a

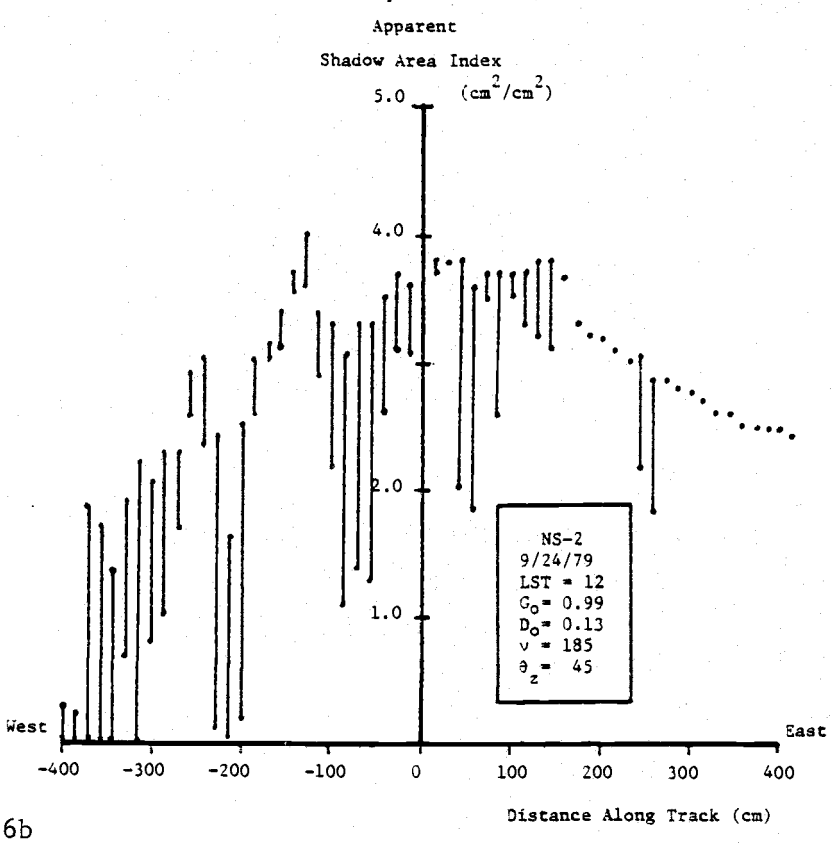

Figure 5.6b

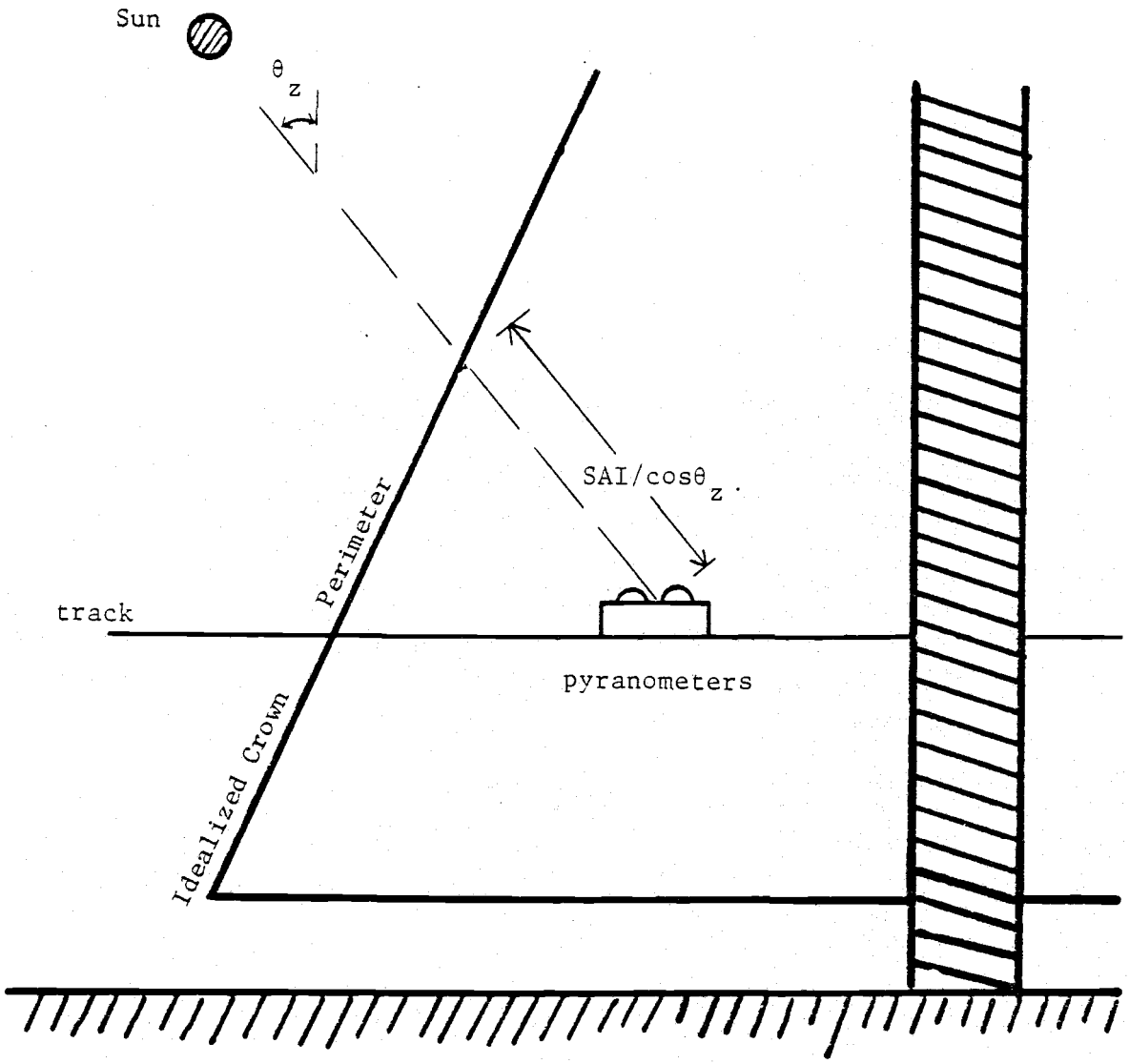

Figure 5.7 Schematic view of crown and pyranometers showing how the apparent shadow area index is measured.

VI. DISTRIBUTION OF POTENTIAL NET PHOTOSYNTHATE WITHIN THE CROWN

Effect Of Light On Photosynthesis

The relation between light intensity and net photosynthesis in Douglas-fir seedlings and shoots is well documented (Fry, 1965; Hodges, 1965; Brix, 1967; Walker et al., 1972; Leverenz, 1974; Salo, 1974; Pope, 1978). Photosynthesis can be thought of as a two step process: a light or photochemical step followed by a temperature-controlled dark step or carbon dioxide (CO_2) fixation reaction (Devlin and Barker, 1971). The photochemical system supplies chemical energy and reducing potential converted from photosynthetically active radiation (PAR, 390-700 nm) and water, to the CO_2 fixation process. As light intensity increases, the rate of supply of energy and reducing potential increase in approximately linear proportions to that of the CO_2 fixation process. Thus photosynthesis rates increase linearly at low light intensities. Above a certain point, called light saturation, the CO_2 fixing system can no longer utilize all of the chemical energy and reducing potential as fast as it is supplied. This results in a diminishing increase in photosynthesis with increasing light intensity.

A typical response curve between light intensity and net assimilation rate is given in Table 6.1 and Figure 6.1 at different leaf temperatures for a ten-year-old Douglas-fir. The maximum net assimilation rates given in Table 6.1 may seem a little low but Salo (1974) conducted his experiments in a controlled environment using

Table 6.1 Average net assimilation rates for ten-year-old potted Douglas-fir saplings as a function of leaf temperature and photon flux density. Data is taken from Appendix 5, page 142 of Salo (1974).

Photon Flux Density (μEinsteins $m^{-2}sec^{-1}$)	Leaf Temperature (°C)						
	0	2	5	10	15	20	25
550		3.64	3.93	4.36	4.05	4.00	3.81
385	3.03	3.65	3.85	4.24	3.74	3.76	3.54
290	3.04						
250	2.77	3.27	3.44	3.70	3.25	3.10	2.78
155	2.27	2.56	2.73	2.83	2.49	2.07	1.74
95	1.79	1.94	2.04	2.05	1.73	1.18	0.98
50	1.25	1.24	1.24	1.20	0.94	0.36	0.19
30	0.87	0.76	0.73	0.71	0.33	-0.12	-1.26
0	0.00	-0.25	-0.34	-0.45	-0.69	-1.00	-1.26

Net assimilation rates are expressed on a one-sided leaf surface area basis (mg CO_2 $dm^{-2}h^{-1}$).

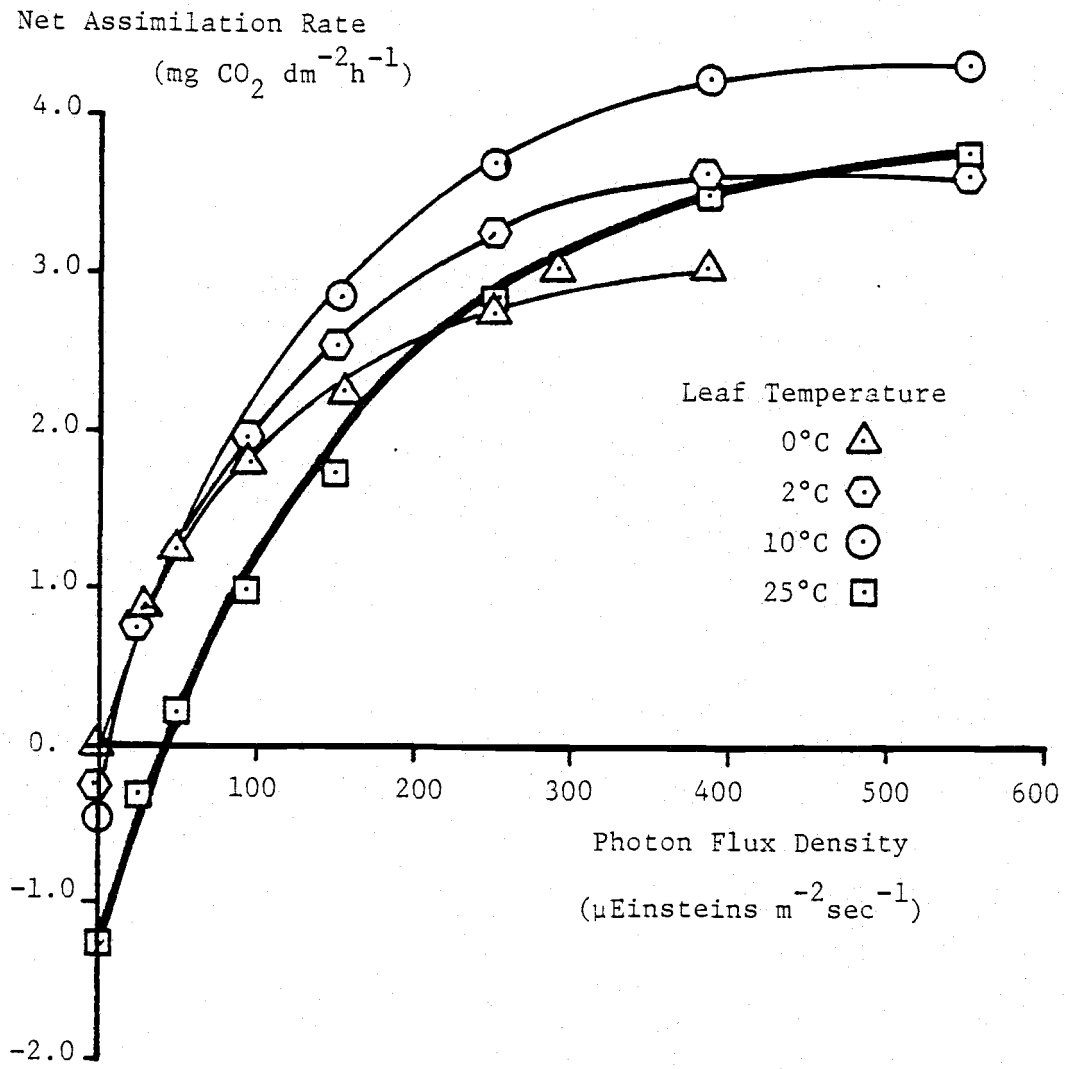

Figure 6.1 Average net assimilation rates for ten-year-old Douglas-fir saplings as a function of photon flux density at four different leaf temperatures. Data is taken from Table 6.1.

greenhouse-grown, potted saplings. Garden-grown plants have a relatively high surface area to dry weight ratio in comparison to plants grown in the field (Salo, 1974). When net assimilation rates are expressed on a gram dry weight basis, Salo found that the maximum net assimilation rates of garden-grown and field-grown Douglas-fir are very similar (i.e., about 5 mg CO_2 $g^{-1}h^{-1}$ at $10^{o}C$).

The negative rates of net assimilation at low light levels in Table 6.1 indicate that more CO_2 is being released than is being taken up by the foliage. This release of CO_2 and consumption of oxygen (O_2) during periods of light seems to be due to processes that are at least partially different from those occuring in the dark (Jackson and Volk, 1970). Conifers, like most dicots and temperate grasses, are C_3 (pentose pathway) plants possessing a substantial rate of photorespiration (Salo, 1974). Typically, from two to three percent of full sunlight is necessary for photosynthesis to balance respiration (Horn, 1971). The point of zero net photosynthesis (i.e., photosynthesis equals respiration) is called the light compensation point. This is the point of zero net CO_2 exchange between the leaf and the atmosphere.

Distribution Of Photosynthate Within The Crown Of A Douglas-fir: A Review

The distribution of light within the crown gives valuable information on the potential ability of the foliage to produce photo-

synthate. There are, however, many additional environmental, morphological and physiological factors besides light that affect photosynthate production. Such factors include leaf temperature, leaf resistance, water potential, crown location and aspect of foliage, needle age, seasonal patterns, nutrient levels, ambient CO_2 concentrations, photorespiration and many others. A more thorough examination of these factors for Douglas-fir trees is given by those authors listed in Table 5.1 and by Kinerson (1974). Additional discussion of the within crown distribution of photosynthate is given below.

As of this time, Woodman (1968, 1971) has probably conducted the most thorough analysis of the spatial and temporal variation in net assimilation rates (NAR) of a forest-grown Douglas-fir tree. Woodman, however, only measured solar radiation and NAR at several outer, exposed or open parts of the crown. Woodman estimated the photosynthate production (mg CO_2) by multiplying the average NAR (on a dry leaf weight basis, mg CO_2 $g^{-1}h^{-1}$) of each needle age class on each whorl times the length of daylight (hours). All photosynthate production values were then standardized to percent of maximum found on any whorl. Some of Woodman's results are given in Table 6.2. From Table 6.2, the current and one-year old needles produced 78% of the tree's total daily photosynthate but these needles only represent 46% of the total foliar weight. Thirty-two percent of total foliar weight is in four-year and older needles but they only produced four percent of the total daily photosynthate.

Salo (1974), however, felt that Woodman's use of dry needle

Table 6.2 Distribution of foliage weight and daily photosynthate production as a function of needle age classes in a Douglas-fir tree. Data is taken from Woodman (1968) who in turn cites a foliage weight study by Dice (1968) on a 35-year old, forest-grown, Douglas-fir tree.

Needle Age Class	% Foliage* Weight	% Photosynthate** Production
current	24	46
1-year	22	32
2-year	15	16
3-year	6	3
≥4-year	32	4

* based on oven dry weight

** total photosynthate production during the day, expressed as a percent of the maximum

weight instead of needle area in the computation of net assimilation rates (NAR) exaggerated the differences between the contributions of NAR by the various foliage age classes since needles become heavier with age. When branches with several year's foliage were monitored, Salo found that the NAR did not appear to decrease very much until needles were three years old (see Table 6.3). Data in Table 6.3 shows that except for the three-year old foliage, the proportion that each age class contributed to total assimilation was close to its fraction of the total leaf area. Subsequently, Salo (unpublished data) observed that NAR (on a needle surface area basis) had not decreased by more than 30 percent at the end of three years in excised branches from unfertilized dominant trees. Salo (1974) concluded that the physiological factors such as plant water status and micrometeorological conditions, especially photon flux (i.e., PAR radiation), were more important in determining maximum CO_2 assimilation of a sample than either height in the crown or crown aspect in his study trees.

The distribution pattern of net photosynthate production within the crown (e.g., by needle age class), however, is not the same for all conifers. Schulze et al. (1977) examined the biomass distribution and diurnal CO_2 uptake in a 89-year old, forest-grown, spruce tree (Picea abies (L.) Carst.). Some of Schulze's results are given in Table 6.4. It appears that the percent yearly uptake of CO_2 is approximately equal to the percent foliage surface area of the various needle age classes.

Comparing Table 6.4 against Table 6.3, it is obvious that the

Table 6.3 Distribution of foliage area and daily photosynthate production as a function of needle age classes in a Douglas-fir tree. Data is taken from page 96 of Salo (1974) who examined a branch located at 18.3 meters in the crown of a 40-year old, forest-grown, Douglas-fir tree (i.e., lysimeter tree #601).

Needle Age Class	% Foliage Area	% Photosynthate* Production
current	40	43.3
1st and 2nd-year	31	33.3
3rd-year	29	23.3

* total photosynthate production during the day, expressed as percent maximum

Table 6.4 Distribution of foliage surface area and photosynthate production in a spruce tree as a function of needle age classes. Data is taken from Table 3 of Schulze et al., (1977).

Needle Age Class	% Foliage Surface Area	% Annual CO_2 Uptake
current	16.0	15.3
1-year	15.3	17.6
2-year	15.9	20.5
3-year	15.1	11.9
4-year	37.7	34.7

Table 6.5 Distribution of Douglas-fir needles within each age class for a 13-year old, open-grown, sapling. Data is taken from Mitchell (1974).

Needle Age Class	% Of Needle* Population
current	43
1-year	28
2-year	18
3-year	8
4-year	3

* as a percent of the total needle polulation

older needles (i.e., 4-year old) in spruce have a significantly greater role in CO_2 uptake than that of the younger needles. The pattern in Douglas-fir needles is just the reverse, with the younger needles providing most of the photosynthate production.

In Douglas-fir, most of the photosynthate was shown (see Table 6.3) to be produced in the current year foliage. The greater relative contribution of the current foliage , however, is not due so much to their greater efficiency but rather it is mostly a result of the greater number of needles being in this age class (see Table 6.5).

There are morphological differences between shade and foliage leaves (Aussenac, 1973), differences in net assimilation rates between primary and secondary lateral shoots (Leverenz, 1974), differences in net assimilation rates between foliage age classes, and between different crown positions (Woodman, 1968, 1971). However, under most environmental conditions and within a given tree, the most important factors in photosynthate production (mg $CO_2 h^{-1}$) are those of photon flux, leaf temperature, and leaf area distribution (Salo, 1974).

Distribution Of Potential Net Assimilation Rates Within The Crown Of The Study Tree

Based on the measured distribution of global radiation within the crown of the study tree, the potential net assimilation rates may be estimated using data such as that in Table 6.1. Salo (1974)

expresses the light response curve in terms of photon flux density (micro Einsteins per square meter per second). McCree (1972) has shown that the photon flux in the 400-700 nm waveband is the best measure of the flux of photosynthetically active radiation (PAR) for both natural and artifical light sources. The relationship between PAR and short wave radiation (SR, 300-3000nm) may be approximated by the expression

$$PAR = 2950\, f_{PAR}\, SR \qquad (6.1)$$

where PAR is expressed in units of photon flux density (μEinsteins $m^{-2} sec^{-1}$), SR is expressed in units of energy flux density (cal cm^{-2} min^{-1}), f_{PAR} relates the proportion of SR to PAR and where the constant 2950 converts the units of energy flux density to those of photon flux density (Sestak et al., 1971). Britton and Dodd(1976) found f_{PAR} to vary with cloud cover, with intensity of incident irradiance and length of photoperiod. On clear days, f_{PAR} averaged out to a value of 0.45. Thus approximately 45% of the incoming energy from short wave radiation occurs between 400 and 700 nm.

Radiation data from Chapter IV and the light response curve of Table 6.1 are used to construct plots showing the distribution of "potential" net assimilation rates within the crown of the study tree. A second-order accurate, Taylor series interpolation/extrapolation routine (see pages 67-70 of Salvadori and Baron, 1961) was used with the data of Table 6.1 to relate a measured value of photon flux density (i.e., short wave global radiation converted to PAR using Eq. 6.1) and leaf temperature (i.e., air temperature) to an esti-

mated net assimilation rate (NAR, mg $CO_2 dm^{-2} h^{-1}$). The estimated value of the net assimilation rate in the crown, NAR(crown), was then normalized by dividing it by the value of the net assimilation rate computed in full sunlight, NAR_o(open).

$$\% \text{ Potential NAR} = [\text{NAR(crown)}/\text{NAR}_o\text{(open)}]\,100 \qquad (6.2)$$

The method used to estimate the potential NAR only accounts for the effect of light and leaf temperature. This method will probably overestimate the actual NAR since plant moisture stress, soil temperature, preconditioning and other effects due to extremes in the environment (e.g., frozen soils, frost, drought, etc.) will usually decrease the NAR (Emmingham, 1974). None-the-less, the procedure used here provides a conceptual framework to analyze the variation of NAR within the crown of a Douglas-fir tree.

In Figures 6.2a-f, the spatial variation in the percent potential net assimilation rates within the crown of the study tree on cloudless days are shown. Along the vertical axis, percent potential NAR is plotted using the global radiation data given in Figures 4.5a-f. Global radiation is first converted to PAR using Eq. 6.1. The PAR values and measured air temperature are then used to estimate the potential NAR using the light response curve given in Table 6.1 and Figure 6.1. Finally, all NAR values are normalized to a percent basis using Eq. 6.2.

Pertinent information concerning the position of the sun (i.e., azimuth, ν, and zenith, θ_z, angles in degrees) and "in-the-open" values of air temperature, T_{air}(°C), short wave global radiation,

Figure 6.2 Spatial variation in the potential net assimilation rates (NAR) within the crown of the study tree on cloudless days at 12 o'clock(LST) during the months of September and October, 1979. Figure 6.2a shows the variation along transect EW-1; 6.2b shows results for NS-1; 6.2c shows for EW-2; 6.2d shows for NS-2; 6.2e shows for EW-3; and 6.2f shows for NS-3.

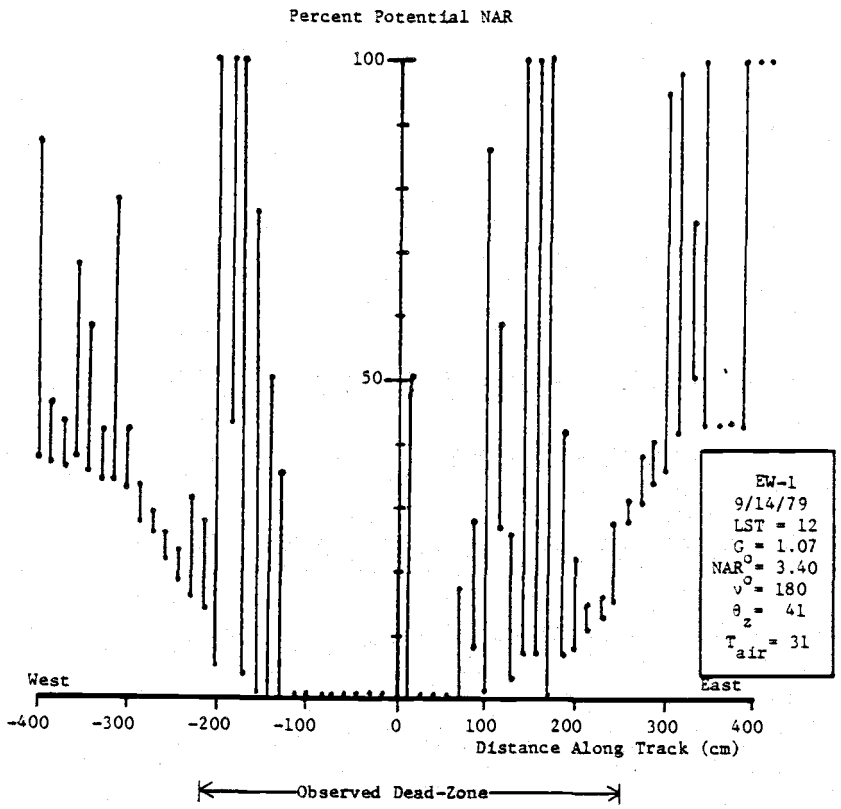

Figure 6.2a

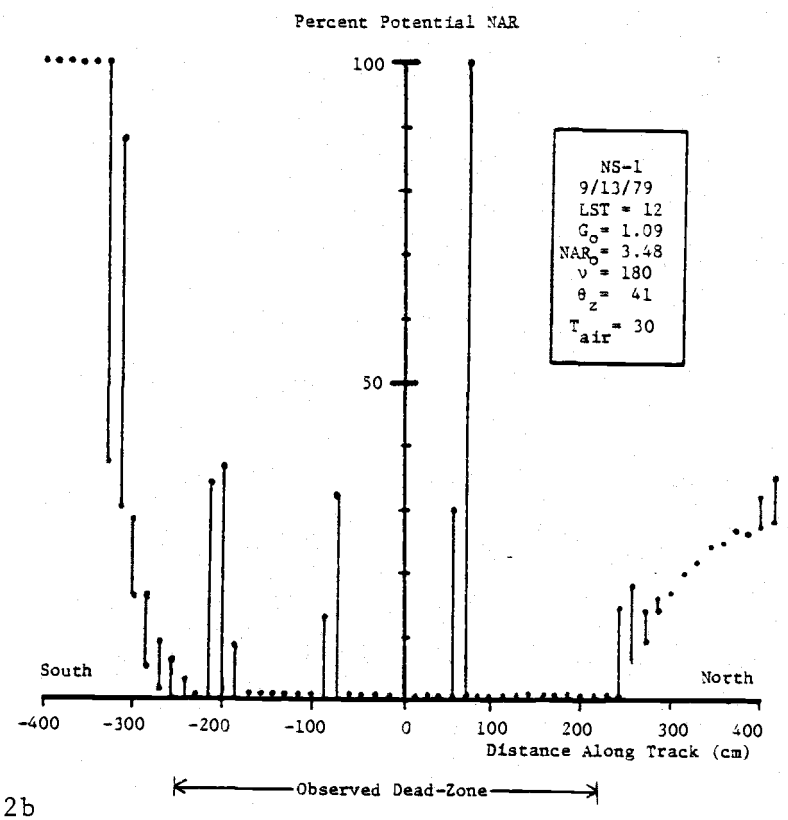

Figure 6.2b

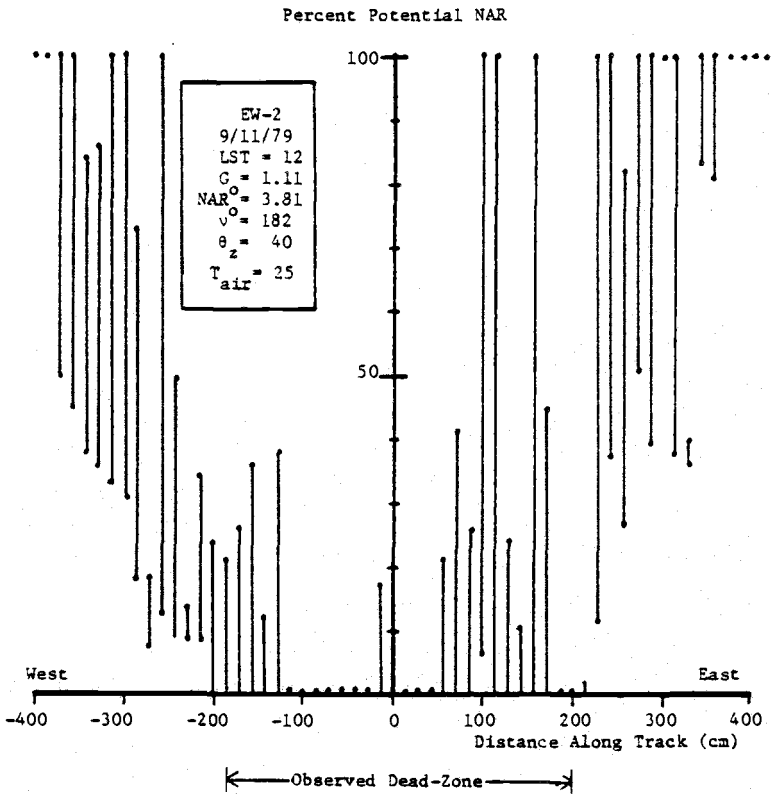

Figure 6.2c

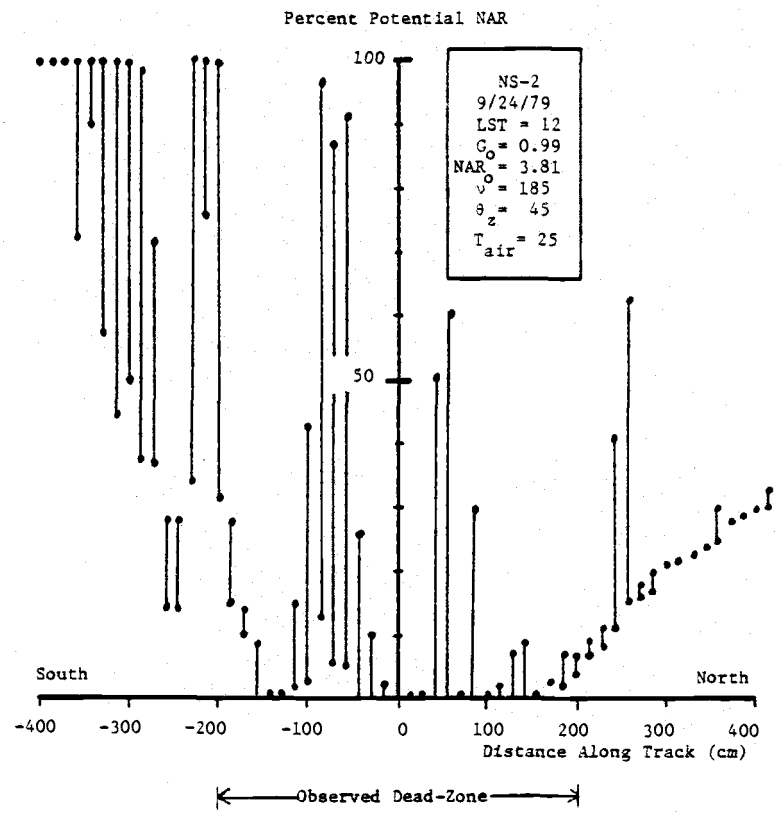

Figure 6.2d

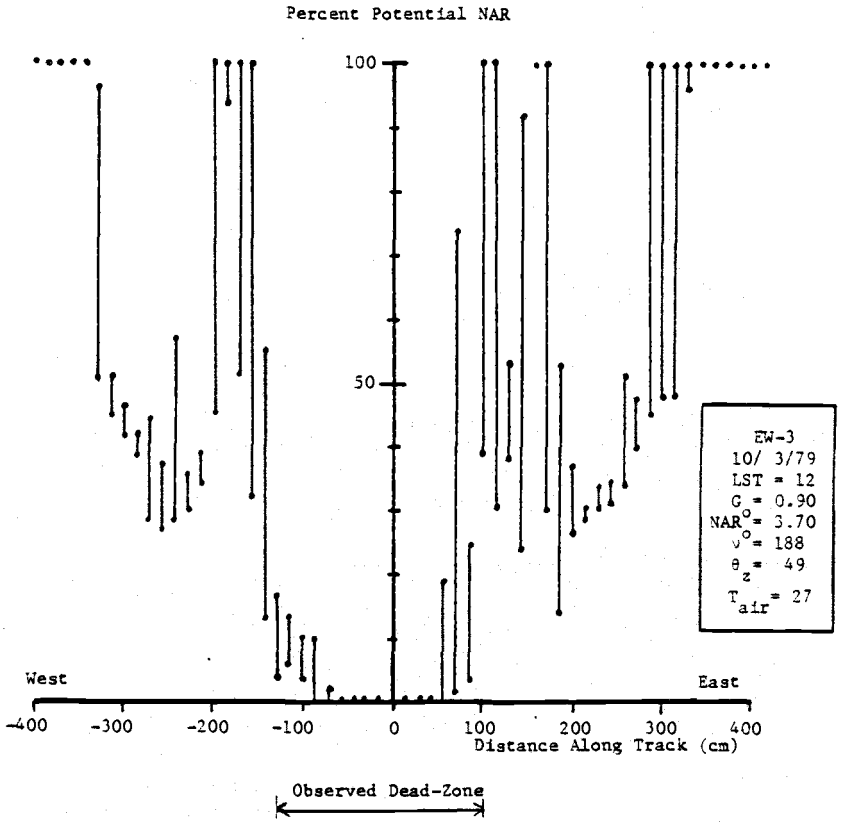

Figure 6.2e

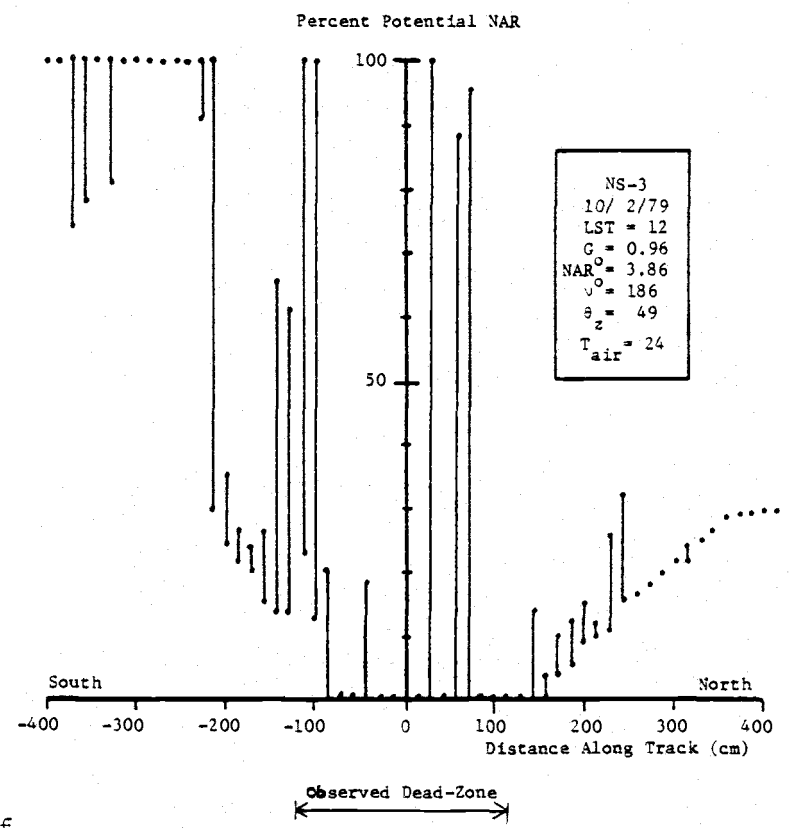

Figure 6.2f

G_o(cal $cm^{-2}min^{-1}$), and potential net assimilation rate, NAR_o(mg CO_2 $dm^{-2}h^{-1}$) are listed inside the small "capsule" in each figure.

From Figure 6.2a, the potential NAR in the open (i.e., NAR_o) equalled 3.40 mg $CO_2dm^{-2}h^{-1}$ at 12 o'clock (local standard time) on September 14, 1979. Along the East-West transect of Level 1, the distribution of NAR is almost symmetrical about the center of the tree. The vertical bars indicate the range of values estimated at any given point using radiation data from the four Kipp pyranometers mounted on the trolley. As one proceeds towards the center of the crown, the NAR values drop quickly as the level of radiation drops. Within the inner 200 cm radius of the crown, NAR becomes negative (i.e., no net gain in CO_2 because respiration is greater than photosynthesis). Negative values of NAR are not plotted in Figure 6.2. Note the similarity in shape between the radiation data of Figure 4.5 and the estimated NAR values in Figure 6.2.

At the bottom of Figures 6.2a-f, the observed location of the foliage dead-live zone is indicated. The dead-zone is defined as that region in the inner crown in which all needles have died and have fallen off. The dead-live zone is that zone in the inner crown in which the needles are just beginning to die (determined visually). The mean distance to the dead-live zone from the center of the bole along six transects is given in Table 6.6. Data used in Table 6.6 is taken from Appendix A. Upon examining Figures 6.2a-f, it is apparent that there is a very close correlation between the location of the observed dead-zone and regions of zero or negative

Table 6.6 Radial distance to dead-live zone in study tree, measured from the center of the bole. Data was collected during the fall of 1979.

Transect Level In Crown	North-South* Distance (cm)	East-West* Distance (cm)
1	N 227 ± 37	E 250 ± 19
1	S 256 ± 26	W 214 ± 55
2	N 203 ± 112	E 202 ± 14
2	S 207 ± 52	W 185 ± 60
3	N 116 ± 42	E 95 ± 48
3	S 122 ± 48	W 128 ± 53

* mean distance and 95% confidence interval, computed using all branches in a given sector (i.e., North, South, East, West) from one whorl above and below each transect.

NAR within the crown (using the minimum value from the range of values indicated by the vertical bar).

From Figures 6.2a-f, it is obvious that the lowest values of NAR are found in the lowest level of the crown (i.e., Level 1). Also note that on the shaded side of the crown (North side at 12 o'clock (LST)), the NAR values remained below full sunlight values. However, less than ten percent of the global radiation penetrates the shaded side of the crown (see Figure 4.5b) but this ten percent produces values of NAR that approach 40% of that in full sunlight. This is a result of the low light compensation point of Douglas-fir needles.

The diurnal variation in the distribution of NAR along transect NS-1 is shown in Figure 6.3 at 12,14 and 16 o'clock. Only the lowest value of NAR (from the four Kipp measurements) is plotted. As the North-South plane of the tree becomes more perpendicular to the direction of the solar rays, the distribution of radiation and hence NAR becomes more symmetrical. Also note the increase in NAR and the increase in the spatial variability of NAR as the sun angle and branch angles line up at 16 o'clock.

A comparison of the distribution of NAR between cloudless and overcast days along transect EW-1 is shown in Figure 6.4a and along transect NS-1 is shown in Figure 6.4b. From Figure 6.4a, it is apparent that the estimated net assimilation rate under overcast conditions is equal or greater than that under cloudless conditions. This is in agreement with Helms (1963, 1965) and Hodges (1965) who

concluded that Douglas-fir shade needles were most efficient on cloudy days. But this is in apparent disagreement with Woodman (1968) who found that bright days always produced the highest rates (on a dry needle weight basis) in both sun and shade-grown needles.

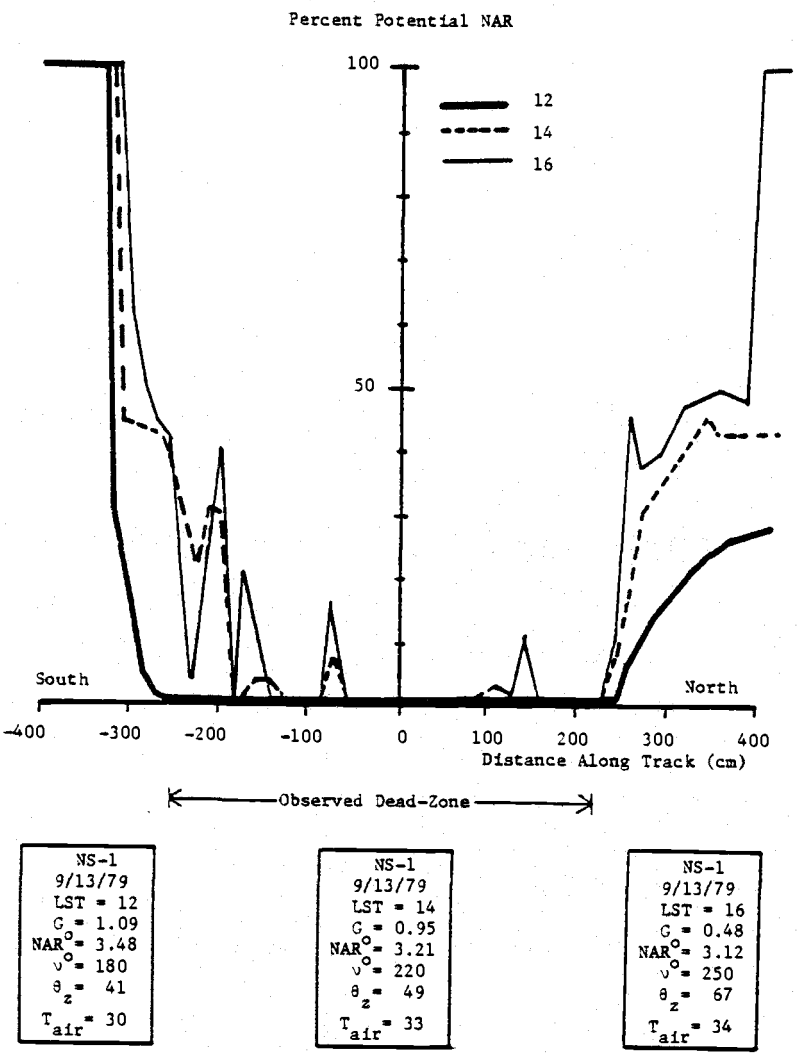

Figure 6.3 Diurnal variation in the pattern of net assimilation rates within the crown along the North-South,Level 1 transect. The percent potential net assimilation rate is computed for 12,14, and 16 o'clock on a cloudless day, September 13, 1979.

Figure 6.4 Comparison of net assimilation rates (NAR) between a cloudless and an overcast day. The percent potential NAR along a East-West, Level 1 transect is shown in Figure 6.4a and along a North-South, Level 1 transect is shown in Figure 6.4b.

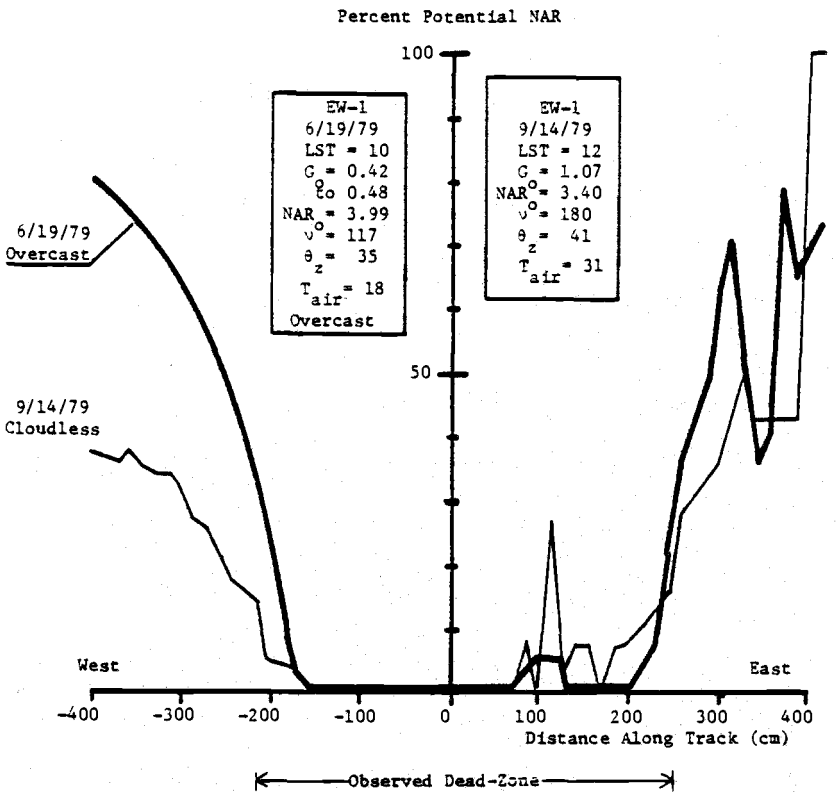

Figure 6.4c

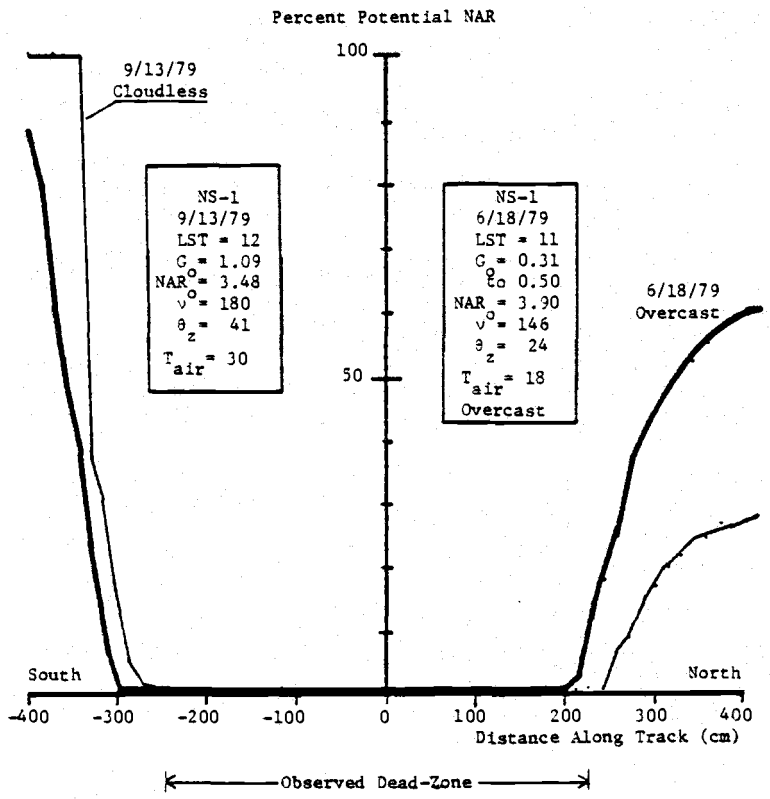

Figure 6.4b

VII. A SIMPLE MODEL OF LIGHT PENETRATION

Introduction

In Chapter IV, the measured distribution of global radiation is presented graphically as a function of distance along different transects. Upon closer examination of the data (e.g., Figures 4.5 and 4.10), it becomes obvious that there are several distinct geometric patterns. These geometric patterns are most noticeable when rays from the sun are normal to the transect (e.g., along a East-West transect at noon).

In Figure 7.1a, data from two cloudless days along the East-West, Level 3 transect at 12 o'clock are shown and in Figure 7.1b, data from an overcast day along the EW-3 transect is shown. The curves in Figures 7.1a-b are "idealized"in that only the minimum penetration (i.e., smallest value of G/G_o) is shown. In addition, the curves are smoothed to eliminate local deviations due to irregularities in the branch distribution in the crown. The distance from the center of the crown is plotted along the horizontal axis and the term $-\ln(G/G_o)$ is plotted along the vertical axis. This logarithmic term is related to the shadow area index by Eq. 5.10. On cloudless days, the term $-\ln(G/G_o)$ represents the amount of foliage along the sun-pyranometer line-of-sight (see Figure 5.7) and on overcast days it represents the "integral" amount of foliage about some point within the crown (i.e., the pyranometer).

It will be shown in the following sections that the curves

Figure 7.1 "Idealized" curves of light penetration versus distance within the crown of the study tree. The term $-\ln(G/G_o)$ is plotted on the vertical axis and distance to the center of the crown is plotted on the horizontal axis. In Figure 7.1a, data from two cloudless days (measured along a East-West transect, Level 3 at 12 o'clock(LST)) are shown. The curve labeled 6/27/79 is taken from Figure 7.2 and the curve labeled 10/ 3/79 is taken from Figure 4.5e. In Figure 7.1b, data from an overcast day on June 19,1979 at 12 o'clock(LST) along transect EW-3 is shown. This curve is obtained by smoothing the data given in Figure 4.10e.

The distortion of the vertical axis in Figure 7.1b is due to the nonsymmetrical distribution of foliage along Level 3. The West side of the crown (at Level 3) has slightly more foliage than does the East side. In addition to the nonsymmetrical distribution of the foliage, additional distortion in the light distribution curves of Figures 7.1a-b is caused by the "off location" of the transect (see Figure 4.4).

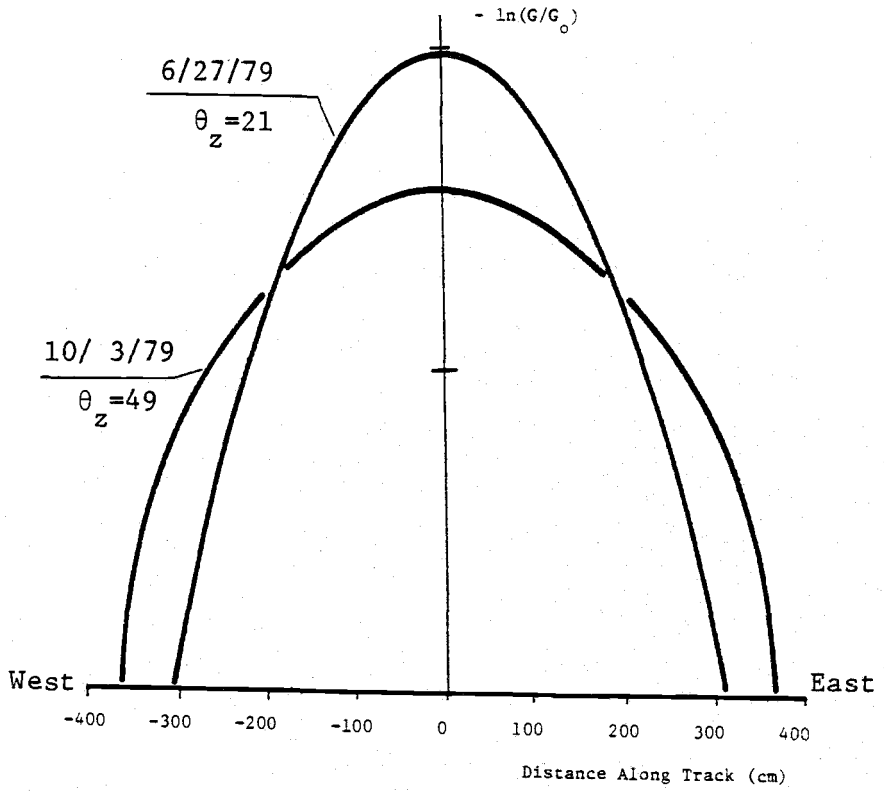

Figure 7.1a

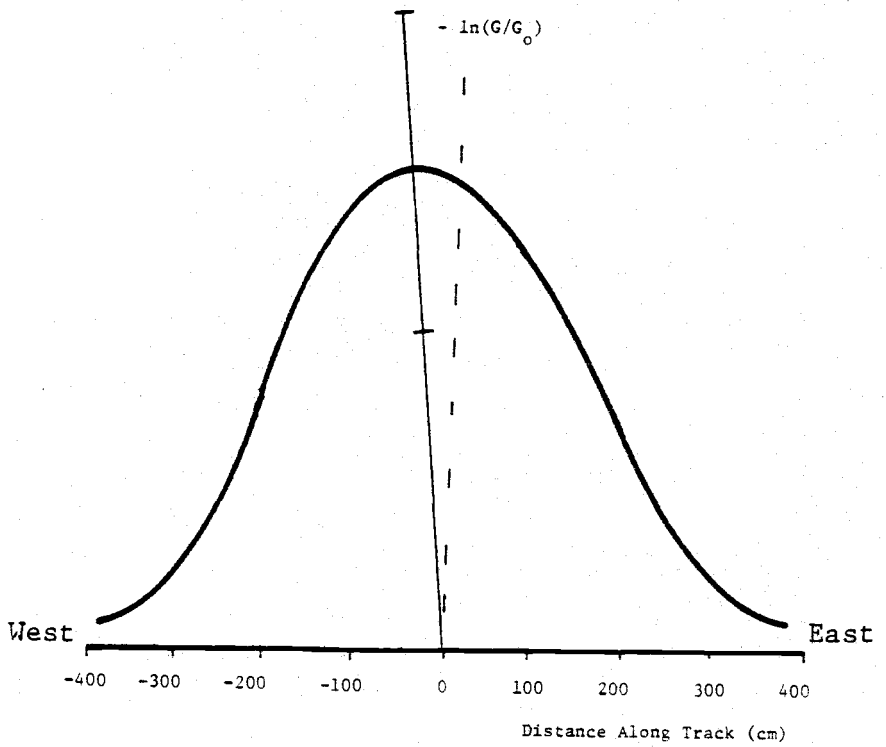

Figure 7.1b

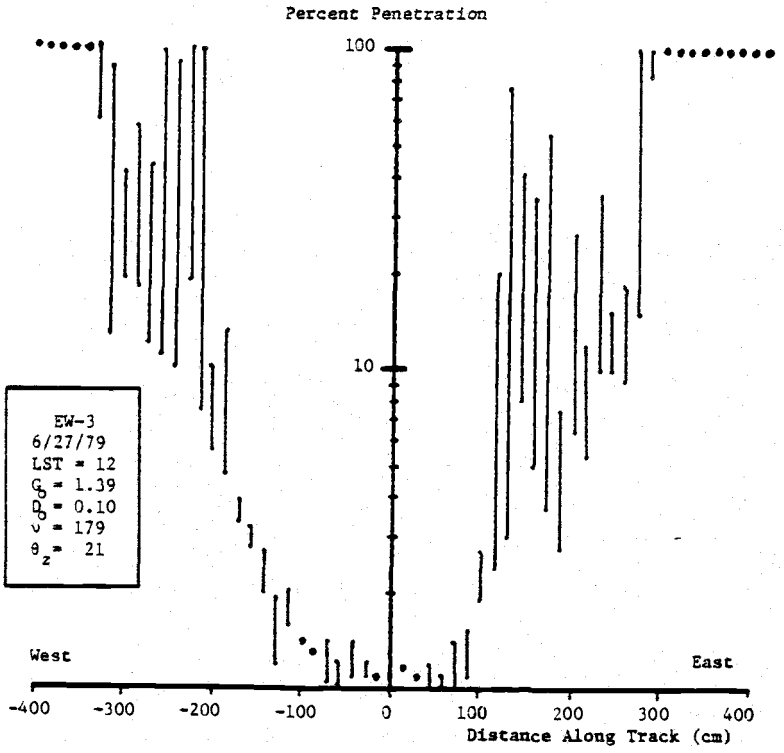

Figure 7.2 Spatial variation in the penetration of global radiation into the study tree along transect EW-3 on June 27, 1979 at 12 o'clock. Note the small solar azimuth angle (i.e., θ_z = 21 degrees).

shown in Figure 7.1a are general conic sections and that the curve shown in Figure 7.1b is a Gaussian curve.

Geometric Interpretation Of Penetration Data : Cloudless Days

Consider, for the moment, the idealized form of a Douglas-fir tree crown. Casual inspection indicates that the crown is in the form of a right circular cone. Other geometric forms may be used (e.g., spheres, cylinders, ellipsoids, or various truncated portions of these) but the basic argument that follows remains the same. Additional discussion on modeling a crown as a cone is given by Jahnke and Lawrence (1965), cylindrical shapes is discussed by Brown and Pandolfo (1969) and ellipsoidal crowns is discussed by Charles-Edwards and Thornley (1973).

The curve formed by the intersection of a plane and a right circular cone is called a conic section (Green, 1941). Depending on the angle that the plane makes with the base of the cone, the conic section may be a circle, an ellipse, a parabola, or a hyperbola. The last three of these cases is illustrated in Figure 7.3. When the "cutting plane" is perpendicular to the axis of a right circular cone, the resulting section is a circle ($\theta_z=90^o$). An ellipse is formed when the cutting plane intersects every element of the cone and is not perpendicular to the axis ($90^o>\theta_z>\beta/2$, where $\beta/2$ is the half-angle of the cone). If the cutting plane is passed parallel to an element of the cone, the resulting section is a

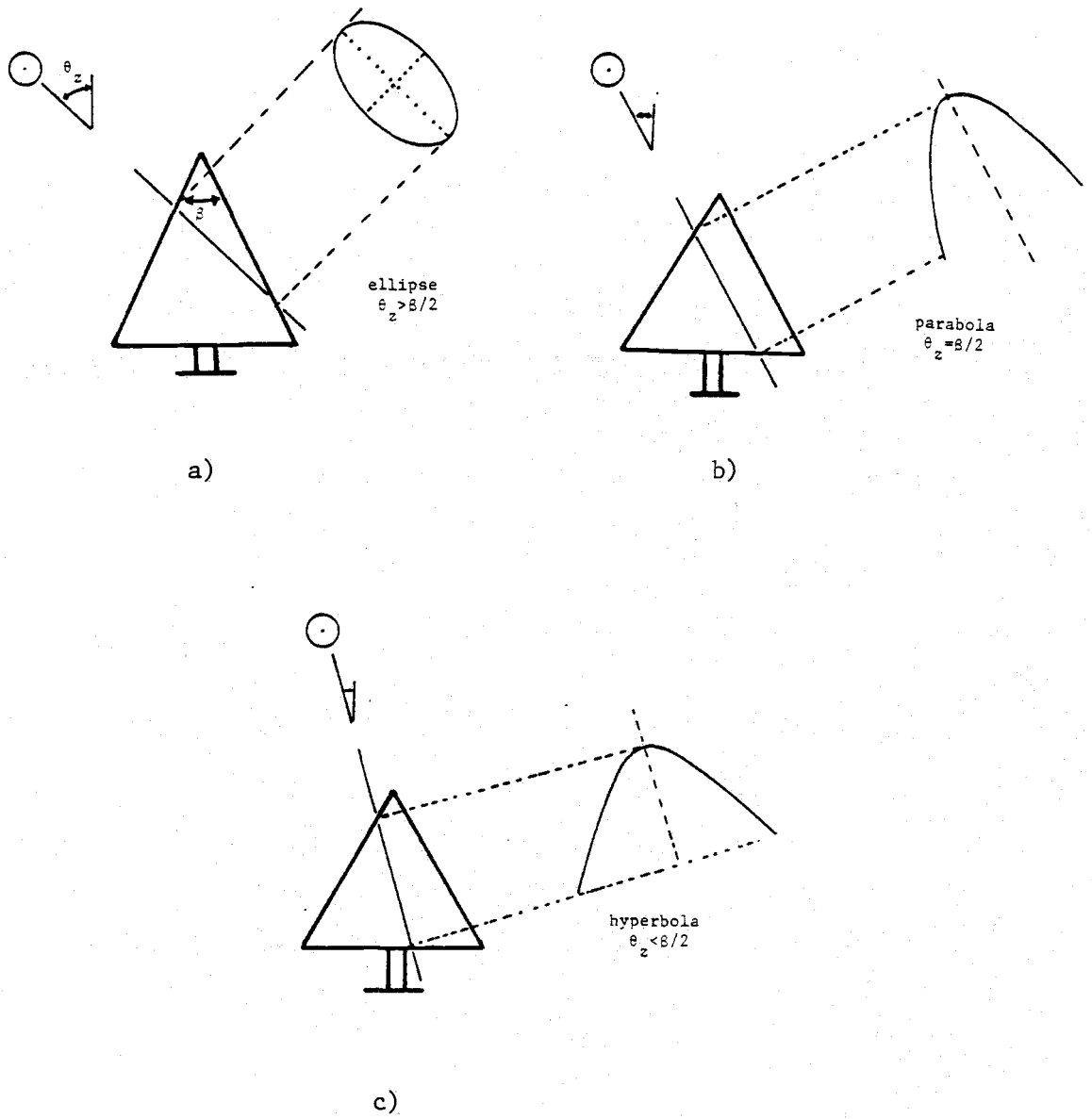

Figure 7.3 The intersection of a plane and a right circular cone is schematically illustrated. Three different conic sections are shown: a) an ellipse; b) a parabola ;and c) a hyperbola.

parabola ($\theta_z=\beta/2$). The hyperbola is formed when the cutting-plane angle θ_z is less than the cone half-angle $\beta/2$ ($0<\theta_z<\beta/2$).

The general equation of a conic section in two-dimensions is given by the expression

$$(x-x_o)^2 + A(y-y_o)^2 = B \qquad (7.1)$$

where A and B are constants, x and y are Cartesian coordinates (see Figure 7.4), x_o and y_o locate the center of the conic section. The value of the constant A in Eq. 7.1 is restricted, depending on the type of conic section (see Table 7.1).

Upon examining Figure 7.1a, it becomes apparent that the curves are conic sections. These conic sections represent the amount of foliage (i.e., shadow area index) along a transect, as viewed by the Kipp pyranometer. The "cutting-plane" forming this conic section is parallel to the solar rays of direct radiation. At sunrise the conic section will be circular (an ellipse with small eccentricity) and at noon the conic section will be an ellipse (with a large eccentricity) and, perhaps, may even be a parabolic or a hyperbolic conic section. At sunset the conic section will once again be a circle. The type of conic section depends only on the solar zenith angle, θ_z, and the half-angle of the crown apex, $\beta/2$.

Data from Figure 7.1a was regressed against a rearranged form of Eq. 7.1 and the results are listed in Table 7.2. The general regression equation is

$$x^2 = a+by+cy^2 \qquad (7.2)$$

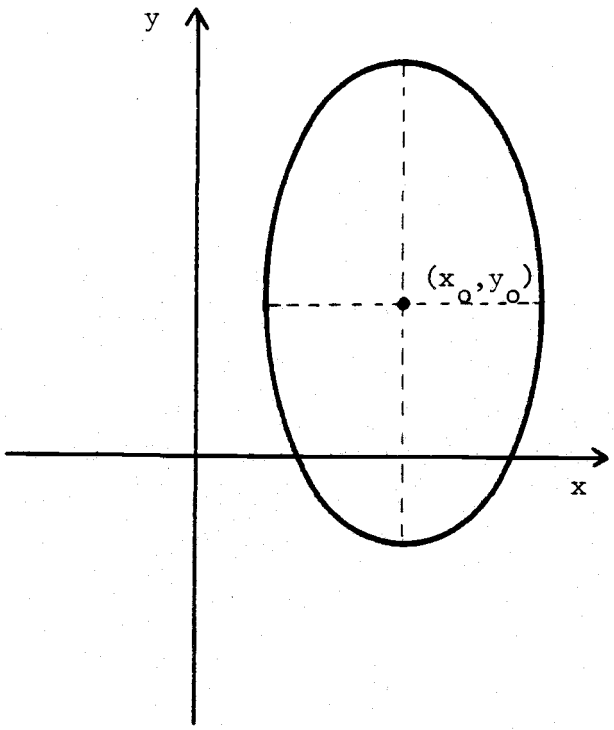

Figure 7.4 Schematic showing the two-dimensional Cartesian coordinate system used to define the equation of a conic section (e.g., an ellipse).

Table 7.1 Restrictions on the use of Equation 7.1 to describe a conic section.

Conic Section	Restrictions
circle	A=1
ellipse	A>0
parabola	A<0; but there is no y^2 term
hyperbola	A<0

Table 7.2 Regression coefficients obtained from modeling the data given in Figure 7.1. The coefficients a,b,c, refer to the coefficients used in Equation 7.2.

Model	a	b	c	R^2 / F Ratio	d.f.
6/27/79: Cloudless (θ_z=21)					
$x^2=a+by+cy^2$	98800 ± 1238	-21500 ± 1227	1.179 ± 248	0.9996 12190	9
$x^2=a+by$	98800 ± 844	-21500 ± 290	—	0.9996 27080	10
10/ 3/79:Cloudless (θ_z=49)					
$x^2=a+by+cy^2$	133100 ± 6738	-3817 ±7401	-9471 ± 7710	0.9984 2262	7
$x^2=a+cy^2$	129800 ± 2496	—	-10360 ± 366	0.9981 4262	8
6/19/79: Overcast					
$\ln(y)=a+bx+cx^2$	1.198 N.A.	0.00299 N.A.	-0.0000339 N.A.	0.9932 N.A.	7
$\ln(y)=a+cx^2$	1.359 ±0.139	—	-0.0000232 ±0.0000197	0.9680 243	8

± 95% confidence interval

N.A. not available

d.f. degrees of freedom

where x equals the distance from the center of the tree (cm) (i.e., along the transect), y equals $-\ln(G/G_o)$, and a,b,c are constants. Note that the x axis is centered in the middle of the conic section (i.e., $x_o=0$) since the crown is symmetrical about the center of the tree but y_o is, in general, not centered ($y_o \neq 0$). Since y_o is usually not equal to zero, the quadratic term $(y-y_o)^2$ in Eq. 7.1 will produce both a first and a second-order term with respect to y when expanded (see Eq. 7.2). Data from the two curves of Figure 7.1a were regressed using Eq. 7.2 and then regressed again after dropping out those terms of the equation which were not significant (see Table 7.2). Final results are given in Table 7.3.

Table 7.3 Final results from modeling the data given in Figure 7.1.

Data	Model	Curve Shape
6/27/79 :Cloudless (θ_z=21)	$x^2=a+by$	Parabola
10/ 3/79:Cloudless (θ_z=49)	$x^2=a+cy^2$	Ellipse
6/19/79 :Overcast	$\ln(y)=a+bx+cx^2$	Gaussian

The above geometric interpretation of light penetration is based on several assumptions. The most important assumptions are that the leaves are uniformly distributed throughout the crown, that light traversing the crown is attenuated according to the Poisson model (i.e., modified Beer's Law), and that scattered light can be neglected. Additional details of the geometric model are given in Appendix E.

Geometric Interpretation Of Penetration Data : Overcast Days

The geometric interpretation of the light penetration data on overcast days is more difficult to explain than that for cloudless days. Comparing Figure 7.1a against Figure 7.1b, it is obvious that there are differences in the shape between these curves. The light penetration curve on overcast days can not be represented by a conic section. Instead, the penetration data on overcast days is described by a Gaussian curve (i.e., an exponential function with a second-order power term).

Radiation from any portion of the sky will exponentially penetrate the crown according to the Poisson model given by Eq. 5.8. On overcast days, radiation, $B(\theta,\nu)$, is emitted from all portions of the sky. The function $B(\theta,\nu)$ describes the luminosity (cal $cm^{-2}min^{-1}$ $steradian^{-1}$) along the direction specified by (θ,ν), where θ is the zenith angle and ν is the azimuth angle of the radiation (see Appendix E). The total amount of diffuse radiation penetrating the crown and reaching any given point (called point P, location of the pyranometer) is (Charles-Edwards and Thornley, 1973)

$$D = \int_0^{2\pi}\int_0^{\pi/2} B(\theta,\nu)\cos\theta\sin\theta\exp(-0.7S)\,d\theta d\nu \quad (\text{cal } cm^{-2}min^{-1}) \tag{7.3}$$

where the term S (cm^2 leaf+stem area cm^{-2} ground area) depends on the angles θ and ν, the coordinates of the point P, and the shape of

the crown. From Chapter V, it was shown that

$$S = SAI/\cos\theta \qquad (cm^2 cm^{-2}) \qquad (7.4)$$

but one can also define

$$S = s\,F \qquad (cm^2 cm^{-2}) \qquad (7.5)$$

where s (cm) is the pathlength from the edge of the crown to point P, along the direction (θ,ν) and where F (cm^2 leaf+stem area cm^{-3} of space) is the shadow-area density (i.e., leaf+stem area density).

To evaluate Eq. 7.3, one must define the sky function B and function S for all possible angles (θ,ν). Additional details are given in Appendix E to compute s. Function B may be represented by several ideal models of luminosity for overcast skies, such as the uniform overcast sky model (UOC) or the standard overcast sky model (SOC). Anderson (1966) gives additional details for these two sky models.

Equation 7.3 was not solved by this author since I considered it beyound the scope of my thesis. However, Charles-Edwards and Thornley (1973) solved Eq. 7.3, where their plant canopy was modeled as a truncated symmetrical ellipsoid. Some of their results are given in Figure 7.5. For the sample problem used by Charles-Edwards and Thornley, there was no significant difference between using either the UOC or SOC overcast sky models for function B in Eq. 7.3. On the vertical axis of Figure 7.5, the term $-\ln(D/D_o)$ is plotted where D_o is the diffuse radiation (cal $cm^{-2} min^{-1}$) measured in the open and D is the diffuse radiation (cal $cm^{-2} min^{-1}$) measured at some

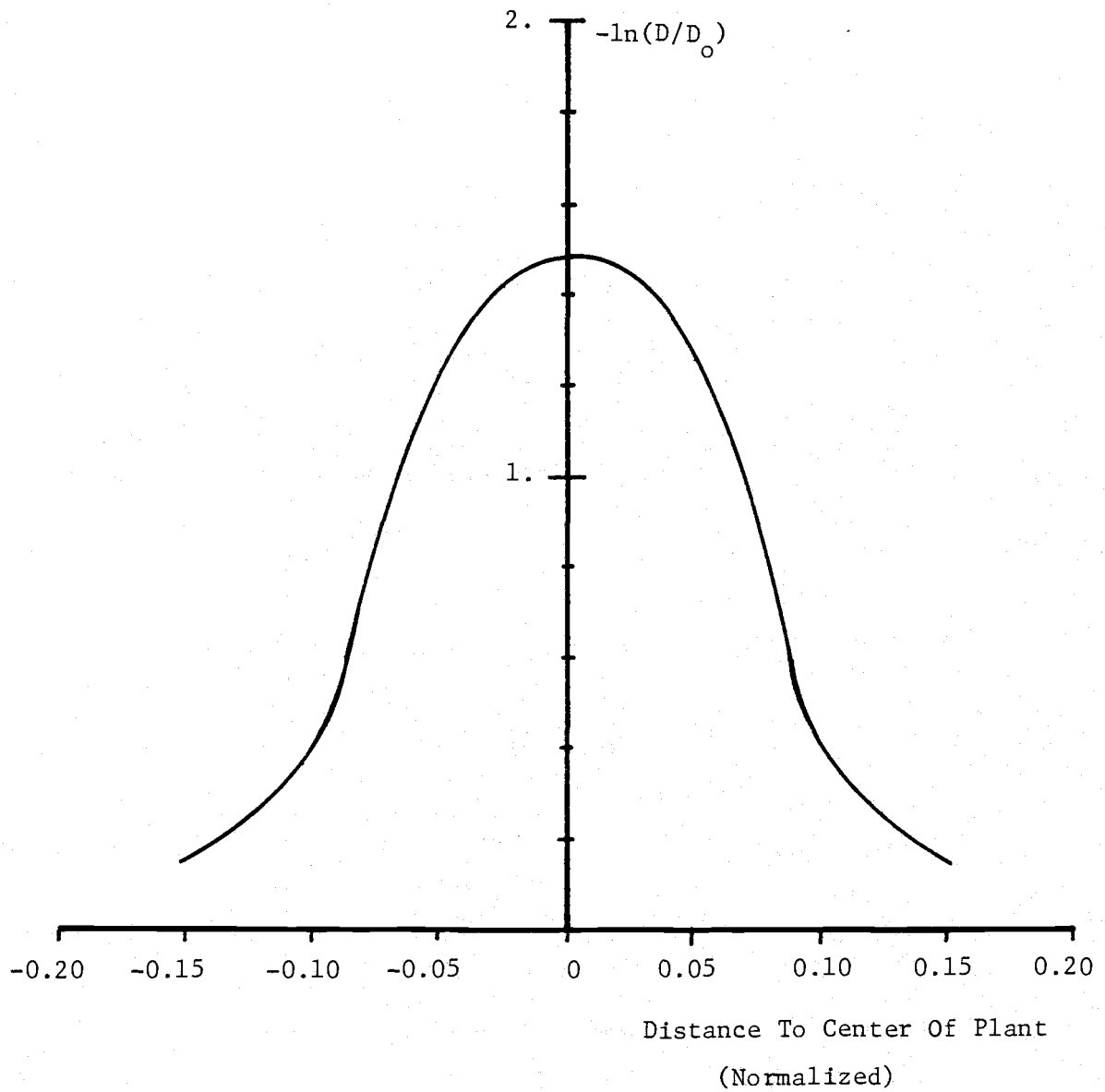

Figure 7.5 The penetration of diffuse radiation into a truncated symmetrical ellipsoidal plant. Data is taken from Figure 5a of Charles-Edwards and Thornley (1973).

point within the plant canopy. The distance to the center of the plant is plotted along the horizontal axis (normalized).

The "general shape" of the light penetration curve for overcast sky conditions was determined by fitting the following Gaussian curve

$$\ln(y) = a+bx+cx^2 \qquad (7.6)$$

where y equals $-\ln(D/D_o)$ and x is equal to the distance to the center of the canopy. Regressing Eq. 7.6 to the data of Figure 7.5 gives a R-square equal to 0.964 and regression coefficients a=0.657, b=-11.85, and c=-24.63.

Using the data of Charles-Edwards and Thornley (1973) may seem arbitrary but the conclusion is still applicable to the geometric interpretation of the penetration of diffuse radiation into the crown of a Douglas-fir tree (i.e., Eq. 7.3). The amount of diffuse radiation that reaches any point in the crown is equal to the integrated sum of all rays of diffuse radiation emanating from the overcast sky. Each ray of diffuse radiation is exponentially attenuated according to Eq. 5.8. When plotted, as in Figure 7.5, the resulting light penetration curve may be represented by a Gaussian function (see Eq. 7.6).

As a check, data from an overcast day (June 19, 1979 at 12 o'clock, along transect EW-3) was plotted in Figure 7.1b. Equation 7.6 was regressed with the data of Figure 7.1b and the results listed in Table 7.2.

Geometric Interpretation Of Penetration Data : Additional Considerations

Several idealized curves of light penetration are given in Figure 7.1. However, upon examining the penetration data of Chapter IV, it is obvious that there are several discrepancies between the idealized curves and the "real data" curves. For example, in Figure 4.7a (note that the ideal curves shown in Figure 7.1 are upside down from that of Chapter IV) the East side (i.e., the sunny side) of the curve is a conic section, the West side (i.e., the shaded side) of the curve is Gaussian and the center of the curve is flat. The previous discussion on the geometric interpretation only considered cases where the radiation was all diffuse (overcast days) or when both sides of the crown were in bright sunlight (at 12 o'clock along a East-West transect on cloudless days). In addition, it was assumed that the foliage was uniformly distributed throughout the crown. However, at any given time on a cloudless day, some portion of the crown is in bright light (mostly direct radiation) and the remaining is in shade (mostly diffuse radiation). The distribution of foliage is fairly symmetrical about the center of the tree but it is not symmetrical along any given radial vector because of the central dead-zone.

The penetration of direct radiation may be represented by a conic section curve (see Figure 7.6a) and diffuse radiation may be represented by a Gaussian curve (see Figure 7.6b). Once radiation

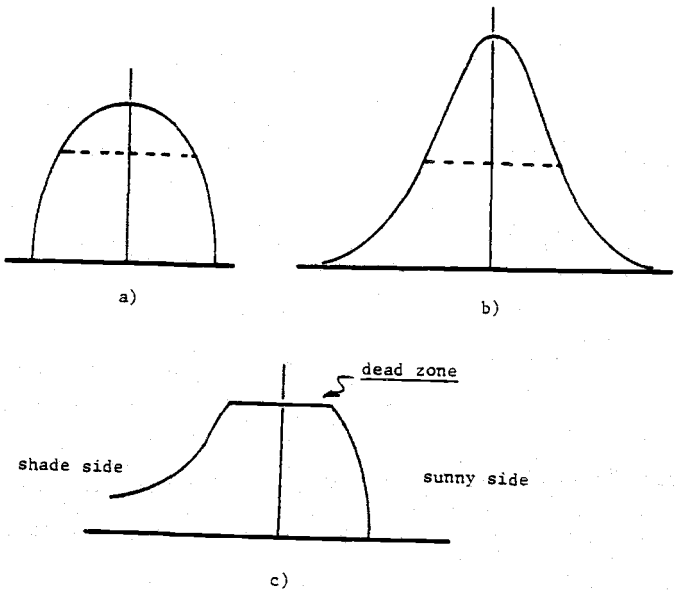

Figure 7.6 Schematic diagram showing the two basic shapes used to describe the light penetration curve. Figure 7.6a shows a conic section and Figure 7.6b shows a Gaussian curve, where the dotted line represents the effect of the dead-zone on the shape of the curve. Figure 7.6c is a composite of Figures 7.6a and 7.6b.

reaches the dead-zone, there is virtually no additional attenuation (excluding the interception by the branch stems). Thus the presence of the dead-zone will "truncate" the shape of the light penetration curve (note the dotted line in Figures 7.6a and 7.6b). On cloudless days, the radiation penetrating the crown will consist of both direct and diffuse radiation components. The net effect on the shape of the light penetration curve will be the composite of these two curve shapes (conic section and Gaussian curve), as shown in Figure 7.6c.

VIII. CONCLUSIONS AND RECOMMENDATIONS

Conclusions

1). By means of a photographic technique, it was shown that a modified form of Beer's Law describes the penetration of direct radiation into the foliage of Douglas-fir branches. Hence, the amount of direct radiation reaching any point within the tree crown is an exponential function of the density of the foliage or absorbing surface along the direction of direct radiation. The amount of diffuse radiation reaching any point within the tree crown is an integrated exponential function of the foliage in the direction of the radiation.

2). The penetration of global (i.e., direct plus diffuse) radiation into the crown on cloudless days is highly variable and is a function of solar position, branch distribution and branch angle. Penetration is greatest when the sun's rays are parallel to branch angle. Ninety percent of the global radiation is intercepted in the first 50 cm of continuous foliage. None-the-less, the remaining proportion of radiation can produce large quantities of photosynthate. This is possible because of the low light saturation point of Douglas-fir foliage.

3). Diffuse radiation is always more penetrating than direct radiation and may play a significant role in the

production of photosynthate in the tree crown. On overcast days the penetration pattern of diffuse radiation is relatively constant and depends only on the integrated distribution of foliage. This penetration pattern may be used as a sensitive test of seasonal changes in crown structure.

4). The penetration pattern of global radiation into the crown of a single Douglas-fir tree can be interpreted in terms of a simple geometrical model : interception of a solid right cone.

Recommendations For Future Research

Since the radiation penetration pattern within the crown can be modeled by a simple geometrical solid, it should be possible to model the radiation regime within a forest stand as a collection of geometrical solids. For simplicity, one may wish to use a right circular cone but other solid objects are also possible. Uneven age stands could be modeled by varying the height and size of the cones and spacing. Thinning schemes could be modeled by varying the horizontal locations of the cones. The radiation regime would then be investigated along horizontal transects through such a model. Global radiation on cloudless days need only be considered since this would provide a worst case scenario for light penetration. The penetration of radiation into each cone is computed and the resulting composite of radiation fields plotted. The location of the "lowest functional crown" position could then be estimated by identifying

regions of radiation that are less than two to three percent of full sunlight, the radiation level below which the needles were not maintained in the study tree.

BIBLIOGRAPHY

Acock,B., J.H.M. Thornley and J.W. Wilson. Spatial variation of light in the canopy. In : Prediction and Measurement of Photosynthetic Productivity. Proceedings of the IBP/PP Technical Meeting, Trebon, 14-21 September, 1969. Wagneningen, Pudoc. pp.91-102. 632p. 1970.

Allen, L.H. and E.R. Lemon. Net radiation frequency distribution in a corn crop. Boundary-Layer-Meteorology, Vol. 3, pp. 246-254. 1972.

Anderson, M.C. Studies of the woodland light climate : I. The photographic computation of light conditions. The Journal of Ecology, Vol. 52, pp. 27-41. 1964.

Anderson, M.C. Stand structure and light penetration: II. A theoretical analysis. The Journal of Applied Ecolopy, Vol. 3, pp. 41-54. 1966.

Anderson, M.C. The role of heat transfer in the design and performance of solarimeters. Journal of Applied Meteorology, Vol. 6, pp. 941-947. 1967.

Anderson, M.C. Radiation and crop structure. In : Plant Photosynthetic Production Manual of Methods (Z. Sestak, J. Catsky and P. Jarvis, eds.), pp. 412-466. Junk Publication, The Hague. 818p. 1971.

Arney, J.D. Computer simulation of Douglas-fir tree and stand growth. Ph.D. Thesis. Oregon State University, Corvallis, Oregon. 79p. 1972.

Aussenac, G. Effect of different microclimates on the morphology and structure of needles. Annales des Sciences Forestieres, Vol. 30, pp. 375-392. 1973.

Baumgartner, A. Licht und Naturverjüngung am Nordrand eines Waldbestandes. Forstwissenschaftliches Centralblatt (Parey, Berlin), Vol. 74, pp. 59-64. 1955.

Britton, C.M. and J.D. Dodd. Relationship of photosynthetically active radiation and shortwave irradiance. Agricultural Meteorology, Vol. 17, pp. 1-7. 1976.

Brix, H. An analysis of dry matter production of Douglas-fir seedlings in relation to temperature and light intensity. Canadian Journal of Botany, Vol. 45, pp. 2063-2072. 1967.

Brocks, K. Die räumliche Verteilung der Beleuchtungsstärke im Walde. Zeitschrift für Forst-und Jagdwesen (Springer, Berlin), Vol. 71, pp. 47-53. 1939.

Brooks, F.A. An Introduction to Physical Microclimatology. University of California, Davis. 264p. 1959.

Brougham, R.W. Interception of light by the foliage of pure and mixed stands of pasture plants. Australian Journal of Agricultural Research, Vol. 9, pp. 39-52. 1958.

Brown, C.L. Growth and form. In: Trees Structure and Function (M.H. Zimmermann and C.L. Brown (eds.)), pp. 125-165. Springer-Verlag, New York. 336p. 1971.

Brown, G.W. Measuring transmitted global radiation with fixed and moving sensors. Agricultural Meteorology, Vol. 11, pp. 115-121. 1973.

Brown, P.S., Jr. and J. P. Pandolfo. An equivalent-obstacle model for the computation of radiative flux in obstructed layers. Agricultural Meteorology, Vol. 6, pp. 407-421. 1969.

Brownlee, K.A. Statistical Theory and Methodology In Science and Engineering, second edition. John Wiley and Sons, New York. 590p. 1965.

Burger, H., Holz, Blattmenge and Zuwachs. II. Die Douglasie. Mitteilungen, Schweizerische Anstalt fuer das Forstliche Versuchswesen, Vol. 19, pp. 21-72. 1935.

Campbell, R.K. Variations in crown form attributes in populations of Pseudotsuga menziesii. Ph.D. Thesis. University of Washington, Seattle, Washington. 143p. 1958.

Carbon, B.A., B.A. Bartle and A.M. Murray. A method for visual estimation of leaf area. Forest Science, Vol. 25, pp. 53-58. 1979.

Charles-Edwards, D.A. and J.H.M. Thornley. Light interception by an isolated plant : a simple model. Annals of Botany, Vol. 37, pp. 919-928. 1973.

Ching, K.K. Hybridization between Douglas-fir and bigcone Douglas-fir. Forest Science, Vol. 5, pp. 246-254. 1959.

Coulson, K.L. Solar and Terrestrial Radiation. Academic Press, New York. 322p. 1975.

Cowan, I.R. The interception and absorption of radiation in plant stands. The Journal of Applied Ecology, Vol. 5, pp. 367-379. 1968.

Davidson, J.L. and J.R. Philip. Light and pasture growth. In : Climatology and microclimatology, pp. 181-187. Proceedings of the Canberra symposium. UNESCO, Paris. 355p. 1958.

Del Rio, E. and A. Berg. Specific leaf area of Douglas-fir reproduction as affected by light and needle age. Forest Science, Vol. 25, pp. 183-186. 1979.

Denison, W.C., D.M. Tracy, F.M. Rhoades and M. Sherwood. Direct, nondestructive measurement of biomass and structure in living old-growth Douglas-fir. Proceedings- Research on Coniferous Forest Ecosystems- A symposium. Edited by J.F. Franklin, L. Dempster and R.H. Waring. Bellingham, Washington, March 23-24, 1972. U.S. Forest Service Pacific Northwest Forest and Range Experiment Station, Portland, Oregon. pp. 147-158. 1972.

Devlin, R.M. and A.V. Barker. Photosynthesis. Van Nostrand Reinhold Company, New York. 304p. 1971.

Dice, S.F. The biomass and nutrient flux in a second growth Douglas-fir ecosystem (A study in quantitative ecology). Ph.D. Thesis. University of Washington, Seattle, Washington. 165p. 1968.

Drew, A.P. and S.W. Running. Comparison of two techniques for measuring surface area of conifer needles. Forest Science, Vol. 22, pp. 231-232. 1975.

Droppo, J.G. and H.L. Hamilton. Experimental variability in the determination of the energy balance in a deciduous forest. Journal of Applied Meteorology, Vol. 12, pp. 789-791. 1973.

Duncan, W.G., R.S. Loomis, W.A. Williams and R. Hanau. A model for simulating photosynthesis in plant communities. Hilgardia, Vol. 38, pp. 181-205. 1967.

Ellenberg, H. Uber Zusammensetzung, Standort und Stoffproduktion bodenfeuchter Eichen-und Buchen-Mischwaldgesellsch. NW-Deutschlands. Mitteilungen der Florist-soziologischen Arbeitsgemeinschaft, Vol. 5. 1939.

Emmingham, W.H. Physiological responses of four Douglas-fir populations in three contrasting field environments. Ph.D. Thesis Oregon State University, Corvallis, Oregon. 162p. 1974.

Evans, G.C. and D.E. Coombe. Hemispherical and woodland canopy photography and the light climate. The Journal of Ecology, Vol. 47, pp. 103-113. 1959.

Federer, C.A. Spatial variation of net radiation, albedo and surface temperature of forests. Journal of Applied Meteorology, Vol. 7, pp. 789-795. 1968.

Frank, E.C. and R. Lee. Potential solar beam irradiation on slopes: Tables for 30° to 50° latitude. U.S. Forest Service Research Paper RM-18, Rocky Mountain Forest and Range Experiment Station. U.S. Dept. of Agriculture. 116p. 1966.

Fry,K.E. A study of transpiration and photosynthesis in relation to the stomatal resistance and internal water potential in Douglas-fir. Ph.D. Thesis. University of Washington, Seattle, Washington. 206p. 1965.

Garnier, B.J. and A. Ohmura. A method of calculating the direct shortwave radiation income of slopes. Journal of Applied Meteorology, Vol. 7, pp. 796-800. 1968.

Gates, D.M. Radiant energy, its receipt and disposal. Meteorological Monographs, Vol. 6, No. 28, pp. 1-26. 1965.

Gay, L.W., K.R. Knoerr and M.O. Braaten. Solar radiation variability on the floor of a pine plantation. Agricultural Meteorology, Vol. 8, pp. 39-50. 1971.

Geiger, R. The Climate Near The Ground. Harvard University Press, London. 611p. 1965.

Gholz, H.L., F.K. Fitz and R.H. Waring. Leaf area differences associated with old-growth forest communities in the western Oregon Cascades. Canadian Journal of Forest Research, Vol. 6, pp. 49-57. 1976.

Green, S.L. Algebraic Solid Geometry. Cambridge University Press, London. 133p. 1941.

Helms, J.A. Seasonal patterns of apparent photosynthesis in Pseudotsuga menziesii in relation to environmental and silvicultural treatment. Ph.D. Thesis. University of Washington, Seattle, Washington. 237p. 1963.

Helms, J.A. Diurnal and seasonal patterns of net assimilation in Douglas-fir, Pseudotsuga menziesii, as influenced by environment. Ecology, Vol. 46, pp. 698-708. 1965.

Herrington, L.P., R.E. Leonard, J.E. Hamilton and G.M. Heisler. The response of moving radiometers. Boundary-Layer-Meteorology, Vol. 2, pp. 395-405. 1972.

Hodges, J.D. Photosynthesis in forest tree seedlings of the Pacific Northwest under natural environmental conditions. Ph.D. Thesis. University of Washington, Seattle, Washington. 177p. 1965.

Horn, H.S. The Adaptive Geometry Of Trees. Princeton University Press, Princeton, New Jersey. 144p. 1971.

Hutchison, B.A. and D.R. Matt. The distribution of solar radiation within a deciduous forest. Ecological Monographs, Vol. 47, pp. 185-207. 1977.

Impens, I., R. Lemeur and R. Moermans. Spatial and temporal variation of net radiation in crop canopies. Agricultural Meteorology, Vol. 7, pp. 335-337. 1970.

Isobe, S. Preliminary studies on physical properties of plant communities. Bulletin of the National Institute of Agricultural Science, Tokyo. Series A, Vol. 9, pp. 29-66. 1962.

Jackson, L.W. and R.S. Harper. Relation of light intensity to basal area of shortleaf pine stands in Georgia. Ecology, Vol. 36, pp. 158-159. 1955.

Jackson, W.A. and R.J. Volk. Photorespiration. Annual Review of Plant Physiology, Vol. 21, pp. 385-432. 1970.

Jahnke, L.S. and D.B. Lawrence. Influence of photosynthetic crown structure on potential productivity of vegetation, based primarily on mathematical models. Ecology, Vol. 46, pp. 319-326. 1965.

Jensen, E.C. The crown structure of a single codominant Douglas-fir. Master of Science Thesis. University of Washington, Seattle, Washington. 83p. 1976.

Kasanaga, H. and M. Monsi. On the light transmission of leaves, and its meaning for the production of matter in plant communities. Japanese Journal of Botany, Vol. 14, pp. 304-324. 1954.

Kinerson Jr., R. and L.J. Fritschen. Modeling a coniferous forest canopy. Agricultural Meteorology, Vol. 8, pp. 439-445. 1971.

Kinerson, R.S. Selected aspects of CO_2 and H_2O exchange in a Douglas-fir stand. American Midland Naturalist, Vol. 91, pp. 170-181. 1974.

Kipp and Zönen. Bulletin SOL 61. 7p. 1961.

Kodak Professional Photoguide, Kodak Publication No. R-28. Eastman Kodak Company. 44p. 1979.

Kubin, S. Measurement of Radiant Energy. In : Plant Photosynthetic Production Manual of Methods (S. Sestak, J. Catsky and P. Jarvis, eds.), pp. 702-765. Junk Publications, The Hague. 818p. 1971.

Kvet, J. and J.K. Marshall. Assessment of leaf area and other assimilating plant surfaces. In : Plant Photosynthetic Production Manual Of Methods (S. Sestak, J. Catsky and P. Jarvis, eds.), pp. 517-555. Junk Publications, The Hague. 818p. 1971.

Lemeur, R. and B.L. Blad. A critical review of light models for estimating the shortwave radiation regime of plant canopies. Agricultural Meteorology, Vol. 14, pp. 255-286. 1974.

Leverenz, J.W. Net photosynthesis as related to shoot hierarchy in a large dominant Douglas-fir tree. Master of Science Thesis. University of Washington, Seattle, Washington. 126p. 1974.

LI-Cor, Inc., Portable Area Meter. Brochure AMI-579. Lincoln, Nebraska. 4p. 1979.

Liu, B.H. and R.C. Jordan. The interrelationship and characteristic distribution of direct, diffuse, and total solar radiation. Solar Energy, Vol. 4, pp. 1-19. 1960.

Mann, J.E., G.L. Curry and P.J. Sharpe. Light interception by isolated plants. Agricultural Meteorology, Vol. 20, pp. 205-214. 1979.

Marshall, J.K. The photographic-photoelectric planimeter combination method for leaf area measurement. Photosynthetica, Vol. 2, pp. 1-9. 1968.

Max, T.A. Crown geometry, light interception and photosynthesis of selected Populus x euramericana clones : a modeling approach. Ph.D. Thesis. Iowa State University, Ames, Iowa. 126p. 1975.

McCree, K.J. Test of current definitions of photosynthetically active radiation against leaf photosynthesis data. Agricultural Meteorology, Vol. 10, pp. 443-453. 1972.

Miller, D.H. Transmission of insolation through pine forest canopy, as it affects the melting of snow. Mitteilungen der Schweizerischen Anstalt für das forstliche Versuchswesen, Vol. 35, pp. 59-79. 1959.

Miller, P.C. Tests of solar radiation models in three forest canopies. Ecology, Vol. 50, pp. 878-885. 1969a.

Miller, P.C. Solar radiation profiles in openings in canopies of aspen and oak. Science, Vol. 164, pp. 308-309. 1969b.

Mitchell, R.G. Estimation of needle populations. USDA Forest Research Paper PNW-181. Pacific Northwest Forest Range Experiment Station, Portland, Oregon.14p. 1974.

Mitchell, K.J. Dynamics and simulated yield of Douglas-fir. Forest Science Monograph #17. 39p. 1975.

Mitscherlich, G. Das Forstamt Dietzhausen. Zeitschrift für Forst- und Jagdwesen (Springer, Berlin), Vol. 72, pp. 149-188. 1940.

Monsi, M. and T. Saeki. Über den Lichtfaktor in den Pflanzengesellschaften und seine Bedeutung für die Stoffproduction. Japanese Journal of Botany, Vol. 14, pp. 22-52. 1953.

Monteith, J.L. Principles of Environmental Physics. Edward Arnold Limited, London. 241p. 1973.

Mood, A.M., F.A. Graybill and D.C. Boes. Introduction to the Theory of Statistics (third edition). McGraw-Hill Book Company, New York. 564p. 1974.

Nägeli, W. Lichtmessungen im Freiland und im geschlossenen Altholzbestand. Mitteilungen der Schweizerischen Anstalt für das Forstliche Versuchswesen, Vol. 21, pp. 250-306. 1940.

Natr, L. Use of image analysing computer for measuring leaf area. Photosynthetica, Vol. 2, pp. 39-40. 1968.

Newbold, P.J. Methods for estimating the primary production of forests. I.P.P. Handbook #2. Blackwell Scientific Publications, Oxford. 62p. 1967.

Niilisk, H., T. Nilson and J. Ross. Radiation in plant canopies and its measurement. In : Prediction and Measurement of Photosynthetic Productivity. Proceedings of the IBP/PP Technical Meeting, Trebon, 14-21 September, 1969. Wagneningen, Pudoc. pp. 165-177. 632p. 1970.

Nilson, T. A theoretical analysis of the frequency of gaps in plant stands. Agricultural Meteorology, Vol. 8, pp. 25-38. 1971.

Norman, J.M., E.E. Miller and C.B. Tanner. Light intensity and sunfleck-size distributions in plant canopies. Agronomy Journal, Vol. 63, pp. 743-748. 1971.

Norman, J.M. and P.G. Jarvis. Photosynthesis in Sitka spruce (Picea Sitchensis (Bong.) Carr.) : V. Radiation penetration theory and a test case. The Journal of Applied Ecology, Vol. 12, pp. 839-878. 1975.

Ovington, J.D. and H.A. Madgwick. Comparison of light in different woodlands. Forestry, Vol. 28, pp. 141-146. 1955.

Palmer, J.W. Diurnal light interception and a computer model of light interception by hedgerow apple orchards. The Journal of Applied Ecology, Vol. 14, pp. 601-614. 1977.

Pangborn, J. Personal communication. University of California, Davis, California. April 2, 1980.

Pope, W.W. Geographic and seasonal variation in photosynthetic efficiency and capacity of Rocky Mountain Douglas-fir, Pseudotsuga menziesii var. Glauca. Ph. D. Thesis. Oregon State University, Corvallis, Oregon. 98p. 1978.

Ramaan, E. Lichtmessungen in Fichtenbestande. Allgemeine Forst- u. Jagdzeitung, Vol. 87, pp. 401-406. 1911.

Reeve, J.E. Appendix on derivation of formulae. In : Inclined point quadrats by J.W. Wilson. The New Phytologist, Vol. 59, pp. 1-8. 1960.

Reifsnyder, W.E. and H.W. Lull. Radiant energy in relation to forests. U.S. Department of Agriculture, Technical Bulletin No. 1344. 111p. 1965.

Reifsnyder, W.E., G.M. Furnival and J.L. Horowitz. Spatial and temporal distribution of solar radiation beneath forest canopies. Agricultural Meteorology, Vol. 9, pp. 21-37. 1971/1972.

Reukema, D.L. A study of the interrelationships between growing space, crown development, and stem development of second growth Douglas-fir. Master of Forestry Thesis. University of Washington, Seattle, Washington. 1957.

Reukema, D.L. Crown development and its effect on stem growth of six Douglas-firs. Journal of Forestry, Vol. 59, pp. 370-371. 1961.

Robinson, N. Solar Radiation. Elsevier Publishing Co., New York. 347p. 1966.

Roussel, L. Recherches theoriques at pratiques sur la prepartition en quantite et en qualite de la lumiere dens le milieu forestier influence sun la vegetation. Annales L'Ecole Nationale Des Eaux et Forests, Vol. 13, pp. 291-400. 1953.

Salo, D.J. Factors affecting photosynthesis in Douglas-fir. Ph.D. Thesis. University of Washington, Seattle, Washington. 150p. 1974.

Salvadori, M.G. and M.L. Baron. Numerical Methods in Fortran, 2nd edition. Prentice-Hall, Inc., Englewood Cliffs, New Jersey. 302p. 1961.

Satterlund, D.R. and J.E. Means. Estimating solar radiation under variable cloud conditions. Forest Science, Vol. 24, pp. 363-373. 1978.

Schulze, E.D., M.I. Fuchs and M. Fuchs. Spatial distribution of photosynthetic capacity and performance in a mountain spruce forest of Northern Germany : I. Biomass distribution and daily CO_2 uptake in different crown layers. Oecologia (Berlin), Vol. 29, pp. 43-61. 1977.

Sestak, Z., J. Catsky and P. Jarvis. Plant Photosynthetic Production Manual of Methods. Junk Publications, The Hague. 818p. 1971.

Silver, G.T. The distribution of Douglas-fir foliage by age. The Forestry Chronicle, Vol. 38, pp. 433-438. 1962.

Smart, W.M. Text Book on Spherical Astronomy (fifth edition). Cambridge University Press, Cambridge. 430p. 1965.

Sommerville, D.M.Y. Analytical Geometry of Three Dimension. Cambridge University Press, London. 416p. 1965.

Stamper, J.H. and J.C. Allen. A model of the daily photosynthetic rate in a tree. Agricultural Meteorology, Vol. 20, pp. 459-481. 1979.

Szeicz, G. Measurement of radiant energy. In : The Measurement of Environmental Factors in Terrestrial Ecology (R. Wadsworth, L. Chapas, A. Rutter et al., eds.), pp. 109-130. Blackwell Scientific Publications, Oxford. 314p. 1968.

Thies, W.G. and R.D. Harvey, Jr. A photographic method for measuring tree defect. Canadian Journal of Forest Research, Vol. 9, pp. 541-543. 1979.

Thompson, E.S. Computation of solar radiation from sky cover. Water Resources Research, Vol. 12, pp. 859-865. 1976.

Trapp, E. Untersuchung über die Verteilung der Helligkeit in einem Buchenbestand. Bioklimatische Beiblätter der Meteorologischen Zeitschrift (Vieweg, Brunswick), Vol. 5, pp. 153-158. 1938.

Verhagen, A.M., J.H. Wilson and E.J. Britten. Plant production in relation to foliage illumination. Annals of Botany, Vol. 27, No. 108,pp.627-640. 1963.

Vermilion, A.B. A numerical model of net radiation in forest stands. Ph.D. Thesis. University of Washington, Seattle, Washington. 115p. 1975.

Walker, R.B., D.R. Scott, D.J. Salo, and K.L. Reed. Terrestrial process studies in conifers : A review. In : Proceedings- Research on coniferous forest ecosystems- A symposium, (J.F. Franklin, L.J. Dempster and R.H. Waring (eds.)), pp. 211-225. Pacific Northwest Forest and Range Experiment Station, Portland. 1972.

Weaving, G.S. An improved method of temperature compensating solarimeters. Journal of Physics E: Scientific Instruments, Vol. 8, pp. 89-91. 1975.

Weaving, G.S. and J. Filshie. A solarimeter utilizing silicon semiconductor diodes. Journal of Agricultural Engineering Research, Vol. 22, pp. 113-126. 1977.

Webber, B.D. Biomass and nutrient distribution patterns in a young Pseudotsuga menziesii ecosystem. Canadian Journal of Forest Research, Vol. 7, pp. 326-334. 1977.

Weisner, J. Derlichtgenuss der Pflanzen. Englemann, Leipzig, Germany. 322p. 1907.

Wellner, C.A. Light intensity related to stand density in mature stands of western white pine type. Journal of Forestry, Vol. 46, pp. 16-19. 1948.

Williams, T. A. An error analysis of the photographic technique for measuring percent vegetative cover. Soil Science Society of America, Journal, Vol. 43, pp. 578-582. 1979.

Wilson, J.W. Inclined point quadrats. The New Phytologist, Vol. 59, pp. 1-8. 1960.

Wilson, J.W. Stand structure and light penetration : I. Analysis by point quadrats. The Journal of Applied Ecology, Vol. 2, pp. 383-390. 1965.

Woodman, J.N. The relationship of net photosynthesis to environment within the crown of a large Douglas-fir tree. Ph.D. Thesis. University of Washington, Seattle, Washington. 188p. 1968.

Woodman, J.N. Variation of net photosynthesis within the crown of a large forest-grown conifer. Photosynthetica, Vol. 5, pp. 50-54. 1971.

APPENDICES

APPENDIX A

PHYSICAL DIMENSIONS OF THE STUDY TREE

The physical dimensions of the main stem of the study tree are given in Table A.1. Note that bole radius is computed from bole circumference assuming a perfect circle. The physical dimensions of all live branches larger than 1.5 cm diameter between whorls 10 and 20 are given in Tables A.2 to A.12. Note that internodal (i.e., non-nodal) branches along the main stem are grouped with the nearest whorl above them because internodal branches grow out the year following whorl initiation. A schematic of the tree showing how some of the measurements are defined is given in Figure A.1.

The average horizontal extension of the branch tip and horizontal distance to the dead-live zone is plotted in Figure A.2 as a function of height in the crown. Except for the lowermost whorls, the crown is fairly conical in shape. Whorls 19 and 20 lie next to the ground and are apparently being overtopped by the whorls immediately above it. The reduced growth of the lowest whorls is due, in part, to the intense shading by those branches above it and by physical damage from lawn mowers, trampling and browsing. From Figure A.2, it is also apparent that the central dead-zone of foliage is well defined and resembles a "cone within a cone" appearance (see Appendix E). The distance between the outer and inner cone is about 200 cm along whorls 10 and 19.

Tabel A.1 Bole circumference, bole radius and whorl height of each whorl in the study tree. Data was collected on October 21, 1979.

Whorl	Circumference* (cm)	Radius* (cm)	Height (cm)
1	N.A.	N.A.	1345
2	N.A.	N.A.	1270
3	N.A.	N.A.	1190
4	N.A.	N.A.	1105
5	33	5.3	1020
6	41	6.5	970
7	44	7.0	900
8	**	**	**
9	55	8.8	845
10	58	9.2	740
11	66	10.5	635
12	75	11.9	540
13	86	13.7	485
14	90	14.3	380
15	96	15.3	345
16	103	16.4	275
17	115	18.3	225
18	121	19.3	165
19	143	22.8	105
20	175	27.9	60

* measured outside of the bark

** snow break, leader broken off during the winter of 1970

N.A. not available

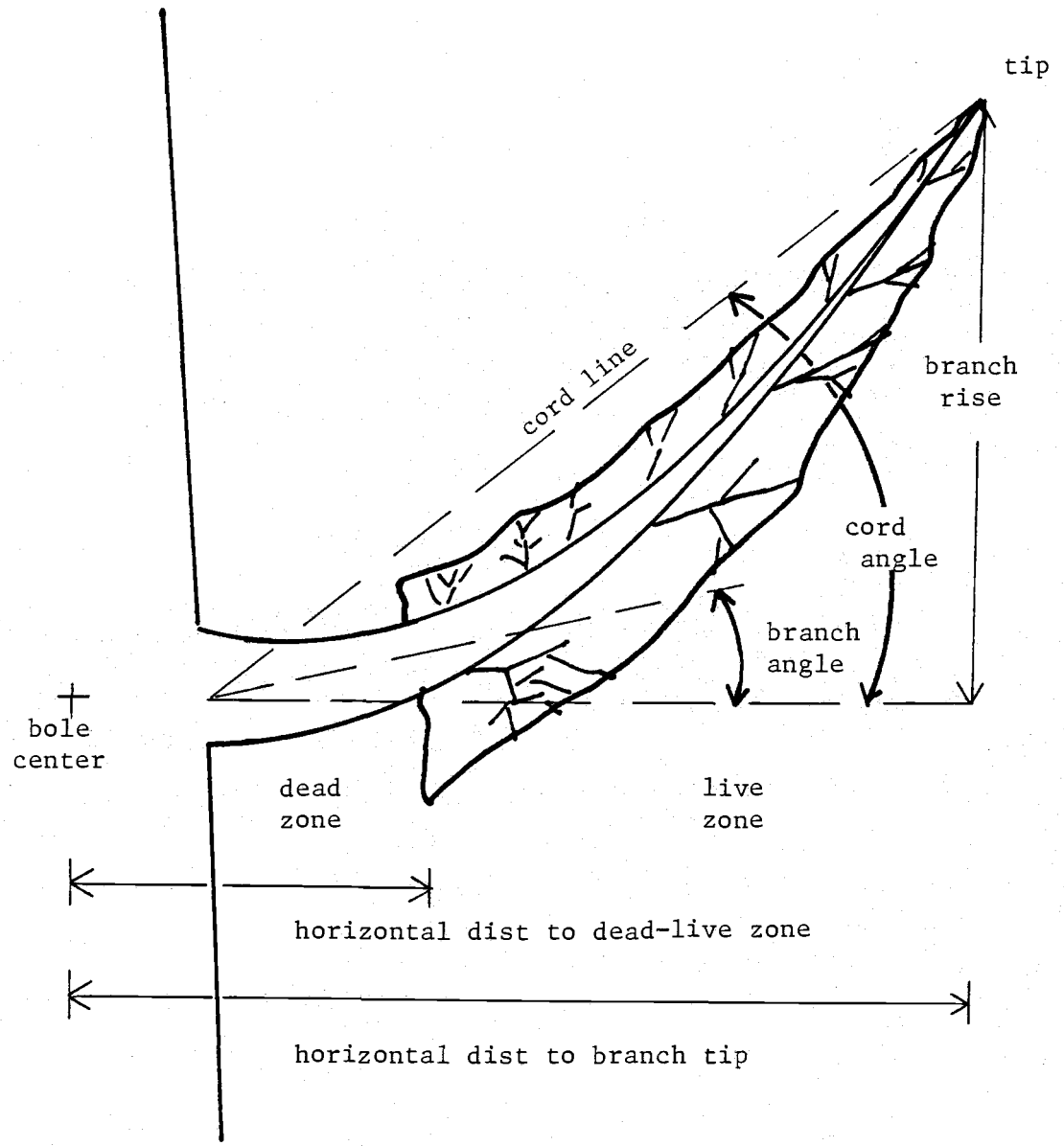

Figure A.1 Schematic showing how various variables used in Tables A.2 to A.12 are defined.

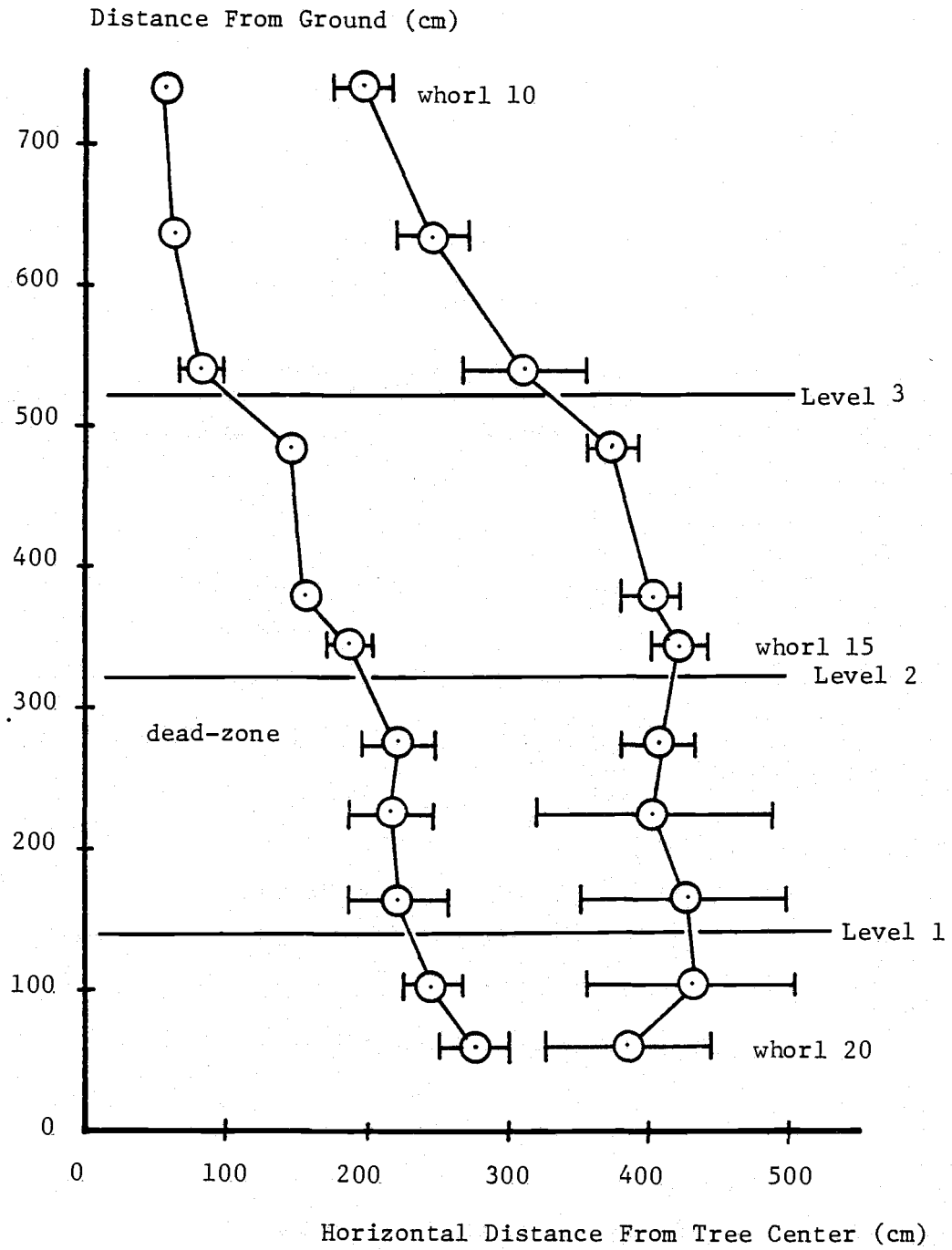

Figure A.2 Mean horizontal distance to the dead-live zone and to the branch tip in the study tree. Bars indicate the ± 95% confidence interval.

The following field measurements were taken of each branch from whorl 10 to whorl 20 in the study tree. Data was collected during the fall of 1979. Data is listed in Tables A.2 to A.12. Notation used in these tables is given below.

Notation		Definition
Nodal	1)	Determined whether or not the branch is a nodal, n, or a non-nodal,nn, lateral branch of a whorl.
Cones	2)	Determined whether or not the branch had cones on it. The letter c denotes that the branch had cones on during the fall of 1979.
Branch Dia At B	3)	Outside bark diameter of the branch stem at the bole, measured to the nearest 0.1 cm. Branch diameter is measured five centimeters from bole to avoid butt swell in branch.
Branch Dia At DZ	4)	Outside bark diameter of the branch stem at the location of the dead-live zone of the branch foliage, measured to the nearest 0.1 cm.
H Dist To DZ	5)	Horizontal distance from the center of the tree to the location of the dead-live zone of branch foliage, measured to the nearest ten centimeters.
H Dist To Tip	6)	Horizontal distance from the center of the tree to the branch tip, measured to the nearest ten centimeters.
Branch Rise	7)	Vertical rise of branch tip, measured to the nearest five centimeters(see Figure A.1).

Cord Angle

8) Branch tip to bole cord angle, computed as the arctangent of the branch rise divided by the horizontal distance to branch tip (i.e., arctan of [Rise/H Dist]), computed to the nearest degree. Horizontal distance is measured from bole.

Branch Angle

9) Vertical angle of the branch stem, measured at the bole and a point 30 cm along the branch stem. Angle is measured positive upwards from the horizon and is measured to the nearest five degrees.

Branch Orient

10) Orientation of each branch stem, measured to the nearest five degrees. The angle is measured positive in a clockwise direction from that of true North along a horizontal plane. Hence a branch with an orientation of +180 degrees is pointing due South.

Sector

11) Location of branch relative to crown aspect. All branches orientated between -45° and +45° are in sector 1 (i.e., the North side of the crown), branches orientated between +45° and +135° are in sector 2 (i.e., the East side), branches between +135 and 225° are in sector 3 (i.e., South side), and branches between +225° and +315° are in sector 4 (i.e., West side of the crown).

Table A.2 Branch characteristics of whorl 10 in study tree.

Branch Number	Nodal	Cones	Branch Dia At B (cm)	Branch Dia At DZ (cm)	H Dist To DZ (cm)	H Dist To Tip (cm)	Branch Rise (cm)	Cord Angle (degree)	Branch Angle (degree)	Branch Orient (degree)	Sector
B1	nn	c	3.1	2.4	60	240	100	24	10	40	1
B2	n	c	4.8	4.3	50	240	160	35	20	0	1
B3	n	c	4.7	3.4	50	210	160	39	25	45	1
B4	n	c	4.1	3.9	60	160	125	40	20	100	2
B5	nn	c	2.9	2.9	50	160	100	34	15	120	2
B6	nn	c	2.3	2.0	50	160	30	11	15	170	3
B7	n	c	4.9	4.4	40	220	200	35	35	185	3
B8	nn	c	3.2	2.3	70	190	100	29	10	230	4
B9	n	c	4.7	4.1	40	210	205	46	30	240	4
B10	nn	c	3.4	3.4	70	210	100	27	25	280	4
B11	n	c	3.5	3.5	50	150	120	41	30	300	4
Mean			3.8	3.3	54	195	127	34	21		
Std Dev			0.9	0.8	10	33	51	10	8		

Table A.3 Branch characteristics of whorl 11 in study tree.

Branch Number	Nodal	Cones	Branch Dia At B (cm)	Branch Dia At DZ (cm)	H Dist To DZ (cm)	H Dist To Tip (cm)	Branch Rise (cm)	Cord Angle (degree)	Branch Angle (degree)	Branch Orient (degree)	Sector
B1	nn	c	2.6	2.1	80	230	90	22	5	20	1
B2	n	c	4.1	4.0	60	220	125	31	15	330	1
B3	n	c	4.6	4.4	50	240	190	40	25	25	1
B4	nn	c	4.2	3.3	60	280	130	26	0	70	2
B5	n	c	4.9	4.3	50	290	200	36	15	100	2
B6	nn	c	3.1	2.4	60	220	140	34	5	140	3
B7	n	c	2.7	2.3	70	230	70	18	10	185	3
B8	nn	c	4.7	4.1	70	300	200	35	20	190	3
B9	n	c	4.6	4.1	60	220	180	41	35	195	3
B10	nn	c	5.1	4.4	70	300	230	38	25	280	4
B11	n	c	4.7	4.1	50	160	200	53	25	310	4
B12	nn	c	3.6	2.9	80	250	120	27	10	315	4
Mean			4.1	3.5	63	245	156	33	16		
Std Dev			0.9	0.9	11	41	50	9	10		

Table A.4 Branch characteristics of whorl 12 in study tree.

Branch Number	Nodal	Cones	Branch Dia At B (cm)	Branch Dia At DZ (cm)	H Dist To DZ (cm)	H Dist To Tip (cm)	Branch Rise (cm)	Cord Angle (degree)	Branch Angle (degree)	Branch Orient (degree)	Sector
B1	n	c	3.1	2.7	70	310	0	0	5	20	1
B2	n	c	5.6	4.2	50	330	170	28	15	25	1
B3	n	c	5.0	4.4	70	350	155	25	20	100	2
B4	n	c	3.2	3.2	70	180	110	33	5	110	2
B5	n	c	6.0	5.0	80	320	220	35	20	200	3
B6	n	c	3.6	2.9	110	320	45	8	10	290	4
B7	n	c	5.0	4.3	90	320	190	32	20	280	4
B8	n	c	4.5	4.3	90	330	145	24	15	315	1
Mean			4.5	3.9	79	308	129	23	14		
Std Dev			1.1	0.8	18	53	74	13	6		

Table A.5 Branch characteristics of whorl 13 in study tree.

Branch Number	Nodal	Cones	Branch Dia At B (cm)	Branch Dia At DZ (cm)	H Dist To DZ (cm)	H Dist To Tip (cm)	Branch Rise (cm)	Cord Angle (degree)	Branch Angle (degree)	Branch Orient (degree)	Sector
B1	n	c	5.2	4.1	150	380	55	9	20	25	1
B2	nn	c	5.7	4.5	110	350	50	8	15	70	2
B3	nn	c	5.1	4.3	130	360	185	28	15	120	2
B4	n	c	5.9	4.8	130	350	245	36	20	140	3
B5	n	c	6.1	5.8	130	350	250	36	30	160	3
B6	n		5.6	4.8	150	360	200	30	20	190	3
B7	nn	c	4.4	3.5	160	340	140	23	10	280	4
B8	n	c	6.2	4.8	150	390	215	30	20	270	4
B9	n	c	4.6	3.7	160	430	100	13	15	320	1
B10	n	c	5.5	4.2	150	380	140	21	20	315	1
B11	nn	c	3.9	3.1	140	370	65	10	10	20	1
Mean			5.3	4.3	142	369	150	22	18		
Std Dev			0.7	0.7	15	25	75	10	5		

Table A.6 Branch characteristics of whorl 14 in study tree.

Branch Number	Nodal	Cones	Branch Dia At B (cm)	Branch Dia At DZ (cm)	H Dist To DZ (cm)	H Dist To Tip (cm)	Branch Rise (cm)	Cord Angle (degree)	Branch Angle (degree)	Branch Orient (degree)	Sector
B1	n		5.2	4.2	140	450	75	10	10	35	1
B2	n		5.8	3.9	140	390	120	18	20	80	2
B3	n	c	5.7	4.6	150	370	150	23	10	120	2
B4	n	c	5.4	4.1	170	410	115	16	20	180	3
B5	nn	c	5.6	4.4	170	400	180	25	5	195	3
B6	n	c	5.8	4.7	150	410	220	29	15	220	3
B7	n		5.6	3.9	160	390	190	27	10	280	4
B8	n		5.9	4.5	150	380	125	19	20	340	1
Mean			5.6	4.3	154	400	147	21	14		
Std Dev			0.2	0.3	12	24	47	6	5		

Table A.7 Branch characteristics of whorl 15 in study tree.

Branch Number	Nodal	Cones	Branch Dia At B (cm)	Branch Dia At DZ (cm)	H Dist To DZ (cm)	H Dist To Tip (cm)	Branch Rise (cm)	Cord Angle (degree)	Branch Angle (degree)	Branch Orient (degree)	Sector
B1	n		5.7	3.8	200	460	115	15	0	35	1
B2	n		4.0	3.0	200	400	20	3	0	60	2
B3	n		4.7	3.4	200	410	80	12	-5	90	2
B4	n		6.3	4.9	200	440	115	15	5	85	2
B5	n	c	6.4	4.4	190	420	170	23	5	180	3
B6	n		5.7	4.1	180	440	180	23	0	250	4
B7	n		5.7	4.0	160	420	90	13	10	300	4
B8	n		5.6	4.1	160	410	150	21	5	290	4
B9	n		4.0	2.7	160	370	25	4	0	340	1
Mean			5.3	3.8	183	419	105	14	2		
Std Dev			0.9	0.7	19	26	58	7	4		

Table A.8 Branch characteristics of whorl 16 in study tree.

Branch Number	Nodal	Cones	Branch Dia At B (cm)	Branch Dia At DZ (cm)	H Dist To DZ (cm)	H Dist To Tip (cm)	Branch Rise (cm)	Cord Angle (degree)	Branch Angle (degree)	Branch Orient (degree)	Sector
B1	n		5.3	3.2	250	440	120	16	10	30	1
B2	n		5.5	2.1	190	410	0	0	10	70	2
B3	n	c	6.3	4.0	220	400	180	25	20	130	2
B4	n		5.9	3.8	200	390	150	22	5	185	3
B5	nn		6.0	4.1	230	370	200	30	15	220	3
B6	n		6.2	4.0	240	430	160	21	20	250	4
Mean			5.9	3.5	222	407	135	19	13		
Std Dev			0.4	0.8	23	26	71	9	6		

Table A.9 Branch characteristics of whorl 17 in study tree.

Branch Number	Nodal	Cones	Branch Dia At B (cm)	Branch Dia At DZ (cm)	H Dist To DZ (cm)	H Dist To Tip (cm)	Branch Rise (cm)	Cord Angle (degree)	Branch Angle (degree)	Branch Orient (degree)	Sector
B1	n		4.1	2.8	230	420	-90	-13	0	20	1
B2	n	c	5.4	3.5	230	490	40	5	15	85	2
B3	nn		3.0	1.8	230	390	-80	-12	5	80	2
B4	nn	c	6.2	4.0	220	450	120	16	15	140	3
B5	n		6.7	4.3	220	390	200	28	25	145	3
B6	n		4.1	3.0	160	270	65	15	40	335	1
Mean			4.9	3.2	215	402	43	7	17		
Std Dev			1.4	0.9	27	75	113	15	13		

Table A.11 Branch characteristics of whorl 19 in study tree.

Branch Number	Nodal	Cones	Branch Dia At B (cm)	Branch Dia At DZ (cm)	H Dist To DZ (cm)	H Dist To Tip (cm)	Branch Rise (cm)	Cord Angle (degree)	Branch Angle (degree)	Branch Orient (degree)	Sector
B1	n		4.2	2.4	210	390	20	3	15	20	1
B2	n		6.1	2.8	260	480	20	3	15	50	2
B3	n		4.6	2.5	260	450	0	0	5	125	2
B4	n		6.3	4.8	240	460	90	12	15	120	2
B5	n		7.6	3.4	240	450	80	11	5	165	3
B6	n		7.3	4.7	260	460	210	26	0	195	3
B7	n		4.8	2.5	240	380	65	10	-5	210	3
B8	nn		6.6	4.0	290	530	90	10	-5	210	3
B9	n		5.6	3.4	280	460	60	8	0	260	4
B10	n		6.2	3.8	190	510	85	10	0	310	4
B11	n		4.8	3.8	240	480	60	7	-5	330	1
Mean			5.8	3.5	246	429	71	9	4		
Std Dev			1.1	0.9	29	109	56	6	8		

Table A.10 Branch characteristics of whorl 18 in study tree.

Branch Number	Nodal	Cones	Branch Dia At B (cm)	Branch Dia At DZ (cm)	H Dist To DZ (cm)	H Dist To Tip (cm)	Branch Rise (cm)	Cord Angle (degree)	Branch Angle (degree)	Branch Orient (degree)	Sector
B1	n	c	6.8	4.2	230	410	130	18	25	10	1
B2	n	c	6.7	4.4	240	520	110	12	15	80	2
B3	nn		7.3	4.8	250	420	210	28	10	195	3
B4	nn		5.5	3.4	220	480	55	7	0	255	4
B5	n		7.2	4.7	220	410	210	28	15	260	4
B6	n		3.2	2.2	160	320	-5	-10	-10	310	4
Mean			6.1	4.0	220	427	118	14	9		
Std Dev			1.6	1.0	32	69	85	13	11		

Table A.12 Branch characteristics of whorl 20 in study tree.

Branch Number	Nodal	Cones	Branch Dia At B (cm)	Branch Dia At DZ (cm)	H Dist To DZ (cm)	H Dist To Tip (cm)	Branch Rise (cm)	Cord Angle (degree)	Branch Angle (degree)	Branch Orient (degree)	Sector
B1	n		4.2	1.6	230	370	15	3	15	40	1
B2	n		3.9	1.5	270	220	0	0	15	60	2
B3	n		4.1	2.0	300	370	0	0	-10	100	2
B4	n		4.5	1.8	290	420	0	0	-5	130	2
B5	n		4.0	2.0	300	470	0	0	5	170	3
B6	n		6.5	3.7	300	520	110	13	-10	170	3
B7	nn		3.8	2.0	300	410	0	0	-10	140	3
B8	n		5.0	2.6	300	400	0	0	0	210	3
B9	nn		3.1	1.9	230	340	0	0	0	280	4
B10	n		3.7	2.6	230	340	-10	-2	-5	280	4
Mean			4.3	2.2	275	385	12	1	-1		
Std Dev			0.9	0.7	32	81	35	4	10		

APPENDIX B

CHARACTERISTICS OF THE BRANCHES USED IN THE BRANCH-CONTROL EXPERIMENT

Photographs of the ten branches used in the branch-control experiment are given in Figures B.1a-j. A description of this experiment is given in Chapter III. A summary of all the leaf area measurements taken with these ten branches are given in Tables B.1 to B.10. A description of all the area measurements is given in Chapter V. The symbol ± indicates the approximate 95% confidence interval of the measured or computed variable.

The term "trim" in Tables B.1 to B.10 refers to the remaining pieces of branch left over after the six or seven 40x40 cm sections were cut out. All leaf and stem weights are on an oven dry basis. Branch sections were dried at 70°C for 24 hours. The larger branch stems were probably not completely dry after 24 hours at this temperature but my main concern was for the needle weights. All leaf area measurements are based on fresh leaf area.

Figure B.1 Photographs of the ten Douglas-fir branches used in the branch-control experiment. Note meter scale in the foreground of each photo. Branch C1 is shown in Figure B.1a, branch C2 is in Figure B.1b, branch C3 is in Figure B.1c, etc.

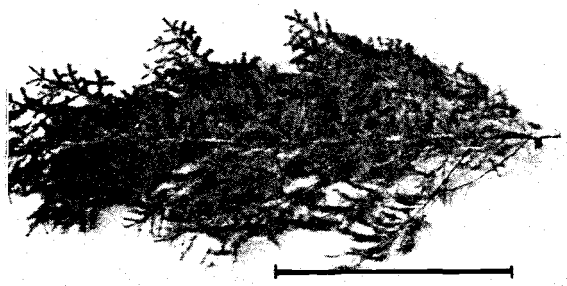

Figure B.1a : branch C1

Figure B.1b : branch C2

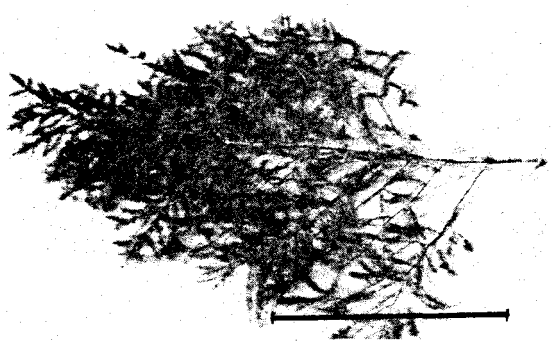

Figure B.1c : branch C3

Figure B.1d : branch C4

Figure B.1e : branch C5

Figure B.1f : branch C6

Figure B.1g : branch C7

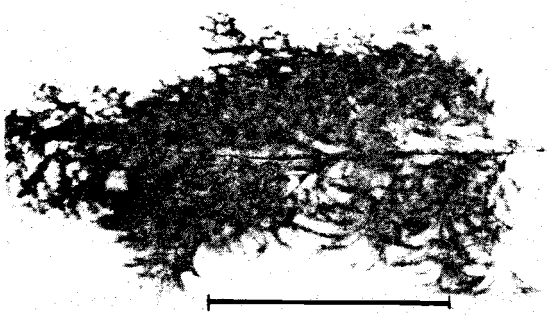

Figure B.1h : branch C8

Figure B.1i : branch C9

Figure B.1j : branch C10

List of variables used in Tables B.1 to B.10 (see Chapter V).

Variable	Definition
A	Total one-sided leaf area.
A_{ht}	Total horizontal shadow area.
A_{hs}	Horizontal stem shadow area.
$A_{h\ell}$	Horizontal leaf shadow area.
A_{grnd}	Ground area.
LAI	Leaf area index.
SAI	Shadow area index.

Table B.1 Leaf area measurements of branch C1.

Segment	Stem Wt (g)	Needle Wt (g)	Specific Leaf Area (cm^2/g)	A (cm^2)	A_{ht} (cm^2)	A_{hs} (cm^2)	$A_{h\ell}$ (cm^2)	A_{grnd} (cm^2)	LAI (cm^2/cm^2)	SAI (cm^2/cm^2)
S1	133.6	12.6	77 ± 21	970 ± 272	689 ± 26	263 ± 13	426 ± 29	1299 ± 130	0.74 ± 0.22	0.94 ± 0.23
S2	131.4	23.4	86 ± 25	2014 ± 583	1028 ± 27	296 ± 13	732 ± 30	1686 ± 170	1.19 ± 0.37	1.37 ± 0.37
S3	101.2	20.6	66 ± 14	1363 ± 298	935 ± 27	235 ± 13	700 ± 30	1612 ± 160	0.85 ± 0.20	0.90 ± 0.21
S4	71.8	24.3	79 ± 16	1915 ± 392	996 ± 27	232 ± 13	764 ± 30	1517 ± 150	1.26 ± 0.29	1.41 ± 0.29
S5	40.9	34.2	78 ± 13	2672 ± 479	1136 ± 28	178 ± 13	958 ± 31	1637 ± 160	1.64 ± 0.33	1.74 ± 0.34
S6	13.6	20.8	78 ± 17	1627 ± 358	761 ± 26	91 ± 13	670 ± 29	1190 ± 120	1.36 ± 0.33	1.43 ± 0.33
trim	117.4	291.6								

± approximate 95% confidence interval

Table B.2 Leaf area measurements of branch C2.

Segment	Stem Wt (g)	Needle Wt (g)	Specific Leaf Area (cm^2/g)	A (cm^2)	A_{ht} (cm^2)	A_{hs} (cm^2)	$A_{h\ell}$ (cm^2)	A_{grnd} (cm^2)	LAI (cm^2/cm^2)	SAI (cm^2/cm^2)
S1	193.4	7.5	64 ± 11	476 ± 83	519 ± 26	244 ± 13	275 ± 29	953 ± 100	0.50 ± 0.10	0.76 ± 0.12
S2	162.7	5.5	68 ± 12	374 ± 66	413 ± 25	203 ± 13	210 ± 28	714 ± 70	0.53 ± 0.11	0.82 ± 0.12
S3	109.2	12.5	67 ± 11	845 ± 145	565 ± 26	182 ± 13	383 ± 29	1068 ± 110	0.80 ± 0.16	0.97 ± 0.17
S4	81.6	23.4	68 ± 10	1578 ± 253	812 ± 26	177 ± 13	635 ± 29	1574 ± 160	1.00 ± 0.19	1.11 ± 0.20
S5	39.0	18.7	69 ± 10	1289 ± 196	523 ± 26	106 ± 13	417 ± 29	814 ± 80	1.58 ± 0.29	1.71 ± 0.29
S6	19.3	38.1	64 ± 11	2440 ± 450	844 ± 27	125 ± 13	719 ± 30	1125 ± 110	2.17 ± 0.45	2.30 ± 0.46
trim	212.1	570.5								

± approximate 95% confidence interval

Table B.3 Leaf area measurements of branch C3.

Segment	Stem Wt (g)	Needle Wt (g)	Specific Leaf Area (cm^2/g)	A (cm^2)	A_{ht} (cm^2)	A_{hs} (cm^2)	A_{ht} (cm^2)	A_{grnd} (cm^2)	LAI (cm^2/cm^2)	SAI (cm^2/cm^2)
S1	207.3	18.7	70 ± 11	1308 ± 209	796 ± 26	348 ± 13	448 ± 29	1326 ± 130	0.98 ± 0.18	1.24 ± 0.20
S2	165.4	14.5	74 ± 12	1071 ± 179	696 ± 26	250 ± 13	446 ± 29	1223 ± 120	0.88 ± 0.17	1.08 ± 0.18
S3	160.8	14.0	77 ± 14	1074 ± 204	720 ± 26	240 ± 13	480 ± 29	1196 ± 120	0.90 ± 0.19	1.10 ± 0.20
S4	82.2	26.3	70 ± 10	1838 ± 281	1023 ± 27	227 ± 13	796 ± 30	1672 ± 170	1.11 ± 0.20	1.24 ± 0.21
S5	59.5	42.6	68 ± 9	2866 ± 419	1212 ± 28	235 ± 13	977 ± 31	1688 ± 170	1.70 ± 0.30	1.84 ± 0.31
S6	32.6	40.0	66 ± 13	2645 ± 546	1159 ± 28	159 ± 13	1000 ± 31	1634 ± 160	1.62 ± 0.37	1.72 ± 0.37
S7	8.5	20.2	65 ± 11	1313 ± 234	671 ± 26	83 ± 13	588 ± 29	1119 ± 110	1.18 ± 0.24	1.25 ± 0.24
trim	279.5	674.4								

± approximate 95% confidence interval

Table B.4 Leaf area measurements of branch C4.

Segment	Stem Wt (g)	Needle Wt (g)	Specific Leaf Area (cm^2/g)	A (cm^2)	A_{ht} (cm^2)	A_{hs} (cm^2)	$A_{h\ell}$ (cm^2)	A_{grnd} (cm^2)	LAI (cm^2/cm^2)	SAI (cm^2/cm^2)
S1	170.1	2.4	69 ± 13	165 ± 33	353 ± 25	218 ± 13	135 ± 28	667 ± 70	0.24 ± 0.06	0.56 ± 0.08
S2	117.4	15.3	64 ± 10	971 ± 154	643 ± 26	228 ± 13	415 ± 29	1046 ± 100	0.94 ± 0.17	0.18 ± 0.18
S3	111.9	34.6	65 ± 11	2237 ± 401	1062 ± 27	289 ± 13	773 ± 30	1560 ± 160	1.44 ± 0.30	1.63 ± 0.31
S4	57.0	30.1	65 ± 14	1953 ± 431	951 ± 27	192 ± 13	759 ± 30	1386 ± 140	1.41 ± 0.34	1.54 ± 0.35
S5	37.0	41.5	69 ± 14	2867 ± 587	1184 ± 28	194 ± 13	990 ± 31	1596 ± 160	1.78 ± 0.40	1.91 ± 0.42
S6	12.8	21.5	69 ± 10	1483 ± 224	694 ± 26	92 ± 13	602 ± 29	1155 ± 120	1.30 ± 0.24	1.38 ± 0.24
trim	259.9	476.3								

± approximate 95% confidence interval

Table B.5 Leaf area measurements of branch C5.

Segment	Stem Wt (g)	Needle Wt (g)	Specific Leaf Area (cm^2/g)	A (cm^2)	A_{lt} (cm^2)	A_{hs} (cm^2)	A_{hl} (cm^2)	A_{grnd} (cm^2)	LAI (cm^2/cm^2)	SAI (cm^2/cm^2)
S1	111.6	9.9	73 ± 18	726 ± 186	589 ± 26	188 ± 13	401 ± 29	1206 ± 120	0.61 ± 0.17	0.76 ± 0.17
S2	86.6	16.4	74 ± 14	1210 ± 237	763 ± 26	187 ± 13	576 ± 29	1337 ± 130	0.91 ± 0.20	1.05 ± 0.20
S3	62.5	28.3	77 ± 13	2166 ± 377	887 ± 27	176 ± 13	711 ± 30	1304 ± 130	1.66 ± 0.33	1.79 ± 0.34
S4	38.4	17.7	66 ± 10	1172 ± 179	646 ± 26	116 ± 13	530 ± 29	1220 ± 120	0.96 ± 0.17	1.05 ± 0.18
S5	20.4	19.8	73 ± 17	1449 ± 343	642 ± 26	92 ± 13	550 ± 29	1106 ± 110	1.30 ± 0.34	1.38 ± 0.34
S6	7.8	16.2	71 ± 14	1149 ± 230	464 ± 26	70 ± 13	394 ± 29	732 ± 70	1.56 ± 0.35	1.66 ± 0.36
trim	92.9	280.9								

± approximate 95% confidence interval

Table B.6 Leaf area measurements of branch C6.

Segment	Stem Wt (g)	Needle Wt (g)	Specific Leaf Area (cm^2/g)	A (cm^2)	A_{ht} (cm^2)	A_{hs} (cm^2)	$A_{h\ell}$ (cm^2)	A_{grnd} (cm^2)	LAI (cm^2/cm^2)	SAI (cm^2/cm^2)
S1	200.5	23.3	67 ± 14	1556 ± 329	809 ± 15	286 ± 25	523 ± 29	1353 ± 140	1.14 ± 0.27	1.35 ± 0.28
S2	148.8	18.8	80 ± 13	1499 ± 252	705 ± 15	256 ± 25	449 ± 29	1187 ± 120	1.25 ± 0.25	1.46 ± 0.26
S3	129.4	24.7	75 ± 14	1847 ± 362	791 ± 15	258 ± 25	533 ± 29	1383 ± 140	1.33 ± 0.34	1.52 ± 0.30
S4	101.0	50.6	76 ± 14	3846 ± 735	1329 ± 16	303 ± 25	1026 ± 30	1716 ± 170	2.24 ± 0.48	2.42 ± 0.49
S5	53.4	43.4	80 ± 17	3491 ± 737	1163 ± 16	202 ± 25	961 ± 30	1580 ± 160	2.21 ± 0.52	2.34 ± 0.52
S6	26.4	31.9	74 ± 17	2374 ± 547	845 ± 15	134 ± 25	711 ± 29	1471 ± 150	1.61 ± 0.41	1.71 ± 0.41
S7	9.7	20.4	79 ± 11	1618 ± 247	570 ± 15	85 ± 25	485 ± 29	1062 ± 110	1.52 ± 0.28	1.60 ± 0.29
trim	193.1	532.9								

± approximate 95% confidence interval

Table B.7 Leaf area measurements of branch C7.

Segment	Stem Wt (g)	Needle Wt (g)	Specific Leaf Area (cm^2/g)	A (cm^2)	A_{ht} (cm^2)	A_{hs} (cm^2)	$A_{h\ell}$ (cm^2)	A_{grnd} (cm^2)	LAI (cm^2/cm^2)	SAI (cm^2/cm^2)
S1	200.7	20.4	83 ± 14	1685 ± 303	905 ± 15	266 ± 25	639 ± 29	1332 ± 130	1.26 ± 0.26	1.46 ± 0.27
S2	180.0	22.4	80 ± 12	1797 ± 290	879 ± 15	302 ± 25	577 ± 29	1364 ± 140	1.32 ± 0.25	1.54 ± 0.27
S3	137.2	23.4	85 ± 13	1979 ± 318	856 ± 15	272 ± 25	584 ± 29	1332 ± 130	1.48 ± 0.28	1.69 ± 0.29
S4	98.4	34.6	81 ± 16	2787 ± 568	1094 ± 16	249 ± 25	845 ± 30	1449 ± 140	1.93 ± 0.47	2.10 ± 0.44
S5	71.4	52.8	75 ± 18	3949 ± 951	1249 ± 16	243 ± 25	1006 ± 30	1525 ± 150	2.59 ± 0.71	2.75 ± 0.68
S6	29.4	40.9	64 ± 15	2615 ± 613	933 ± 15	151 ± 25	782 ± 29	1280 ± 130	2.04 ± 0.52	2.16 ± 0.53
S7	14.4	31.5	74 ± 17	2320 ± 549	860 ± 15	109 ± 25	751 ± 29	1359 ± 140	1.70 ± 0.44	1.78 ± 0.44
trim	301.0	803.6								

± approximate 95% confidence interval

Table B.8 Leaf area measurements of branch C8.

Segment	Stem Wt (g)	Needle Wt (g)	Specific Leaf Area (cm^2/g)	A (cm^2)	A_{ht} (cm^2)	A_{hs} (cm^2)	$A_{h\ell}$ (cm^2)	A_{grnd} (cm^2)	LAI (cm^2/cm^2)	SAI (cm^2/cm^2)
S1	152.0	1.3	81 ± 12	105 ± 16	238 ± 14	171 ± 25	67 ± 29	387 ± 40	0.27 ± 0.05	0.72 ± 0.11
S2	154.1	10.7	88 ± 14	937 ± 154	644 ± 15	291 ± 25	353 ± 29	1288 ± 130	0.73 ± 0.14	0.96 ± 0.15
S3	107.7	11.8	82 ± 12	970 ± 146	641 ± 15	243 ± 25	398 ± 29	1215 ± 120	0.79 ± 0.14	0.99 ± 0.16
S4	70.5	32.7	74 ± 14	2436 ± 491	1010 ± 16	247 ± 25	763 ± 30	1443 ± 140	1.69 ± 0.38	1.86 ± 0.39
S5	33.9	27.8	80 ± 18	2212 ± 518	861 ± 15	145 ± 25	716 ± 29	1370 ± 140	1.48 ± 0.41	1.73 ± 0.42
S6	11.2	24.4	76 ± 14	1861 ± 345	802 ± 15	91 ± 25	711 ± 29	1283 ± 130	1.45 ± 0.31	1.53 ± 0.31
trim	242.5	517.2								

± approximate 95% confidence interval

Table B.9 Leaf area measurements of branch C9.

Segment	Stem Wt (g)	Needle Wt (g)	Specific Leaf Area (cm^2/g)	A (cm^2)	A_{ht} (cm^2)	A_{hs} (cm^2)	$A_{h\ell}$ (cm^2)	A_{grnd} (cm^2)	LAI (cm^2/cm^2)	SAI (cm^2/cm^2)
S1	237.7	8.6	73 ± 10	624 ± 91	598 ± 15	305 ± 25	293 ± 29	1261 ± 130	0.50 ± 0.09	0.74 ± 0.11
S2	194.2	6.9	66 ± 12	458 ± 89	514 ± 15	266 ± 25	248 ± 29	953 ± 100	0.48 ± 0.11	0.76 ± 0.13
S3	141.9	13.4	71 ± 14	955 ± 195	651 ± 15	264 ± 25	387 ± 29	1076 ± 110	0.88 ± 0.20	1.12 ± 0.22
S4	90.0	12.9	70 ± 15	908 ± 194	589 ± 15	203 ± 25	386 ± 29	1247 ± 120	0.72 ± 0.17	0.89 ± 0.18
S5	56.3	13.7	70 ± 13	955 ± 188	578 ± 15	135 ± 25	443 ± 29	1264 ± 130	0.76 ± 0.17	0.87 ± 0.17
S6	29.2	9.4	62 ± 9	583 ± 87	413 ± 15	88 ± 25	325 ± 29	1160 ± 120	0.50 ± 0.09	0.57 ± 0.10
S7	14.7	11.9	66 ± 14	783 ± 170	510 ± 15	77 ± 25	433 ± 29	1302 ± 130	0.60 ± 0.14	0.66 ± 0.15
trim	438.1	594.4								

± approximate 95% confidence interval

Table B.10 Leaf area measurements of branch C10.

Segment	Stem Wt (g)	Needle Wt (g)	Specific Leaf Area (cm^2/g)	A (cm^2)	A_{ht} (cm^2)	A_{hs} (cm^2)	$A_{h\ell}$ (cm^2)	A_{grnd} (cm^2)	LAI (cm^2/cm^2)	SAI (cm^2/cm^2)
S1	209.3	18.9	65 ± 12	1235 ± 227	896 ± 15	316 ± 25	580 ± 29	1639 ± 160	0.76 ± 0.16	0.95 ± 0.17
S2	174.8	33.9	69 ± 11	2332 ± 378	1129 ± 16	297 ± 25	832 ± 30	1672 ± 170	1.40 ± 0.27	1.58 ± 0.28
S3	133.8	38.4	74 ± 11	2852 ± 442	1190 ± 16	286 ± 25	904 ± 30	1759 ± 180	1.61 ± 0.30	1.72 ± 0.31
S4	104.8	48.4	58 ± 13	2802 ± 661	1228 ± 16	320 ± 25	908 ± 30	1770 ± 180	1.58 ± 0.41	1.76 ± 0.41
S5	71.9	56.3	55 ± 12	3085 ± 671	1327 ± 16	272 ± 25	1055 ± 30	1849 ± 180	1.67 ± 0.40	1.81 ± 0.40
S6	43.6	52.1	58 ± 11	3044 ± 575	1181 ± 16	212 ± 25	969 ± 30	1688 ± 170	1.80 ± 0.39	1.93 ± 0.39
S7	12.1	26.7	61 ± 12	1626 ± 341	702 ± 15	104 ± 25	598 ± 29	1108 ± 110	1.46 ± 0.34	1.53 ± 0.35
trim	174.4	663.7								

± approximate 95% confidence interval

APPENDIX C

PRODUCT AND QUOTIENT OF RANDOM VARIABLES

One can compute the product and quotient of two random variables, X and Y, in terms of moments of the two random variables. See Mood et al. (1974) for additional details.

Define E[X] and E[Y] as the expected values of X and Y, and Var[X] and Var[Y] as the variance of X and Y , respectively. For random variables X and Y for which Var[XY] exists and if X and Y are independent then the expected value of XY is

$$E[XY] = E[X]E[Y] \tag{C.1}$$

The variance of XY is

$$Var[XY] = E[X]^2Var[Y] + E[Y]^2Var[X] + Var[X]Var[Y] \tag{C.2}$$

In general, there are no simple exact formulas for the mean and variance of the quotient in terms of moments of the two random variables, but an approximate formula for the expected value of X/Y is (where X and Y are independent)

$$E[X/Y] \simeq E[X]/E[Y] + E[X]Var[Y]E[Y]^{-3} \tag{C.3}$$

and the variance is approximately

$$Var[X/Y] \simeq \{Var[X]E[X]^{-2} + Var[Y]E[Y]^{-2}\}E[X]^2E[Y]^{-2} \tag{C.4}$$

APPENDIX D

COMPUTER PROGRAM TO COMPUTE SOLAR POSITION

The following FORTRAN IV subroutine called "SOLAR" computes the altitude, zenith and azimuth angles of the sun for any given day and hour of the year. Program is accurate to approximately ± 0.1 degrees. Program was written from equations derived by Smart(1965).

Example :

In Corvallis, Oregon at 12:24 PM (LST) on December 26, 1979 the sun is located at

ALTS = 20.0 (degrees)

ZENITH = 70.0 (degrees)

AZMTHS = 182.5 (degrees)

where the time of day and location of observer are defined as

DAY = 360. (Julian day)

HOUR = 12.40 (hours, LST)

LONGOB = 123.28 (degrees)

LATOB = 44.55 (degrees)

```
      SUBROUTINE SOLAR (DAY,HOUR,LONGOB,LATOB,ALTS,ZENITH,AZMTHS)        M   1
C                                                                        M   2
C                                                                        M   3
C     COMPUTE THE ALTITUDE AND AZIMUTH OF SUN IN DEGREES FOR A           M   4
C     GIVEN DAY AND HOUR                                                 M   5
C                                                                        M   6
C                                                                        M   7
      INTEGER OUT,PNCH                                                   M   8
      COMMON /IO/ IN,OUT,PNCH                                            M   9
C        ALTS      ALTITUDE OF SUN(DEGREES)                            M  10
C                       POSITIVE IF ABOVE THE HORIZON                    M  11
C                                                                        M  12
C        AZMTHS    AZIMUTH OF SUN(DEGREES)                             M  13
C                       MEASURED POSITIVE CLOCKWISE FROM NORTH, ALONG    M  14
C                       THE HORIZON                                      M  15
C                                                                        M  16
C        DAY       JULIAN DATE, DAYS SINCE JANUARY 1, HENCE DAY=2      M  17
C                    ON JANUARY 2                                        M  18
C        HOUR      LOCAL STANDARD TIME ( 24 HOUR WALL CLOCK TIME OF THE M  19
C                    OBSERVER)                                           M  20
C                    NOTE  DURING DAYLIGHT SAVINGS  ,ONE MUST SUBTRACT   M  21
C                    ONE HOUR FROM THE  WALL CLOCK TIME                  M  22
C        LATOB     LATITUDE OF OBSERVER(DEGREES)                       M  23
C                       POSITIVE IF NORTH OF THE EQUATOR                 M  24
C                                                                        M  25
C        LONGOB    LONGITUDE OF OBSERVOR(DEGREES)                      M  26
C                       POSITIVE IF WEST OF GREENWICH                    M  27
C                                                                        M  28
C        STZM      STANDARD TIME ZONE MERIDIAN(DEGREES)                M  29
C                     NOTE  PACIFIC TIME ZONE, STZM=120                  M  30
C        ZENITH    ZENITH OF SUN(DEGREES)                              M  31
C                    MEASURED POSITIVE FROM THE VERTICAL                 M  32
C                                                                        M  33
C                                                                        M  34
      REAL NS,LMDAMS,MS,LMDAS,LONGOB,LATOB,LATOBR,LOWER                  M  35
      PI = 3.141593                                                      M  36
      IF (LONGOB.LT.75.) WRITE (OUT,20) LONGOB                           M  37
 20   FORMAT (/////,50X,27HERROR FROM SUBROUTINE SOLAR,//,20X,79HALL OBS M  38
     1ERVER LONGITUDES MUST BE MEASURED WEST OF THE 75TH MERIDIAN OF GRE M  39
     2ENWICH,//,20X,24HYOU SPECIFIED  LONGOB = ,E12.5)                   M  40
      IF (LONGOB.LT.75.) STOP                                            M  41
      IF (HOUR.GT.-.01.AND.HOUR.LT.24.01) GO TO 60                       M  42
      WRITE (OUT,40) DAY,HOUR                                            M  43
 40   FORMAT (/////,50X,25HERROR IN SUBROUTINE SOLAR,//,20X,13HYOU SPECI M  44
     1FIED,/,50X,7H DAY = ,E12.6,/,50X,7HHOUR = ,E12.6,/,10X,96HHOWEVER, M  45
     2 HOUR MUST BE BASED ON A 24 HOUR CLOCK TIME, HENCE HOUR MUST LIE B M  46
     3ETWEEN  0 AND 24 HOURS)                                            M  47
      STOP                                                               M  48
 60   CONTINUE                                                           M  49
      IF (HOUR.LT.0.) HOUR = 0.                                          M  50
      IF (HOUR.GT.24.) HOUR = 24.                                        M  51
```

```
C     FIND THE LOCAL STANDARD TIME ZONE MERIDIAN (DEGREES)                M  52
      IL = LONGOB/15.+1.E-05                                              M  53
      XIL = IL                                                            M  54
      STZM = 15.*XIL                                                      M  55
      TIME = DAY+HOUR/24.                                                 M  56
C     MEAN DAILY MOTION(RADIANS/MEAN SOLAR DAY)                           M  57
      NS = .01720279                                                      M  58
C     REFERENCE DATE(MARCH 22.5)                                          M  59
      TAU1 = 81.5                                                         M  60
C     MEAN SOLAR LONGITUDE(RADIANS)                                       M  61
      LMDAMS = NS*(TIME-TAU1)                                             M  62
C     SOLAR ECCENTRICITY(1960)                                            M  63
      ES = .01672592                                                      M  64
C     MEAN ANOMALY OF SUN (RADIANS)                                       M  65
      MS = 1.356949+LMDAMS                                                M  66
C     SUN"S TRUE LONGITUDE (RADIANS)                                      M  67
      LMDAS = LMDAMS+2.*ES*SIN(MS)+1.25*ES*ES*SIN(2.*MS)                  M  68
C     OBLIQUITY OF THE ECLIPTIC (1960) (RADIANS)                          M  69
      EPSLNS = .4093185                                                   M  70
C     SUN"S TRUE DECLINATION (RADIANS)                                    M  71
      DLTAS = ASIN(SIN(EPSLNS)*SIN(LMDAS))                                M  72
C     EQUATION OF TIME (HOURS)                                            M  73
      E = (-97.8*SIN(LMDAMS)-431.3*COS(LMDAMS)+596.6*SIN(2.*LMDAMS)-1.9*  M  74
     1COS(2.*LMDAMS)+4.*SIN(3.*LMDAMS)+19.3*COS(3.*LMDAMS)-12.7*SIN(4.*   M  75
     2LMDAMS))/3600.                                                      M  76
C        HOUR ANGLE OF REAL SUN (HOURS)                                   M  77
      HARS = E-12.+HOUR+(STZM-LONGOB)/15.                                 M  78
C     HOUR ANGLE OF REAL SUN IS MEASURED POSITIVE IN A CLOCKWISE          M  79
C     DIRECTION FROM SOUTH                                                M  80
C     ADJUST HARS SO THAT IT RANGES FROM 0 TO 24 HRS  (I.E. HARS=0 AT     M  81
C     NOON, HARS=12 AT MIDNIGHT, AND HARS=22 AT 10AM)                     M  82
      IF (HARS.LT.0.) HARS = HARS+24.                                     M  83
      IF (HARS.GT.24.) HARS = HARS-24.                                    M  84
C     CONVERT TO RADIANS                                                  M  85
      HARSR = HARS*2.*PI/24.                                              M  86
      LATOBR = LATOB*2.*PI/360.                                           M  87
C     ALTITUDE OF SUN (RADIANS)                                           M  88
      ALTS = ASIN(SIN(LATOBR)*SIN(DLTAS)+COS(LATOBR)*COS(DLTAS)*COS       M  89
     1(HARSR))                                                            M  90
C     AZIMUTH OF SUN (RADIANS)                                            M  91
      UPPER = -SIN(HARSR)*COS(DLTAS)*COS(LATOBR)                          M  92
      LOWER = SIN(DLTAS)-SIN(LATOBR)*SIN(ALTS)                            M  93
      AZMTHS = ATAN2(UPPER,LOWER)                                         M  94
C     KEEP ALL ANGLES POSITIVE                                            M  95
      IF (AZMTHS.LT.0.) AZMTHS = AZMTHS+2.*PI                             M  96
C     CONVERT TO DEGREES                                                  M  97
      ALTS = ALTS*360./2./PI                                              M  98
      ZENITH = 90.-ABS(ALTS)                                              M  99
      AZMTHS = AZMTHS*360./2./PI                                          M 100
      RETURN                                                              M 101
      END                                                                 M 102-
```

APPENDIX E

GEOMETRIC MODEL OF THE CROWN

The crown of the Douglas-fir is assumed to be of the general shape of a right circular cone. The equation describing the outer surface of a right circular cone is defined as (see Figure E.1)

$$X^2 + Y^2 = (H-Z)^2 \tan^2(\beta/2) \qquad \text{(E.1)}$$

$$\text{iff } Z \geq HLC$$

The term H is equal to the distance (cm) from the top of the cone to the ground, HLC is the distance (cm) from the base of the live crown to the ground, RLC is the maximum crown radius (cm) (assumed to be at the base of the live crown), β is the cone angle (degrees), and X,Y,Z are three Cartesian coordinate axis (cm), where Z is measured positive upwards from the ground. Note that the cone half-angle, $\beta/2$, can be computed from the equation :

$$\tan(\beta/2) = RLC/(H-HLC)$$

Hence, all foliage of the tree must lie within the volume of space that is bounded by the surface described by Eq. E.1. A more general describtion of the equations for geometric solids is given by Green (1941), Sommerville (1939) and a similar problem using an ellipsoid model is given by Charles-Edwards and Thornley (1973).

In Figure E.2b, point $P(X_p,Y_p,Z_p)$ defines the spatial location (which is known) of the Kipp pyranometer, point $Q(X_q,Y_q,Z_q)$ defines

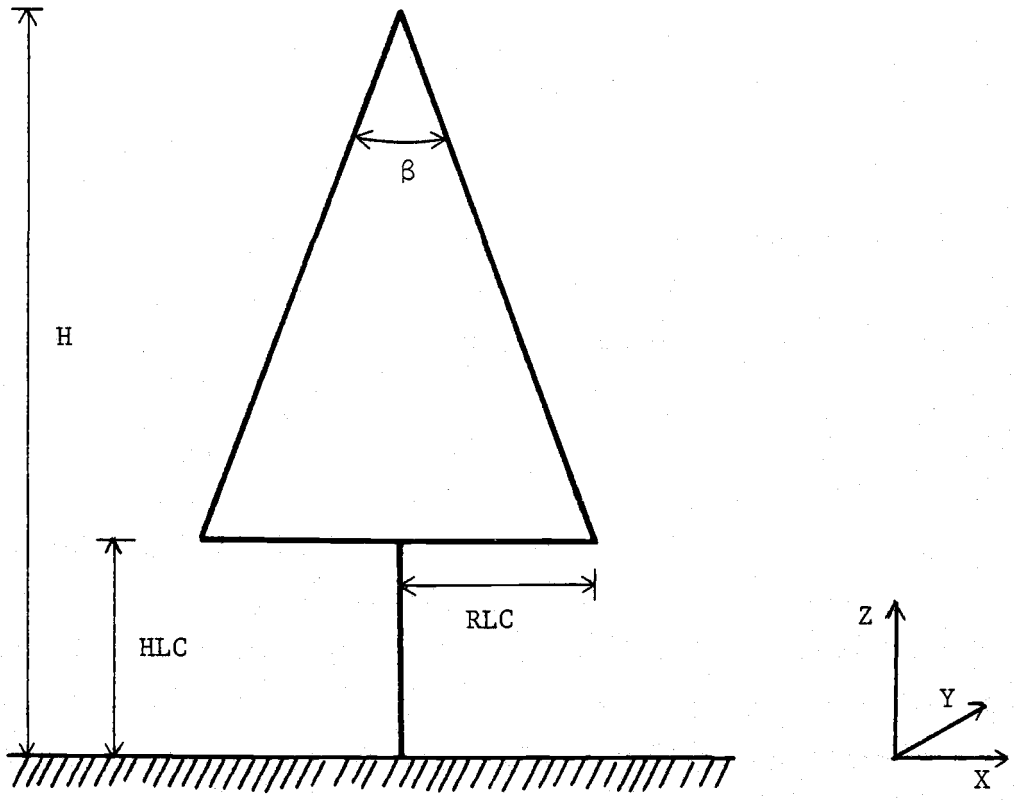

Figure E.1 Schematic of a Douglas-fir tree crown showing the relationship between various terms. Crown shape is assumed to resemble a right circular cone.

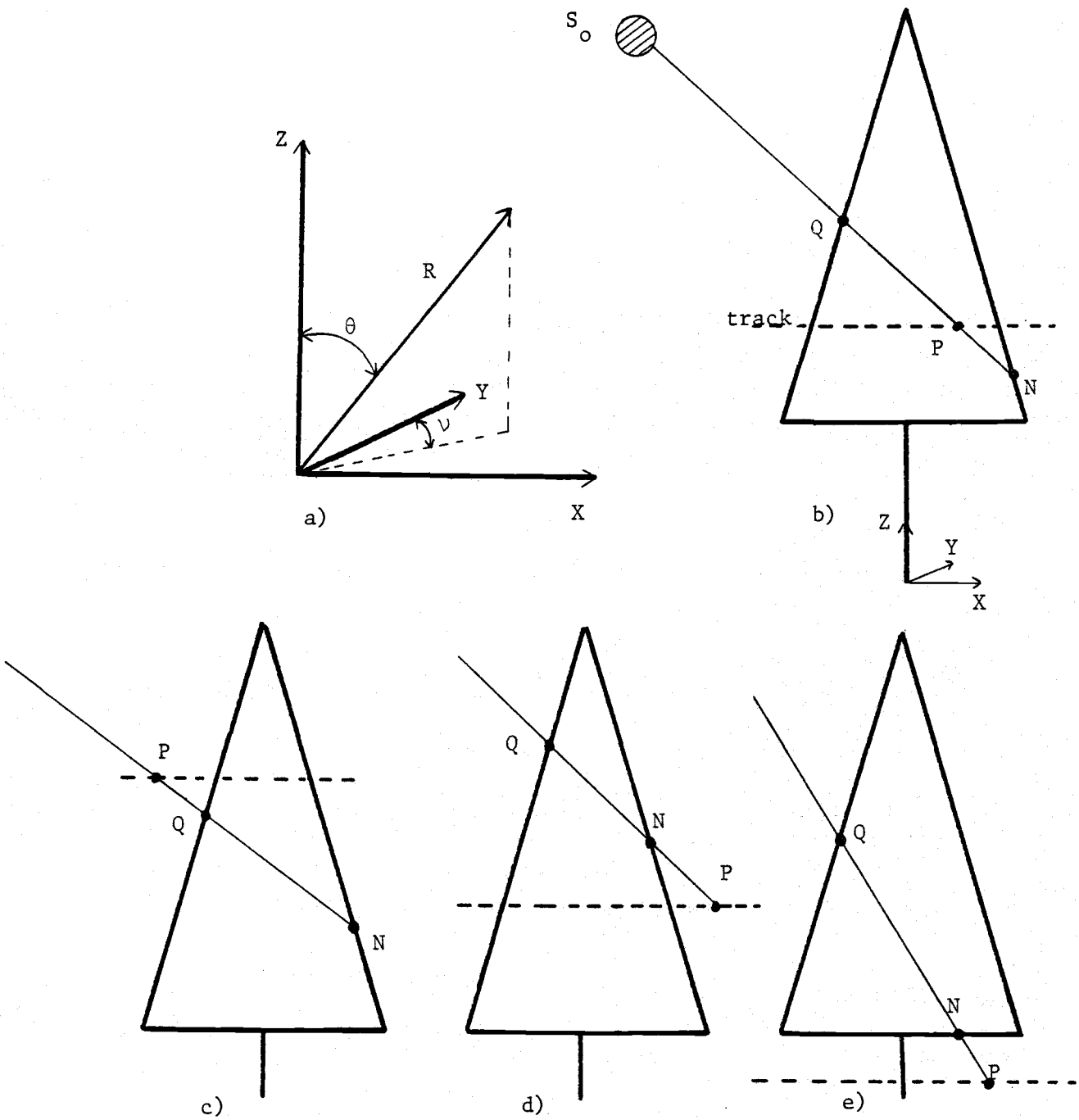

Figure E.2 Relation of coordinate system is illustrated in a). Various situations concerning canopy pathlengths are shown in b), c), d), and e) (see text).

the uppermost point of intersection of line S_oP on the outer boundary of the cone, where S_o refers to the location of the sun. The path S_oQP intersects the crown at a second point $N(X_n,Y_n,Z_n)$, where $Z_q \geq Z_n$. If P lies within the crown, the pathlength over which the light is attenuated is QP (see Figure E.2b). If P lies outside of the plant and if $Z_p > Z_n$, light is not attenuated (see Figure E.2c). If P lies outside of the crown and if $Z_p \leq Z_n$, the pathlength over which light is attenuated is QN (see Figures E.2d-e). The pathlength of attenuation is always denoted by s. The shadow-area index traversed along the path s is denoted by S and is obtained by integrating the shadow-area density F(X,Y,Z) along the path

$$S = \int_0^s F(X,Y,Z)ds \qquad (E.2)$$

However, if the shadow-area density is assumed to be a constant (see Eq. 7.5), then Eq. E.2 reduces to

$$S = sF \qquad (E.3)$$

In order to integrate Eq. 7.3 in Chapter VII, the path length s has to be evaluated at all values of θ and ν (see Figure E.2a). Thus one needs to specify the value of s as a function of (θ,ν).

If P lies within the crown, then

$$s = (Z_q - Z_p)/\cos\theta \qquad (E.4)$$

If P lies outside the crown and $Z_q \geq Z_p$ then compute s as

$$s = (Z_q - Z_n)/\cos\theta \tag{E.5}$$

If P lies outside of the crown and $Z_q < Z_p$, then

$$s = 0 \tag{E.6}$$

Since the location of point $P(X_p, Y_p, Z_p)$ is known, the problem reduces to finding the unknown point $Q(X_q, Y_q, Z_q)$. The direction of the line PQ can be defined by the direction cosines of PQ (Green, 1941)

$$(\sin\theta\sin\nu,\ \sin\theta\cos\nu,\ \cos\theta) \tag{E.7}$$

The coordinates of P and Q must satisfy the equations

$$\frac{(X_q - X_p)}{\sin\theta\sin\nu} = \frac{(Y_q - Y_p)}{\sin\theta\cos\nu} = \frac{(Z_q - Z_p)}{\cos\theta} \tag{E.8}$$

Since Q always lies on the outer surface of the crown (modeled as a right circular cone), it must satisfy Eq. E.1

$$X_q^2 + Y_q^2 = (H - Z_q)^2 \tan^2(\beta/2) \tag{E.9}$$

From Eq. E.8, solve for X_q and Y_q in terms of Z_q and (θ,ν).

$$X_q = A\sin\nu + X_p \tag{E.10a}$$

$$Y_q = A\cos\nu + Y_p \tag{E.10b}$$

where

$$A = (Z_q - Z_p)\tan\theta \tag{E.11}$$

Substitute Eq. E.10 into Eq. E.9

$$(A\sin\nu+X_p)^2 + (A\cos\nu+Y_p)^2 = (H-Z_q)^2\tan^2(\beta/2) \qquad (E.12)$$

Rearranging and substituting Eq. E.11 into Eq. E.12

$$X_p^2 + Y_p^2 + (Z_q^2 - 2Z_pZ_q + Z_p^2)\tan^2\theta + 2(X_p\sin\nu+Y_p\cos\nu)(Z_q-Z_p)\tan\theta = (H-Z_q)^2\tan^2(\beta/2) \qquad (E.13)$$

Collecting terms, Eq. E.13 reduces to

$$Z_q^2U + Z_qV + W = 0 \qquad (E.14)$$

where the coefficients U,V, and W are defined as

$$U = \{\tan^2\theta - \tan(\beta/2)\} \qquad (E.15a)$$

$$V = \{-2Z_p\tan^2\theta+2(X_p\sin\nu+Y_p\cos\nu)\tan\theta + 2H\tan^2(\beta/2)\} \qquad (E.15b)$$

$$W = \{X_p^2+Y_p^2+Z_p^2\tan^2\theta - 2Z_p(X_p\sin\nu+Y_p\cos\nu)\tan\theta - H^2\tan^2(\beta/2)\} \qquad (E.15c)$$

Solve for Z_q from Eq. E.14

$$Z_q = \frac{-V \pm\sqrt{V^2-4UV}}{2U} \qquad (E.16)$$

When solving Eq. E.16, there are two possible roots (note the ± sign). Of these two roots, only the feasible roots are of interest. A root of Eq. E.16 is feasible if and only if the root is real and if its value is less than H (the height of the tree crown). If the roots are imaginary, distance s=0.

If point P (i.e., location of the pyranometer) is located within the live crown, then coordinate Z_q is equal to the largest feasible root of Eq. E.16, such that $HLC \leq Z_q \leq H$ (see Figure E.2b). The remaining feasible root of Eq. E.16 (if it exists) is equal to coordinate Z_n, such that $Z_n \leq Z_q$. The distance between point P and point Q is computed using Eq. E.4.

If point P lies outside of the crown, there are at least three possible cases that one needs to consider.

Case 1: (See Figure E.2c), the largest feasible root of Eq. E.16 is smaller than Z_p (i.e., $Z_p > Z_q$). In this case, set s=0.

Case 2: (See Figure E.2d), the smallest feasible root of Eq. E.16 is larger than Z_p but greater than HLC. Distance s is computed from Eq. E.5. Thus $Z_q \geq Z_n \geq Z_p$ and $Z_p \geq HLC$, where HLC is the distance to the base of the live crown from the ground.

Case 3: (See Figure E.2e), point P lies below the base of the live crown, $Z_p \leq HLC$. The largest feasible root of Eq. E.16 is set equal to Z_q and Z_n is set equal to HLC. Thus $Z_q \geq Z_n \geq Z_p$ and $Z_n = HLC$. The distance s is computed from Eq. E.5.

Additional Considerations

In the above analysis, no mention was given to the dead-zone

portion of the crown. In order to solve the integral of Eq. 7.3, one may use either Eq. E.2 or Eq. E.3 to compute S. If one wishes to assume a constant shadow-area density, F, everywhere within the live portion of the crown and a zero density within the dead-zone, the following steps can be taken.

Step i) Compute distance s from Equations E.4 to E.16 using variables H, HLC and RLC (see Figure E.1). Label this distance as s_t (i.e., the total pathlength).

Step ii) Compute distance s again, but instead of H use HDZ and instead of RLC use RDZC. Label this distance as s_d (i.e., the pathlength through the dead-zone, see Figure E.3).

Step iii) The path distance (cm) through the live crown is now defined as

$$s_\ell = s_t - s_d \qquad \text{(E.17)}$$

The term s_ℓ is used instead of s in Eq. 7.5. Over distance s_ℓ, the density F is assumed to be a constant.

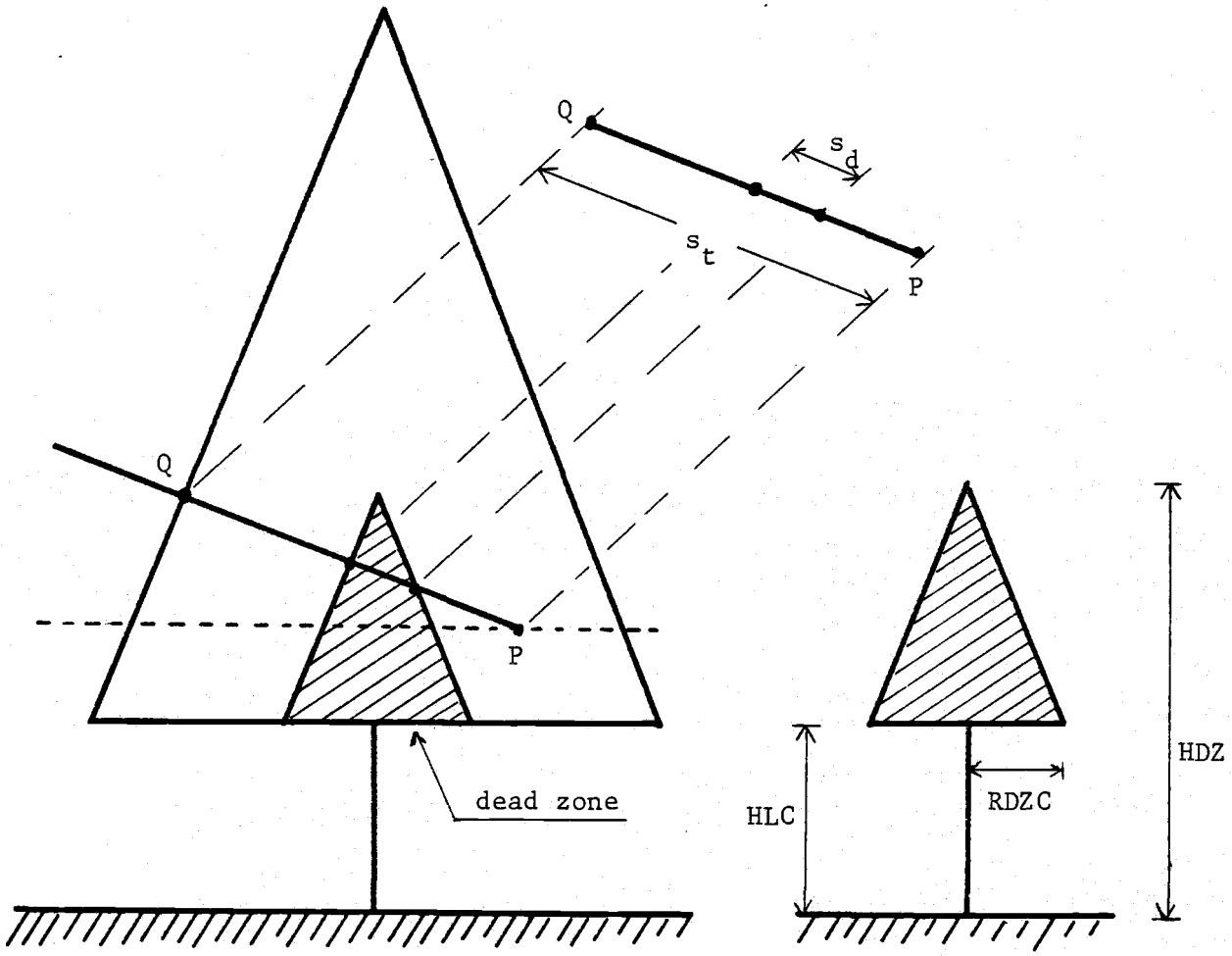

Figure E.3 Schematic showing the relationship between the live crown and the dead-zone portion of the crown. The shape of the dead-zone is assumed to resemble a right circular cone. The term HDZ means the distance (cm) from the ground to the top of the dead-zone and term RDZC means the maximum radius (cm) of the dead-zone (assumed to be located at the base of the live crown).